Analyse expérimentale et simulation numérique de sections de pales pour application aux hydroliennes

Jean-Baptiste Marchand

To cite this version:

Jean-Baptiste Marchand. Analyse expérimentale et simulation numérique de sections de pales pour application aux hydroliennes. Mécanique des fluides [physics.class-ph]. Ecole nationale supérieure d'arts et métiers - ENSAM, 2014. Français. NNT : 2014ENAM0038 . tel-03510192

HAL Id: tel-03510192
https://pastel.hal.science/tel-03510192

Submitted on 4 Jan 2022

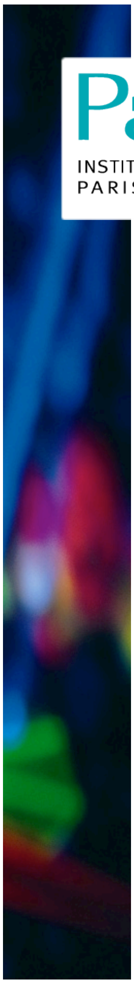

ParisTech
INSTITUT DES SCIENCES ET TECHNOLOGIES
PARIS INSTITUTE OF TECHNOLOGY

ARTS
ET MÉTIERS
ParisTech

2014-ENAM-0038

École doctorale n° 432 : Sciences et Métiers de l'ingénieur (SMI)

Doctorat ParisTech

THÈSE

pour obtenir le grade de docteur délivré par

l'École Nationale Supérieure d'Arts et Métiers

Spécialité “ Mécanique des Fluides et Energétique (MFE) ”

présentée et soutenue par

Jean-Baptiste MARCHAND

le 1er décembre 2014

Experimental Analysis and Numerical Simulation of Foil Sections for Tidal Turbine Applications

Directeur de thèse : **Jacques André ASTOLFI**

Jury

M. Marc RABAUD, Professeur des université, FAST, Université Paris-sud	Président
M. Jean-Pierre FRANC, Directeur de recherche, LEGI, Université de Grenoble	Rapporteur
M. Smaïne KOUIDRI, Professeur des universités, LIMSI, Université Pierre et Marie Curie	Rapporteur
M. Mohamed FARHAT, Maître de conférence HdR, Ecole Polytechnique Fédérale de Lausanne	Examinateur
M. Jacques André ASTOLFI, Maître de conférence HdR, IRENav, Ecole Navale	Examinateur
M. Jonathan BOSSARD, Dr Ingénieur Hydrodynamicien, Alstom Ocean Energy	Invité

THÈSE

Arts et Métiers ParisTech
Institut de Recherche de L'Ecole Navale

Acknowledgements

Avant tout développement, je tiens à remercier les personnes qui ont permis la réalisation de ce projet.

En tout premier lieu, je tiens à exprimer ma reconnaissance à André, mon directeur de thèse, pour son soutien inconditionnel et son expérience du travail expérimental qui ont permis la réussite de cette thèse. J'aimerais aussi remercier Patrick, François, Frédéric, Jean-Yves et Céline pour avoir partagé leurs expériences respectives du chaos, du numérique, de l'expérimental, du tunnel et de la PIV.

Mes sincères remerciements à Christophe Claramunt, directeur de l'IRENav, qui m'a accueilli dans son laboratoire.

Cette thèse a été conduite dans le cadre d'un partenariat avec l'Entreprise Alstom Ocean Energy, aussi je tiens à remercier tout particulièrement Jonathan Bossard, Benoît Kerling et Frédéric Pilorge pour leur encadrement efficace et leurs conseils, qui sont pour une part majeure dans la réussite de ce travail. Merci à l'ensemble de personnel d'Alstom à Nantes que j'ai apprécié côtoyer au cours de mes séjours au sein de l'entreprise: Antonin, Maxime, Christine, Philippe, ...

Ces études n'auraient tous simplement pas été possibles sans l'intervention du personnel technique de l'IRENav que je remercie vivement: Jean-Michel, Alain, Laurent, Eric, Raymond, Bernard. Un grand merci par ailleurs aux services administratifs de l'IRENav: Marie, Magalie et Christine, les deux Stéphane, Luc et Jacques, Sophie. Enfin merci aux autres enseignant-chercheurs, avec une mention spéciale pour PLD pour ses coups de main en CFD.

l'IRENav ne serait pas le laboratoire qu'il est sans la presqu'île de Crozon. Je tiens donc à remercier tous les Jean de la presqu'île, qui se reconnaitrons j'espère et avec qui nous avons partagé de sacrés bon moments: Jean-Clément pour les gadgets, Jean-Jérèm pour la pêche, Jean-Fab pour les promos, Omi Hannah pour les bons petits plats, Jean-Sam pour les soirées joebarteam quantiques, les Jean-Beunoit et Jean-Bénoit pour le Fun et les astucieux systèmes de contre-poids, Jean-Guéguette pour les planches cassées, Alek pour le bois et les planches, Jean-Vennec et Jean-Yannick, Mich pour les bières ... Enfin je tiens à remercier les animaux qui ont participé à la réussite de ce projet, en particulier Jean-Falco pour la chasse aux mouches.

Le meilleur pour la fin: un grand merci à ma famille élargie pour leur soutien, en particulier: JF, Brigitte, les frères et soeurs, ALFred, René, Roselyne, Aline, Didier ... et surtout Julie.

A mes grand-mères.

Contents

List of Figures

List of Tables

List of symbols

A	: Sweep area of the turbine	m^2
AR	: Aspect ratio of a wing, $AR = \frac{l}{c}$	/
c	: Foil chord	m
C_{Di}	: Lift induced drag, $C_{Di} = \frac{Cl^2}{\pi e AR}$	/
Cd	: Drag coefficient, $Cd = \frac{D}{(1/2)\rho U_\infty^2 S}$	/
Cd_{3D}	: Three-dimensional value of the drag coefficient, $Cd_{3D} = C_{D,0} + C_{Di}$	/
Cd_{sym}	: $Cd_{sym} = Cd$	/
Cf	: Viscous drag coefficient, $Cf = \frac{\tau_p}{(1/2)\rho U_\infty^2}$	/
CFL	: Courant number, $CFL = U_\infty \times \frac{\Delta t}{\Delta x}$	/
Cl	: Lift coefficient, $Cl = \frac{L}{(1/2)\rho U_\infty^2 S}$	/
Cl_{sym}	: $Cl_{sym} = -Cl$	/
Cm	: Pitching moment coefficient at $0.25c$ from the conventional leading edge, $Cm = \frac{M_x}{(1/2)\rho U_\infty^2 Sl}$	/
Cp	: Pressure coefficient, $Cp = \frac{P-P_0}{(1/2)\rho U^2}$	/
Cp_{min}	: Minimum value of the pressure coefficient	/
$Cpow$	: The turbine power coefficient	/
D	: Drag force	N
Di	: Diameter	m
e	: Foil efficiency factor	/
f	: Frequency of vortex emission	s^{-1}
F_{yB}	: Force in the balance coordinate frame, along the y axis	N
F_{zB}	: Force in the balance coordinate frame, along the z axis	N
I	: Turbulence intensity, $I = \frac{u'}{\bar{u}}$	/
L	: Lift force	N
l	: Foil span	m
M	: Characteristic length of the turbulence generating grid	m
M_x	: Pitching moment	$N.m$
M_{xB}	: Pitching moment in the balance coordinate frame, around the x axis	$N.m$
P	: Pressure at the foil surface	Pa
P_0	: Ambient pressure	Pa
P_{extrac}	: Theoretical power extractable from a stream using a turbine, $P_{extrac} = \frac{1}{2} A \rho V_t^3 C_p ow$	W
P_k	: Power into a stream coming from kinetic energy, $P_k = \frac{1}{2}\rho V_t^3$	W
P_v	: Vapor pressure at bulk temperature in the liquid	Pa
R	: Radius of the turbine	m
Re_c	: Reynolds number relative to the foil chord, $Re_c = \frac{U_\infty c}{\nu}$	/
Re_{Di}	: Reynolds number relative to the diameter of a cylinder, $Re_{Di} = \frac{U_\infty Di}{\nu}$	/
R_M	: Reynolds number relative to grid turbulence generators, $R_M = \frac{U_\infty M}{\nu}$	/

R_λ	: Reynolds number relative to λ_t, $R_\lambda = \frac{u'\lambda}{\nu}$	/
Rb	: Coordinate frame linked to the balance	/
Rv	: Coordinate frame linked to the test section	/
S	: Foil surface $S = c.l$	m^2
S_t	: Strouhal number, $S_t = \frac{fT}{U_\infty}$	/
T	: Foil thickness	m
TSR	: Tip speed ratio, $TSR = \lambda = \frac{\Omega.R}{U_\infty}$	/
u'	: Root mean square of the turbulent velocity fluctuations	m/s
$\bar{u}$	: Average velocity	m/s
U_∞	: Inflow velocity	m/s
Uy	: Tension in the drag strain bridge (along the yB axis)	mV/V
Uz	: Tension in the drag strain bridge (along the zB axis)	mV/V
Umx	: Tension in the pitching moment bridge	mV/V
u_τ	: Friction velocity, $u_\tau = \left(\frac{\tau_p}{\rho}\right)^{1/2}$	m/s
u_w	: Average wall velocity	m/s
V_t	: Estimated inflow velocity in a tidal stream	m/s
y	: Distance to the wall	m
y^+	: $y^+ = \frac{u_\tau y}{\nu}$	/
α	: Angle of attack of the foil	deg
$\alpha_{F_{yB}=0}$	: Angular position of the balance for which F_{yB} is zero	deg
α_{vert}	: Angle made by the foil chord relative to the flow direction at mid test section	deg
Λ_t	: Taylors macro scale of turbulence	mm
λ_t	: Taylors micro scale of turbulence	mm
μ	: Dynamic viscosity of the fluid	$Pa.s$
ν	: Cinematic viscosity of the fluid	m^2/s
ρ	: Fluid density	kg/m^3
σ	: Cavitation number, $\sigma = \frac{P-P_v}{\frac{1}{2}\rho U_\infty^2}$	/
τ_p	: Wall shear stress, $\tau_p = \mu \left(\frac{\partial u_w}{\partial y}\right)_{y=0}$	Pa
Ω	: Rotational speed of the turbine	rad/s

Introduction

In a context of development of renewable energies, there is growing interest in marine energies. Among them tidal currents are presented as a potential candidate because of the high density of seawater and the predictability of tides at any given location.

However, the toughness of the marine environment makes harvesting the kinetic energy of tides a technical challenge, with the objective to propose an efficient and reliable tidal turbine application with industrial purpose. This requires the development of appropriate solutions for turbines in order to guarantee sufficient energy production while reducing maintenance needs.

The design of the rotor is significant for the performance of the turbine. Among the steps included in the rotor design process, the choice of the blade section is critical. The challenge for the designer is to predict the constraints induced by the tidal current and the machine at the scale of the blade section so as to guide his choice of the adequate hydrofoil.

One of the most remarkable properties of high velocity tidal streams is the near bidirectionality of the flows produced by ebb and flood alternation. In the case of a horizontal axis turbine, adaptation of the rotor can be made with several systems. An individual reversing system for each blade can be used. Orientation of the whole turbine can also be achieved through a yaw adjustment system, controlling the position of the nacelle. Nevertheless it involves complex mechanical systems, with the risk of lower robustness and reliability of the turbine.

A simpler solution can be to use the blades in forward and reversed flow without any mechanical adjustment. The power regulation can therefore be achieved by controlling the rotational speed. In this case, specific rotationally symmetric bidirectional blades or a unidirectional section in forward and reversed flow can be used (OG+1 et al. [2007], Nicholls-Lee et al. [2011a]). Nonetheless both solutions result in geometrical specificities. In the case of the reversed hydrofoil, a thick rounded trailing edge and a sharp leading edge may lead to specific hydrodynamic behaviors. Bidirectional hydrofoils are a compromise and also result in a relatively round trailing edge and a sharper leading edge compared to a standard foil.

However, designing a turbine without returning systems involves some important issues that may reduce the amount of power captured. On most of the potential production sites, there is a current deviation between ebb and flood. A fixed turbine, depending on the variation angle, may experience a severe decrease in efficiency unless it is equipped with a flow canalizing device. But variations of the tidal current velocity due to waves or large scale turbulences are making the design of a ducted turbine a challenge.

Therefore numerous companies have chosen to develop wind energy inspired tidal turbines, equipped with a pitch and a yaw regulating system. This type of turbine generally works at a higher rotational speed compared to the inflow velocity which is achieved by a low solidity type of rotor. Structural constraints on the blades are increased and have to be handled by blades characterized by a reduced chord length. For this purpose, high performance thick foils were developed by the wind energy industry.

As bidirectionality of the flow is dealt with by the yaw returning system, constraints on the blade section are changed. Even though they also affect fixed yaw and pitch turbines, issues such as surface roughness and upstream turbulence are becoming predominant on wind energy inspired types of tidal turbines. They are even more significant as roughness due to biofouling and turbulence intensity and scale in a tidal stream far exceed conditions occurring on wind turbines, for which the foil were designed.

Before performances of the whole turbine are studied, it is necessary to study the turbine configuration at the scale of the blade section on an academical setup. This is the purpose of the work presented here. Experimental and numerical investigations are proposed here, as a first-stage performance assessment to be used for tidal turbine design.

Objectives of the thesis are part of one main issue: **How tidal current constraints affect the choice of the turbine blade section?** In agreement with the two main turbine design strategies presented above, it as been divided in two subquestions:

1. **Which strategy to choose for the blade to respond to the bidirectionality of the flow without a returning system ?**
2. **What is the response of a classic blade to major onsite flowing constraints?**

This project has been carried out under the framework of a partnership between the Research Institute of the French Naval Academy (IRENav) and the company ALSTOM Power Hydro. The path described above is approximatively the one followed by the industrial partner of this research project, and the objectives of the thesis have been adjusted to the evolutions of the industrial turbine design. They are detailed below.

1. **Study of two strategies at the scale of the blade section to meet with the bidirectionally of the flow while removing any returning system.**
    - **Academic hydrofoil in forward and reversed flow (NACA 0015, respectively Figure 1(a) and 1(b))**
    - **Bidirectional hydrofoil (Elliptical, cambered, Figure 1(c))**
2. **Study of a high-performance, cambered and relatively thick foil for a machine with pitching and yawing systems (DU91-W2-250, Figure 1(d)).**
    - **Effect of laminar-turbulent transition**
    - **Effect of surface roughness**
    - **Effect of upstream turbulence**

These situations were studied using both experimental analysis and numerical simulation, applied to two-dimensional academic foil configurations. The whole studies were designed to be carried out within the limits of the tunnel capacity, with regard, for example, to the inflow velocity or the hydrodynamic force on the foil. For each of the cases, force measurements were carried out and lift force, drag force and pitching moment were measured. This was completed by flow observation and inflow velocity measurements, using PIV. Calculations were compared to experimental data.

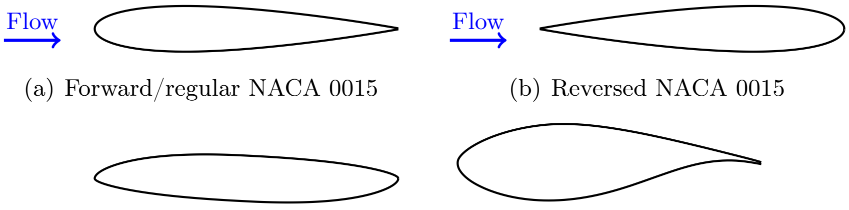

(a) Forward/regular NACA 0015 (b) Reversed NACA 0015

(c) Elliptical (d) DU 91-W2-250

Figure 1: Foil configurations

The present document is divided in five chapters, as detailed below.

First, the global context is introduced. Tides and the tidal current environment are presented from the point of view of the hydrodynamic flowing conditions. A progressive focus is applied to the rotor, the blade and finally the foil section.

A significant part of the work was experimental, and thus the second chapter focuses on the experimental setup which is described in detail. Force measurement was a major aspect, therefore the hydrodynamic balance and a new calibration procedure are presented in depth. Finally the measurement protocol is introduced.

Experiments were completed by CFD investigations. The numerical model is introduced in the third chapter. The numerical model strictly speaking, is at first presented with the details of the boundary conditions, turbulence models and mesh strategies. Then a sensitivity study regarding the mesh size and the time step are presented. Finally a comparison is done with experiments carried out on the NACA 0015 hydrofoil.

Chapter four presents a comparative study of two solutions to account for the bidirectionality of the flow at the scale of the blade section. The NACA 0015 in forward flow is presented first. Then its properties in the reversed flowing configuration are described. Finally, a specific bidirectional foil section is studied. For all foils, smooth and turbulent configurations are used. Both strategies are then compared with regard to the global properties of the foil sections, being critical for the power production of the turbine: the maximum lift to drag ratio and the maximum lift.

Chapter five focusses on a Delft University foil. After a presentation of the foil properties as measured and calculated with a smooth and a turbulent configurations, the effect of surface roughness is studied for two Reynolds number values. The effect of a high upstream turbulence intensity is then investigated. Performances are then discussed and compared on the basis of the maximum lift to drag ratio and the maximum lift.

A global conclusion is finally presented regarding both problematics. Perspectives for further investigations are introduced regarding the results themselves but also the experimental and numerical setups, as well as application of the results in the blade design process of the industrial partner.

Chapter 1

Tidal streams and tidal turbines

Summary: Designing a tidal turbine requires a global understanding of tides and the properties of tidal streams. The choice of the turbine's operating strategy also sets the main constraints for the blade section design. This first chapter attempts to propose an overview of the tidal kinetic energy environment and its consequences on the design of the tidal turbine.

Contents

1.1 Tides, an energy ressource

Predicting the energy production of a tidal turbine requires a reliable estimation of tidal currents. Tidal models form the basis of this estimation.

It is a well-known fact that tides are produced by the conjugated gravitational attractions of the moon and the sun. The static tidal theory is the direct application of this statement, through the tidal bulges concept, referring to the gravitational influence of the moon and the sun on an hypothetical global ocean. However, tides are also influenced locally by the shape of the basin, and therefore a more complete theory is needed. The dynamic tidal theory accounts for the basin geometry and enables to propose a more accurate tidal current and water level estimations through a dynamic analysis of the tidal signal.

These two theories are succinctly presented. The energy available in a tidal current and theoretically extractable, is then presented.

1.1.1 Static tidal theory, Kvale [2006]

Static tides are defined through the combined gravitational attraction of the moon and the sun, applied to an ideal earth. The ideal earth is entirely covered with uniformously deep water areas able to instantly respond to fluctuations in the attraction forces (MacMillan [1966]). In this static model, moon and sun attractions, in addition to the effect of the earth's rotation around an Earth-Moon mass-center, produces oceanic bulges on both sides of the globe (Figure 1.1(a)). The bulge tends to follow the movement of the moon, as its proximity to earth makes account for about 70 % of the tidal forces. Earth's rotation inside these bulges produces two tides per day (semi-diurnal). Subsequently, when a location enters in the bulged zone, the tide rises (flood). As well when a location goes toward the exterior of the bulge, the tide falls (ebb). This model is incomplete and, for example, diurnal tides using static tidal theory are only possible at very high latitudes.

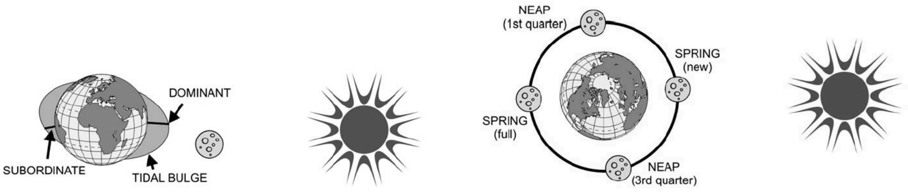

(a) Semi diurnal cycle, static tidal theory (b) Synodical cycle

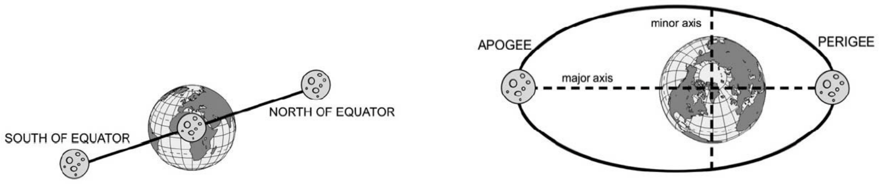

(c) Tropical cycle (d) Anomalistic cycle

Figure 1.1: Cycles for the Equilibrium/Static theory of tides, adapted from Kvale [2006]

In the static tidal theory, several types of variations in tidal intensity can be identified. The most important is the neap tide - spring tide cycle illustrated in Figure 1.1(b). It is associated with changes in the moon phases. Spring tides are therefore occurring at new and full moons, every 14.76 days, when the earth, the moon and the sun are aligned. Neap tides occur when the moon and the sun are "perpendicular", during first and third moon quarters. As a result, water level is higher during spring tides, in comparison with neap tides. The duration between two new moons is called the synodic period and is 29.53 days.

The rotation plan of the moon is also tilted in comparison with the equatorial plan, meaning that the tidal level also depends on the position of the moon relative to the equator. This fact is called the tropical oscillation and lasts 27.32 days (Figure 1.1(c)). In the static tidal theory, this phenomenon is responsible for the difference between two diurnal tides. In an ideal case this difference is non-existent on the equator.

Finally the elliptic trajectory of the the moon's orbit around the earth is responsible for the anomalistic period (27.55 days, Figure 1.1(d)). The moon runs along its elliptic trajectory between the apogee and the perigee, generating the difference observed between the two spring tides in a month.

1.1.2 Dynamic tidal theory

The static tidal theory is incomplete as it does not take aspects of the local environment in consideration, such as the bathymetry or the shape of the basin. Thereby, it fails to accurately predict tidal parameters at a given location. The dynamic tidal theory is based on onsite analysis and is more realistic.

This theory is applied through an the analysis of tidal oscillation harmonics. Measurements of sea level at a given location are used to determine the harmonic components. Hundreds of components have been identified and each of them can be modeled using a fictive satellite as described by Pugh [1987]. Satellites allow to represent movements and angular velocity of the moon and the sun compared to the equator. Each of the satellites has its proper mass and movement, resulting in its own tidal wave. These components are moving around amphidromic points and major tides are the function of the convergence or divergence of some predominant harmonic components. Geometry of the basin allows to determine which of the components will be locally amplified. Generally, as noticed by Defant [1961], generally seven components are sufficient to describe 80 % of the tidal range. A reconstitution of a tidal wave using 9 components and proposed by MacMillan [1966] is given in Figure 1.2 as an example.

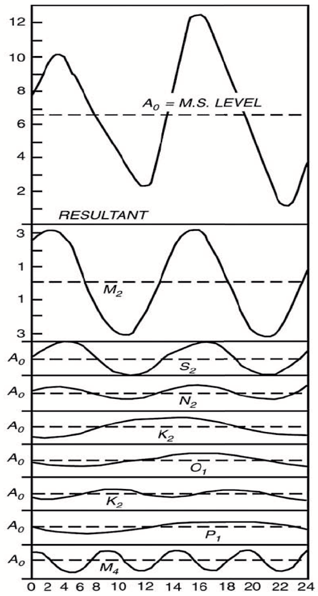

Figure 1.2: Example of a tidal oscillation modeled using nine components, MacMillan [1966]

1.1.3 Kinetic energy of a tidal current

The dynamic tidal theory is used for to predict flowing velocity and water level at a given location. Using the predicted flowing velocity, extractable energy can be calculated. Fraenkel [2002] gives an example of a simplified model using a double sinusoid. A first period corresponds to the daily ebb and flood cycle (12.4 hours) and a second one models the bimonthly repetition of ebb and spring tides (353 hours). The following Equation (1.1) then allows for an evaluation of flowing velocity:

$$V_t = \left[K_0 + K_1 cos\left(\frac{2\pi t}{T_1}\right)\right] cos\left(\frac{2\pi t}{T_0}\right) \tag{1.1}$$

K_0 et K_1 are constants derived from neap tide mean peak and mean neap-tide and spring tide currents. T_1 is the period between neap and spring tides and T_0 is the diurnal period.

This is a first approximation and several other factors that can induce local flowing velocity variations should be taken into account for more accurate power estimations. These are, for example, global oceanic circulation, wind surface currents, wave induced velocities or the velocity gradient along the depth.

Once the tidal velocity is modeled, power from kinetic energy of the flow can be expressed using Equation 1.2. It is obviously a function of the velocity and the fluid density.

$$P_k = \frac{1}{2}\rho V_t^3 \tag{1.2}$$

Due to the high density of seawater, tidal streams are characterized by a particularly high power density compared to wind or solar energies, as presented in Table 1.1.

Energy ressource							
	Marine currents					**Wind**	**Solar**
Velocity (m/s)	1	1.5	2	2.5	3	13	Max.
Velocity ($knot$)	1.9	2.9	3.9	4.9	5.8	25.3	
Power density (kW/m^2)	0.52	1.74	4.12	8.05	13.91	1.37	$\simeq$1.0

Table 1.1: Power density for the main renewable energies, Fraenkel [2002].

The theoretically extractable power is however a function of the turbine efficiency and its size, as expressed in Equation 1.3.

$$P_{extrac} = \frac{1}{2}A\rho V_t^3 C_{pow} \tag{1.3}$$

The potential for energy extraction from tides is therefore sufficiently promising, and technologies able to harvest tidal streams with sufficient reliability and efficiency are the focus of a great interest.

1.2 Constraints for harvesting the kinetic energy of tides

Predictability as well as high power density are making tidal currents a promising energy. However, to achieve economic viability over time, tidal turbines must reach a high level of performance and reliability. Several constraints have to be taken into account to understand the underlying technical challenge. The profitability of a given turbine for a given site is roughly a compromise between the actual performances of the machine and its robustness, disregarding farm effect. Therefore, providing an efficient tidal turbine requires the knowledge and the understanding of operating constraints encountered in a tidal flow. The following part introduces the main constraints encountered locally by a tidal turbine.

1.2.1 Tidal Streams

High velocity

The first and most obvious constraint encountered in a tidal flow is the high average current velocity.

For example, and according to the European-Commission [1996], a site for tidal turbine application has to reach a rated velocity of at least 1m/s to be economically viable. The more the tidal stream exceeds this limit, the more interesting is the site. For example, in the Alderney race, the tidal current is most of the time higher than this rated current limit. Associated with an interesting bathymetry, the Alderney race can be considered as a high potential site (Myers and Bahaj [2005]). Another interesting site is the Minas passage in the Bay of Fundy, Canada. According to Karsten et al. [2013] and Karsten et al. [2008], the average tidal current exceeds 9 to 10 knots, depending on the position in the passage. The EMEC site of the Fall of Warness also experiences very strong currents (Norris and Droniou [2007]), reaching 7.5 knots during spring tides.

Potentially interesting sites are therefore reaching the minimum 1m/s flowing velocity required, but are also experiencing very high current velocities. Structural requirements for turbines in such a current stream are significant.

Turbulence

In addition, the flow is generally very turbulent and the flowing velocity varies locally.

As presented by Gooch et al. [2009], tidal turbine installation sites are subjected to high turbulence intensities – up to 25 % –, with very large length scales (Guinot and Le Boulluec [2008] and Master et al. [2007]). This can be explained by the fact that most high potential sites are located in regions of flow contraction, along a point or in a straight, meaning shallow or narrow passages. This results in important shear zones, in both vertical and the horizontal directions (Lundin and Leijon [2001]).

At the scale of the turbine, it results in large fluctuations in direction and magnitude of the inflow velocity. It has an effect on both the turbine performance and its wake properties (Maganga et al. [2009], Maganga et al. [2010], Germain et al. [2010] and Tedds et al. [2012]). More precisely, Milne et al. [2010] have shown that using simulations, the longitudinal intensity of turbulence is the dominant parameter where blade loads are concerned. If we look at this from the scale of the blade section, predicting the effect of turbulence requires heavy computation methods such as LES or DNS, as shown in the work done by Gilling [2009] applied to wind turbines.

Moreover, turbulence properties are site-dependent, which requires onsite characterization using ADCP measurements for example (Rippeth et al. [2002], Trevethan et al. [2010]) and the proper qualification for tidal energy application as proposed by Thomson et al. [2010].

Cyclicity, reversibility

Tides are also a cyclic phenomenon which is characterized by several time scales. This induces cyclic variations of the flow properties, once again in velocity level and direction.

For example, ebb and flood alternations generates tidal stream variations. Some sites can be considered to be bidirectional with regard to the current direction, but for others, the alternation between ebb and flood is more progressive and there is no clear direction. Moreover, bidirectional does not mean that the flow is perfectly reversed between ebb and flood. Most of the time, specificities of the site are inducing a different channeling between ebb and flood, depending on the direction of the incoming current the bathymetry and the geometry of the basin.

An example extracted from Gooch et al. [2009] is given in Figure 1.3 for two locations. There is a clear difference between the two side regarding the range of direction and intensity of the current velocity. Asymmetry and deviation can be used for tidal current description, such as the difference between ebb and flood angle; and the standard deviation on both ebb and flood. In this example (Figure 1.3) the site called "C5" presents more asymmetry and deviation compared to the "Admiralty inlet", resulting in a site that is probably less productive and more constraining for the machine.

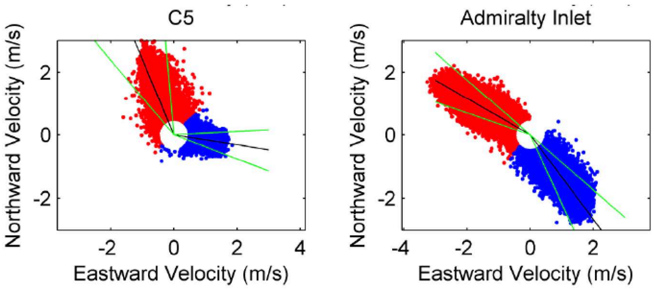

Figure 1.3: Ebb (red) and flood (blue) tidal current properties at two locations, Gooch et al. [2009]

Tidal current is also three-dimensional and this aspect affects the turbine. The more important the diameter of the turbine, the more significant the three-dimensional effects. In a first approach, the tidal stream can be considered as a boundary layer. In that case a classic power law (1/7th or 1/5th) can be used to describe evolution of the average inflow velocity with depth (barotropic tidal wave). However, in some cases, the velocity variation along depth can be significantly more complicated with for example the case of baroclinic tidal wave (Figure 1.4). In that latter case, important shear will occur on the machine.

There is therefore a variability of direction and intensity with regard to the incoming flow field. The timescale ranges from the year to the second, which can be translated into a variety of incoming flow with regard to the velocity level and direction, at several times scales. At the scale of the machine, some can be considered to be quasi-static, while others are clearly dynamic.

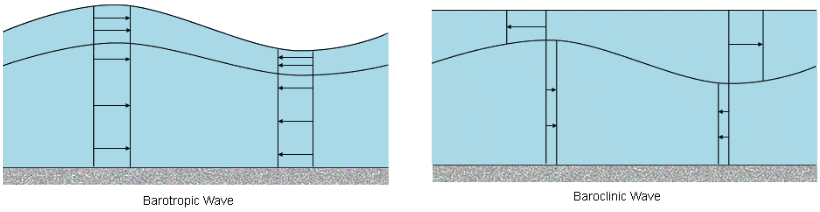

Figure 1.4: The two types of tidal waves with regard to velocity variation along depth, Department of Oceanography

1.2.2 Waves

Tidal currents are not the only phenomenon generating water displacements on a tidal stream extraction site. Among others, swell waves are significant.

Waves are inducing an almost circular movement of the water particles, the amplitude of which decreases with depth (WMO [1998]). This circular movement comes with a more limited water displacement in the direction of wave propagation. These particle movements are a function of the wave height, period and direction. They are also affected by the bathymetry and exposure of the site. At the scale of the turbine, the velocity variation is a function of the wave properties: height, period and direction at the turbine position, compared to the position of the rotation axis.

Furthermore, there is a wave-current interaction, as explained by Hedges [1987]. Currents alter wave celerity and subsequently affect the relationship between wavelength and the observed period. It has an effect on wave height (Merkoune et al. [2012]) and current-induced refraction can occur. Waves are therefore modifying the tidal current velocity and its direction depending on depth. As was also noticed by Rey et al. [2008], current can be homogenized by the action of waves in relatively shallow waters. As for the turbulence, onsite observations are generally required to calibrate numerical models and properly quantify the effect of waves on the energy potential of a given site. However, as noticed by Rey et al. [2008], wave-current interactions are generally difficult to quantify onsite due to the rotational movement of particles.

Waves are an issue as soon as some of the most interesting sites for tidal turbine application are exposed to ground swells. For example the well known site of the Orkney European Marine Energy Center (EMEC) site is subjected to wave-induced currents, according to Norris and Droniou [2007]. Velocity fluctuations were measured using ADCP, and velocity fluctuations between 1m/s and 3.5 m/s were observed relatively close to the surface. At about 20m from the seabed, the fluctuations were lower: 1m/s to 2m/s, which can still be significant. The Alderney race also is exposed to ground swells from the Atlantic Ocean.

Basically, waves are inducing variations of the current velocity and direction that must be predicted. Waves can be modeled on a given site through spectrum and general circulation models, as noticed by Holthuijsen et al. [2003]. Wave-current interactions can also be predicted, even in an irregular bathymetry (Guinot et al. [2008]). However, one of the most commonly used approaches is the direct application of wave-induced velocity profiles as boundary condition in commercial CFD codes (Gant and Stallard [2008] and Lawson et al. [2011]). As noticed by McCann [2007] this computational solutions has to be fed with accurate onsite measurements if more effective designs are to be achieved.

1.2.3 General underwater marine constraints

In addition to factors having a direct influence on tidal current properties, several factors linked to the marine environment have an indirect impact on the performance of the machine. Underlying constraints are influencing the lifetime, the design, as well as the hydrodynamic performances of the turbine.

The number one factor is the wet and salty environment. For metal parts, corrosion drastically reduces the lifetime of components. However, composite materials are also subject to changes due to ageing in seawater. For example, according to Roy [2012], failure mode can be changed and weight gains between 1 % and 5 % can also be expected. Both static and fatigue behaviors are changed. These issues have an indirect influence on the performance of the turbine through higher structural requirements, met by less hydrodynamic components. For example, thickening the blade sections is the usual way of structurally reinforcing the rotor, however this increases the sensitivity of the blade to surface roughness.

Increasing the scale of the tidal turbines to meet with profitability objectives, also raises the pressure gradient issue. Due to the density of seawater, pressure changes with rotation, as the blade travels through the height of the tidal stream. Phenomena such as cavitation may be affected by this variation, meaning foil properties are affected as well. It generates some issues regarding structural design when hollow composite blades are used for example. Fluctuating loads can be expected and they must be accounted for in the structural design, resulting in generally less effective blades with regards to hydrodynamics.

Seawater is also riddled with all sorts of marine life. As noticed by Turnock et al. [2009], any surface immersed in seawater is subject to fouling, it is just a matter of time. Biofouling is site-dependent but is also affected by the properties of the object. Polagye and Thomson [2010] or Brient [2004] have shown that parameters such as material, surface finish and color may influence the extent of fouling. This natural roughness at the turbine surface may drastically alter its performances. At a first stage, biofouling can induce an increase in surface roughness which could influence performance. If more developed, marine growth can also affect the geometry. As noticed by Polagye and Thomson [2010], fouling mainly occurs on edges and in crevices, more than it does on smooth surfaces. As a result, leading and trailing edges of blades may be the most affected, which could be critical for blades performance. This may lead to unexpected blade properties, rendering inadequate the rest of the machine design. In practice a more reasonable process is to account for the use of antifouling in the design. However, the inherent roughness of the antifouling must be taken into account, as it alters the surface finish (Atlar et al. [2002]).

Finally, ocean engineering is subjected to rough and technical operating conditions that may result in unsuspected situations for the machine and unsuspected constraints. An example could be the installation of a floating turbine. In that case, the machine is towed to the site. This towing operation have an impact on machine integrity as it leads to unusual flowing conditions, at the scale of the blade for example.

1.3 Tidal turbines

Concepts and designs for harvesting the kinetic energy of a flow are numerous (see Rokke and Nilssen [2013]).Still, three main turbine designs can be highlighted and are presented below.

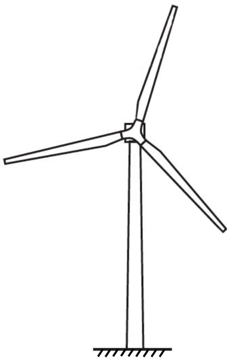

Figure 1.5: Schematic view of the most commonly used design for vertical axis turbines, adapted from Burton et al. [2011]

1.3.1 Horizontal axis turbines, HATT

A horizontal axis turbine is a machine for which the rotational axis is parallel to the flow. It is the most well-known design, commonly used for wind turbine applications (particularly for medium to large sized turbines).The technology comes from windmills and has been optimized gradually through design and structural improvements. Three-bladed turbines are the most widely used currently for wind energy (Figure 1.5), as it is a good compromise between adjusted rotational speed, reduced force variations and performance.

For tidal turbine applications, horizontal axis turbines have become a standard and several prototypes as well as pre-industrial machines have been developed. The marine environment introduces new constraints, resulting in a diversity of design strategies. For example, the density of seawater enables the design of RIM driven turbines, for which the generator is placed around the rotor. In that case it is possible operate the turbine at relatively low tip speed ratio, which reduces cavitation risk but decreases performances. An example of such a design is the project developed by Open Hydro, which also includes a duct and bidirectional blades.

More conventional wind turbine designs are also used with some variations in the design strategies. For example the machine designed by Alstom uses classical pitch regulated blades with unidirectional foil sections, while Voith is testing similar three bladed turbine which are not pitch regulated and use bidirectional blades. These turbines are not ducted and the generator is placed at the center of the rotor. They generally work at a higher tip speed ratio compared to the previous example and their performances are greater.

More original designs are also proposed, such as double rows of contra-rotating blades O'Doherty et al. [2009] or the composite ducted turbine described by Wang et al. [2013] and even using blades inspired from humpback whales (Gruber et al. [2011]).

The three designs are illustrated in Figure 1.6.

1.3.2 Vertical axis turbine, VAT

Vertical axis turbines have a rotational axis that is perpendicular to the direction of the flow. They are inspired by watermills and have the advantage to of being insensitive to inflow velocity direction. The two main vertical axis types of turbines are illustrated in Figure 1.7.

(a) Open Hydro (b) Voith (c) Alstom

Figure 1.6: Tidal turbines developed by Open Hydro,Voith and Alstom

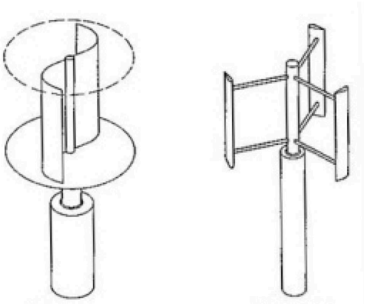

(a) Savonius (b) Darrieus

Figure 1.7: Types of vertical axis turbines

The Savonius type of horizontal turbine uses drag force on the blades to generate rotation. Performance is low but it is compensated by the simplicity of the set-up. The Darrieus type of turbine uses lift, which drastically improves performance. This last type of machine is subjected to many developments and design variations are plentiful.

These types of turbines are generally used for shallow waters or rivers. Their performance is generally slightly lower compared to classical horizontal axis turbines, however use of advanced pitch regulating systems have greatly improved the power extracted (Paillard [2011]).

1.3.3 Oscilating wings

The last category of kinetic energy capturing devices is the oscillating wing. It is based on a wing in vertical oscillation, which results in extractable mechanical energy. The movement is obtained by pitching the wing alternatively, which generates an alternative vertical effort. The Stingray project by the company Engineering Business is a direct application of this concept (Figure 1.8). Several variations exist with, for example, designs using horizontal or multiple oscillating wings.

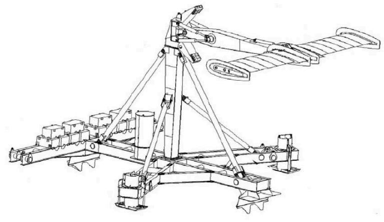

Figure 1.8: Example of an oscillating wing, Stingray project

1.4 Horizontal axis tidal turbine, requirements for a blade section

For horizontal axis turbines, there are two main strategies that can be highlighted for the design of the machine. The following part presents design principles and parameters, with a focus on their impact on blade section design.

1.4.1 Design strategies

The two main designs are: low speed/high torque as well as high speed/low torque machines. As presented in Figure 1.9 and as summed up by Schubel and Crossley [2012], each of the two solutions has advantages and drawbacks.

The low rotational speed, high torque solution is also characterized by a low tip speed ratio, which is the ratio of rotational speed over inflow velocity. The solidity, i.e. the ratio of the rotor surface on the swept surface, needs to be relatively high with numerous and relatively large blades. For tidal turbine applications this has the advantage of reducing the risk of cavitation. However, the efficiency remains relatively low, due to important rotational wake (Gash and Twele [2002]). Moreover, as the proportion of the apparent velocity due to rotation reduces,

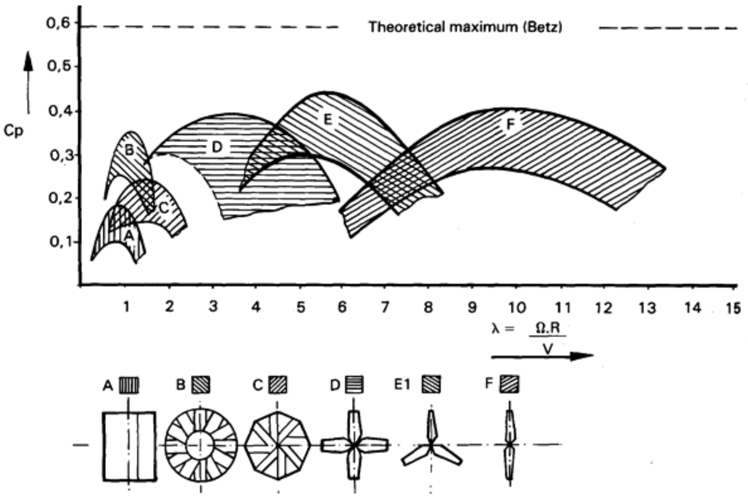

Figure 1.9: Relation between solidity, tip speed ratio and power from a horizontal axis kinetic energy capturing device, Fraenkel [1986]

the device is more sensitive to properties of the incoming current (fluctuation of the velocity amplitude and direction). For these two latter reasons such turbines are generally designed with a duct. Many studies have been conducted on the use of a duct for enhancing wind or tidal turbine performances (Lawn [2002], Kirke [2003], Al-Bahadly and Petersen [2007], Münch et al. [2009], Gaden and Bibeau [2010], Luquet et al. [2010], Shives [2011] and even more original designs such as that proposed by Wang et al. [2013]). The duct channels the flow through the convergent, which increases the fluid's velocity as well as the turbine's power production. By channeling the flow it also cleans up the incoming fluid and reduces turbulence. It makes the turbine less sensitive to the flowing direction, which reduces the need for the machine to be equipped with an orientation system. More specifically, it allows to decrease blade tip vortices which also slightly increases performance. If the machine is RIM driven, it drastically reduces stresses on the blades, but mechanical constraints on the duct are high.

The second strategy for turbine design is high rotational velocity and low torque. Such a type of turbine works at relatively high tip speed ratio (generally around TSR=8), which drastically reduces sensitivity to the incoming flow. Indeed, the apparent velocity at the scale of the blade section is driven by the rotation, which smooths variations of the upstream flow. Higher tip speed ratio is also associated with reduced rotor solidity but structural stresses remain, particularly centrifugal ones (Gash and Twele [2002]). This requires the development of thicker blades.

1.4.2 Blade design

The blade design is dependent on the chosen design strategy.

In the first case, blades are used at low TSR, also meaning lower Reynolds numbers at the scale of the blade section. Structural constraints on the blade are low and solidity is higher, translating into blades with large chord lengths and a moderated relative thickness for the foil sections. Moreover, it can be envisaged not to use a blade/machine returning system, partially due to the use of a duct. Therefore two solutions can be considered: use of a standard foil in forward and reversed flow, or designing a specific bidirectional section that works identically in both directions (OG+1 et al. [2007], Nicholls-Lee et al. [2011a]).

In the second case, relatively high tip speed ratio induces important stresses on the blade, which are significant due to the low solidity of the rotor. This results in a type of foil section that has a more important relative thickness compared with the previous case, but able to work at high reynolds number values while avoiding cavitation. In that last case the flow is not channelled and the blades must be pitched in order to reach adequate performances. This makes it possible to control the amount of power produced and it could be used to counter variations in the incoming velocity. It is combined with a yaw orientation system for the whole turbine.

Some constraints shared between the two machine strategies.

Regarding the functioning cycle of a machine in both cases and from the point of view of blade action design, the mode of operation of the turbine can be divided into two parts (Van Rooij and Timmer [2004]). The first is the increase of the extracted power from the start to reach the rated power of the turbine. The second is the power restriction part, where the rated power is reached and the machine is tuned to maintain this value. In the first case, the main characteristic required for the foil is a high lift to drag ratio, while in the second case considerations focus on the maximum lift.

Sections at the base of the blade are the least productive in terms of energy but are significant for structural reasons. The root part of the blade, however, is the most important for starting the machine, as the chord is larger. The requirement for these sections is a high amount of lift, as long as it is this component of the hydrodynamic force which is used for starting the machine when it is not rotating.

Conversely, tip blade sections are significant for energy production and subject to lower structural constraints. At this position on the blade, the fluid velocity is increased. Moreover these sections are efficient when the rotational speed of the turbine is at the rated value. There is an important displacement of the blade in the fluid perpendicularly to the rotational axis of the turbine. Therefore, the drag enters in the balance and the design objective for tip blade sections focusses more on the maximum lift to drag ratio.

Cavitation also is a significant aspect. The diameter and rotational speed of the current tidal turbine designs are making it likely to occur, and even more so when the blade is closest to the surface, as the pressure is the lowest (Wang et al. [2007]). When cavitation occurs, performances of the blade are altered and generally lowered, while the blade's ageing process can be accelerated due to erosion by cavitation. At the scale of the foil section, geometrical parameters can be modified to avoid cavitation by smoothing the pressure drop at the suction side. A classic example is the modification of the nose radius (Valentine [1974]).

Two axes of reflection can be drawn from this study.

The first is about behavior of a moderately thick (15 %) profile for application to a ducted low TSR machine. The blade section must be able to correctly operate in forward and reversed flow. The question is to know whether the use of a classic unidirectional section in forward and reversed flow is possible; or is it required to develop a specific bidirectional section, that is able to operate identically in both flowing directions.

The second strategy is a machine inspired from wind turbines. Thicker high performance foils can be used. They are generally directly coming from wind energy industry, but some are specifically developed for tidal turbines (Grasso [2011]). As these turbine are equipped with reversing systems, the issue becomes the effect of transition, roughness or upstream turbulence on the properties of such a foil.

Chapter 2

Experimental setup

Summary: A major part of the present thesis deals with experimental analyses. They have been carried out in a hydrodynamic tunnel, equipped with several measurement tools. Objectives of thePhD required that forces, inflow velocity, velocity fields and turbulence level be measured, and simultaneously for some. This requires measurement tools that are capable of repeatability, stability and accuracy. This chapter of the thesis presents the experimental materials and procedures that have been used. Firstly, a presentation of the tunnel is provided. In a following section, hydrofoils are described as well as the mechanical setup. Then the hydrodynamic balance and a calibration procedure are detailed. PIV and LDV measurement methods are also introduced. Finally, the measurement protocol is presented.

Contents

2.1 Hydrodynamic tunnel

Measurements were carried out in the hydrodynamic tunnel of the French Naval academy Research Institute (IRENav). The tunnel had its standard setup for most of the tests, and for certain particular investigations, turbulence generating grids were added. An overview of the tunnel and its turbulence generating system operating principles is presented below.

2.1.1 Overview

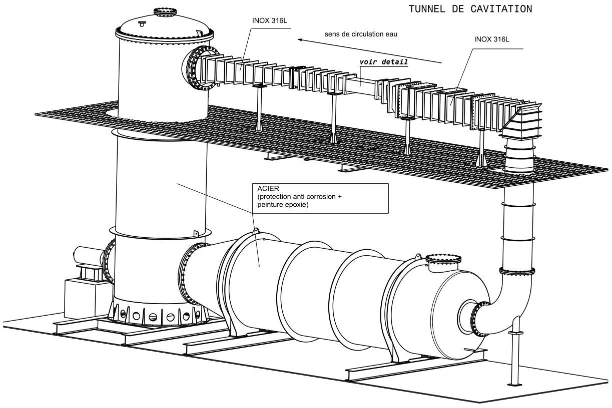

Figure 2.1: Hydrodynamic tunnel of the French Naval academy Research Institute.

The tunnel (Figure 2.1) is designed for studies of flows around two-dimensional or three-dimensional types of obstacles such as hydrofoils, installed in the test section. The whole installation, which is 15 m long and stretches over two floors, is pressurized. The flow is produced by an electric propeller pump, controlled by a converter with an accuracy of 0.1 % on the rotational speed. Pressure regulation is achieved through two servo-valves controlled by a Yokogawa type regulator and which has a theoretical accuracy of 2.5 mbar.

These valves let the residual air reserve, located in the downstream tank; to communicate with a high pressure (6 bar) and a low pressure (0.05 bar) reserve respectively. Regulation is controlled by an automaton which runs the flowing velocity as well as the pressure regulators.

The tunnel test section is 192 mm*192 mm and 1 m long downstream of a 1/9 contraction convergent (Figure 2.2). A slight divergent is included in the test section geometry (Figure A.1). It is designed to counterbalance boundary layer development. The hydrofoil is generally located at 96 mm from the top of the test section, close to mid-height of the section.

In the test section, velocity ranges from 2.5 m/s up to 12 m/s and pressure can be set between 0.1bar and 3 bar. Inflow velocity is measured by two pressure sensors located upstream of the convergent section and at the test section entrance respectively. The velocity is then computed from the pressure difference between upstream and downstream sensors. As a double check, velocity is also calculated from PIV measurements (see Section 2.5). Measurements are

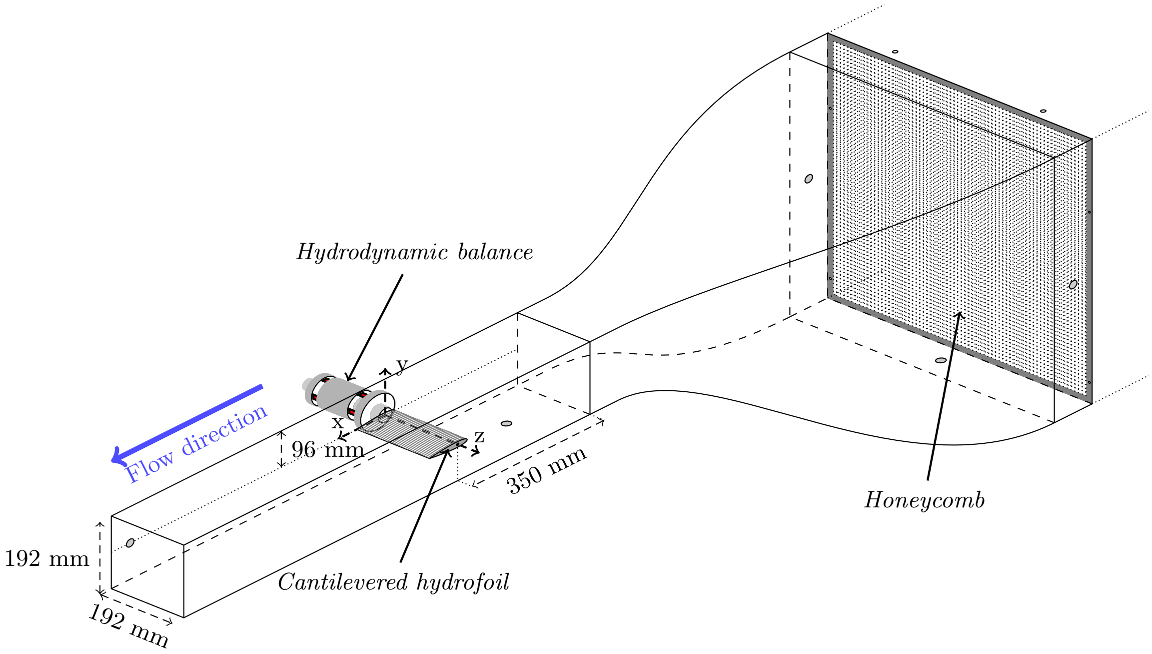

Figure 2.2: Tunnel test section characteristics and hydrofoil position.

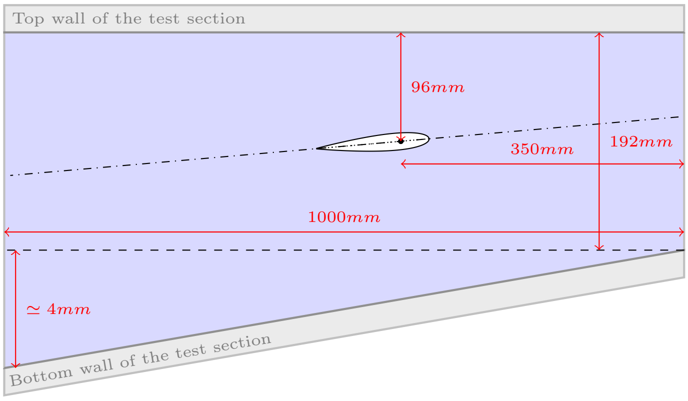

Figure 2.3: Geometrical characteristics of the tunnel test section, (the slope of the bottom face is exaggerated)

generally carried out at 5 m/s, 7.5 m/s, and/or 10 m/s. For a 100 mm hydrofoil, this results in Reynolds number values ranging from $Re_c = 5 \times 10^5$ to $Re_c = 10^6$.

2.1.2 Turbulence generation

The standard tunnel design includes two honeycombs upstream of the convergent in order to smooth the flow. Combined with the convergent effect, this results in a reference turbulence level of 1.8%, measured using LDV (see Section 2.6) and for a flowing velocity of $5m/s$, similar to values given by Leroux [2003] and Ducoin [2008].

For the generation of higher turbulence levels two techniques have been tested.

First, honeycombs were removed. This resulted in only a slight increase of turbulence intensity. This also indicates that the turbulence level is mostly controlled by the convergent, which removes turbulences by channelling the flow. It has therefore been decided to install grid turbulence generators. As shown by Chassaing [2000], for homogeneous and isotropic turbulence, grids are only able to generate between 3 % and 5 % of turbulence intensity. For tidal currents, studies by Milne et al. [2010] and Thomson et al. [2010] highlighted levels of turbulence between 7.5 % and 15 %, probably non homogeneous and anisotropic.

Given the dimensions of the hydrodynamic tunnel and the fact that the convergent is a turbulence killing device, it was chosen to install two turbulence generating grids in series downstream of the convergent, the first being at the test section entrance – which is relatively close to the hydrofoil. Other than generating high levels of turbulence, the generator must meet several practical criteria: it has to be safe for the tunnel installation, easy to install with minor modifications and quick to build.

Grids are composed of a 4 mm square frame made of stainless steel rods. On this frame, a 4 mm diameter rope net is installed using a fishing net braiding method. It is interesting to note that the plaiting method resulted in 15 mm diameter nodes at mesh junctions. Two grids are built using this method (Figure 2.4). A first one is 193 mm by 193 mm with a 30 mm mesh size and it is wedged into the tunnel test section just downstream of the convergent. A second, larger one, – 260 mm by 260 mm, mesh size 40 mm –, is installed 200 mm upstream of the first grid.

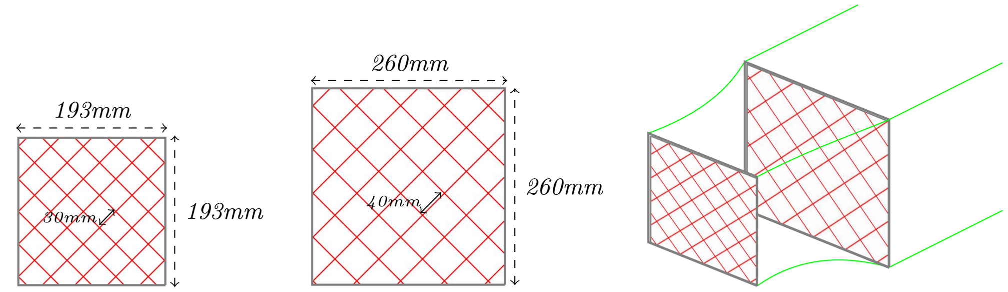

(a) First grid, $M = 30mm$ (b) Second grid, $M = 40mm$ (c) Setup

Figure 2.4: Characteristics of the turbulence generating grids.

Both grids are linked together with braids and the upstream grid is secured to the honeycomb supporting frame using four inelastic 2 mm diameter Dyneema braids. A trapdoor above the honeycombs is used for the adjustment of the braids. An overview of the grid setup is given in Figure 2.5. This solution was chosen as the convergent is made of smooth plexiglas and its modification was not possible for the grid fastening.

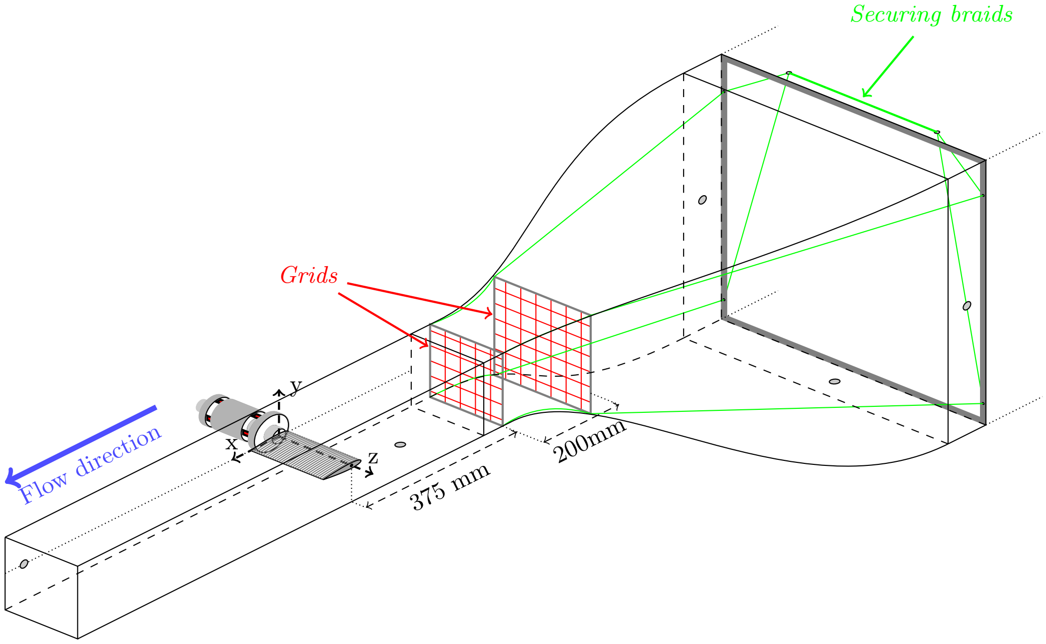

(a) Perspective view

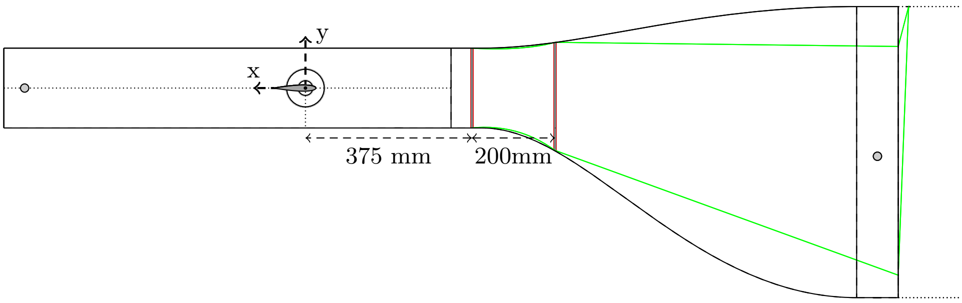

(b) Side view

Figure 2.5: Turbulence generation, flexible grids setup

A summary of the turbulence levels and scales for the three main setups is given in Table 2.1.

Name	Turbulence type	Intensity $I(\%)$	Taylor's micro-scale $\lambda_t(mm)$	Taylor's macro-scale Λ_t (mm)	R_M	R_λ
TL1	With honeycombs	1.81	0.59	1.19	$\emptyset$	5586
TL2	Without honeycombs	1.88	0.36	0.71	$\emptyset$	3527
TL3	With grids	8.31	3.32	9.18	152685 or 203580	140546

Table 2.1: Turbulence levels in the tunnel test section at $5m/s$.

The turbulence Reynolds number is given by the Equations 2.1 and 2.2.

$$R_M = \frac{U_0 M}{\nu} \tag{2.1}$$

$$R_\lambda = \frac{u' \lambda}{\nu} \tag{2.2}$$

$M(m)$ is the characteristic length of the turbulence generating grid and $\lambda(m)$ is the Taylor micro scale of turbulence.

The Reynolds number relative to the grid-type obstacle (R_M) cannot be calculated for the TL1 and TL2 configurations as there is no grid-type obstacle.

According to Chassaing [2000], the turbulence development zone is generally located between the grid location and 10 to 40 times the characteristic length of the grid (i.e. mesh size M) downstream. The foil is located downstream the grid position, between 10 and 20 time the mesh size (depending on which grid is considered), which is surely in the development zone. Therefore the turbulence cannot be considered homogeneous and isotropic at the foil position.

For further investigations, it is interesting to note that at this flowing velocity and for high angles of attack, blockage becomes very important and the tunnel's mechanical system reaches its limits when turbulence generators are present in the test section. For higher turbulence levels, an alternative way of generating turbulence needs to be designed. The idea being the use of an active method instead of a passive one (for example Thole et al. [1994]).

TL1 and TL3 configurations will only be used for the investigation of turbulence effect on the DU 91-W2-250 section characteristics. TL2 is too close from TL1 to present a real interest, at least for a tidal turbine application.

2.2 2-D Foil

Three hydrofoils have been studied and they have been used with several roughness configurations. The complete geometrical and roughness properties are presented below.

2.2.1 Geometry

The test hydrofoils are two-dimensional sections of 100mm chord and 191.5mm span (Figure 2.6). The span was chosen to be half a millimeter lower than the test section width to allow for the movement of the foil and force measurement. Hydrofoils are made of stainless steel.

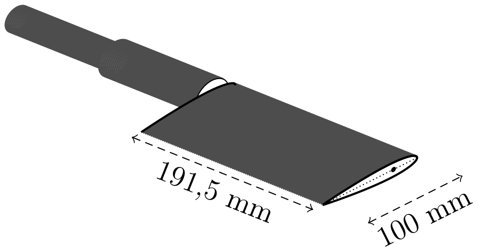

Figure 2.6: Test profile geometry, NACA 0015

A tail extends from the wing part of the tested hydrofoil, it is located located at 25 % from the LE and materializes the rotation axis. The foil is fastened into the hydrodynamic balance using this tail, as explained in more detail in Section 2.3. On the front face of the foil, the rotation axis is also materialized by a conical hole that results from the machining process and is used for the calibration procedure. The chord is also traced on the front face and used for 0° AoA positioning.

Experimental hydrofoils' geometry is controlled using a laser scanner (Figure 2.14).

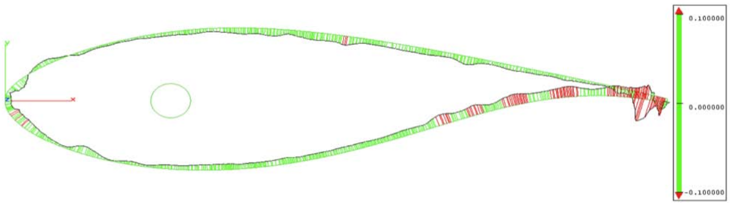

Figure 2.7: Example of laser scanner section control on the DU type hydrofoil section. Red zones are those exceeding the $0.1mm$ tolerance.

Three foil sections were tested: an academic unidirectional foil (S1) tested both in forward and reversed flow, a bidirectional foil (S2), and a cambered unidirectional section (S3). Geometries are presented in Figure 2.8.

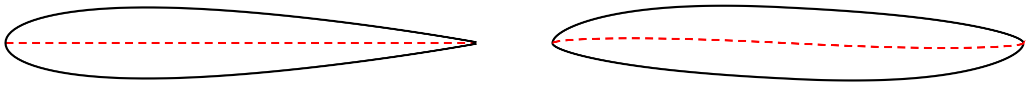

(a) S1 – NACA 0015

(b) S2 – Elliptical

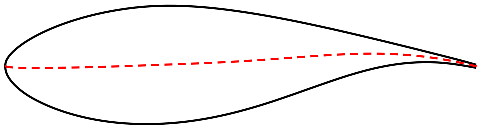

(c) S3 – DU91-W2-250

Figure 2.8: Studied blade sections, $\alpha = 0°$

The reference section is a NACA 0015, which is also used for validation of the experimental setup and numerical models. The bidirectional section is designed to provide identical hydrodynamic properties in both forward and reversed flow. It is based on a 15 % relative thickness ellipse. A parabolic camber is then applied from mid chord to both leading and trailing edges. It is rotationally symmetric.

For the NACA 0015 study, the convention for forward/regular and reversed flow is given in Figure 2.9.

(a) Forward/regular configuration

(b) Reversed configuration

Figure 2.9: Forward and reversed flowing configurations

Note that the first two hydrofoils (S1 and S2) have a relative thickness of 15 %, while the last foil (S3) is 25 % thick.

2.2.2 Surface state

Two types of roughnesses have been used. They address two objectives, namely turbulence triggering and the surface state sensitivity study.

Turbulence triggering roughness

Regarding turbulence triggering roughness, several methods have been compared. A preselection was carried out based on the reversibility, the stability and the reproducibility of the roughness application process. Methods such as calibrated sand addition using a special varnish, or manually glued and applied fine water proof sand-paper have been tested and discarded due to their difficult repeatability or lack of stability during measurements. Therefore, self-adhesive materials were chosen. Two different types of materials were tested.

- Sand-paper sticker ("100 grit" thereafter)

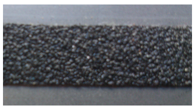

- Smooth aluminium sticker ("Alu" thereafter)

The sand-paper sticker uses thickness and surface roughness to trigger turbulence, while the smooth aluminum sticker only uses thickness, being perfectly smooth.

Two shapes were also tested: a one-piece roughness, covering the whole leading edge and a split roughness placed on either sides of the leading edge (Figure 2.10). Split roughness bands are 4 mm large and positioned at 3 % of the foil chord from the leading edge. Full roughness covers the whole leading edge up to 3 % of the chord.

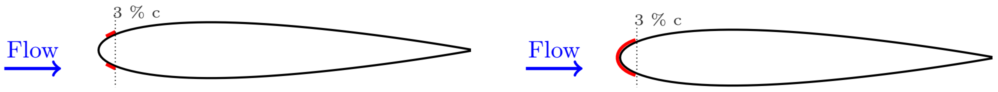

(a) Split roughness ("Split") (b) Full leading edge roughness ("Full")

Figure 2.10: Turbulence-triggering roughness strategies.

The full roughness has the advantage of not producing a rupture into the foil's surface geometry but is not suitable with thin leading edges. On the other hand, the split roughness produces a step into the foil geometry, but does not thicken the foil's leading edge.

A summary of the different configurations tested is given in Table 2.11.

Name	Roughness type	Architecture	Roughness height (μm)	Total height (mm)
RT1	100 grit	Full	140	0.675
RT2	100 grit	Split	140	0.675
RT3	Alu	Split	$\simeq 0$	0.225

Table 2.2: Properties of roughness setups tested for turbulence triggering.

These configurations were applied to the NACA 0015 foil section at 5 m/s ($Re_c = 5 \times 10^5$). Force measurements obtained with each of the roughness types are shown in Figure 2.11.

The difference observed between RT1 and RT2 shows that rather than the surface roughness , it is the total height of the added material that trigger turbulence. RT1 and RT2 show a relatively low maximum lift level, and a generally high drag. RT3 solely uses the thickness of the sticker to generate turbulence. Its behavior is closer to that of smooth foil, but it removes

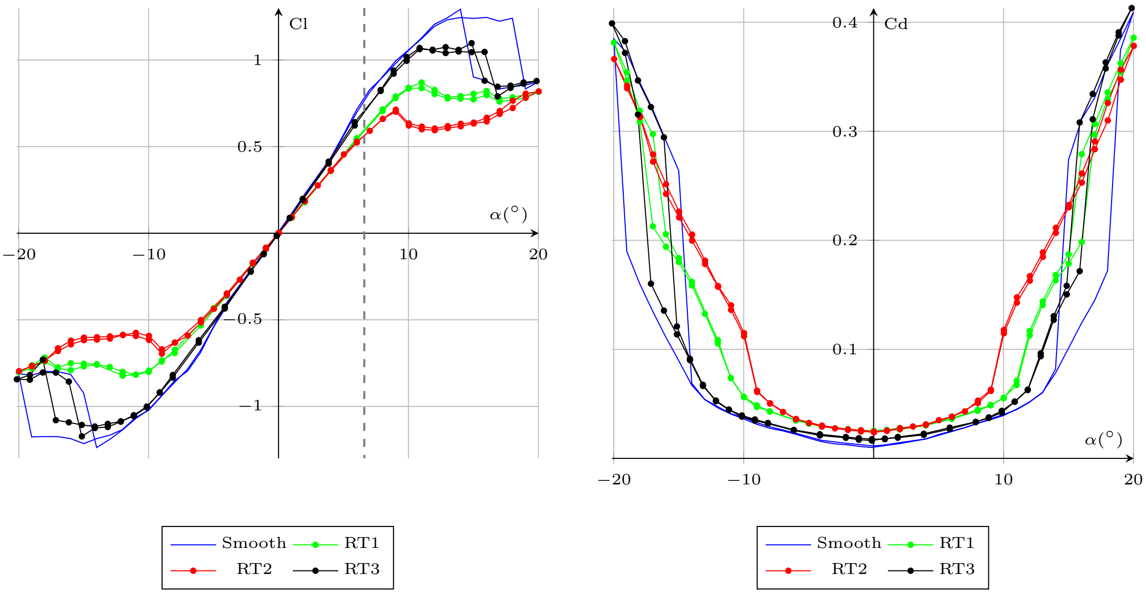

(a) Lift (b) Drag

Figure 2.11: Experimental data for lift and drag coefficients using the three types of turbulence triggering roughnesses. NACA 0015 hydrofoil at $Re_c = 5 \times 10^5$ in forward flow. The smooth behavior is also added for comparison.

the transitional effects, materialized by a lift discontinuity located around 7° AoA and similar to observations made by Delafin et al. [2014].

Therefore, for further experiments, it was decided to use the RT3 surface, as it is repeatable, easy to install, stable and efficient. The use of a split type of roughness also avoids modification of the leading edge geometry, which is a critical aspect regarding the measurements on the reversed hydrofoil.

This type of roughness is used for the entire experimental foil studies as a reference to the fully turbulent behavior (named: "Exp. **Trig. Turb.**" thereafter).

Full surface roughnesses

In the case of the study of roughness effect on the DU type hydrofoil, a second group of roughness was also used. In this case roughness covers the entire foil surface.

Four different roughnesses were used. Their properties were measured using a Time TR200 roughness tester for low roughness levels and a visual and tactile Rubert type comparator for higher roughnesses (Figure 2.12).

TR200 measurements were carried out on both upper and lower surfaces. Four measurements were carried out on each side and averaged to obtain the final roughness (Figure 2.13). The arrangement of measurement areas was dictated by the TR200 roughness sensor, whose support base needs to be flat and fully in contact with the foil surface to be measured.

Results are summarized in the following table (Table 2.3).

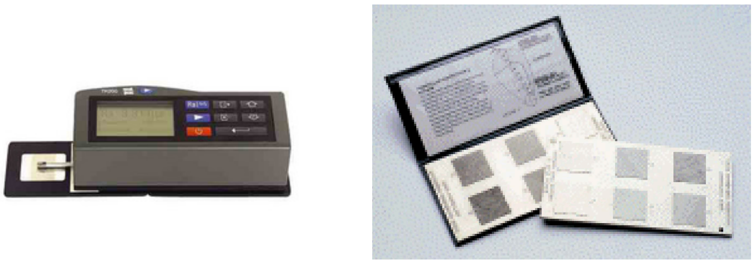

(a) TR200 roughness tester (b) Rupert "hand" roughness tester

Figure 2.12: Roughness measurement tools

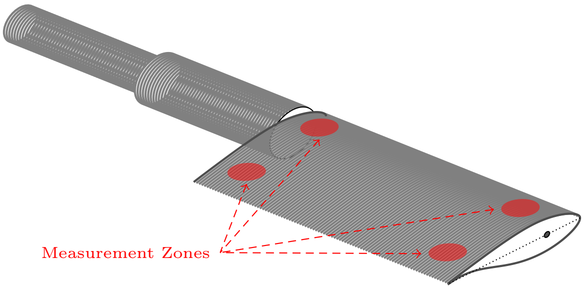

Figure 2.13: Position of the roughness measurement areas for surface state sensitivity studies, example on the upper surface of the DU hydrofoil.

Name	Roughness type	Meas. Tool	$Ra(\mu m)$	$Rq(\mu m)$	$Rz(\mu m)$
DU-RS1	Mirror polished	TR200	0.088375	0.119625	0.6935
DU-RS2	Sanded	TR200	0.374375	0.482125	3.174875
DU-RS3	Sandblasted	TR200	1.375	1.873125	11.418
DU-RS4	Sandpaper sticker	Rupert	16.6	$\emptyset$	97

Table 2.3: Surface roughness properties used for the roughness sensitivity study of the DU foil (ISO 4287).

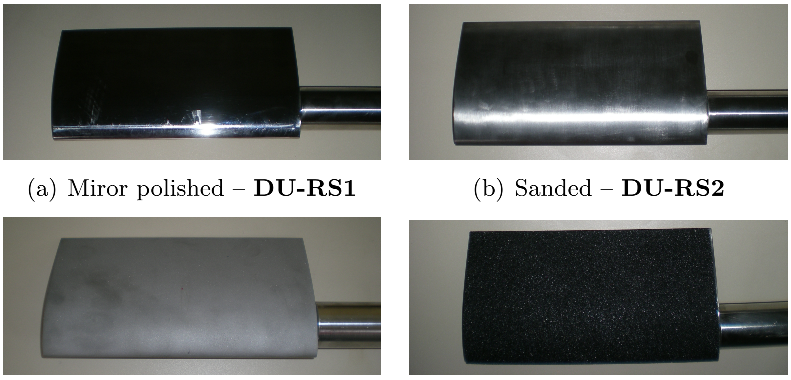

(a) Miror polished – **DU-RS1** (b) Sanded – **DU-RS2**

(c) Sandblasted – **DU-RS3** (d) Sand-paper sticker – **DU-RS4**

Figure 2.14: Illustration of the four different surface roughnesses studied on the DU foil section.

2.3 Mechanical setup and foil positioning

2.3.1 Mechanical setup

The foil tail is inserted through the back wall of the tunnel test section. It is fastened into the balance which is fixed into a supporting frame, mounted on bearings and moved into rotation by a stepper (Baldor). The link between the stepper and the hydrodynamic balance is achieved by a hydraulic clamping ring (ETP Express). Figure 2.15 gives an overview of the mechanical setup.

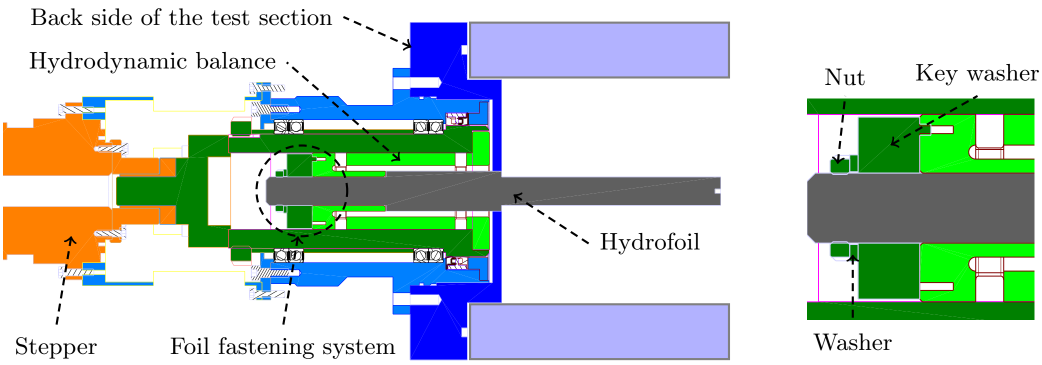

(a) Side view (b) Foil fastening system

Figure 2.15: Overview of the mechanical setup of the hydrodynamic balance and zoom on the fastening system.

The stepper allows for 600 000 impulsions per rotation, i.e. a minimum angle step of $6 \times 10^{-4\circ}$. However, the observed angular accuracy on the foil positioning using the Baldor is lower than 0.01°. The control is made with the angular position, but rotational speed and acceleration can also be adjusted by means of a generator driven by a Labview software, which includes a graphical user interface. Maximum rotational speed and acceleration are set respectively at the lowest and highest values (1 rpm and 2000 ms) in order to make the transition between two angles of attack as smooth as possible. It ensures a relative consistency in the flowing configuration and avoids oscillation of the tunnel regulation system. Moreover, violent increases in pitching moment are avoided, which reduces the risk of mechanical slack occurring, which would result in angular positioning errors.

The hydrofoil is fastened into the balance through its tail. It is secured with a tight fitted key/nut system. This key is held by a ring to the balance and limits angular slack. To reduce angular floats, each profile has its dedicated key. The nut is tightened sufficiently so as to support the maximum amount of pitching moment, which is produced by the displacement of the application point of the resultant hydrodynamic force along the foil chord.

After the setup, particular attention is paid to the foil position. For that purpose functioning gaps between the foil and the test section walls are re-checked before each measurement (at the foil base and at the extremity along the span). These gaps are necessary for the balance to deform properly under foil solicitations. The occurrence of angular slack is also checked visually and manually.

2.3.2 Foil angular positioning

For testing purposes, the zero angle of attack is defined by means of the foil chord, which will be placed in parallel to the flow direction. Because of the complexity of the setup, some positioning errors might occur if accurate checks are not carried out. Therefore, an accurate procedure was proposed in order to obtain a repeatable and accurate positioning of the 0° AoA.

As the flow direction is not yet well-defined yet when the foil is being installed, an intermediate reference needs to be set-up. The direction of the gravity is chosen for this purpose.

Once mounted, the foil is positioned vertically and the chord is aligned with the direction of the gravity using a very thin plumb-line. The stepper is then set to 0° in this position and a rotation of 90° is applied to set the foil horizontally – with an accuracy of 0.01° – (Figure A.2).

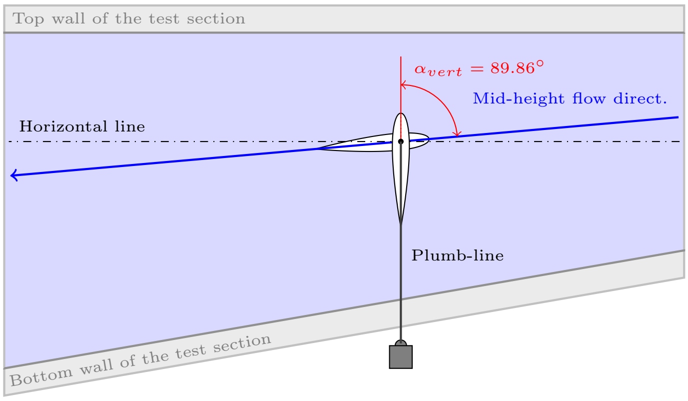

Figure 2.16: Relative positioning of the geometrical and hydrodynamic 0° AoA, the angle of the bottom wall is exaggerated.

A force measurement with a symmetric foil (NACA 0015) is then carried out at the desired flowing velocity (generally 5 m/s) and the zero lift angle of attack is measured. On that type of foil, the zero lift angle is also the geometric 0° AoA. Thanks to this procedure the "hydrodynamic" zero angle of attack is determined as being relative to the gravity (α_{vert}) with an accuracy of 0.01°. Any foil can then be set parallel to the flow direction from the vertical position of its chord.

In practice, α_{vert} is found to be 89.86°, as the hydrodynamic 0° AoA is 0.14° over the horizontality, at 5 m/s.

2.4 Hydrodynamic balance

A hydrodynamic balance is used for force measurements. A large amount of work has been done on this tool to make measurements reliable, accurate and repeatable. An appropriate calibration procedure was developed during this work and it is presented below, following a description of the balance.

2.4.1 Architecture, design

The foil is mounted at the mid section, in a 3-component hydrodynamic balance. The range is up to 170 daN for lift force, 18 daN for drag and 4.3 daN.m for pitching moment. It is equipped with 3 strain gauge bridges placed on deformable supports, as presented in Figure 2.17(a).

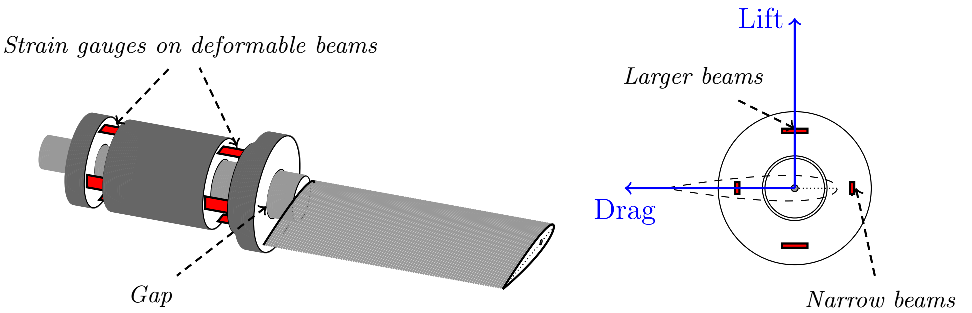

(a) Overview of the hydrodynamic balance design

(b) Front view, layout of the strain gauges support beams at 0° AoA

Figure 2.17: Hydrodynamic balance

The beams supporting the strain gauges have two different sizes. The main objective is to accentuate the deformation of the balance along the drag axis while remaining stiff enough in the lift direction in order to withstand lift forces. Two sets of two large deformation beams are located along the axis perpendicular to the foil chord, corresponding to lift direction at 0° AoA. Narrower beams are set along the horizontal axis (drag, parallel to the foil chord). Figure 2.17(b) presents a front view of the deformation bars.

As the balance follows the rotation of the foil, this design is appropriate for angles of attack of the hydrofoil within -20° and 20°. Over this range of angles, support beams are still correctly oriented compared to the directions of the lift and drag components of the hydrodynamic force.

The force application point is located approximatively at mid span. However, due to three-dimensional effects, its position is not accurately known. Strain gauge bridges are therefore doubled (Figure 2.17(a)) to measure forces independently of the position of the application point along the span (Délery et al.).

An IOtech strainbook 616 is used for the strain gauges' electrical supply as well as primary data collection. Data can then be viewed using a graphical user interface. At last, processing can be reworked from raw data text files using a Matlab routine, which is also used for application of data corrections.

Several steps are needed to obtain the final forces from the raw measured data. Figure 2.18 shows the data processing procedure.

The raw signal is received by the computer, and it is then converted from V to mV/V, using the supply tension. Each load cell gives a value of tension corresponding to a specific force. However the mechanism is highly coupled and therefore a calibration matrix is needed to obtain forces in the Balance coordinate frame (Rb, Figure 2.19, which rotates whith the foil). The calibration matrix is obtained by static measurement on a dedicated test bed and provided by the balance builder. Table 2.4 details the actual calibration matrix, for tensions in mV/V and to obtain forces and moments in daN and daN.m respectively.

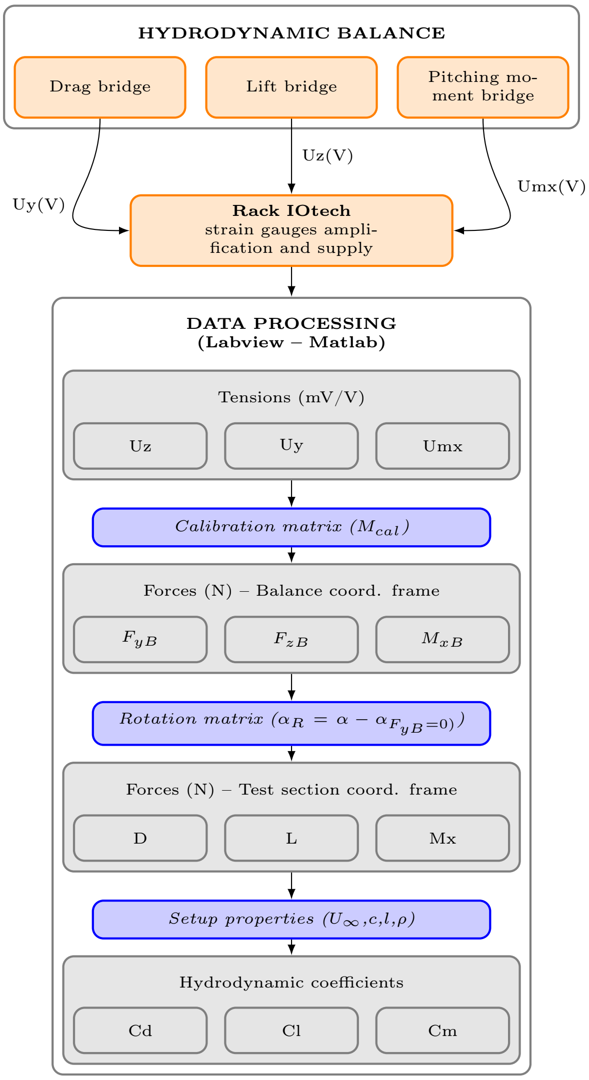

Figure 2.18: Hydrodynamic balance, data processing

		Uy(mV/V)	Uz(mV/V)	Umx(mV/V)	$\|Uy\|$	$\|Uz\|$	$Umx \times Uz$
Drag	$F_{yB}(daN)$	**38.39**	**9.17**	**-2.65**	**0**	**0**	**0**
Lift	$F_{zB}(daN)$	**-0.96**	**226.32**	**-0.84**	**0**	**0**	**0**
Mom.	$M_{xB}(daN.m)$	**-0.07**	**0.43**	**8.45**	**-0.06**	**0.36**	**-2.34**

Table 2.4: Calibration matrix (M_{cal}), expressed in the Balance coordinate frame

Using this matrix, forces and moments applied to the foil can be expressed as:

$$F_{yB} = 38.39 \times Uy + 9.17 \times Uz - 2.65 \times Umx \tag{2.3}$$

$$F_{zB} = -0.96 \times Uy + 226.32 \times Uz - 0.84 \times Umx \tag{2.4}$$

$$M_{xB} = -0.07 \times Uy + 0.43 \times Uz + 8.45 \times Umx - 0.006 \times |Uy| + 0.36 \times |Uz| - 2.34 \times Umx \times Uz \tag{2.5}$$

The hydrodynamic balance rotates with the test hydrofoil. Thus a rotation matrix is then required to project forces in the coordinate frame of the tunnel test section, which is called "Veine" (Rv) (Figure 2.19). The rotation angle is the angle of attack of the foil, with the addition of an angular offset determined by the calibration and which is dependent on the amount of force measured.

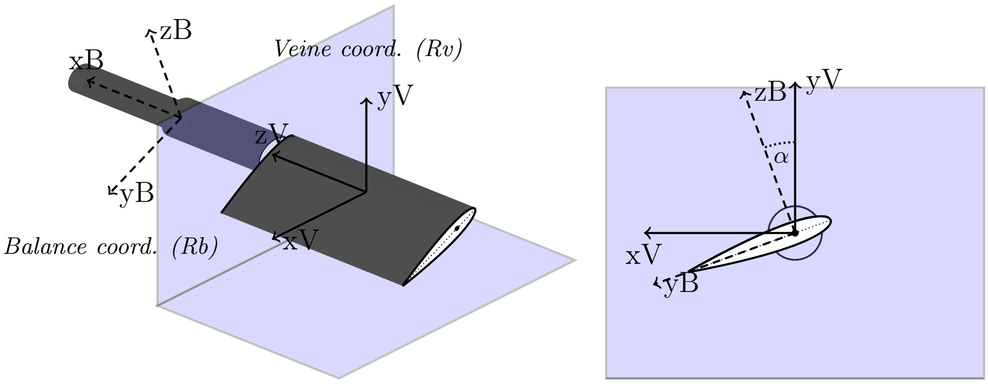

(a) Perspective view (b) Front view

Figure 2.19: Relative positionning of Veine and Balance coordinate frames.

2.4.2 Calibration

The force generated by a hydrofoil can be characterized as a vector, and therefore fully described using a direction, a norm and an angle. It is then decomposed into its perpendicular and parallel components to the flow direction (lift and drag respectively).

In the present study, the force vector is measured using the balance, which moves with the foil. A rotation is therefore needed to obtain lift and drag forces relative to flow direction.

The present calibration procedure is designed to account for angular errors due to the mechanical adjustment of the foil fastening system. It also accounts for the evolution of the balance property with the force level applied.

Forces on a 2-D hydrofoil

Before any calibration protocol is applied, it is interesting to quantify the amount of hydrodynamic force and its angular variation to the balance for an academic case.

A hydrofoil generates hydrodynamic force, generally decomposed into lift and drag components, respectively along the vertical and horizontal axis. The application point of this hydrodynamic force moves along the foil chord, which generates a pitching moment variation if measured at a fixed given location (generally 1/4 chord). The measured force can be expressed as a vector in terms of norm, angle and direction. An example of the hydrodynamic force vector representation is proposed in Figure 2.20, with both calculations and experimental results.

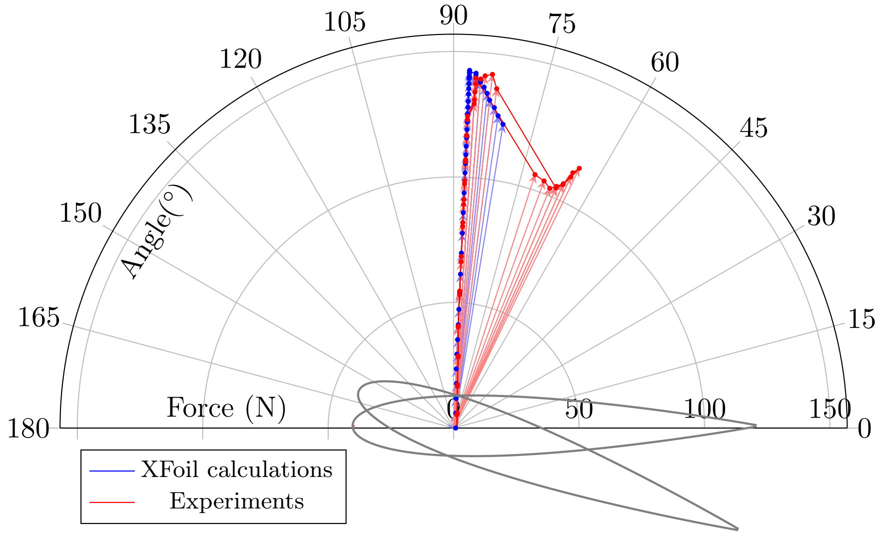

(a) Force vector in the **test section coordinate frame** (Rv, fixed)

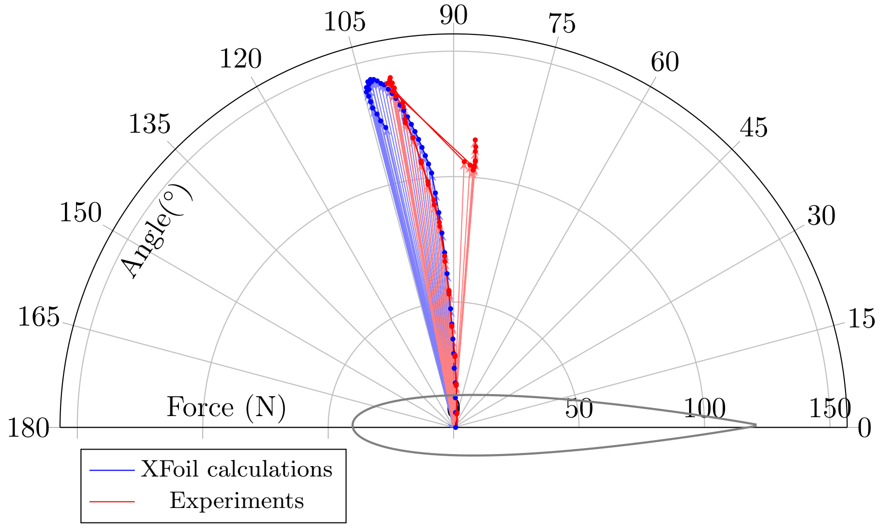

(b) Force vector in the **hydrodynamic balance coordinate frame** (Rb, rotating)

Figure 2.20: Hydrodynamic force vector as estimated using XFOIL calculations (normalized) and hydrodynamic tunnel measurements, for $Re_c = 5 \times 10^5$ and angles of attack between 0° and 20°, NACA 0015

As shown in Figure 2.20(a) the angle of the force vector in the test section coordinate frame is located between 90° and 60°, resulting in an angular range of approximatively 30°, which could lead to linearity problems.

It is observed on Figure 2.20(b) that the balance experiences a narrower angle range, from 85° to 105°, almost centered around 90°. The hydrodynamic force is therefore almost completely lift-driven, except for the zero lift angle for which there is only a drag component. Force value is generally between $100N$ and $150N$, meaning that a few hundred newton force is a representative value for the operation of the balance.

Note that XFoil calculations are accurate enough to be used for the definition of the range of forces and angles for the calibration. The computational setup is described in more details in appendix D.

As an example, the evolution of a constant weight of $200N$ applied along $-yV$ and decomposed into vertical and horizontal components in the balance coordinate frame, as the Balance coordinate frame rotates around the xB axis, is shown in Figure 2.21.

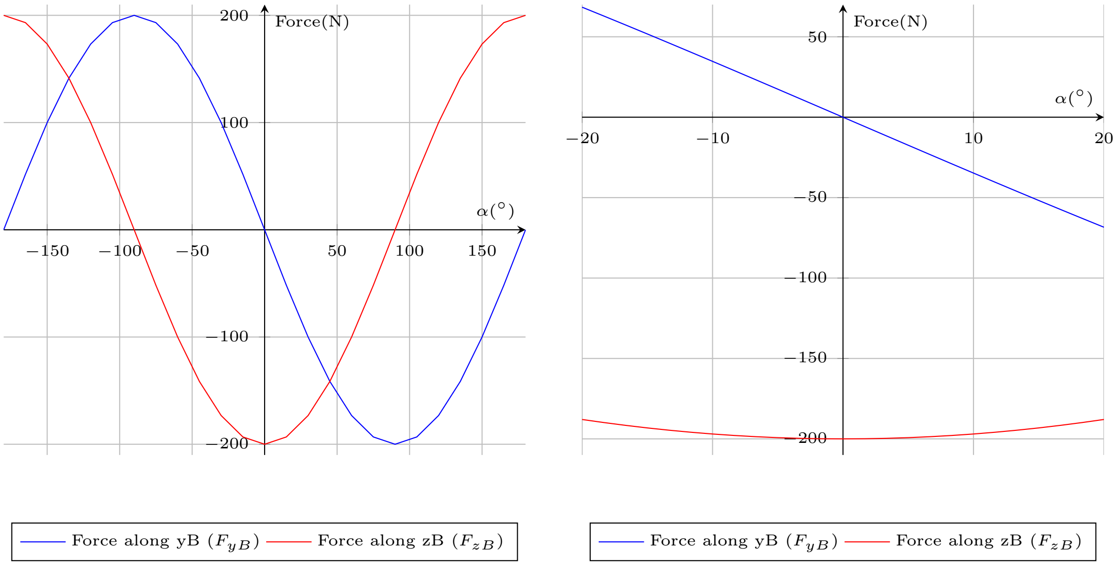

(a) Full range

(b) Focus on the range of angles of attack from -20° to 20°

Figure 2.21: Force projection into the balance coordinate frame, example for 200 Newton along -yV

It can be observed that the yB component is a sinusoidal function of the angle of the balance and can be considered linear over a range from $-20°$ to $20°$. On the other hand, the zB component is a cosines function of the angle and can be considered as a constant in that same range. This shows that a variation of the angular position of the balance with regard to the force direction may principally affect the "drag component" of the force, i.e. along yB.

The linearity of the yB component of the force in the balance coordinate frame is the base of the calibration procedure detailed below.

Calibration protocol

Linearity of the yB force (called F_{yB}) in the balance coordinate frame is studied for a range of pure vertical forces (along -yV, Figure 2.22). The zero F_{yB} angle is studied as well, as a reference for the angular positioning of the balance.

The balance is set at the gravity geometrical 0°, meaning that the foil chord is perpendicular to the direction of the gravity. Consequently, the calibration is set-up dependent and must be repeated as soon as the foil is fastened.

A specific tool was designed for this purpose. As shown in Figure 2.23, it is composed of

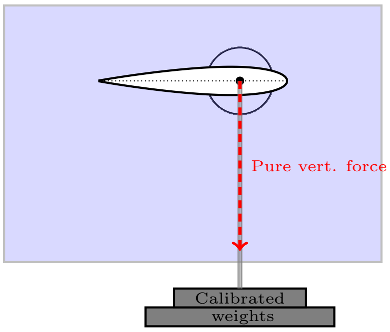

Figure 2.22: Force application method used for the calibration.

rectangular aluminum parts assembled to form a plier. The hydrofoil is clamped inside the plier using 6 screws and thin soft wedges – to avoid the plier slipping and to protect the foil surface. A pulley is installed at the extremity, mounted on high quality bearings to avoid pitching moment. For zero moment application, a pin is set inside the plier, in order to maintain the alignment of the rotation axis of the pulley in accordance with the pitching axis of the foil – materialized by a conical hole (see section 2.2).

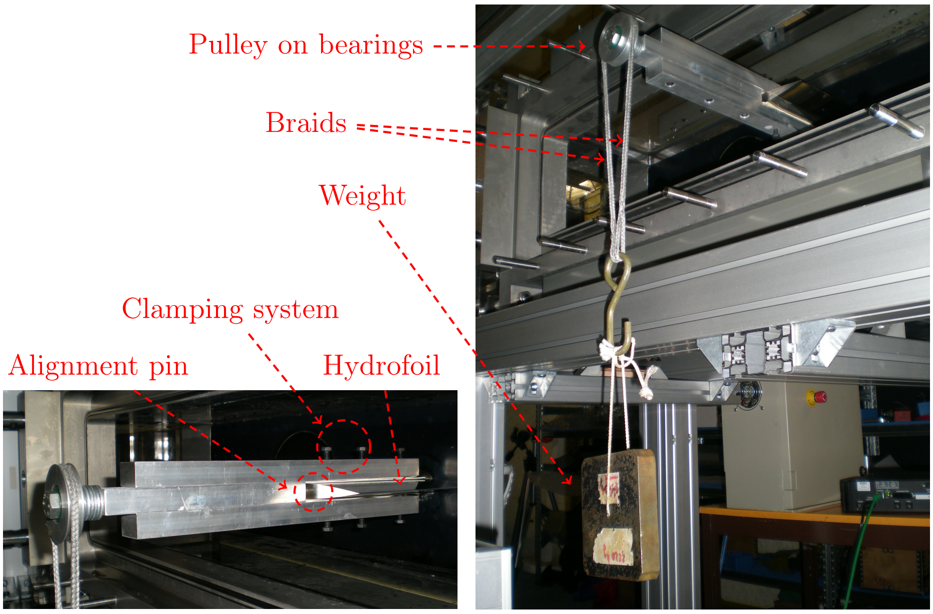

Figure 2.23: Tool for pure vertical force application

Once the plier is installed, two sets of measurements are carried out.

Firstly in order to confirm the linearity of F_{yB} with the rotation of the balance, a constant weight is set and the balance angle is varied between $-20°$ and $20°$. Results are presented in Figure 2.24 for the NACA 0015 foil section with a weight of 216 N.

It can be observed that the measured F_{yB} is a linear function of the angle of attack. An offset of the angle can also be noted, as the zero yB force angle ($\alpha_{F_{yB}=0}$) does not occur at the geometrical 0°.

Because of the presence of this offset, a second set of measurements was carried out to

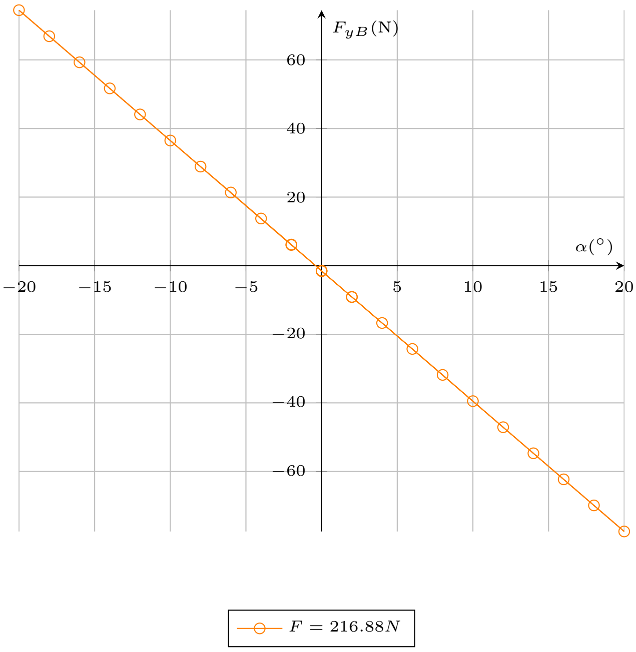

Figure 2.24: Drag force in the balance coordinate frame function of the angle of attack for a constant weight, example with the NACA 0015 foil section

study the evolution of the F_{yB} zero angle with the variation of forces. Forces between 20N and 500N are applied; for each force, the balance is oriented with an angle between $-8°$ and $+8°$. Measured F_{yB} as a function of the angle of attack and for each weight are presented in Figure 2.25.

Also in this case, the component of force along the yB axis can be modeled as a linear function of the angle of attack. Zero F_{yB} angle can therefore be determined and plotted as a function of the measured resultant force (Figure 2.26). Note that the zero F_{yB} angle changes slightly with the resultant force value.

Figure 2.27 presents $\alpha_{F_{yB}=0}$ as a function of the applied force for three cases. It can be noticed that $\alpha_{F_{yB}=0}$ is a function of the applied force, and dependent on the assembly used. Therefore, this calibration must be carried out for each foil setup. It also implies a direct link with the mechanical setup, meaning that this variation of the $\alpha_{F_{yB}=0}$ includes positioning error at the setup. Moreover, $\alpha_{F_{yB}=0}$ is an almost linear function of the applied force when lift exceeds $100N$ to $200N$.

However, $\alpha_{F_{yB}=0}$ needs to be known with great accuracy, and therefore a linear interpolation is not sufficient to describe its variation with the force. Therefore a polynomial approximation is used, the degree of which is adjusted to fit calibration data.

The zero F_{yB} angle is used for the angular positioning of the balance. It is used as an angular offset for the rotation matrix. The offset is calculated on the basis of the resultant force measured on the foil using a polynomial approximation of $\alpha_{F_{yB}=0}$ and resulting from the corresponding calibration measurement.

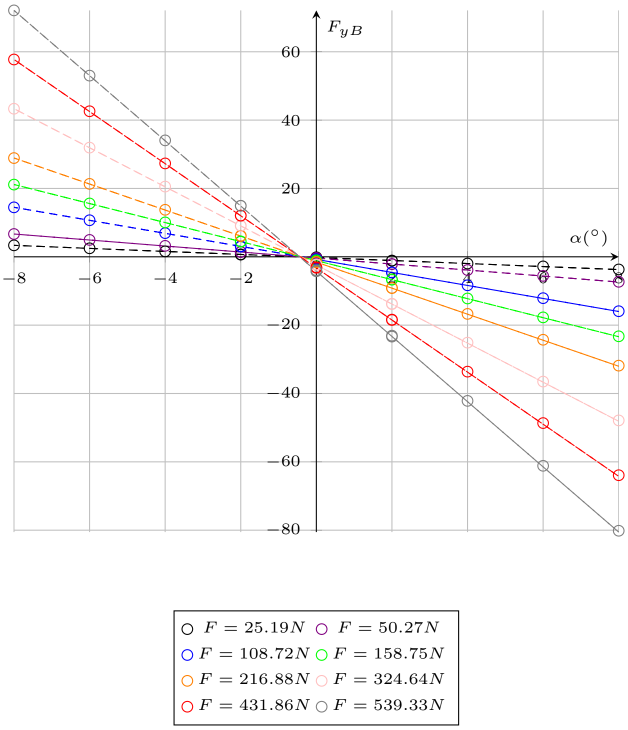

Figure 2.25: F_{yB} as a function of the angle of attack for several pure forces along the vertical axis, example using a setup with the NACA 0015 foil section

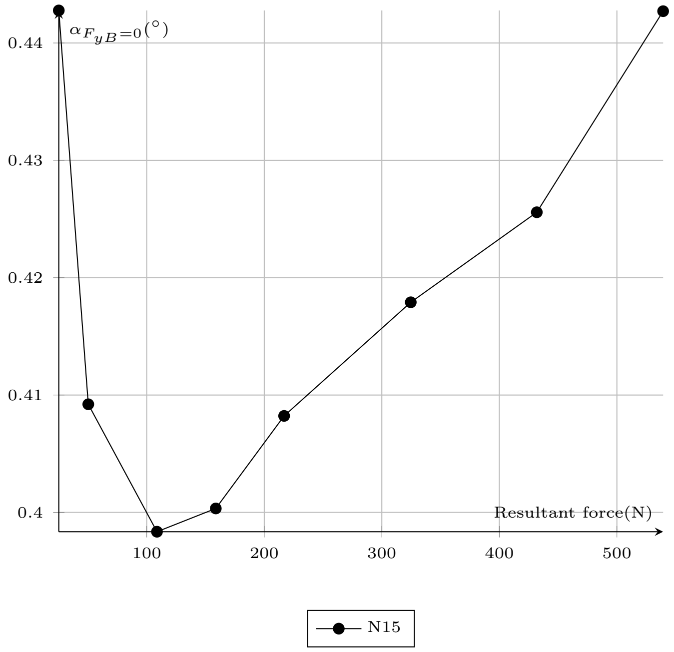

Figure 2.26: Zero F_{yB} angle as a function of the measured resultant force, example with the NACA 0015 foil section.

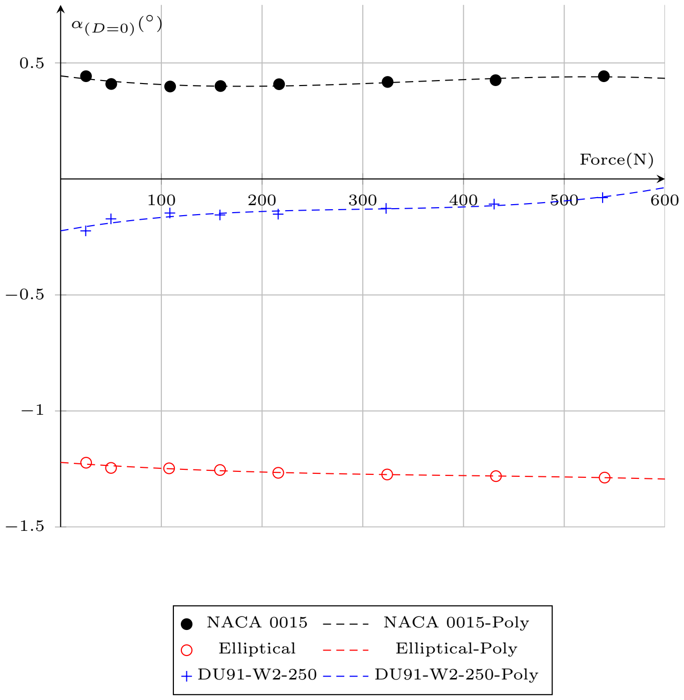

Figure 2.27: $\alpha_{F_{yB}=0}$ as a function of the applied force for three foil setups, polynomial approximation (Poly.).

Validation

To verify the procedure, the hydrodynamic balance was used on a smooth cylinder which only generates a drag force and for which a large amount of reference data is available. A 191.5 mm by 20 mm cylinder is used, geometry is given in Figure 2.28.

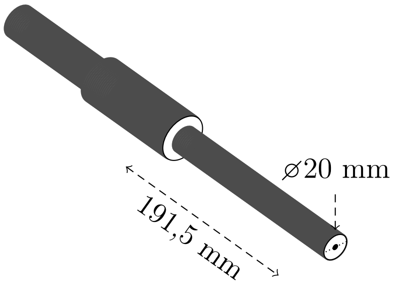

Figure 2.28: Geometry and dimensions of the cylinder used for validation of the calibration procedure

Measurements of lift and drag were carried out at a Reynolds number value of $Re_D = 9 \times 10^4$ (U_∞=4.5m/s). Several angles of rotation – corresponding to angles of attack on a hydrofoil – were investigated. This time the calibration is based on the zero F_{zB} angle as the main force is applied along the yB axis. Measured forces with and without calibration are illustrated in Figure 2.29. Moreover, as the norm of the hydrodynamic force is constant, the angular correction remains constant as well ($\simeq 3.18°$).

As shown in Figure 2.29, lift and drag without calibration are constant with the angle of

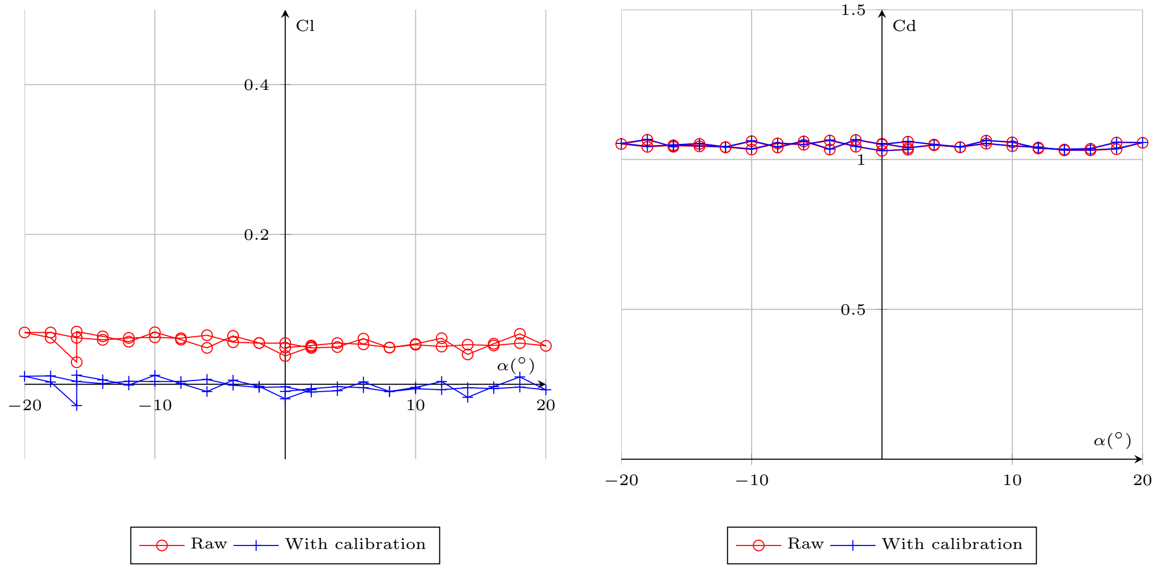

(a) Lift (b) Drag

Figure 2.29: Effect of the calibration on the average values of lift and drag coefficients for a smooth cylinder, diameter 20 mm and $Re_D = 9 \times 10^4$.

attack. The average value of the drag coefficient is 1.04, which is an expected value for a $20mm$ diameter cylinder at $Re_D = 9 \times 10^4$, as shown in figure 2.30. The average lift is not equal to zero as expected and small fluctuations are observed. These results show that apart from some inaccuracies on the relative positioning of the balance and the test section coordinate frames, the balance measures an accurate resultant force intensity.

It can also be observed on Figure 2.29 that the correction on the angular position of the balance removes lift offset and does not affect the value of drag. Lift is then very close to zero and drag remains in agreement with literature data, thus validates the calibration procedure.

The calibration procedure was also tested on measurements carried out on the NACA 0015 hydrofoil. In this case, measured forces have to comply with at least three constraints. The first one is that the value of measured lift and pitching moment have to be zero at 0° of angle of attack. The second is that drag is symmetric between positive and negative angles of attack. Last is the anti-symmetry of lift and pitching moment between positive and negative angles of attack. All these properties come from the geometrical chord-symmetry of the foil and are used for testing the calibration method.

Figure 2.31 presents measured values of lift and drag coefficients variation with the angle of attack. To highlight the symmetry of each curve, an additional curve is added which is symmetrical to the measured forces. Those curves are obtained the following way:

$$Cl_{Sym} = -Cl \tag{2.6}$$

$$Cd_{Sym} = Cd \tag{2.7}$$

Each of the Sym coefficients is plot as a function of -α.

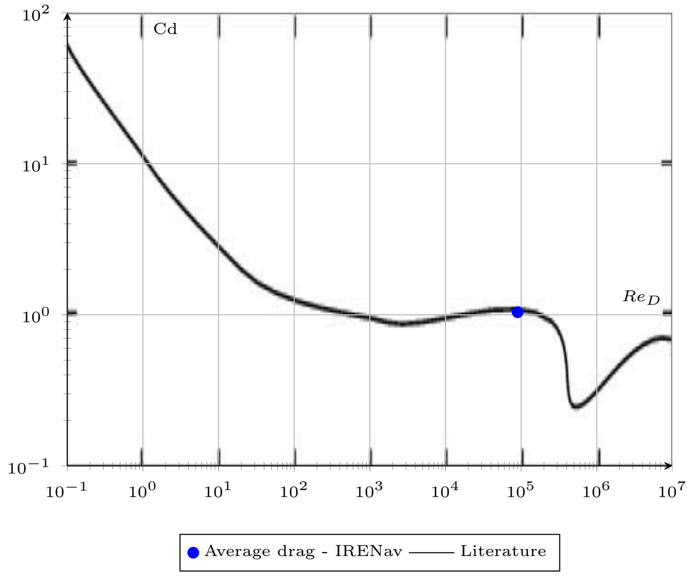

Figure 2.30: Drag coefficient function of the Reynolds number. Comparison of measurements carried out in the IRENav tunnel to a reference curve on a smooth cylinder. Logarithmic scales.

Figure 2.31 gives an overview of the original lift and drag properties without application of the calibration.

It can be seen that the lift coefficient is anti-symmetric on a range from −10 to 10°. The zero lift angle is also 0° AoA. Around the stall angle and higher, a slight asymmetry is visible. It is very likely due to a highly unstable hydrodynamic situation occurring over this range of angles. Lift is, at that location, very sensitive to surface roughness, upstream velocity fluctuations and confinement.

On the other hand, drag is much more asymmetric even at low angles of attack, for which the flow is stable.

Figure 2.32 shows the same lift and drag measurements when the calibration is applied. The rotation parameter is corrected for each angle of attack (see 2.4).

Lift is not much affected by the correction, while drag recovers its symmetry, particularly at low angles of attack.

Conclusion

The calibration showed that the angular positioning of the zero F_{yB} depends on the resultant force intensity. It results in an angular correction that is dependent on the force measured and on the set-up, which is determined from an approximation of the measured $\alpha_{F_{yB}=0}$ behavior using calibrated weights.

This additional rotation corresponds to a correction of a small angle in the positioning of the balance coordinate frame relative to that of the test section. This angle is generally low – less than 2° – and it affects drag, mainly.

It is interesting to note that this angular correction is force dependent but also remains contained in a relatively narrow range. It confirms that the usual set-up method is resulting

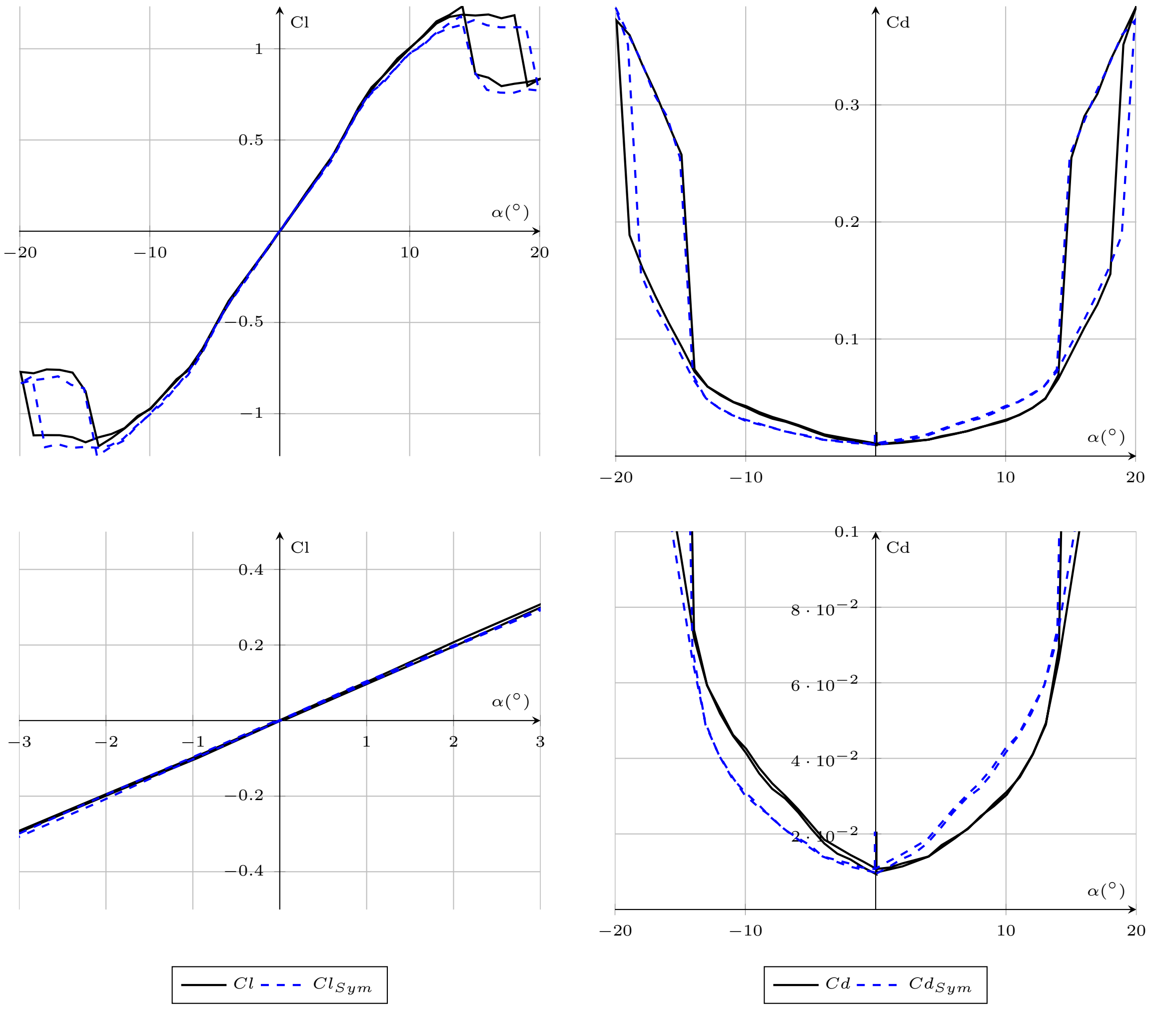

(a) Lift (b) Drag

Figure 2.31: Raw lift and drag coefficients, experimental data obtained with the NACA 0015 hydrofoil at $Re_c = 5 \times 10^5$ in forward flow (no correction).

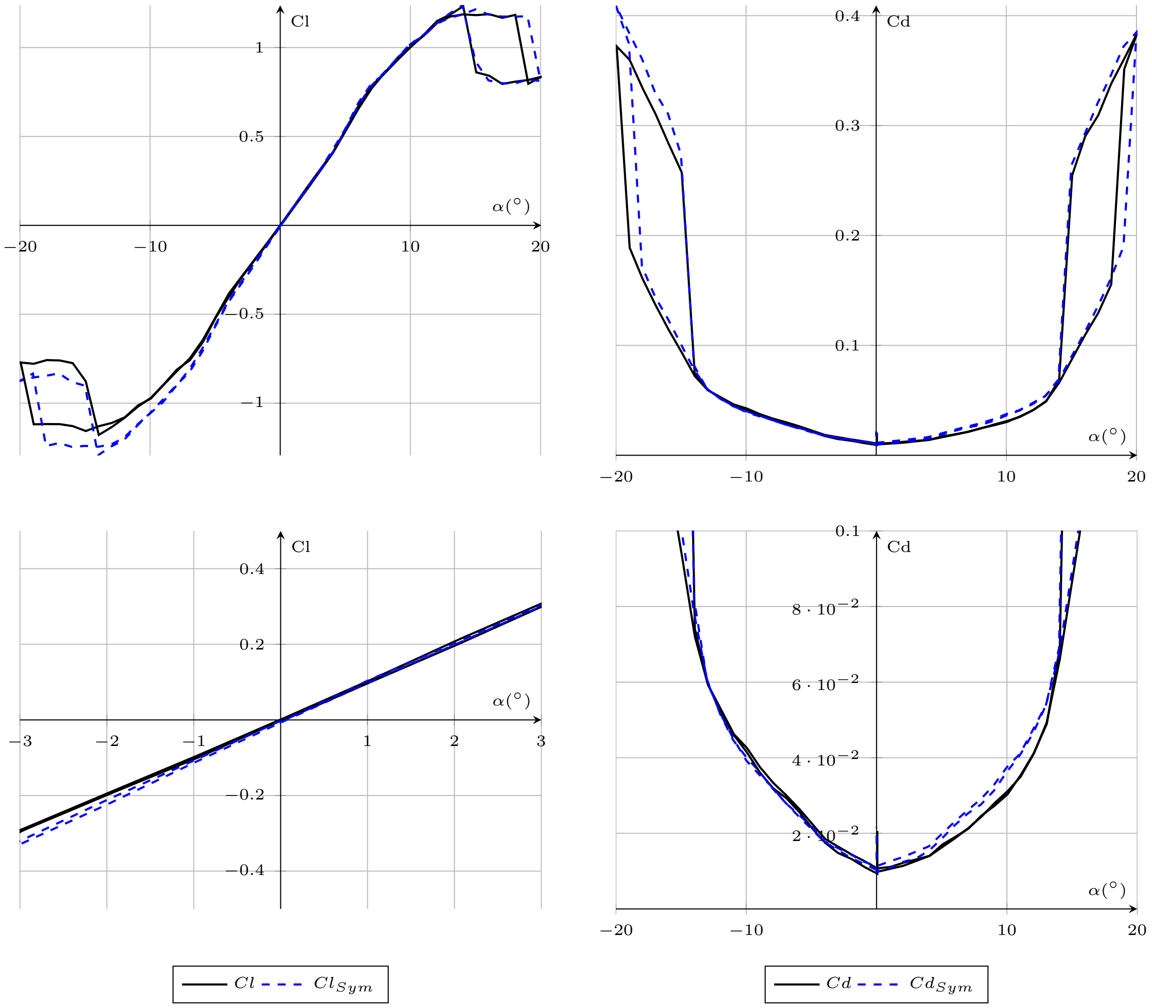

(a) Lift (b) Drag

Figure 2.32: Lift and drag coefficients, experimental data obtained with the NACA 0015 hydrofoil at $Re_c = 5 \times 10^5$ in forward flow (corrected values).

in a stable mechanical configuration, meaning that there is no angular slack occurring during measurements. The angular offset due to the mechanical setup is constant. It may result from the geometrical adjustment of the key fastening system for the foil setup.

Measurements on a smooth cylinder have shown that the calibrated measured forces are accurate for both lift and drag values.

Finally, this calibration is a way to correct measurements carried out with the current balance configuration – i.e. calibration matrix – however the definition of a full onsite calibration procedure could improve the quality of the results and facilitate future measurements.

2.5 Particle Image Velocimetry

The originality of the present work partially comes from the simultaneous measurement of the forces on the foil (using the balance) and the flow (using PIV). More precisely, particle Image Velocimetry (PIV) is used for two purposes: flow velocity measurement and flow visualization for physical analysis of the flow as well as comparison with computations.

2.5.1 Overview

The Particle Image Velocimetry (PIV) is a well known non-intrusive method for flow visualization. It is used to obtain the velocity field of a seeded flow through the light of a laser plane. A camera is used for the observation of the particle scheme and comparison between successive images allows us to determine particle movements and velocity vectors.

In the present case, a pulsed Nd-YAG type laser is used (Newwave Gemini Solo 2 15Hz). A vertically oriented laser plane is generated using a cylindrical lens. A CDD camera is also used with a resolution of 1280 by 1024 pixels and a sampling frequency of $4Hz$ in double frame. The software – Flowmanager version 3.1 – triggers a double frame between the laser plane and the camera. The time step between pulses is adjusted depending on the Reynolds number. 100 images are used for global value calculation at each angle of attack.

The laser plane is positioned at mid span and above the foil (Figure 2.33). Two horizontal mirrors are placed below the foil and used for lighting the bottom face.

A view of the final laser sheet is given in Figure 2.34. It can be observed that the use of mirrors enables the laser sheet to cover the whole contour of the foil.

An example of the resulting measured flow field is given in Figure 2.35.

2.5.2 Inflow velocity

For comparison with computations, two velocity profiles are defined. Both are positioned vertically in the midspan plane. They range from 7 cm above the foil to 7.5 cm below. The upstream one is located 7cm away from the rotation axis of the foil and the downstream one is located 15 cm from the same axis.

Inflow velocity is also calculated based on PIV. For this study, the full velocity profile upstream of the hydrofoil is used. It is located 7 cm upstream of the foil rotation axis and

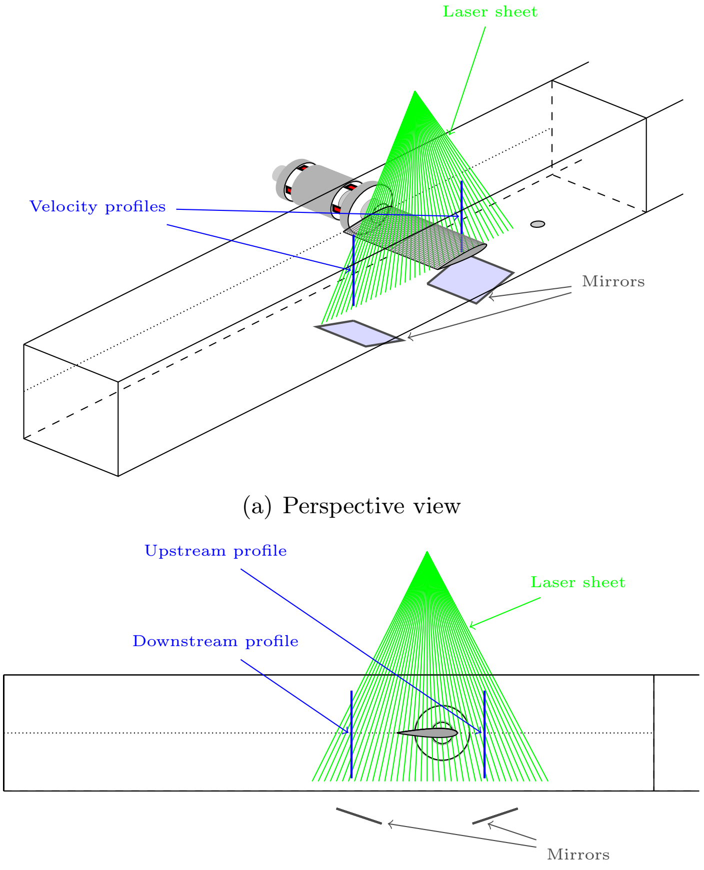

(a) Perspective view

(b) Front view

Figure 2.33: Position of the PIV plane into the test section for flow field measurements and position of the velocity profiles for flow velocity measurements.

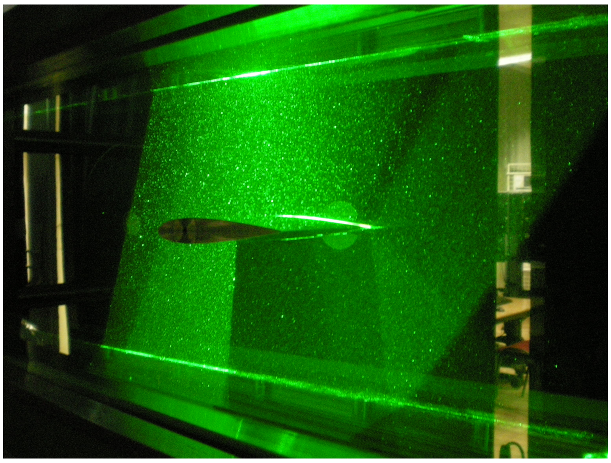

Figure 2.34: View of the laser sheet used for PIV, example on the NACA 0015 reversed

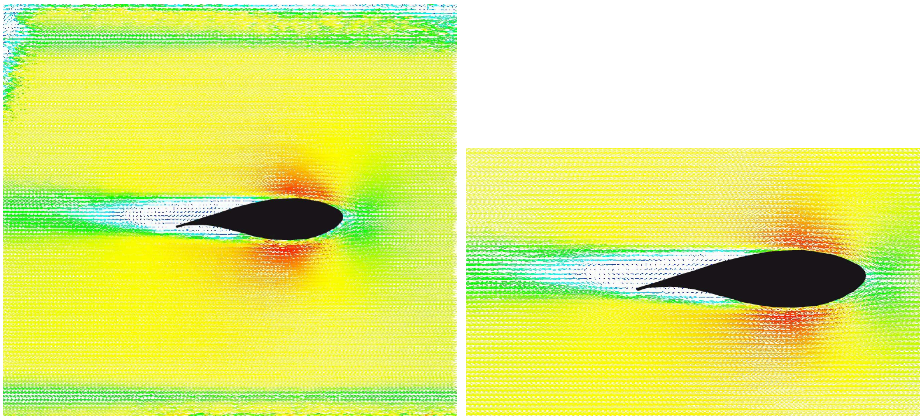

Figure 2.35: Velocity field obtained using PIV, DU foil section $Re_c = 5 \times 10^5$ and 4° AoA

covers the whole height of the test section. For each angle of attack, the inflow velocity is an average of the velocities on the full upstream profile. It is then averaged over the whole range of AoA. The velocity average is mainly used for normalizing hydrodynamic forces, as direct inflow velocity measurement using pressure sensors is not suitable with all the configurations (turbulence generators).

Note that for each foil, for each surface state configurations and each Reynolds number values, PIV measurements were carried out for the whole range of angles of attack. 100 couples of PIV images were captured for each angle of attack. For the reversed hydrofoil configuration this number was increased to 300 images. As a result, approximatively 100 000 couples of images were captured and processed.

2.6 Laser Doppler Velocimetry

Turbulence intensity and scales in the test section are measured using a Laser Doppler Velocimetry (LDV), which is briefly described below.

2.6.1 Overview

LDV measurements were carried out using a two-component system BSAFlow from Dantec, equipped with a Spectra-Physics Argon laser.

The flow is sowed with reflective Iriodin micro-metric particles $(1 - 10\mu m)$. The measurement principle is based on retro-diffusion of the light by these particles as they travel through the set of straight fringes generated by interference of the two laser beams. The Doppler frequency of these particles (sparkling frequency) is directly proportional to the normal velocity regarding the set of fringes and to the distance which separates them.

The system is composed of coherent beams (blue $\lambda_B = 488nm$, green $\lambda_B = 514.5nm$ and blue-green (called the "common")) which allows for measurement of two orthogonal velocities u' and v'. The velocity directions depend on the orientation chosen for the laser beams and can be different to that of the normal and longitudinal directions of the flow. In our case, the laser beam velocity directions and the flow are aligned.

The laser is installed on a micro-metric three axis positioning system in order to adjust the position of the measurement point in three dimensions.

The origin of the coordinate frame is set at the hydrofoil rotational axis. The laser beam focus point is placed at mid span, 300 mm upstream of the hydrofoil. Measurements are carried out on a 10 cm long vertical profile line, centered vertically and with one measurement each 5 mm (Figure 2.36).

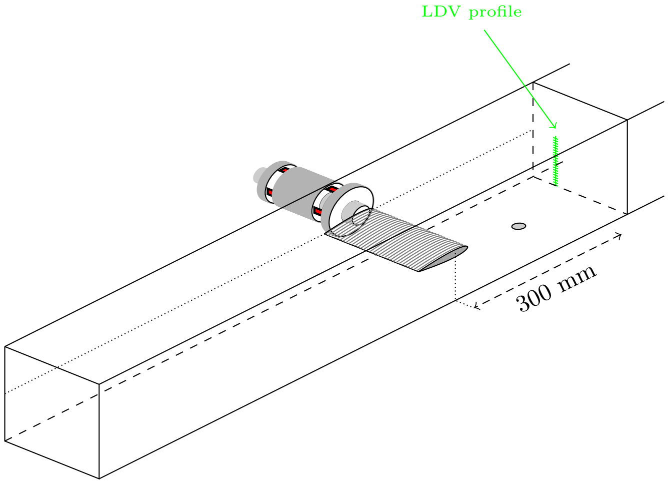

(a) Perspective view

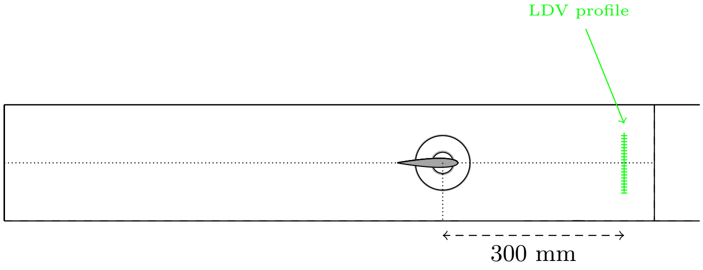

(b) Front view

Figure 2.36: Position of the LDV profile into the test section for upstream turbulence measurements.

2.6.2 Turbulence intensity

Measured flowing velocities obtained with LDV are used to determine turbulence intensity (I) using equation 2.8.

$$I = \frac{u'}{\bar{u}} \tag{2.8}$$

Where u' is the root mean square of the turbulent velocity fluctuations and $\bar{u}$ is the mean velocity. In our case, turbulence intensity is calculated for each point of the measurement profile and averaged over the whole profile.

2.6.3 Turbulence length scales

Turbulence integral length scales can also be estimated based on temporal data from LDV measurements. As given in equations 2.9 and 2.10, Taylor's frozen field hypothesis allows for calculation of the integral length scale (Taylor's macro-scale, Λ) as the integral of the normalized autocorrelation function ($R_{u'u'}$).

$$\Lambda = \bar{u} \int_0^\infty R_{u'u'}(\tau)\mathrm{d}\tau \tag{2.9}$$

$$\bar{R}_{u'u'}(\tau) = \frac{\frac{1}{T}\int_0^T u'(t)u'(t+\tau)\mathrm{d}t}{\frac{1}{T}\int_0^T u'^2(t)\mathrm{d}t} \tag{2.10}$$

With $T(s)$ as the total time of the recording and $\tau(s)$ the autocorrelation time lag.

LDV temporal data is characterized by a non uniform time-step. For calculation of the autocorrelation function, a resampling is required. A time step of the fifth of the lowest initial time step is chosen for resampling. A linear interpolation is used to obtain the value of u' for interpolated time steps (Figure 2.37).

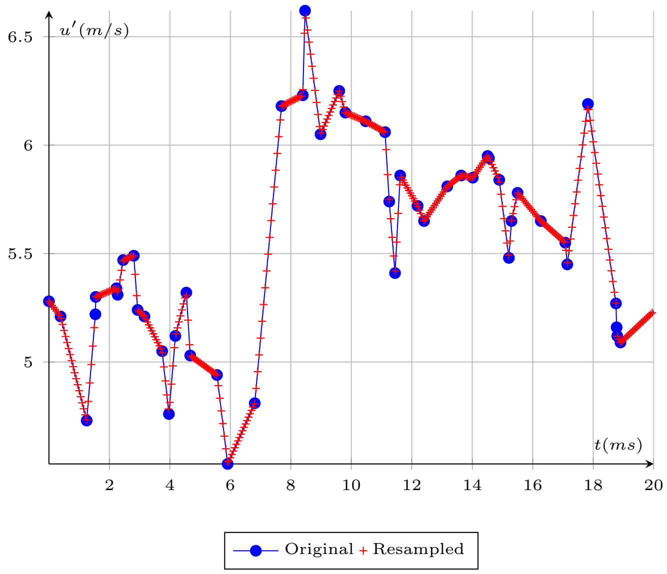

Figure 2.37: Example of the resampling of a part of the velocity signal measured with LDV.

Once the autocorrelation function is calculated, Taylor's micro-scale of turbulence ($\lambda(t)$) can also be calculated through definition of the osculating parabola which can be described as a function of Taylor's micro-scale (Equation 2.38).

$$y(\tau) = 1 - \frac{1}{\lambda^2} * \tau^2 \tag{2.11}$$

An example of the autocorrelation function and the corresponding osculating parabola is given in Figure 2.38. The term $\frac{1}{\lambda^2}$ is the value taken by the parabola at the intersection with the ordinate axis.

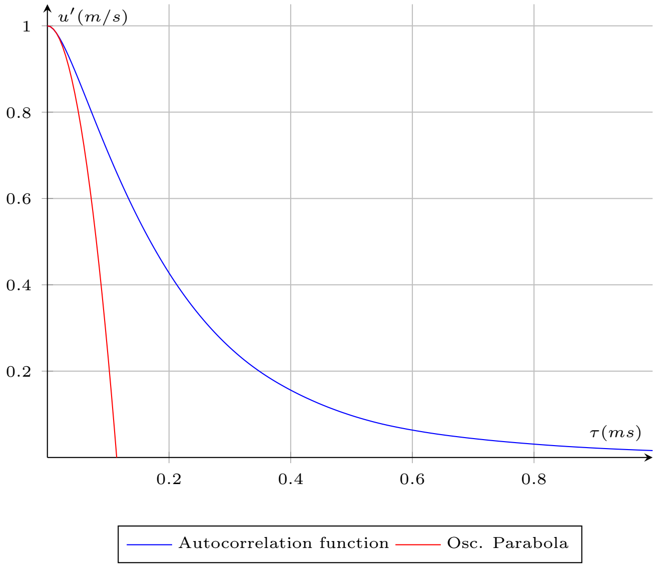

Figure 2.38: Autocorrelation function and the corresponding osculating parabola for the TL1 configuration (see Section 2.1).

2.7 Measurement protocol

An overview of the whole measurement path is given in Figure 2.39

Measurements can be separated into two parts. The first is relative to the force measurement and the second to turbulence measurement in the flow (LDV).

2.7.1 Force measurement

Force measurements are begin at the foil set-up. Attention is paid to every detail of the foil mechanical setup (tightening, angular plays, correct position of the balance) as no angular slack or unwanted contact areas are allowed – for instance between the foil and the back wall of the test section. Correct foil installation results in a constant angular positioning error (Figure 2.40).

Once the foil is correctly installed, calibration is carried out and measurements are post-processed to obtain the angular correction as a function of the force intensity for the current setup (Figure 2.41).

The calibration tool is then removed and the PIV calibration geometry is installed inside the test section, which is then closed and filled with water. PIV laser and camera are positioned and PIV parameters set depending on the flowing velocity and the zone to be observed. Calibration images are recorded and a scale factor is determined. The test section is then emptied, the calibration geometry removed and the test section filled again.

Before the flow is set, measurements at zero load is carried out with the balance in order to account for initial loads acting on the foil (weight of the foil, buoyancy). It is done for every angles of attack planned to be measured.

The flow is then set to the desired inflow velocity. Direct force measurement starts after

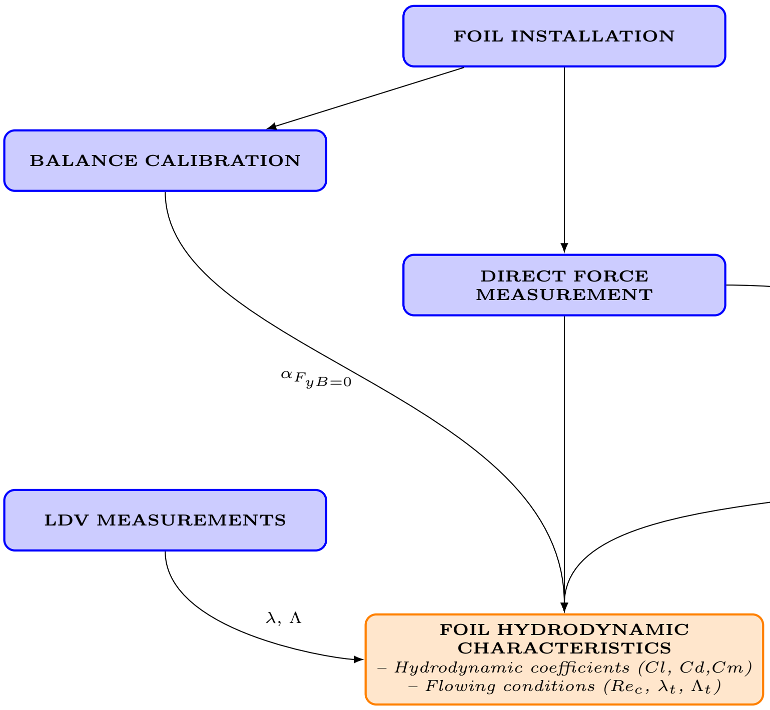

Figure 2.39: General measurement protocol

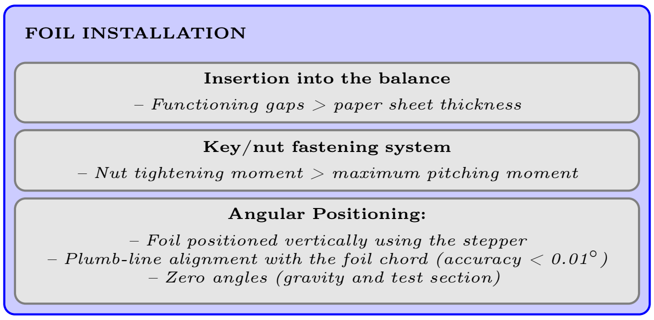

Figure 2.40: Foil installation

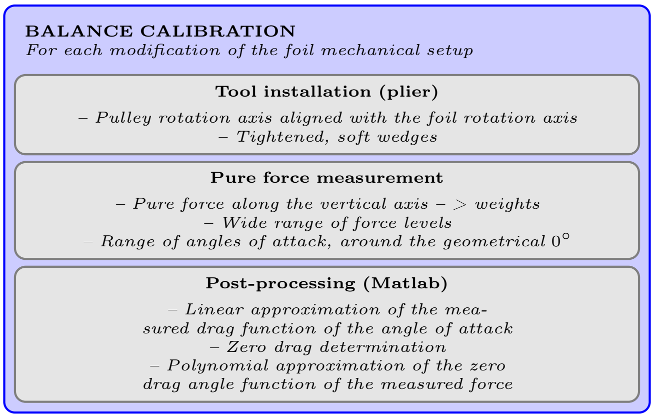

Figure 2.41: Hydrodynamic balance calibration

at least 30 s of delay from the beginning of the measurement, in order to wait for the flow to stabilize. For each angle of attack a 10 s measurement is carried out at an acquiring frequency of 1 000 Hz. Measurements are done continuously following both increasing and decreasing angles of attack and starting at 0°. The angle step is generally 1° but in more critical zone it is refined up to 0.1° and coarsened to 2° in less critical zones (Figure 2.42).

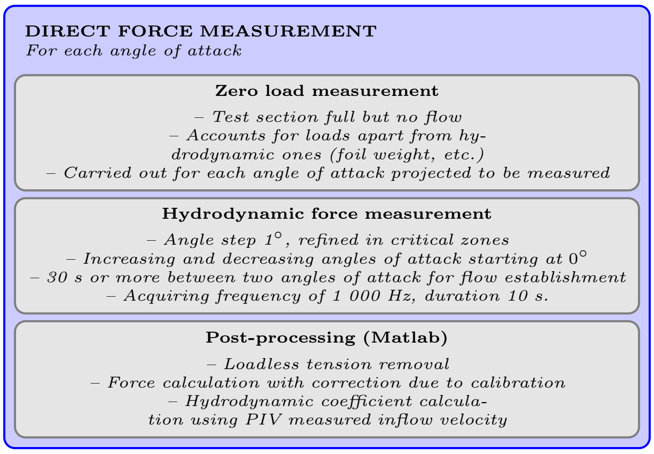

DIRECT FORCE MEASUREMENT
For each angle of attack

Zero load measurement
– Test section full but no flow
– Accounts for loads apart from hydrodynamic ones (foil weight, etc.)
– Carried out for each angle of attack projected to be measured

Hydrodynamic force measurement
– Angle step 1°, refined in critical zones
– Increasing and decreasing angles of attack starting at 0°
– 30 s or more between two angles of attack for flow establishment
– Acquiring frequency of 1 000 Hz, duration 10 s.

Post-processing (Matlab)
– Loadless tension removal
– Force calculation with correction due to calibration
– Hydrodynamic coefficient calculation using PIV measured inflow velocity

Figure 2.42: Direct force measurement using the hydrodynamic balance

PIV measurements are hand triggered with the force measurements. For each angle of attack, PIV images are taken during balance measurements (Figure 2.43).

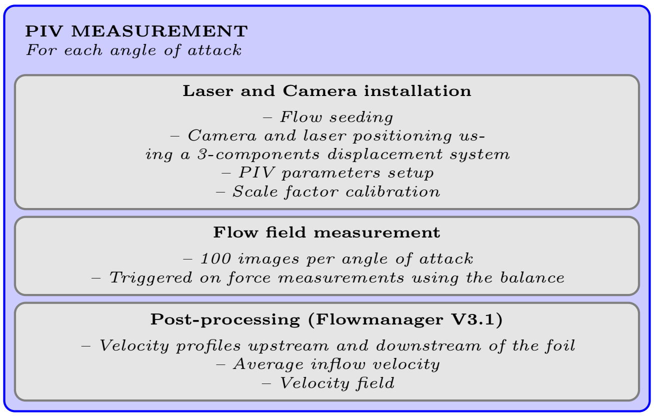

PIV MEASUREMENT
For each angle of attack

Laser and Camera installation
– Flow seeding
– Camera and laser positioning using a 3-components displacement system
– PIV parameters setup
– Scale factor calibration

Flow field measurement
– 100 images per angle of attack
– Triggered on force measurements using the balance

Post-processing (Flowmanager V3.1)
– Velocity profiles upstream and downstream of the foil
– Average inflow velocity
– Velocity field

Figure 2.43: PIV measurements

A Matlab post-processing enables the calculation of hydrodynamic forces occurring on the foil section and the application of the adequate corrections and parameters obtained by calibration and PIV measurements respectively.

The procedure is repeated for every new foil or flow configuration.

2.7.2 Turbulence measurement

Upstream turbulence measurement is carried out separately, only on the DU type foil section. Once the test section filled, the laser is installed in the right position with regard to the foil rotation axis. In the test section, the reference volume for measurements is set at mid span and mid height, 300 mm upstream of the foil axis using a 3-dimensional linear positioning system. LDV measurements are then done on the defined vertical profile (Figure 2.44).

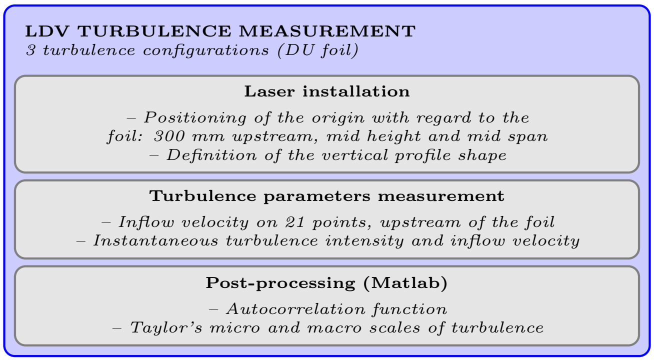

Figure 2.44: Turbulence measurement using LDV

Turbulence parameters are calculated using a dedicated Matlab post-processing routine. Results are associated to corresponding force measurements.

Chapter 3

Numerical configuration

Summary: Calculations on the blade sections are part of the design process of the industrial turbine. Accurate turbine performance prediction requires the computations to be validated on academic configurations. However, measurements constitute the largest part of the PhD, 2-D numerical investigations were also conducted using the tools and methods of the industrial partner, to be compared to the experimental data.This chapter presents the numerical model used, a sensitivity study and a comparison with experimental results on the NACA 0015 in forward flow.

Contents

3.1 Model

URANS/RANS code Ansys-CFX is employed. Both unconfined and tunnel-confined configurations are used.

The main properties of the numerical studies are listed below:

- *CFD software : CFX 12.0*
- *Mesher : ICEM 12*
- *Fully structured hexahedral mesh, with automatic mesh deformation procedure*
- $y^+_{avg} < 1$ *and* $y^+_{max} < 3.5$ *for* $Re_c = 10^6$

Calculations are considered valid when maximum residual values are under 0.00001 for steady cases and 0.0001 for unsteady cases.

Furthermore, for unsteady calculations, the total simulation time is set to 2s. This is done to let the fluid "cross" the domain several times, in order to guarantee numerical stability. The full time is only required in some particular situations and it often can be reduced, with regard to convergence of the studied variables–in our case hydrodynamic coefficients. However, it has to remain larger than $0.2s$ which is the approximate time for the fluid to travel once through the whole domain at $10m/s$.

3.1.1 Calculation domain

Two calculation domains have been used. Both are bi-dimensional but the first one (Dom1) is made for unconfined calculation and the second (Dom2) is made to account for vertical blockage effect occurring during experimental work. Dimensions of the two domains are given in Table 3.1.

Name	Min x (mm)	Max x (mm)	Min y (mm)	Max y (mm)
Dom1	-550 (-5c)	1050 (+10c)	-500 (-0.96c)	500 (+5c)
Dom2	-550 (-5c)	1050 (+10c)	-96 (-0.96c)	96 (+0.96c)

Table 3.1: Mesh domain size

An overview of both domain sizes is provided in Figure 3.1

For Dom2, the top and bottom walls are meshed with the same requirement as that of the foil surface in order to properly capture the boundary layer development and the adequate blockage effect.

3.1.2 Foil geometry

The foil geometry is defined by two splines built on a set of points that describe the initial geometry. As presented in Figure 3.2, the two curves are meeting around the half chord so as to preserve the continuity of the leading edge. For the same purpose, the initial set of points presents a refinement in the leading edge zone.

3.1.3 Mesh (ICEM 12.0)

The final mesh results from the convergence study which is presented later in the report. It consists in a fully structured hexahedral mesh. It is based on an OH architecture including an O-grid of 80 layers distributed in a zone of 20 to $25mm$ around the foil. The profile is

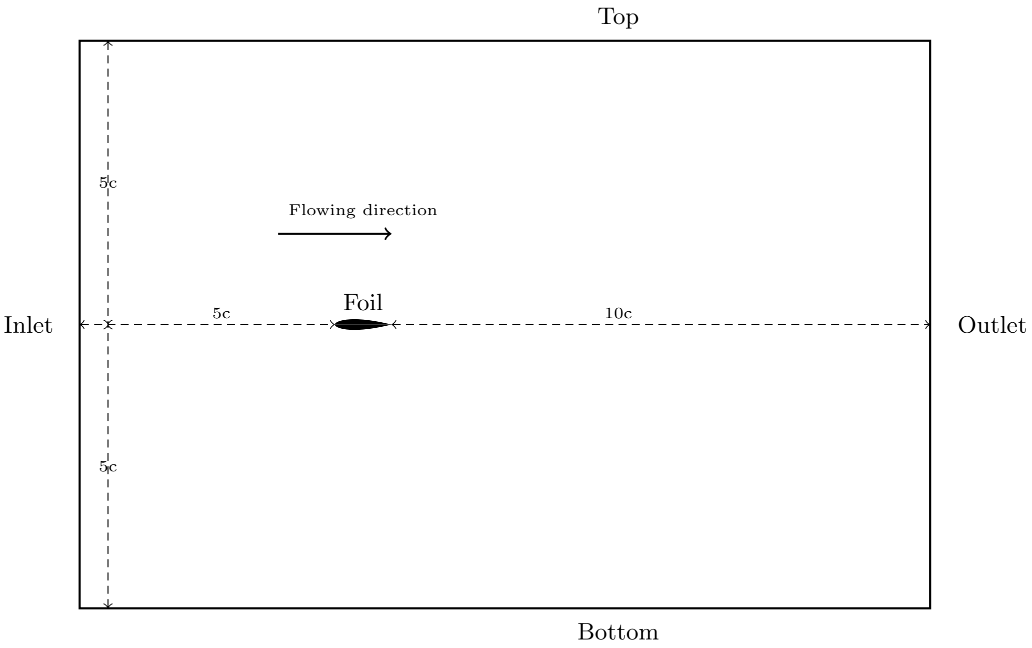

(a) **Dom1**, unconfined

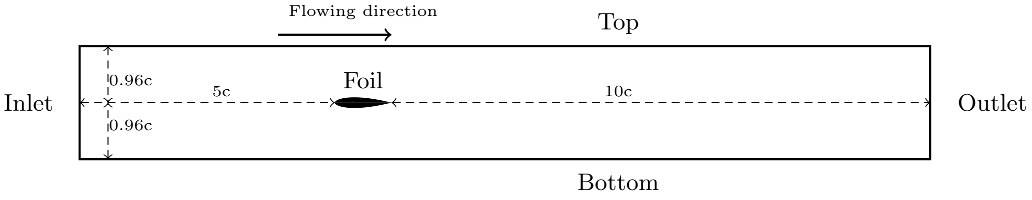

(b) **Dom2**, tunnel confinement

Figure 3.1: Mesh domains for numerical investigations

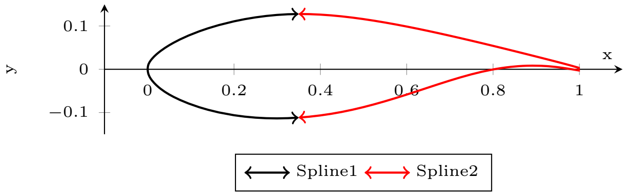

Figure 3.2: Foil geometry definition for calculation, example on the DU section

described by 460 points, with refinements in high curvature zones such as leading and trailing edges. Points distribution at the profile surface is adapted to the foil geometry.

A refined zone is also set in the wake, one chord and a half downstream. The goal is to correctly capture wake, which influences the global foil performance calculation. This is particularly the case for thick or rounded trailing edge profiles for which a Von Karman vortex shedding can occur. Figure 3.3 shows vortex structures captured by calculations.

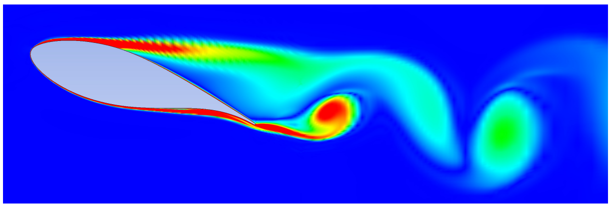

Figure 3.3: Vortex structure downstream of the uni-directional DU foil section (Vorticity), $\alpha = 18°$, $Re_c = 10^5$.

Figure 3.4 schematically shows the organization of mesh blocks. In red are blocks constituting the O-grid.

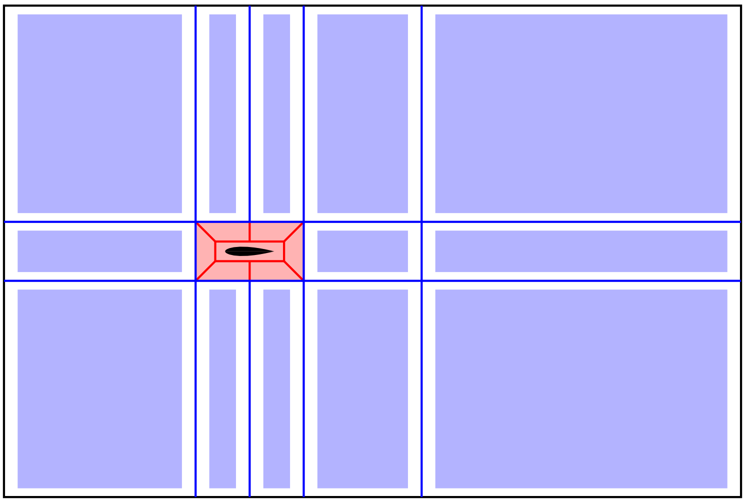

Figure 3.4: Architecture of mesh blocks

The mesh is composed of approximatively 130000 nodes. At the profile surface, the first cell thickness is set to $10^{-6}m$ (reminder: chord $c = 100mm$). A preliminary study has been carried out to approximate first cell thickness at the foil surface from theSchlichting [1960] formula. The method presented enables to analytically determine the first cell thickness for a given value of y^+. A sufficient refinement at the foil surface requires y^+ between 1 and 5. First cell thickness associated whith $y^+ = 1$ is around $10^{-6}m$. The chosen calculation model – previously described – is set to employ a low Reynolds resolution of the boundary layer when $y^+ < 5$. Moreover, for $y^+ = 25$ and more, the mesh does not allow "direct" resolution and a wall law is applied. This means that $5 < y^+ < 25$ is an undetermined zone, in which difficulties will appear in the resolution. The mesh deployed is characterized by $y^+_{avg} < 1$ and $y^+_{max} < 3,5$ at the profile surface.

Mesh propagation at the boundary layer is done using a geometric expansion law in the

O-grid. Value of the expansion ratio is set between 1.1 and 1.2 at the wall. Figure 3.5 presents a near-wall velocity profile obtained at $Re_c = 1 \times 10^6$ at the leading edge of the example profile. The first vector is located at $1 \times 10^{-6} m$ from the wall. This part of the flow around the profile is where the velocity gradient is the most important and the boundary layer the thinnest. However there are still 5 to 10 cells to describe the velocity profile.

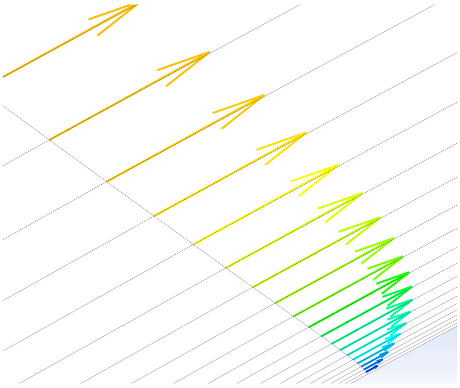

Figure 3.5: Near-wall velocity profile captured at the foil surface, leading edge

Once the "flat" mesh is created, it is extruded with one cell thickness. Indeed Ansys CFX is not able to solve 2-D meshes as itself and required at least one cell thickness. Anyway it is the procedure described for 2D calculation in the code documentation and this method has been shown not to affect results.

In order to obtain an homogeneous mesh, an automatic smoothing process is applied. It improves the global mesh quality by means of - among others - cell orthogonality at the profiles surface. Views of the final mesh applied to the DU foil section are presented in Figure 3.6.

For each profile studied, an initial mesh is built at 0° of angle of attack. This mesh is then deformed using a deforming mesh procedure to obtain the mesh for other angles of attack. Deformation consists in a rotation of the profile with the rotation center defined at a quarter of the foil chord from the leading edge. A stiffness (value: 1) is allocated near small volumes in order for the deformation not to affect boundary layers cell quality. This way, global quality is conserved and a very consistent range of meshes is obtained relatively quickly.

Deformation is done through a "false" unsteady calculation, for which only convergence of mesh deformation really matters. Calculation is initialized with the steady result at 0° of angle of attack and the profile is animated with a relatively low angular velocity. Intermediate result files are extracted at regular time-steps, preliminarily defined considering simulation time-step, rotational velocity and required angle-step. These intermediate results can then be used for mesh definition of "real" calculations.

Figure 3.5 also shows good orthogonality of the near-wall mesh cells, despite of the automatic mesh deformation procedure.

Concerning the NACA 0015 in reversed flow, numerical investigations had been carried out using the generic mesh configuration described above. However both fully turbulent and transitional models where not able to predict lift discontinuity observed around 0° of angle of attack, in the experiments. Mesh accuracy at the leading edge was suspected to be one of the parameters requiring imrpovement. Therefore, to take this hypothesis into account, finer mesh was built on the basis of observations of the trailing edge with binoculars. A photography of the edge observed using binoculars is given in Figure 3.7.

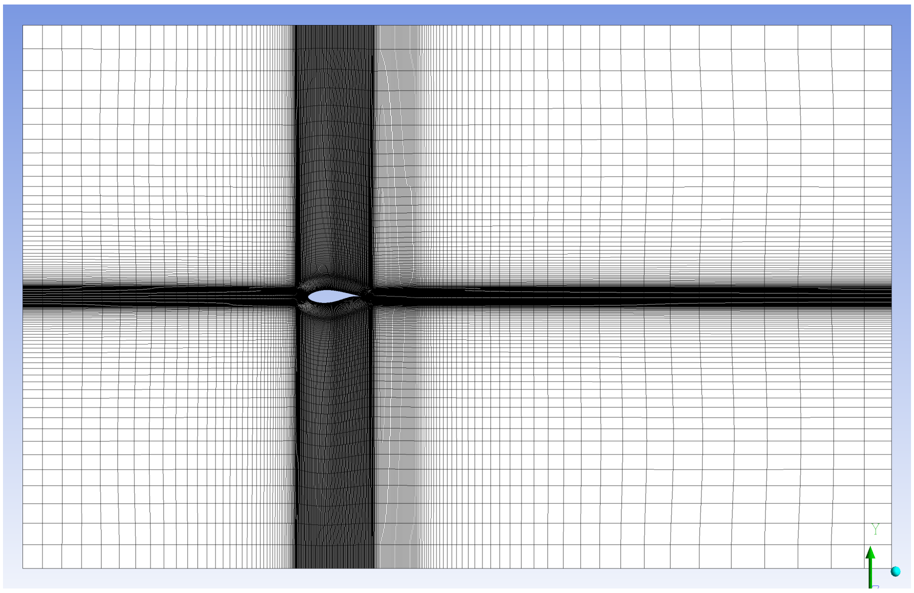

(a) Full domain

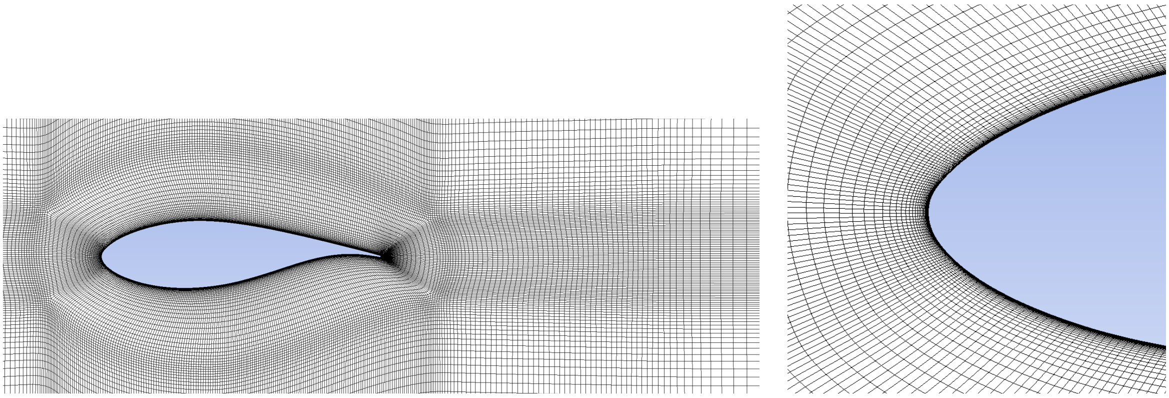

(b) Foil section and close wake

(c) Leading edge

Figure 3.6: View of the final mesh, $\alpha = 0°$

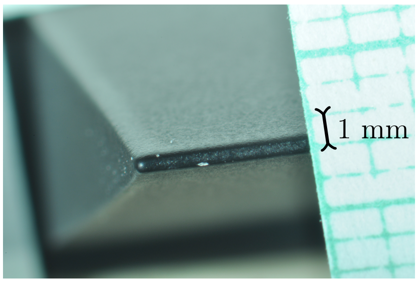

Figure 3.7: View of the trailing edge of the NACA 0015 test profile using binoculars. Graduations are in millimeters.

Geometry of the leading edge – in reversed configuration – is recreated using these observations. Particular attention is paid to mesh cell thickness at this location. The resulting mesh is illustrated in Figure 3.8.

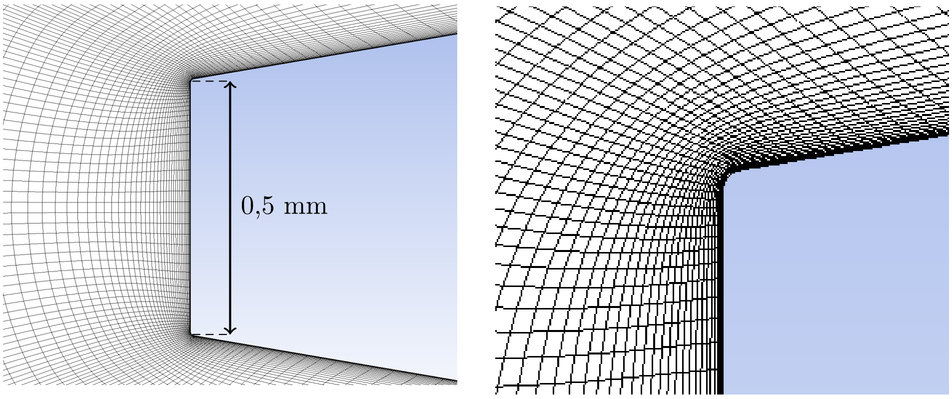

(a) Close leading edge mesh. Front face is 0.5 mm in height.

(b) Focus on the leading edge mesh, geometry sharpness.

Figure 3.8: Views of the close leading edge mesh of the NACA 0015 designed for reversed flow calculations.

3.1.4 Boundary conditions

The *Inlet* is set with a velocity uniform and parallel to the foil chord at 0° of angle of attack. Value of the flowing speed is of course adjusted to the requested value of the Reynolds number.

A condition of null average pressure is set at the *Outlet*. This allows local pressure variations but average pressure is constrained.

A no-slip wall condition is applied to the foil surface ($Profil$). In the case of the unconfined domain, the left ($Side1$), right ($Side2$), top (Top) and bottom ($Bottom$) sides are described as symmetries, in order to consider an infinite domain. For the tunnel domain, top and bottom boundaries are defined as walls to account for boundary layer development.

Reference pressure is set to the atmospheric pressure 101 500 Pa. Specification of this pressure is not essential, however it limits round-of errors. Indeed, the flow is led by pressure fluctuations and these variations can be very small compared to absolute pressure. This way, specifying a reference pressure allows for a better description of the flow.

3.1.5 Turbulence and transition models

As previously said, the solver is the RANS/URANS code Ansys-CFX.

Steady and unsteady simulations have been conducted. Unsteady calculations are initialized with the steady result at the same angle of attack.

The chosen turbulence model is a $k - \omega$ SST, as described by Menter [1993] and Menter et al. [2003]. It combines a $k - \epsilon$ model in the far field and a $k - \omega$ model near wall. $K - \epsilon$ model has difficulties representing behavior of the detached boundary layer, whereas the $k - \omega$ model as presented by Wilcox [1991] is known to better capture the detached boundary layer.

With this model, a High Resolution scheme is used. This allows for the use of an accurate second order Euler resolution method with possible return to a first order, stronger, when required - for convergence reasons.

The turbulence model is also applied with the option "Turbulence Numerics High Resolution". The role of this option is to adapt turbulence resolution depending on the local range of solutions. The idea is to adjust the accuracy and robustness of the model to the studied configuration. Blend Factor is employed to make this adjustment. Its value changes depending on the gradient of local variables and leads the accuracy or robustness of the solution. For example $BlendFactor = 1$ for a small evolution of the gradient allowing for improved accuracy; or $BlendFactor = 0$ when an important variation of the gradient occurs, requiring maximum robustness.

In some cases a transition model is also used. It is a $\gamma - \theta$ model, as described by Menter et al. [2006], which is used to account for the laminar/turbulent transition occurring at the foil surface. This is employed with most of the geometries and for several reasons. For example in the case of the bi-directional section, with a relatively thick trailing edge, the laminar part of the flow may be important and this model could be required. Unidirectional profiles, such as DU type profiles, can be particularly sensitive to boundary layer scheme. In the case of a tidal turbine design, transition effect can be crucial and can be taken into consideration numerically, through application, or not, of a transition model in addition to the turbulent model.

3.2 Sensitivity study

The numerical configuration originates from a sensitivity study of the mesh size and architecture but also of the time-step value for unsteady calculations, as well as residual values.

3.2.1 Mesh sensitivity

Three mesh sizes have been studied:

- 95 000 nodes (mesh N°1)
- 134 000 nodes (mesh N°2)
- 184 000 nodes (mesh N°3)

Steady calculations were carried out for three angles of attack: 0°, 8° and 12°. The lift and drag coefficients are presented in Figure 3.9 below.

Table 3.2 provides lift and drag coefficient differences. The difference is calculated as a percentage of mesh N°2 for the first comparison and of mesh N°3 for the second one. Important gap can be noticed between mesh N°1 and N°2. Indeed, Mesh N°1 presents generally lower lift values (between -2 % and -20 %). For this same mesh, drag is over estimated by 48 % at 12° of angle of attack, whereas it is around under estimated by 60 % at 0°, compared to mesh N°2. Gap between mesh N°2 and N°3 is not as significant. Mesh N°2, with slightly fewer cells, proposes quite a lower lift (between 1 % and 3 %) and higher drag (2 % to 7 %) compared to mesh N°3.

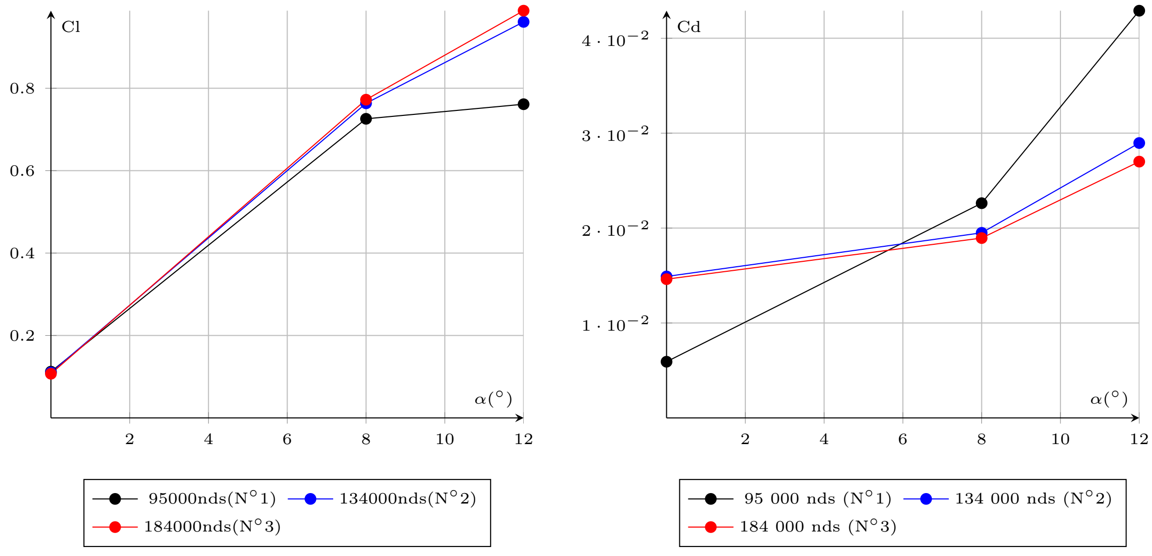

(a) Lift coefficient

(b) Drag coefficient

Figure 3.9: Lift and drag coefficients for three different mesh sizes. $Re_c = 1 \times 10^6$.

	Diff.(%) N°1-N°2		Diff.(%) N°2-N°3	
α(°)	Cl	Cd	Cl	Cd
0	-1.91	-60.29	-2.76	1.96
8	-4.92	16.01	-1.14	2.91
12	-20.79	48.13	-2.75	7.26

Table 3.2: Difference between lift and drag coefficients for three mesh sizes.

Mesh N°2 seems to be an interesting balance between accuracy of the domain discretization and calculation time. Moreover, a very highly refined mesh also requires a small time-step for accurate unsteady calculation. Time saving can be substantial.

As previously described, a geometric expansion law is chosen for the mesh layers' distribution around the foil, including the boundary layer. This kind of law has been selected as it is commonly used for this type of application. An expansion coefficient makes it possible to control growth of cell thickness. Various values of the expansion coefficient have been briefly studied and the final coefficient is set to 1.1, aligned with commonly used values.

3.2.2 Time-step sensitivity

This convergence study was carried out using the bidirectional section as presented previously in the section of this report describing experimental means.

A 134 000 nodes mesh – as described in previous reports – is used for the sensitivity study. Six time-steps are tested: $1 \times 10^{-2}s$, $5 \times 10^{-3}s$, $1 \times 10^{-3}s$, $5 \times 10^{-4}s$, $1 \times 10^{-4}s$ and $5 \times 10^{-5}s$.

Preliminary investigation

The Courant number or CFL is defined by the following equation:

$$CFL = \frac{U_\infty \Delta t}{\Delta x} \tag{3.1}$$

Δt is the time-step (s), Δx a length interval (m) and V the flowing velocity (m/s). The CFL number is employed to guarantee the stability of explicit calculation schemes. The following condition is used:

$$CFL = \frac{U_\infty \Delta t}{\Delta x} < 1 \tag{3.2}$$

Although an implicit resolution scheme is used in the present case, the CFL number can also be considered as an indication of the number of cells covered by a fluid particle during a time-step. A value of the CFL number that is too high indicates a time-step that is too important resulting in information loss. In that case, flow dynamics cannot be well described. The mesh studied has a minimum cell size of $1 \times 10^{-6}m$ at the profile surface. The inlet flowing velocity is set between 5 m/s and 10m/s for a Re_c between 5×10^5 and 1×10^6 . From this data, and to reach the CFL number conditions given in Equation 3.2, the time-steps have to be lower than $2 \times 10^{-5}s$ and $1 \times 10^{-5}s$, respectively.

A second criterion is the Strouhal number. It describes a relationship between foil section and flow properties, such as vortex shedding frequency for example. The Strouhal number is defined in equation 3.3.

$$S_t = \frac{fD}{V} \tag{3.3}$$

U_∞ is the flowing velocity (m/s), D a characteristic length of the profile (m) and f represents vortex emission frequency (Hz).

For the kind of flow and foil studied herein, the value of the Strouhal number can be considered as $St \simeq 0.2$. Using that condition, a value of the vortex shedding frequency can be calculated (f). If thickness (15 mm) is considered as characteristic length of the profile, for a flowing speed of 10 m/s the vortex shedding frequency is around 133 Hz. The period of force oscillations, linked to vertices emission, is $7.5 \times 10^{-3}s$. Twenty points are generally required to capture the full behavior of an oscillation, meaning that at most $3.75 \times 10^{-4}s$ is required as a time-step value.

Average Values

Lift, drag and pitching moment are calculated for several values of the angle of attack and for each of the time-steps. Average values are presented in Figure 3.10.

The two largest time-steps ($10^{-2}s$ and $5 \times 10^{-3}s$) are exhibiting a different behavior compared to smaller ones – even in the linear zone. It is characterized, on the lift curve, by an early stall angle and a more important slope at angles of attack prior to stall. Time-steps lower than

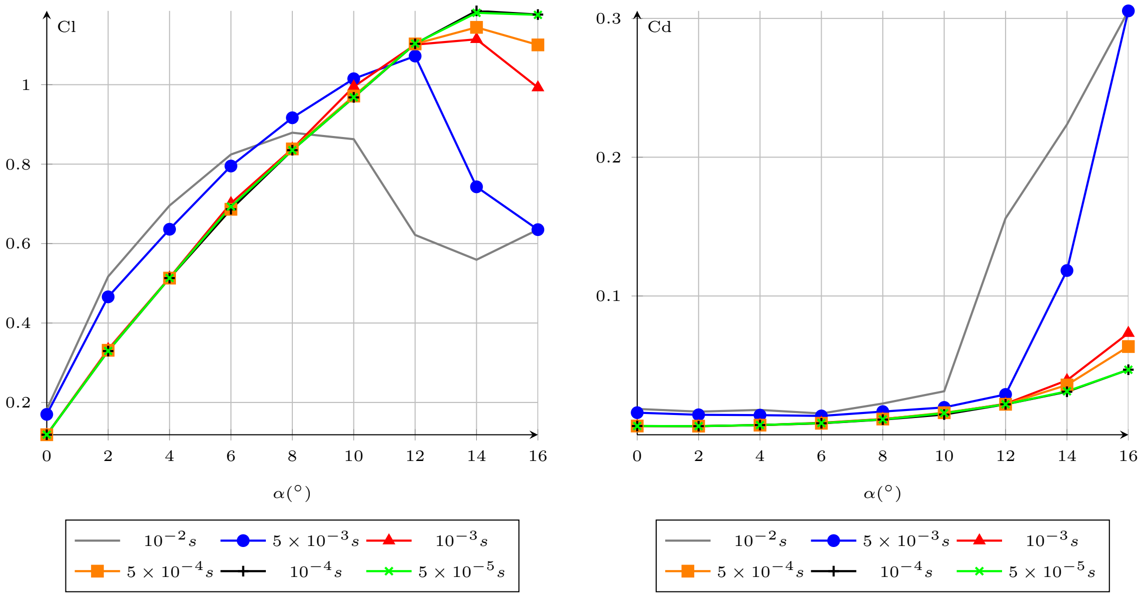

(a) Lift coefficient (b) Drag coefficient

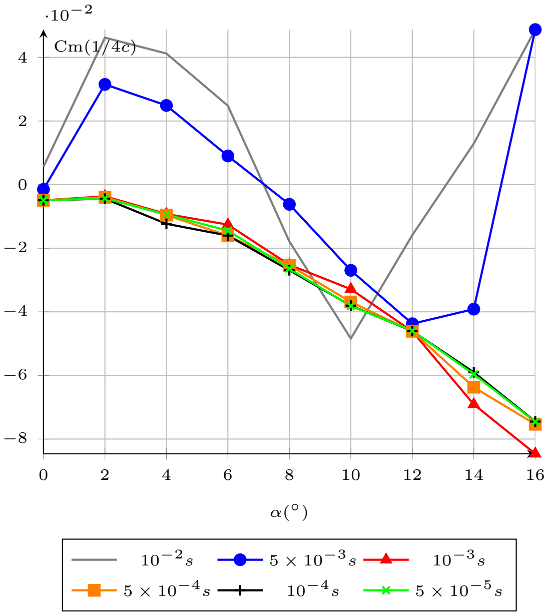

(c) Pitching moment coefficient

Figure 3.10: Hydrodynamic properties of the bi-directional section for six time-steps, $Re_c = 1 \times 10^6$.

$10^{-3}s$ are resulting in similar forces in the range of angles of attack from 0° to 12°. Beyond, little difference is observed regarding the stall angle.

Regarding the pitching moment, conclusions are similar. Time-steps over $10^{-3}s$ are showing very different behaviors, compared to finer ones. At low angles of attack this is characterized by sign changes of the pitching moment. Also, stall position and after-stall behaviors are more "pessimistic" in that case. Drag is also showing the stall point fluctuations that are also observed on both other coefficients for these time-steps.

Time-steps of $10^{-4}s$ and $5 \times 10^{-5}s$ gave identical results on the whole range of angles of attack. This is particularly the case for lift and drag values. Small differences are however observed on the pitching moment between these two values, at around 4° of angle of attack.

According to these results, a time-step value of $10^{-4}s$ or less is required to obtain valid results on average values.

Based on this study of average values, a time-step selection can be done and the largest two can be excluded. Indeed, observation of average hydrodynamic forces has not shown coherent foil behavior compared to finer values. Moreover, $10^{-4}s$ appears to be sufficient for a good accuracy solution including at high angles of attack.

Dynamic behavior

For the four remaining time-step values, evaluation of dynamic behavior allows for step selection. Both the evolutions of hydrodynamic forces and residual values are linked to time-step ad-equation to conditions of calculation. According to the previous part of the convergence study, for steady calculations, a maximum value of residuals of 10^{-5} is enough to obtain converging hydrodynamic forces. In the case of unsteady calculations, the residual limit is fixed at 10^{-4}. As seen in a previous study on a steady state case, such a residual value induces force variations below 1 %.

Figure 3.11 shows the evolution of the lift coefficient for several time-steps. Although results are obtained at 0° of angle of attack, small force fluctuations are observed, due to the rounded trailing edge of the bi-directional foil.

A reduction of the time-step induces a decrease of the amplitude of oscillations. Two main trends can be observed. Time-steps of $10^{-3}s$ and $5 \times 10^{-4}s$ are quite similar , and so are $10^{-4}s$ and $5 \times 10^{-5}s$.

The two largest time-steps are resulting in a rough evolution of lift compared to the two finer ones. The amplitude and period of the oscillations are also larger. However, $5 \times 10^{-4}s$ results in a more regular and refined lift variation than $10^{-3}s$ with less amplitude but more period. The two finest time-steps are producing very regular lift oscillations, with a similar overall aspect. The finest time-step ($5 \times 10^{-5}s$) induces a slightly lower period and amplitude. Nevertheless, no clear period convergence is observed following reduction of the time-step value.

These observations have to be linked to the evolution of residual values, which are presented in figure 3.12.

As can be observed, residuals inside a time-step of $10^{-3}s$ are not entirely under the 10^{-4} upper limit. Also, the finest time-steps make it possible to reach the residual value limit and obtain periodic and regular variations.

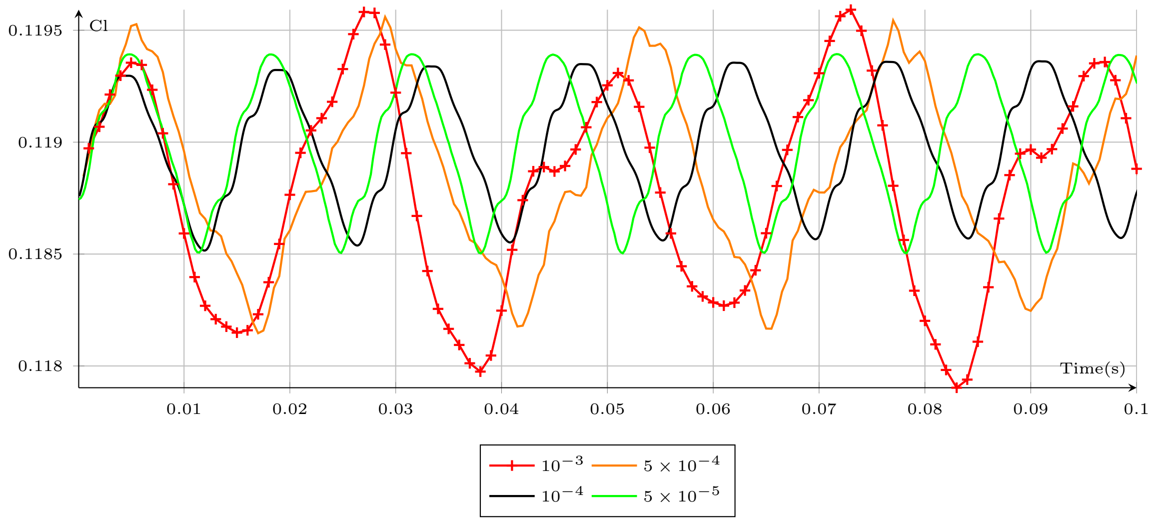

Figure 3.11: Evolution with time of lift coefficient for four time-steps, bi-directional profile. $\alpha = 0°$ et $Re_c = 1 \times 10^6$.

Preliminary investigations are suggesting a maximum time-step lower than $7.5 \times 10^{-3}s$. $10^{-5}s$ is too fine, as is illustrated in the following table (Table 3.3), which displays calculation properties for the four most refined time-steps. Indeed this is resulting in a particularly long computation time, despite time savings linked to a reduction of the iteration number per time-step. This table also shows that variations of the CFL value are occurring amid the fluid domain, due to local fluid velocity variation. As a consequence, the CFL condition presented in equation 3.2 cannot be reached for the entire domain.

Tstep(s)	**RMS CFL Num.**	**Max CFL Num.**	**It./Tstep**	**CPU time (s)**
10^{-3}	22.97	277.49	4 to 5	7.156×10^4 ($\simeq$0.8 day)
5×10^{-4}	11.48	138.70	3	1.441×10^5 ($\simeq$1.6 day)
10^{-4}	2.30	27.72	2	4.601×10^5 ($\simeq$5.3 day)
5×10^{-5}	1.15	13.87	2	8.132×10^5 ($\simeq$9.4 day)

Table 3.3: Flow characteristics and calculation general properties for different time-step values at 1 s of simulation time

Considering all these statements, the final time-step is set to 10^{-4} s for all unsteady numerical studies.

3.2.3 Residual values

Steady state calculations are considered valid when maximum residual values are under 10^{-5}. This value is commonly used for internal numerical studies on hydraulic turbines. The simultaneous observation of both the evolution of residuals and the hydrodynamic loads confirms this choice. Figure 3.13 shows the evolution of lift coefficient and residuals for the bi-directionnal profile at Re=1×10^6 and 14° of angle of attack. It can be seen that a convergence is reached passed residual values of 10^{-5}. Indeed, under 10^{-4} of residual value, variation of hydrodynamic coefficient is below 1 % of the final value.

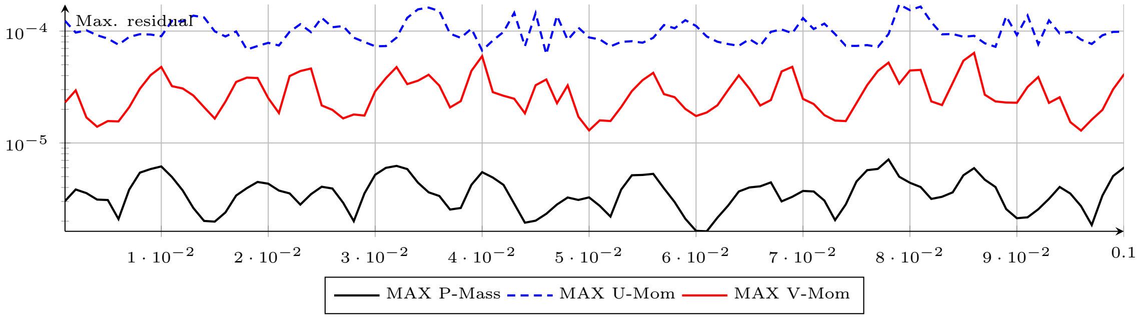

(a) Tstep=$10^{-3}s$

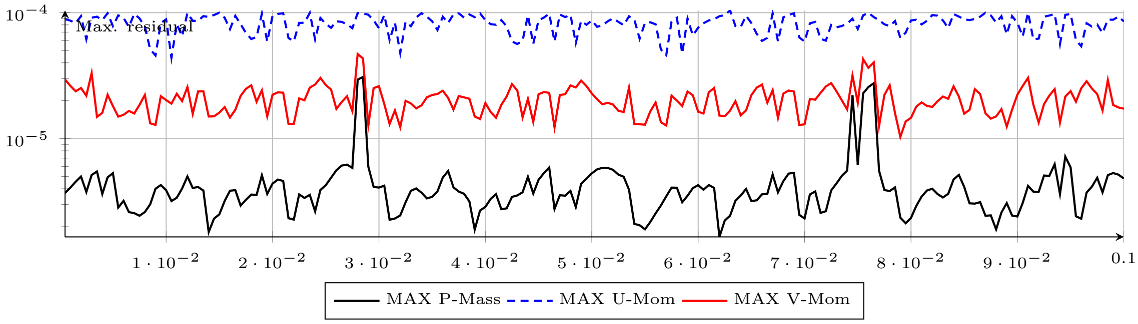

(b) Tstep=$5 \times 10^{-4}s$

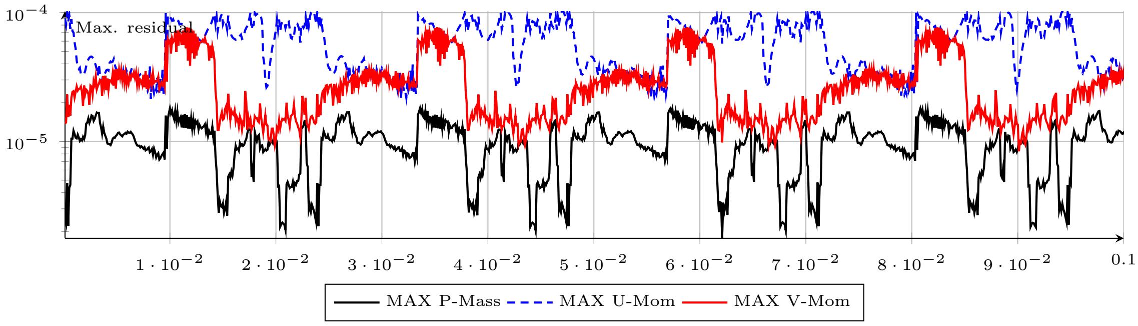

(c) Tstep=$10^{-4}s$

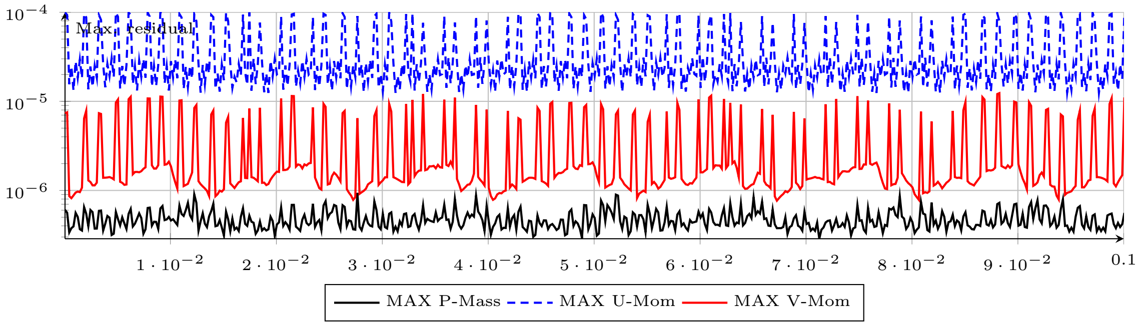

(d) Tstep=$5 \times 10^{-5}s$

Figure 3.12: Evolution of residual values over 0.1 s and for four time-steps. $\alpha = 0°$ and $Re_c = 1 \times 10^6$.

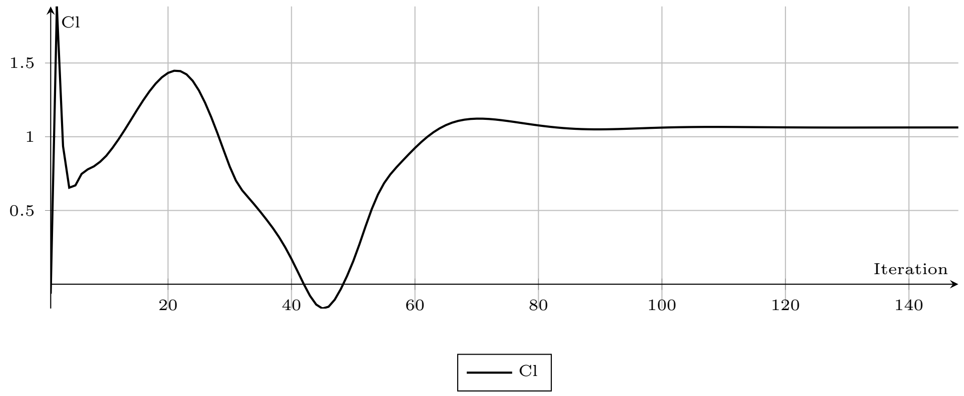

(a) Evolution of lift coefficient

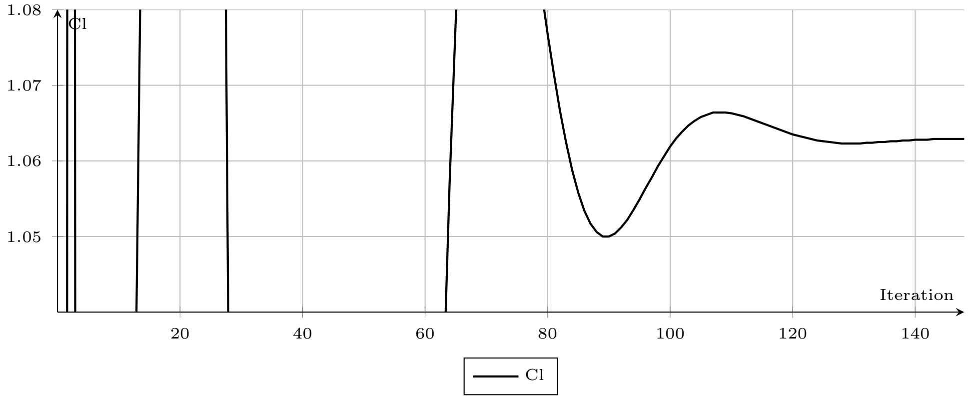

(b) Evolution of lift coefficient, detail

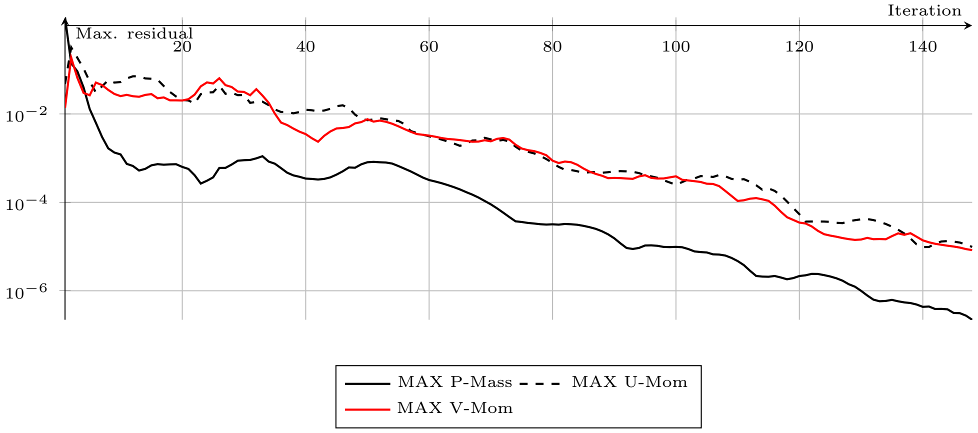

(c) Evolution of residual values

Figure 3.13: Evolution of lift coefficient and maximum residual values for a 2-D steady state calculation. Bi-directional profile, $Re_c = 1 \times 10^6$ and $\alpha = 14°$.

3.3 Comparison with experiments

The numerical model is compared to measurements for validation. Data such as average forces and velocity profiles are compared. Validation of the numerical setup is done on the NACA 0015 foil section.

3.3.1 Average forces

Average forces obtained with the hydrodynamic balance are compared to numerical results (Figure 3.14).

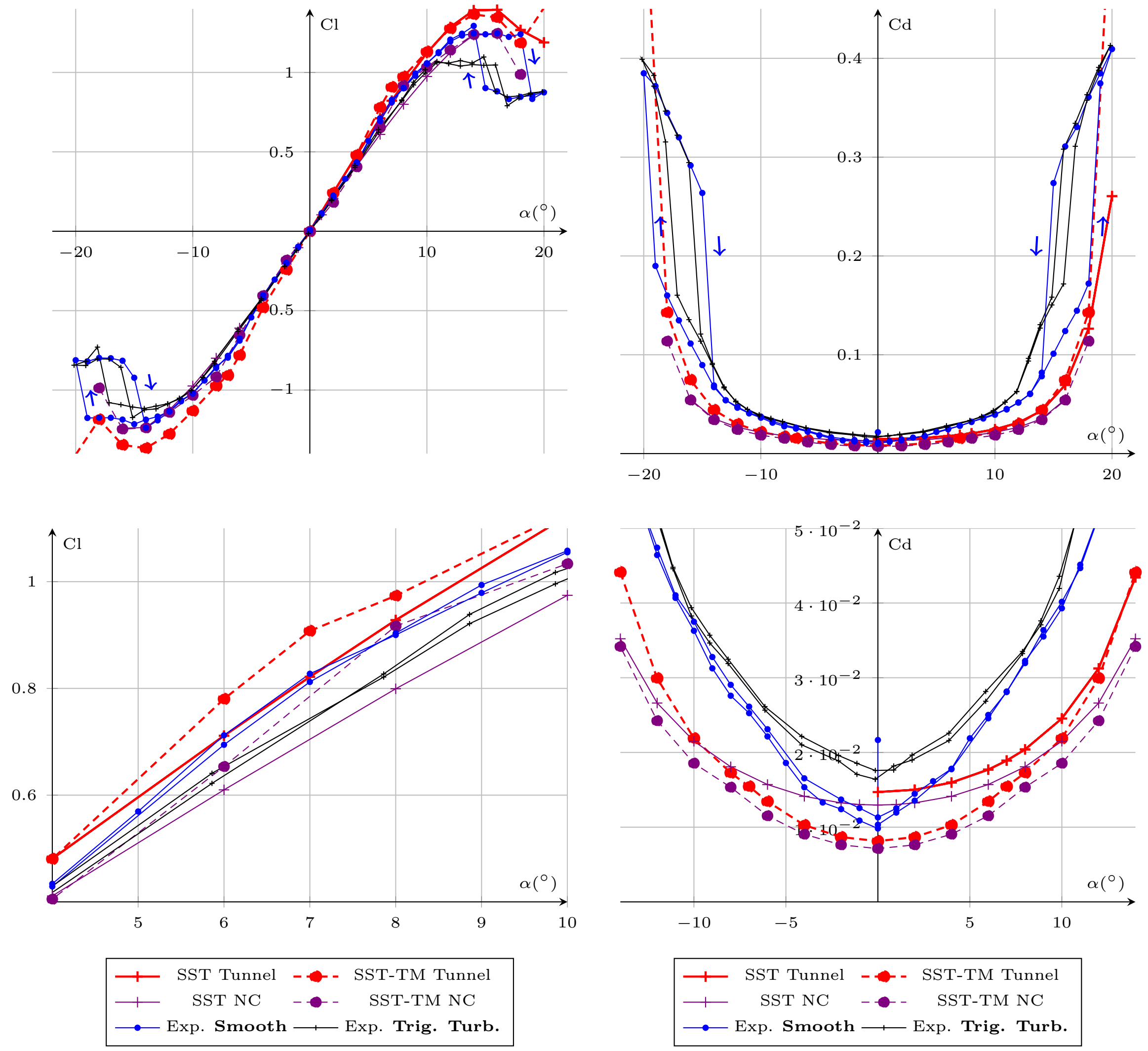

(a) Lift (b) Drag

Figure 3.14: Experimental and numerical data for lift and drag coefficients. NACA 0015 hydrofoil at $Re_c = 5 \times 10^5$ in forward flow. SST are the fully turbulent calculations and SST-TM represents calculations with the transition model.

The tunnel (Tunnel) mesh domain has been designed to account for blockage effect on a two-dimensional basis. It is closer to experiments than the unconfined mesh configuration however, regarding boundary conditions, it only partially represents the experimental setup. Indeed, the top and bottom wall effects are taken into account but span wise three-dimensional effects are not taken into account.

As shown in Figure 3.14, the use of an unconfined (NC) domain leads to generally lower lift and drag levels. Lift obtained with the unconfined configuration best suits experiments. On the other hand, increased drag level induced by the tunnel confinement best fits experimental drag. It can also be noticed that the lift curves obtained numerically are very similar to experiments, whereas numerical drag does not correctly model drag increase with the angle of attack. The level of drag at 0° AoA is however relatively accurately predicted by calculations.

Drag measured using the hydrodynamic balance is clearly three-dimensional. In the present case three-dimensional effects in experiments are:

- The horseshoe vortex occurring at the angle between the foil and the back face of the test section
- The induced drag, linked to the level of lift and principally materialized through a tip vortex which develops into the gap between the foil tip and the vertical front wall of the test section.

As results presented in Figure 3.14 have been obtained using the NACA 0015, measured drag at 0° AoA cannot be lift-induced, as lift is null at this angle.

3.3.2 2-D velocity Profiles

Velocity profiles obtained numerically are compared with PIV measurements at a location upstream of the foil and downstream (Figure 3.15, see section 2.5 for more detail). For comparison, velocity profiles are normalized based on the average inflow velocity calculated on the upstream profile.

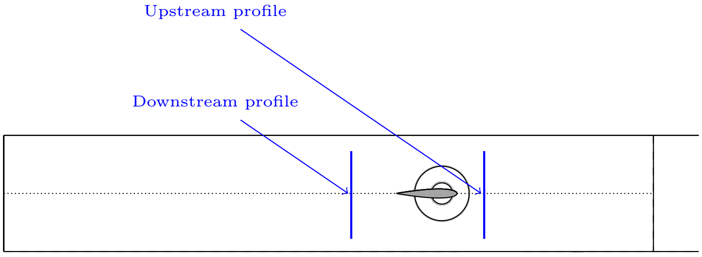

Figure 3.15: Position of the velocity profiles for flowing velocity measurements.

Results are presented in Figure 3.16 for two angles of attack (0° and 10°).

At 0°AoA, both experimental and numerical velocity profiles are in very good agreement. Upstream velocity variation along height is however slightly lower in measurements than in numerical results. Moreover, the velocity deficit into the wake is very well predicted.

At 10°AoA, the same statement can be made regarding velocity deficit and overall velocity profiles. Variation of the measured inflow velocity along the vertical is also more visible.

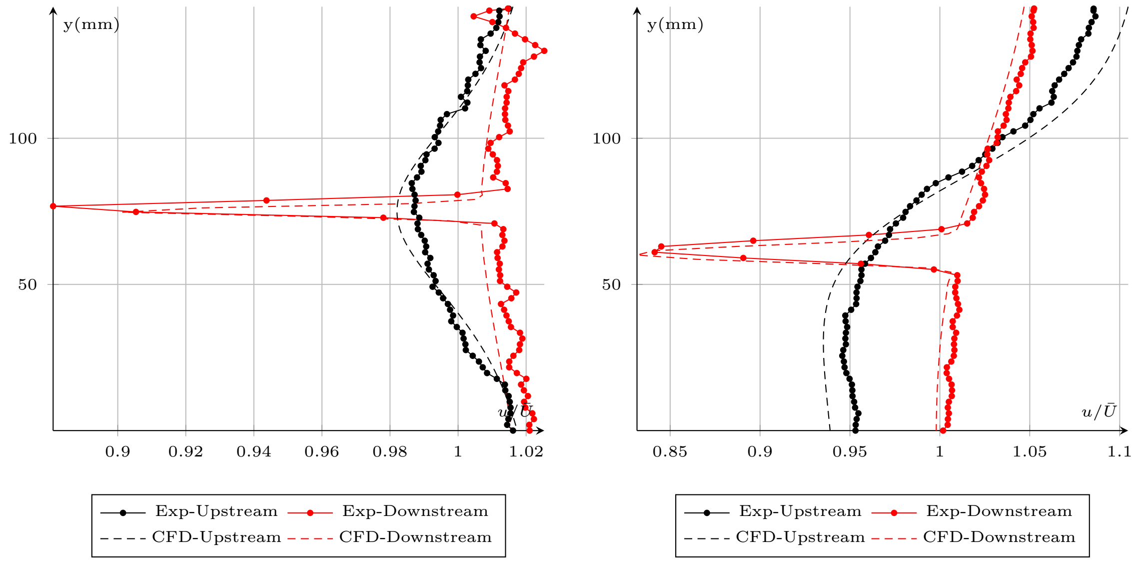

(a) $\alpha = 0°$

(b) $\alpha = 10°$

Figure 3.16: Comparison of the upstream and downstream velocity profiles for the NACA 0015, obtained through calculation and PIV measurements, $Re_c \simeq 5 \times 10^5$.

There is a good agreement between experiments and numerical results. Velocity variations along the vertical length obtained experimentally are lower than those predicted by calculations.

3.3.3 Induced Drag

Calculations are two-dimensional and even though the top and bottom walls are modeling the major part of the blockage effect, horizontal confinement is not taken into account. Observations during measurements have shown that horseshoe and tip vortices are occurring which are not taken into account in calculation. Combination of the two effects are generating an important additional drag while lift is less affected.

To account for these three-dimensional components of the drag, adequate three-dimensional calculations could be carried out. However, to properly capture both vortices, a thorough three-dimensional mesh is required, with adequate refinements in the functioning gap as well as at the foil junction with the back wall. This means large meshes as well as large computation times, without accounting for unsteady calculations that are required at high angles of attack.

With regard to drag – which is more subject to span wise three-dimensional effects – an alternative solution is to use the concept of induced drag in order to match calculations with measurements. The objective is to convert numerical 2-D results into 3-D using experiments. As given in the following equation (3.4), 3-D drag for a wing can be decomposed in a two dimensional drag completed by an induced drag function of the lift and the wing properties (Clancy [1986]).

$$Cd_{3D} = C_{D,0} + C_{Di} \tag{3.4}$$

$$C_{Di} = \frac{Cl^2}{\pi e AR} \tag{3.5}$$

Where $C_{D,0}$ is the two-dimensional drag, C_{Di} is the induced drag, Cl is the lift coefficient, AR is the aspect ratio of the wing (span/chord) and e is the wing efficiency, which is dependent on the span wise load distribution.

Using this formulation, the numerical 2D drag can virtually be set to 3-D using experimental foil section properties (i.e. $AR = 1.915$).

Figure 3.17 presents the application of this method so as to convert numerical 2-D results into three-dimensional ones for the NACA 0015 hydrofoil.

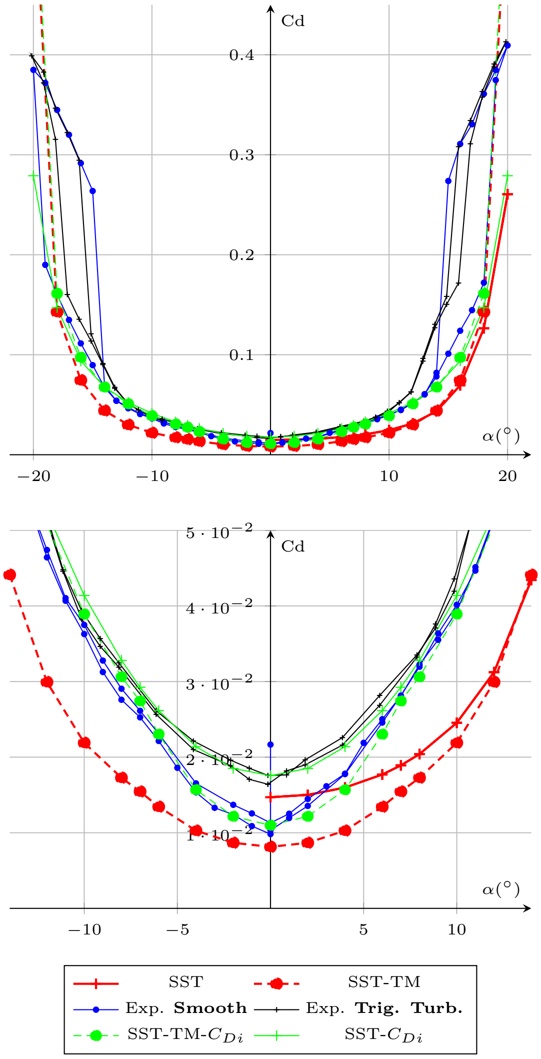

Figure 3.17: Experimental and numerical results including induced drag for the NACA 0015 hydrofoil at $Re_c = 5 \times 10^5$ in forward flow.

In that particular case, $C_{D,0}$ is the combination of the real 2-D drag and a constant. This constant is representative of lift-independent three-dimensional drag and is set using the difference between numerical and experimental drag at 0° AoA (where lift is zero). In the present case it is set to 0.00285.The efficiency is then set to best fit experimental results, in practice for that case $e = 15$. This efficiency should be representative of the experimental setup. An infinite wing (2-D) has an infinite efficiency as the induced drag is zero. On the other hand, an unconfined finite wing should have an efficiency that is less than the unity. The present case is situated between the infinite wing and the finite case.

Results with induced drag correction are showing that the major part of the difference between experiments and calculations is caused by three-dimensional effects.

This method could be a basis for correction of three dimensional effects. However further work must be conducted to make it reliable and representative of the tunnel test section for the whole range of profiles. Therefore it has not been used and all the measurements are three-dimensional.

Chapter 4

Comparative study of two blade design strategies

Summary: As presented in the introduction, the global issue deals with the behavior of tidal turbine blade sections subjected to marine currents constraints. One of the major constraints is the quasi bidirectionality of the flow between ebb and flood. Avoiding the use of a returning system requires the use of a unidirectional foil in forward and reversed flow, or the design of a bidirectional section. The objective of this chapter is to compare the properties of a standard unidirectional section in forward and reversed flow to a bidirectional foil section. Properties of a NACA 0015 foil in forward and reversed flow are compared to an elliptic bidirectional foil.

Contents

4.1 Introduction

It can be thought that avoiding the installation of a reversing system on the machine is as simple as it is to design a rotor for one flowing direction and then let it work in the reversed configuration without modifications. However, this requires that the blade works properly in the reversed configuration. At the scale of the blade section, the reversed flowing configuration results in an uncommon flowing situation. The trailing edge becomes rounded and thick whilst the leading edge is sharp. This should result in a specific behavior.

Another solution to achieve the reversibility of the turbine without a returning system is to use bidirectional types of sections, designed to work identically in both flowing directions: regular and reversed.

A bidirectional section is rotationally symmetric, which means that LE and TE are identical. This way the leading edge is thinner and the trailing edge thicker compared to conventional hydrofoils.

These two options to achieve reversibility of the turbine are studied using academic foil sections.

Firstly, a NACA 0015 is studied in forward and reversed flow as illustrated in Figure 4.1

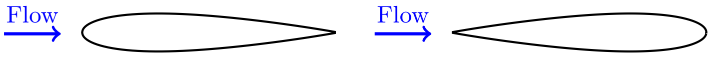

(a) Regular (b) Reversed

Figure 4.1: Regular and reversed foil configurations

A bidirectional hydrofoil is studied as well. It is designed using an elliptical thickness law, cambered with a parabolic law. The camber law is rotationally symmetric around the foil center. It is characterized by a relative thickness of 15 %, comparable to the NACA 0015. The geometry is presented in Figure 4.2.

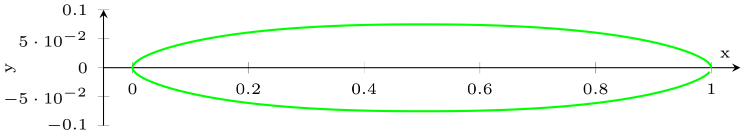

(a) Thickness law

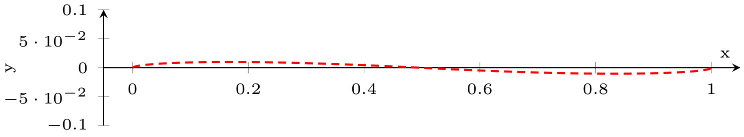

(b) Camber law

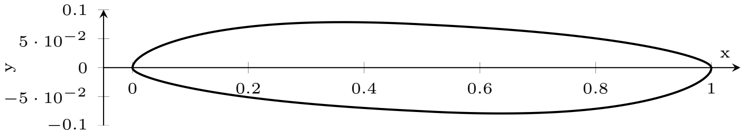

(c) Resulting foil

Figure 4.2: Normalized elliptical bi-directional geometry, $\alpha = 0°$.

In a first part, a reminder of properties of the NACA 0015 in forward flow is provided. Then, reversed flowing configuration specificities are displayed in detail. The third part presents the characteristics of the bidirectional hydrofoil. Finally, results are discussed.

4.2 NACA 0015 in forward flow

The properties of the NACA 0015 in the regular flowing configuration are presented in this section. But before experimental and numerical results are presented, a comparison is carried out with data from literature.

4.2.1 Comparison WITH literature

Experimental results on the smooth NACA 0015 are compared to data available in the literature. Figure 4.3 presents experimental data obtained in the hydrodynamic tunnel compared to those from Sheldahl and Klimas [1981], obtained in wind tunnel at $Re_c = 5 \times 10^5$ and $Re_c = 6.8 \times 10^5$.

Other reference data obtained in wind tunnels are available from Jacobs and Sherman [1937] and Jacobs et al. [1935] or more recently from Bertagnolio [2008] but at higher Reynolds numbers than those used in the present work.

Lift measurements are in good agreement on most of the range of angles of attack. Particularly on the linear part of lift (Figure 4.3). The slopes of lift curves are identical. At 7°, the slope changes for all the three data sets and experimental results from Sheldahl and Klimas [1981] are lower than ours on that point. The maximum lift measured in the present case is also higher than that which is given in the literature, but its angular position is similar.

Experimental drag data from the literature is globally lower than that obtained in the IRENav. At 0° AoA, our data is relatively close to literature, but remains slightly higher. The difference increases as the angle of attack increases, and lift as well. Three-dimensional effects are increasing the drag measured in the cavitation tunnel. Note that the drag as given in the literature is not symmetric, which should be the case.

Data from Sheldahl and Klimas [1981] were obtained in a wind tunnel on a wing with an aspect ratio of 2, similar to the one used in the present case. However data are corrected for the blockage effect and the tunnel parameters. Therefore, lift and drag measured by Sheldahl and Klimas [1981] are lower than ours.

Finally, it can be observed that the pitching moment curve presented in the Figure 4.4 is very similar across the three sets of data, particularly at negative angles of attack. For positive angles of attack, our pitching moment results are lower compared to the literature but the trend remains very close. Changes in the pitching moment sign are similarly seen on the three sets of data, their angular position is common but moment level varies between data. Where drag and lift are concerned, it must be noticed that the pitching moment is not anti-symmetric between positive and negative angles of attack in the data from Sheldahl and Klimas [1981].

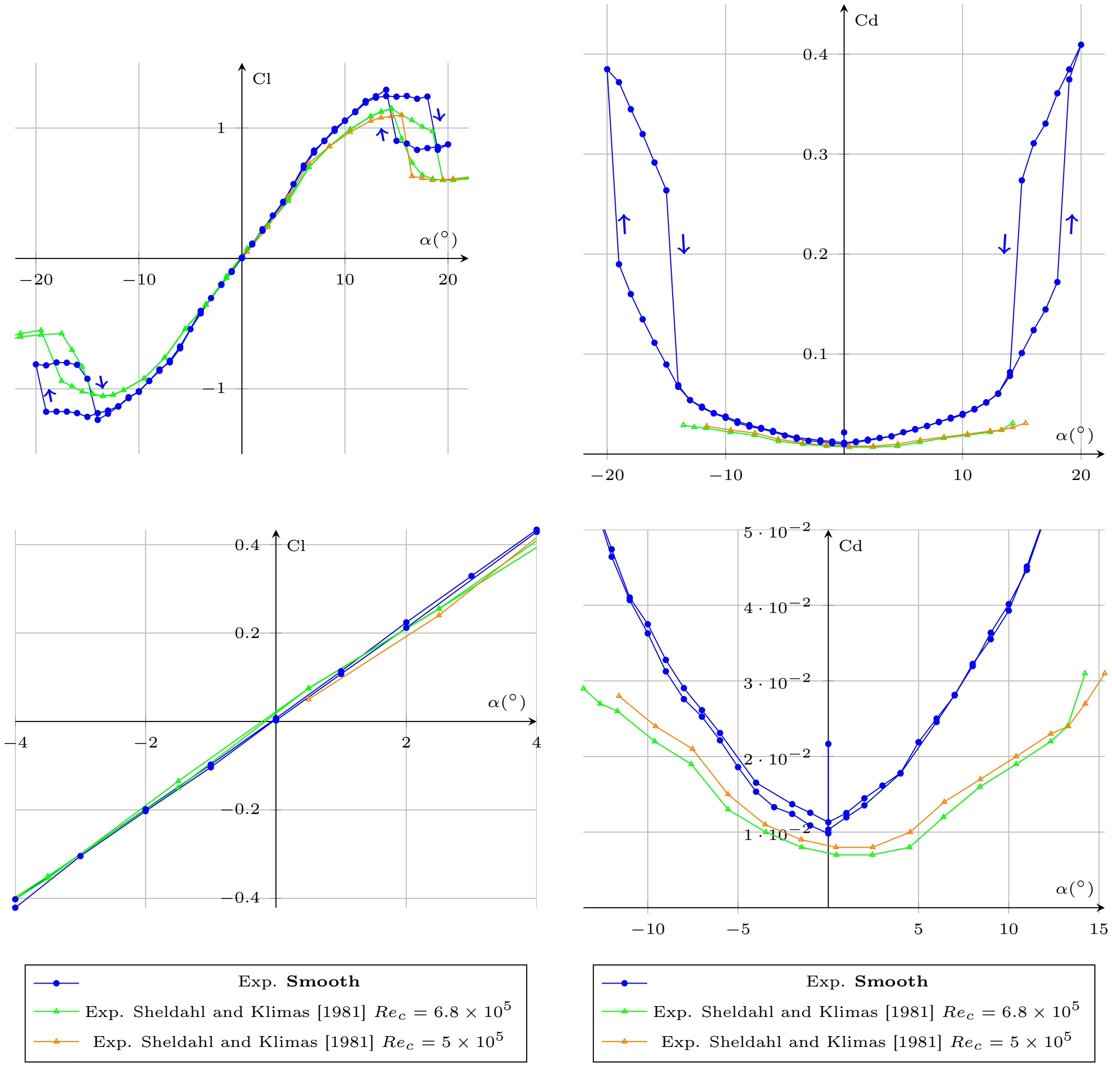

(a) Lift (b) Drag

Figure 4.3: Experimental and numerical data for lift and drag coefficients. NACA 0015 hydrofoil at $Re_c = 5 \times 10^5$ in forward flow.

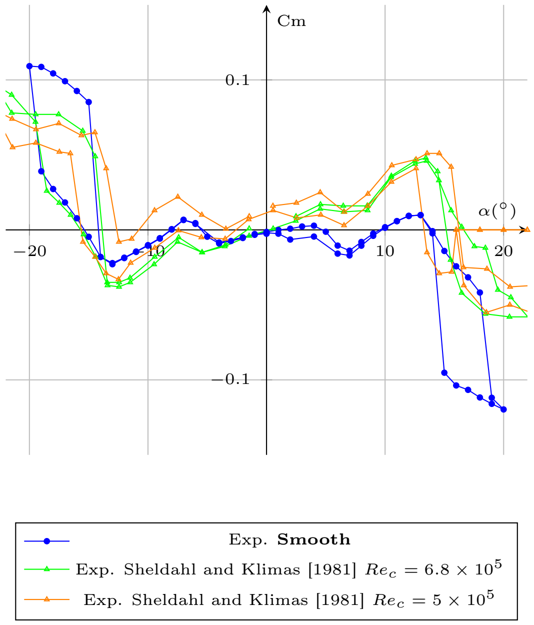

Figure 4.4: Experimental and numerical data for the pitching moment coefficient. NACA 0015 hydrofoil at $Re_c = 5 \times 10^5$ in forward flow.

4.2.2 Experimental analysis and numerical simulation

The NACA 0015 in forward flow is used as a reference for the comparison of the reversed foil with the bidirectional foil. Experiments and computations are presented thereafter.

Lift and drag coefficients at a Reynolds number value of $Re_c = 5 \times 10^5$ are given in Figure 4.5.

In the smooth configuration, maximum lift coefficient reaches 1.2 at around 15° of angle of attack. Beyond that angle, stall occurs. It leads to a lift drop as well as an important increase of the drag.

A hysteresis loop is observed on both lift and drag near stall angle, which is visible in data from Sheldahl and Klimas [1981] as well. This phenomenon generally occurs at relatively low Reynolds numbers and several studies have been conducted on the subject (Yang et al. [2008], Mueller [1985], Biber and Zumwalt [1993] and Mittal and Saxena [2002]). According to Mueller [1985], this is linked to laminar transition and separation, introducing a delay in flow reattachment when angles of attack are decreasing, compared to when they are increasing. Baragona [2004] showed that the Laminar Separation Bubble bursting in the leading edge zone is responsible for the occurrence of the hysteresis loop. In the present case, the loop could also be favored by the low turbulence level in the tunnel, as suggested by Hoffmann [1991a].

Moreover, the laminar/turbulent transition generates a discontinuity on the lift curve in comparison to the linear behavior, located around 7° AoA. It is also visible in experimental data from Sheldahl and Klimas [1981] and is well predicted by computations using the SST-TM configuration.

The discontinuity occurs when the transition point reaches the trailing edge on the pressure side. On the suction side, this also matches with positioning of the transition point close to the leading edge (Figure 4.6). The occurrence of this discontinuity has also already been

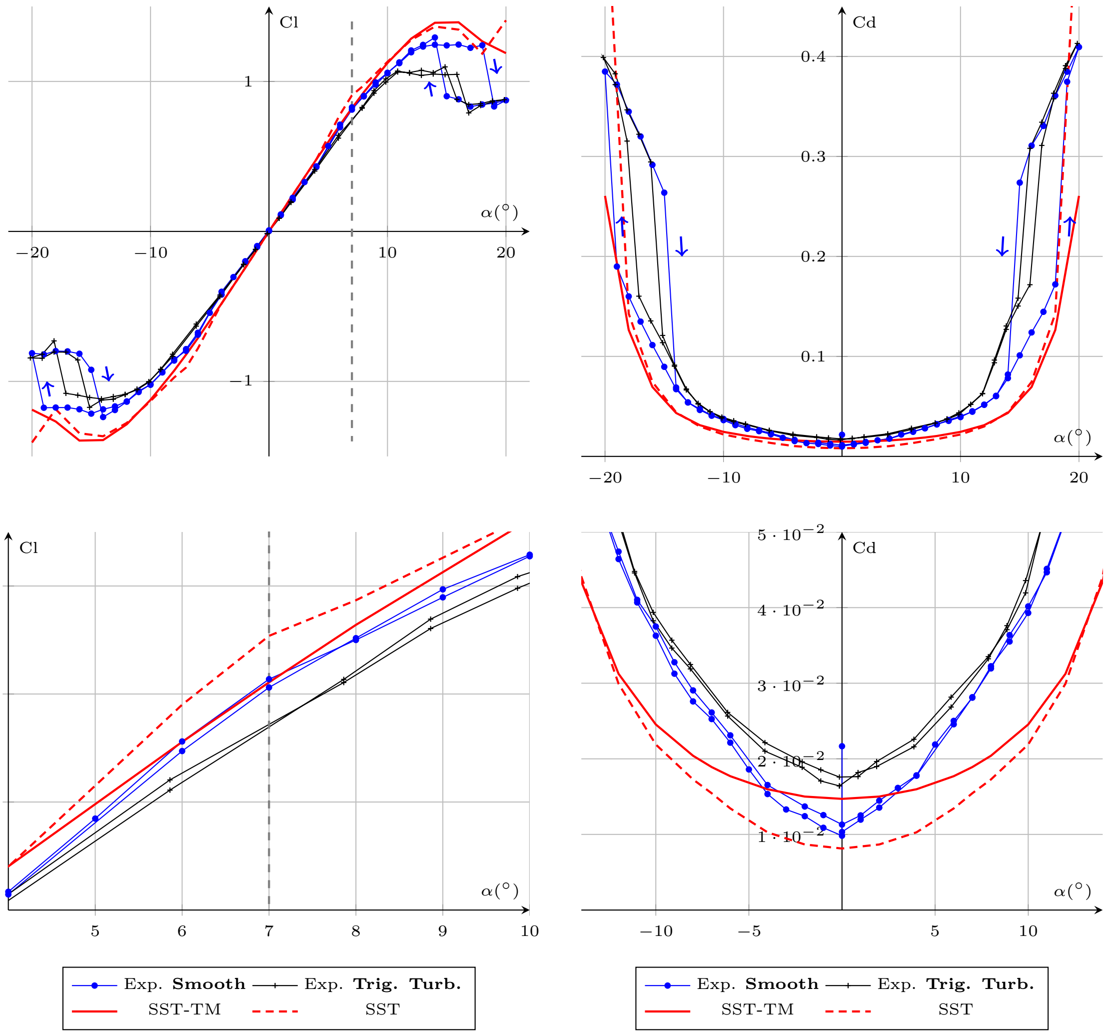

(a) Lift

(b) Drag

Figure 4.5: Experimental and numerical data for lift and drag coefficients. NACA 0015 hydrofoil at $Re_c = 5 \times 10^5$ in forward flow.

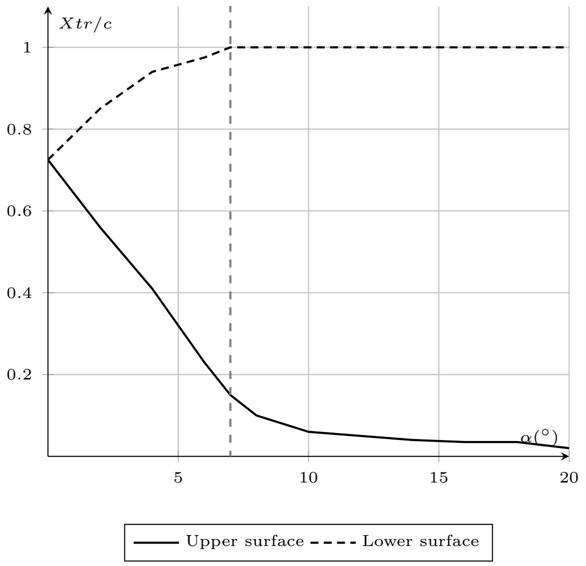

Figure 4.6: Location of the transition, NACA 0015 SST-TM numerical data, forward flow $Re_c = 5 \times 10^5$.

observed on a NACA 0018 at similar Reynolds number values by Timmer [2008]. He suggested the discontinuity to be linked to the positioning of the pressure side transition bubble at the trailing edge.

As shown in Figure 4.5, the addition of roughness changes the behavior of lift, and the maximum lift level is slightly lower in the rough case. The discontinuity also disappears, confirming its relation with the transition phenomenon. Moreover, the hysteresis loop observed in the case of the smooth surface and between increasing and decreasing angles of attack is removed by the installation of leading edge roughnesses.

The level of drag obtained with the addition of roughness is globally higher than in the smooth case. However, beyond the stall angle, both configurations are producing the same amount of drag. As stated for the lift, the hysteresis loop is removed when turbulent boundary layers are forced using roughness.

The pitching moment is presented in Figure 4.7. There is a good adequacy between experiments and numerical results for both smooth and turbulent configurations until 14° AoA. For higher absolute angles, experimentally measured pitching moment becomes higher than computations. The pitching moment also shows a specific behavior at 7° AoA. While on most of the angular range both smooth and turbulent data are very similar, around 7° AoA the pitching moment of the smooth configuration changes sign. This evolution implies a displacement of the position along the chord of the application point of the hydrodynamic force, the origin being the transition.

In the same Figure 4.7 the lift to drag ratio is presented. In the case of a smooth hydrofoil, lift to drag ratio is maximum at 7° AoA, with a value of 28 in experiments. For the the turbulent case the maximum lift to drag ration is lower (25) but located at higher angles of attack. And for both cases numerical models are accurately predicting angular position of the maximum lift to drag. However, the level is overestimated principally due to three-dimensional effects on the drag measured in the hydrodynamic, which considerably increases the value of drag.

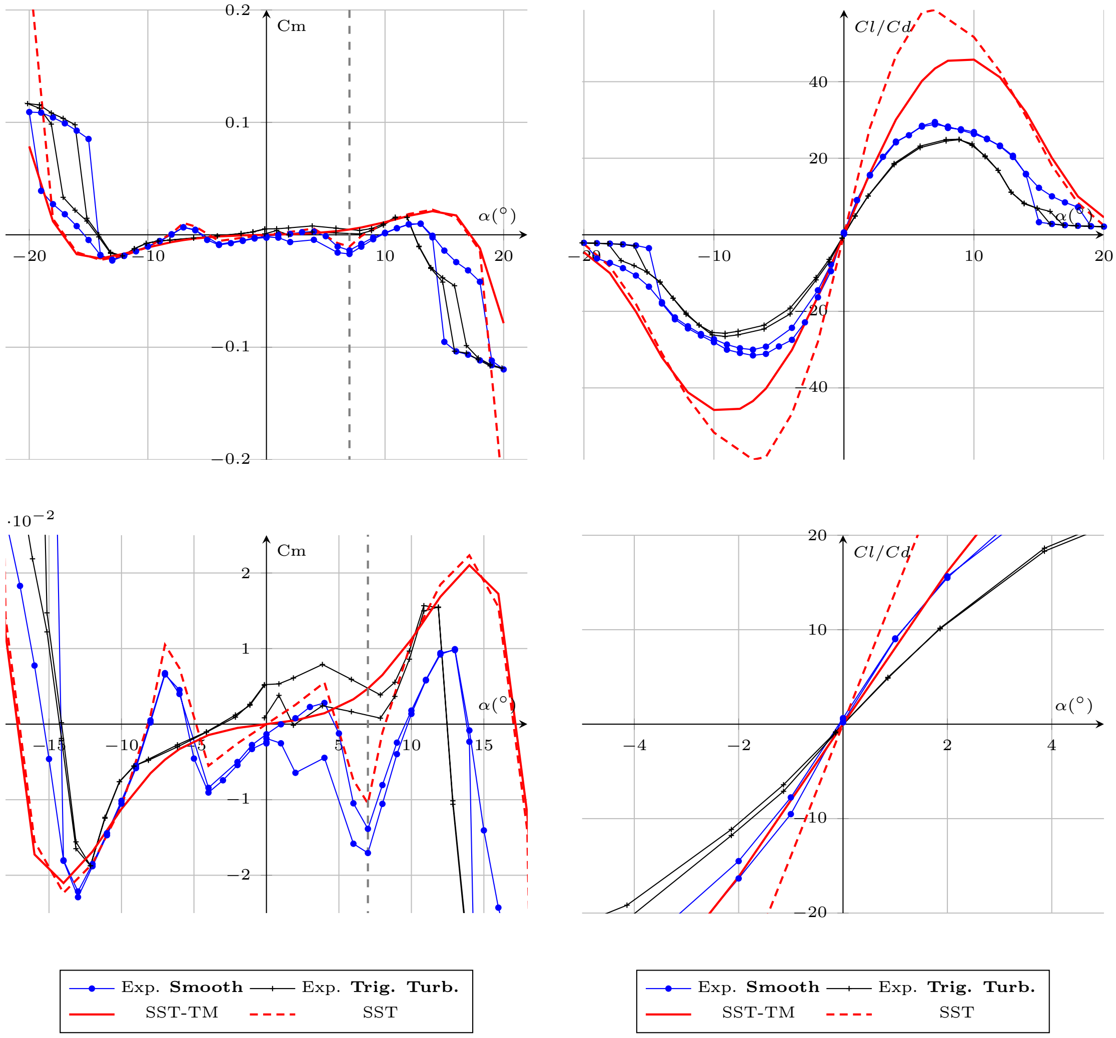

(a) Pitching moment

(b) Lift to drag ratio

Figure 4.7: Experimental and numerical data for the pitching moment coefficient and the lift to drag ratio, NACA 0015 forward flow $Re_c = 5 \times 10^5$.

4.3 NACA 0015 in reversed flow

The reversed hydrofoil is characterized by a thick rounded trailing edge and a sharp leading edge. This may lead to specific hydrodynamic behaviors.

After a literature review, experimental and numerical results obtained on the NACA 0015 in reversed flow are detailed.

4.3.1 Hydrofoil in reversed flow in the literature

For the reversed foil, detailed studies are rare in the literature, even more so regarding hydrofoils. However partial properties of two-dimensional reversed foil sections can be found. Indeed, several studies were conducted on several airfoils for a complete range of angles of attack from 0° to 360°, including the reversed configuration (180°).

Pope [1947] studied a NACA 0015 foil over the complete range of angles of attack. Measurements were carried out at the Georgia institute of technology on a smooth foil. At a Reynolds number value of $Re_c = 1.23 \times 10^6$, both balance measurements and pressure integration gave a maximum lift coefficient of 0.8 occurring at 10° AoA. As noticed by Smith et al. [2011], lift force and pitching moment are not null at 180°, meaning 0° reversed. Pope [1947] attributes this to tare and interference effects.

Critzos et al. [1955] showed lower performance of the reversed NACA 0012 airfoil regarding lift to drag ratio in comparison with the regular configuration. They also noticed a lift discontinuity at 180° angle of attack (i.e. reversed) for $Re_c = 5 \times 10^5$. The discontinuity disappears when the Reynolds number increases to 1.8×10^6. It is stated to be generated by an asymmetry in the location of the detachment point along the chord, between the upper and lower surfaces of the foil.

Several other studies have been carried out for the complete range of angles. However there is no apparent focus on the reversed flow configuration resulting in large angle steps in that zone.

For example, Sheldahl and Klimas [1981] present performances of several NACA foils for a large range of Reynolds number values. Their data is based on both numerical and experimental investigations. Hoerner [1985] also gives an overview of reversed foil behavior in comparison with forward flow. He observed that in most cases a lift coefficient of 0.7 - 0.8 can be expected, which is approximatively 50 % to 70 % of the lift reached in forward flow. The lift coefficient limit seems to be linked to a long bubble type leading edge separation, as stated by Hoerner [1985]. Obviously, drag is drastically increased compared to a forward configuration. Robinson [1995] also presents some 0° to 180° airfoil properties carried out in the framework of studies about bullet impact effect on the aerodynamic properties of helicopter blades. Laitone [1997] also gives an overview of reversed NACA 0012 characteristics but measured at lower Reynolds Number. He concluded that, at low Reynolds Number, a sharp leading edge can be an advantage. More recently, Timmer [2010] has explored performances of DU type sections on the whole range of angles of attack and at relatively high Reynolds number ($Re_c = 7 \times 10^5$) for application to wind turbines.

Finally, Smith et al. [2011] have presented a numerical study of two foils: a NACA 0012 and a SC1095 in reverse-flow configuration. This study was conducted under the framework of rotor craft development, as at high advance ratio a portion of the blade experiences reversed flow. Numerical studies conducted using URANS, $k-\omega$ SST and LES models have been compared to experiments from Critzos et al. [1955], Leishman [1993] and Pope [1947]. Numerical results when reversed have been shown to be particularly grid sensitive, with for example a lift difference that can reach 25 % between an O-grid and a C-Grid architecture. They also noticed the importance of the leading edge geometry in such a flow configuration.

Generally, these works have shown relative performance as well as specific behavior of reversed profiles. However, most of the available data is proposing a quite a large angle-step (2°) around 180° AoA, meaning that the behavior of the reversed foil may be only partially captured. This angle step choice is critical as the discontinuity seems to be relatively sharp.

4.3.2 Results

Lift and drag coefficients for the NACA 0015 in reversed flow at $Re_c = 5 \times 10^5$ are presented in Figure 4.8. As for the previous hydrofoil configuration, both experimental and numerical results are presented.

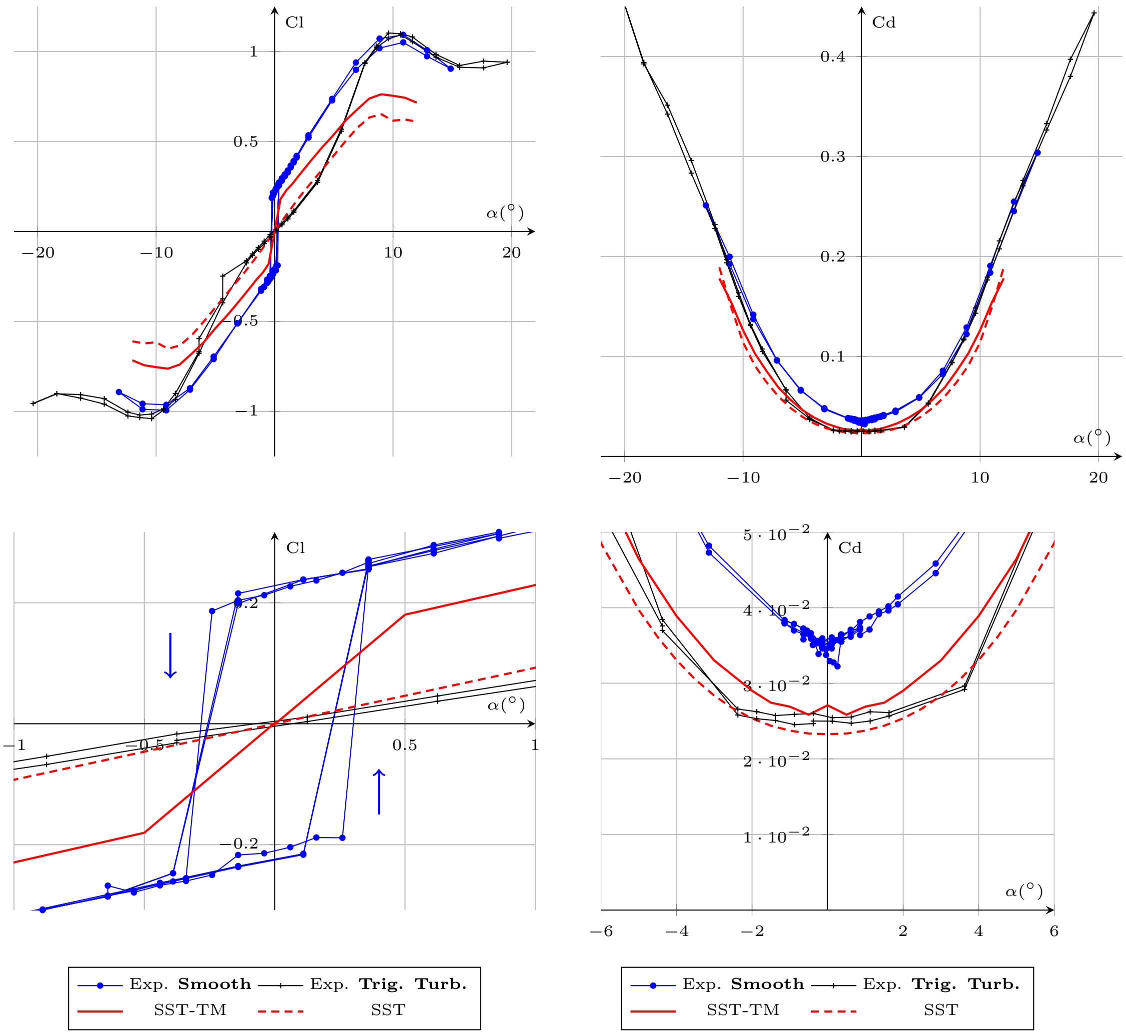

(a) Lift (b) Drag

Figure 4.8: Experimental and numerical data for lift and drag coefficients. NACA 0015 hydrofoil at $Re_c = 5 \times 10^5$ in reversed flow.

As shown in Figure 4.8(a), the smooth configuration is characterized by a discontinuity in lift at around the 0° AoA. About 20 % of the maximum lift is achieved between 0° and 0.25° of absolute angle of attack – 0.1° refinement. It is accompanied by a hysteresis loop, particularly observed in experiments. Stall occurs at around 10° AoA, with a maximum lift coefficient close to 1. This discontinuity could be thought to be generated by a mechanical float, resulting in an angular slack. However, the equivalent angular slack required to linearise the lift would be 4°, negative and positive, which means that the amplitude of the angular float would be 8°. Photos made during PIV are not showing such an angle.

Roughness addition removes lift discontinuity and lift is therefore linear between -4° and 4° AoA. A slope increase then makes it possible to reach the same maximum lift value as in the smooth case, also at around 10° AoA. The lift curve obtained with roughness addition is very similar to that published by Yates [1980] from experiments by Smith on a reversed NACA 0012.

The overall average lift level thus is not as low as might have been thought, but it is counter balanced by a higher drag level. For both the smooth and the roughened configurations, drag level when reversed is generally higher than in the forward case, although at high angles of attack, after stall, this difference tends to decrease. Between -7° and 7° AoA, the drag of the roughened measurements is surprisingly lower than is the smooth case.

Critzos et al. [1955] showed similar lift characteristics for a NACA 0012 airfoil in reversed configuration. As presented in Figure 4.9, a discontinuity in lift was noticed at around 180° of angle of attack and for $Re_c = 5 \times 10^5$ – meaning 0° AoA when reversed. He explains that an asymmetry in position of the detachment point along the chord, between upper and lower surface of the foil, could be responsible for this discontinuity. His measurements also to the present ones are showing the same maximum lift level.

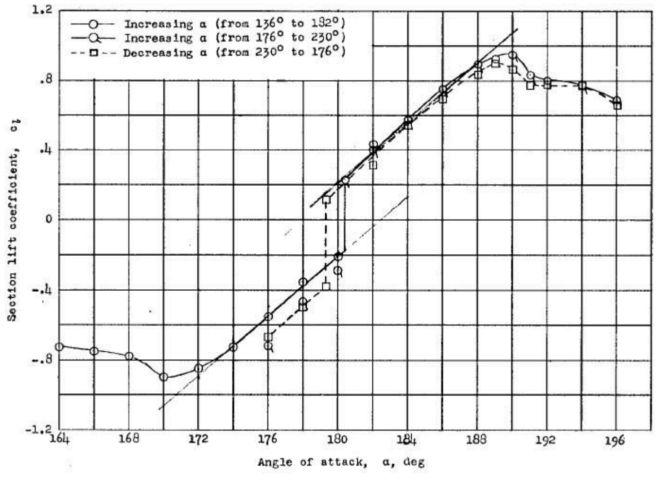

Figure 4.9: Lift coefficient measured in a wind tunnel by Critzos et al. [1955] on a NACA 0012 at $Re_c = 5 \times 10^5$, reversed.

The hysteresis loop observed for both lift and drag coefficients in forward flow and at high angles of attack, also no longer appears in the reversed configuration.

Results obtained from the numerical investigations are compared to the specific behavior observed experimentally. A specially refined mesh was needed for this purpose (see section 3.1).

The overall lift level is generally under-predicted by both numerical models. It can be seen that the fully turbulent calculation fails to predict the jump in lift observed in experiments. It is interesting to observe that the addition of the transition model the discontinuity appears, however lift discontinuity is not as important as in measurements. This corroborates the difference observed between smooth and rough experiments, confirming the close link between the transition and the lift discontinuity.

Both models show the occurrence of an early leading edge bubble as presented in Figure 4.10. The extent of the leading edge bubble at low AoA is sensitive to the boundary layer model. Activation of the transition model allows the development of a longer leading edge bubble, which contributes to the increase in lift. At higher angles, the difference is much more limited between SST and SST-TM calculations.

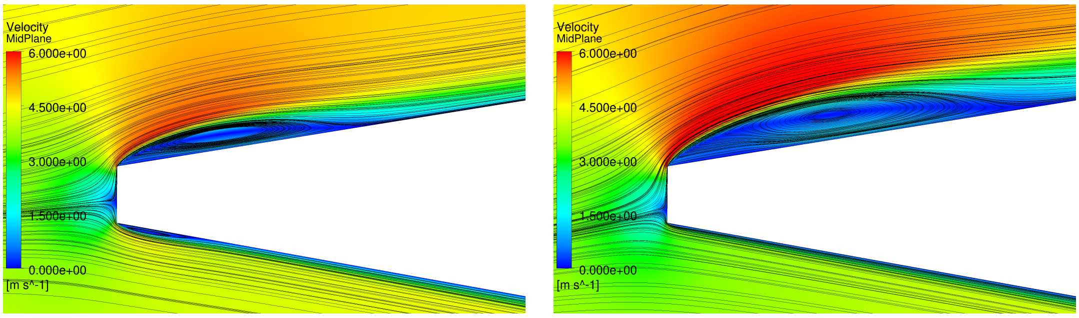

(a) SST – $\alpha = 0.5°$ (b) SST-TM– $\alpha = 0.5°$

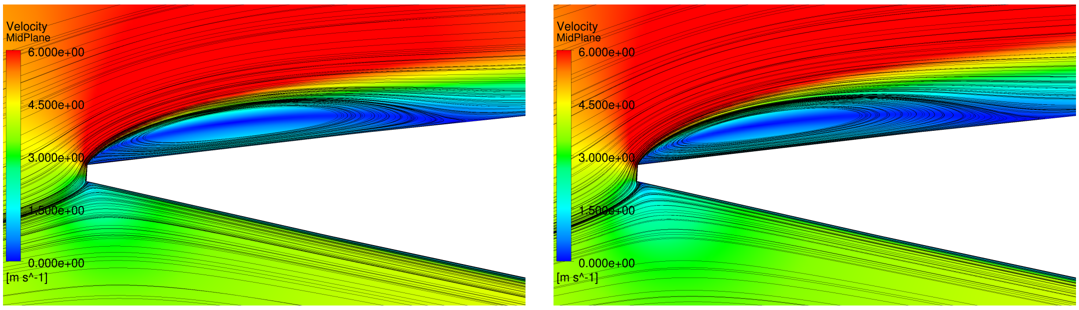

(c) SST – $\alpha = 3°$ (d) SST-TM – $\alpha = 3°$

Figure 4.10: Velocity streamlines showing the leading edge bubble on the reversed NACA 0015, 2-D calculations $Re_c = 5 \times 10^5$.

The corresponding measurements carried out using PIV show that computations are generally underestimating the size of the bubble. Views of the flow field obtained by PIV, with the smooth configuration at 0.5° and 3° are presented in Figure 4.11

The size of the bubble observed experimentally is 0.035 c and 0.12 c respectively at 0.5° and 3°. The bubble is 10 % more developed in reality than estimated by calculations (0.02 c at 0.5° and 0.10 c at 3°). This underestimation of the leading edge bubble could be a reason for the global underestimation of lift by calculations.

The increase in lift at low angles of attack when the transition model is used, is also visible on the pressure coefficient (Figure 4.12).

A wider pressure difference between the upper and lower surfaces of the hydrofoil is obtained with the transition model, resulting in more lift. Extra lift brought by the leading edge bubble is also clearly visible. In addition, a high and narrow minimum pressure peak is visible very close

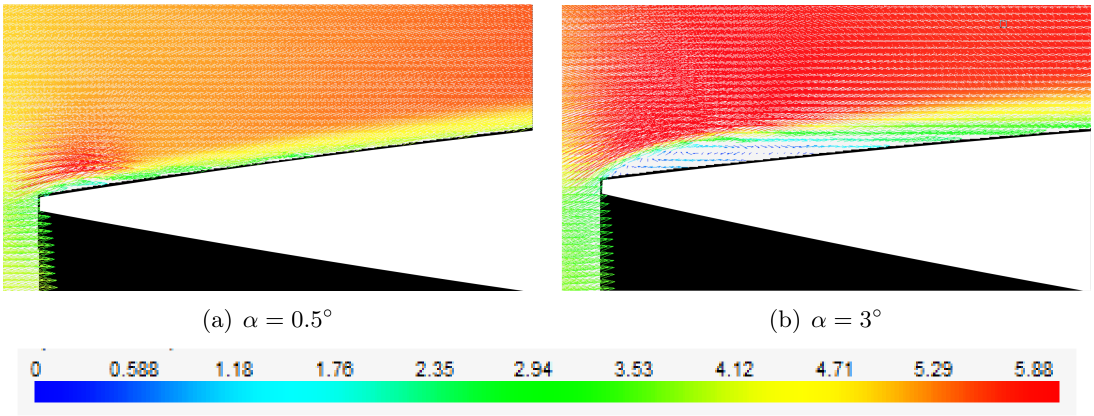

(a) $\alpha = 0.5°$ (b) $\alpha = 3°$

Figure 4.11: Flowfield measurements carried out on the reversed NACA 0015 using PIV, smooth configuration, $Re_c = 5 \times 10^5$

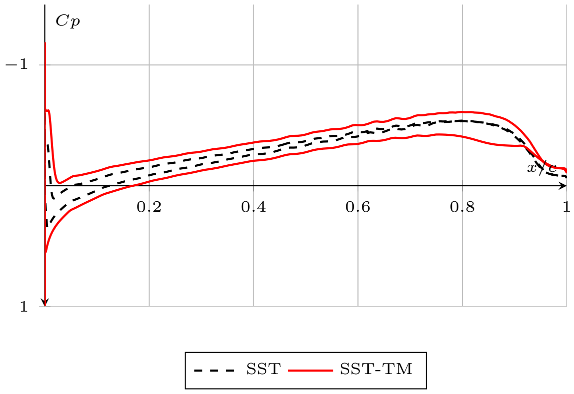

(a) $\alpha = 0.5°$

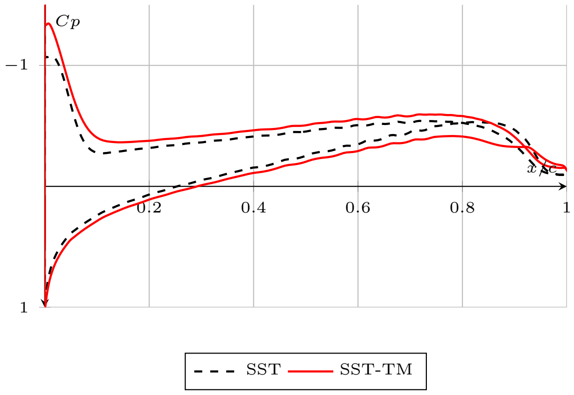

(b) $\alpha = 3°$

Figure 4.12: Evolution of the pressure coefficient at the foil surface and along the foil chord, numerical results 2-D, $Re_c = 5 \times 10^5$.

to the leading edge due to geometry sharpness. It contributes to the overall lift and, besides, should result in early cavitation development. Note that in numerical results, the transition model induces a lift offset over the fully turbulent curve and when set at around 0° AoA. It is then maintained, constant, over the whole range of angles of attacks.

Plots of the wall shear coefficient at the foil surface support these statements (Figure 4.13). Indeed the leading edge bubble is clearly visible. It is also 30 % longer using the transition model as the stagnation point is slightly closer to the pressure side of the foil than in fully turbulent results. In addition, the use of such a model allows the pressure side to have a low friction laminar boundary layer, while the suction side boundary layer is turbulent, triggered by the leading edge bubble. This results in an asymmetry of the boundary layer behavior between the pressure side and the suction side even at angles close to 0°, which could not be captured by the fully turbulent model and which is linked to lift discontinuity.

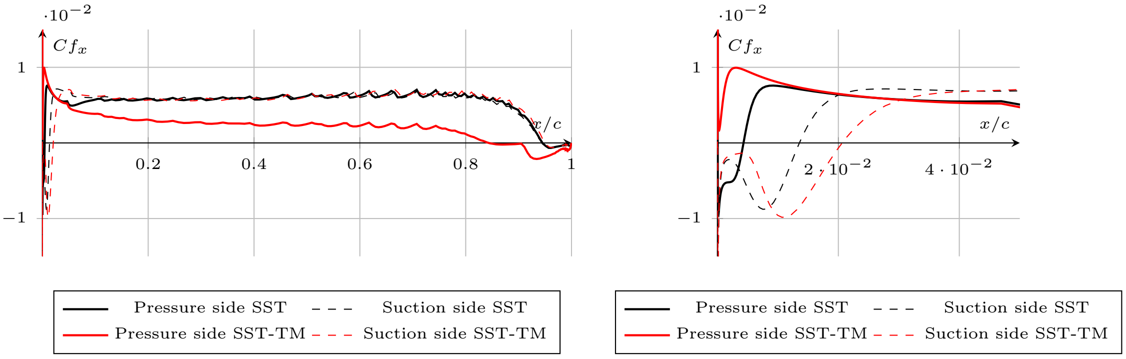

(a) Full chord (b) Detail of the transition bubble

Figure 4.13: Evolution of the friction coefficient (x axis – flow axis) along the foil chord, numerical results 2-D, $\alpha = 0.5°$ and $Re_c = 5 \times 10^5$.

This is confirmed by the study of the chord-wise position of the transition point, indicated by the appearance of turbulent kinetic energy at the foil surface (Figure 4.15). Figure 4.14 provides a schematic view of the boundary layer situation as predicted by calculations on the reversed NACA 0015.

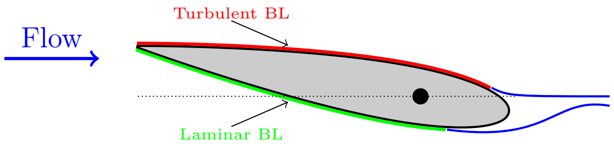

(a) $\alpha > 0.25°$

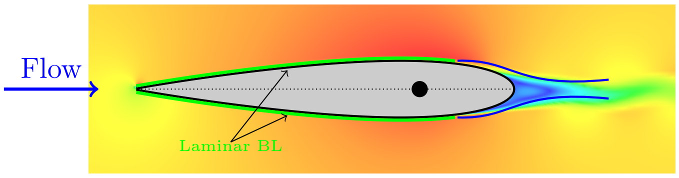

(b) $\alpha = 0°$

Figure 4.14: The boundary layer configuration at the NACA 0015 foil surface in the reversed configuration

At 0° angle of attack the transition point is located near the trailing edge on both sides of the foil. A recirculation is visible at the leading edge, due to the front face of the sharp leading edge, but it does not trigger the turbulent boundary layer. At 0.5° AoA, this recirculation develops and becomes sufficient to trigger turbulence in the BL. This induces the immediate migration of the upper surface transition point to the leading edge whilst on the lower surface it stays near the trailing edge. At the same time an important amount of lift is generated.

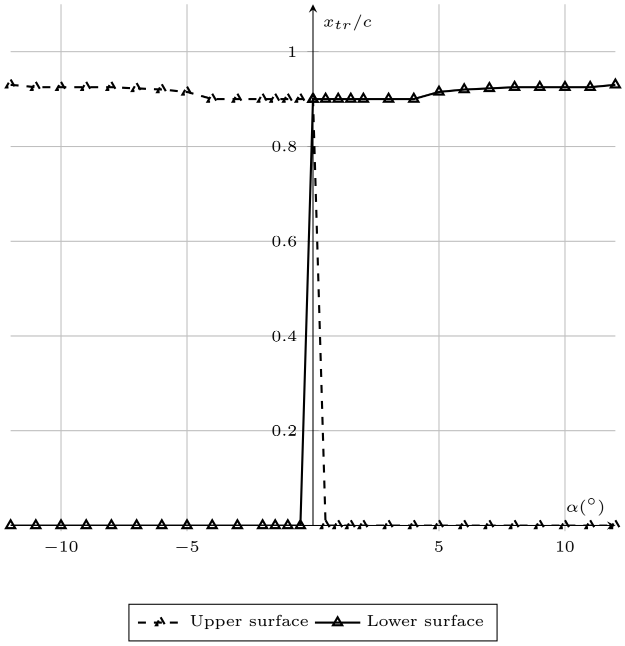

Figure 4.15: Position of the transition point along the foil chord on both faces of the NACA 0015 reversed flow, $Re_c = 5 \times 10^5$, numerical study

Regarding drag, calculations are partially capturing experiments. SST-TM drag is higher than SST drag between −10° and 10°, which corroborates relative positions of smooth and roughness triggered experimental drag curves. 0° drag level in the turbulence triggered experiments is well predicted by the SST model. However this is not the case with the SST-TM model compared to experiments on the smooth foil.

The slight drag increase visible on the SST-TM calculation at 0° AoA is not visible in experiments. It occurs in calculation due to a decrease of the viscous drag at this particular angle (Figure 4.16).

In the fully turbulent configuration, 0° AoA is clearly the point where the viscosity contribution to the overall drag is the highest. With the SST-TM model, 0° AoA is an exception regarding viscous drag. In comparison with 0.5° AoA, more than half the viscous drag is lost because both upper and lower surfaces of the foil are mainly laminar, as shown by plots of the positioning of the transition point (Figure 4.15). Transition occurs near the trailing edge (0.85c) and most of the boundary layer is laminar despite a small bubble occurring at the leading edge, but too small to trigger transition. Viscous drag is thus reduced. The low energy laminar boundary layer detaches earlier than a turbulent boundary layer, as visible in Figure 4.17. This way, early detachment of the laminar boundary layer at 0° AoA increases pressure drag by generating a low pressure zone behind the foil's trailing edge.

When the angle of the foil is increased, turbulent boundary layer is triggered on the upper

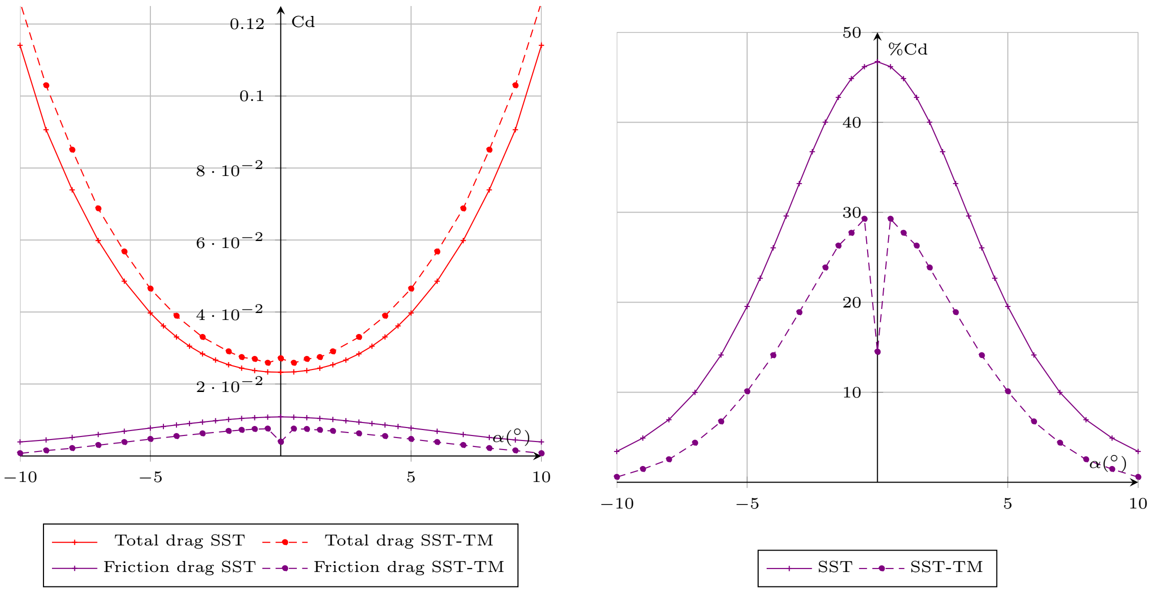

(a) Drag decomposition (b) Friction drag proportion (% Total Drag)

Figure 4.16: Drag decomposition, numerical results NACA 0015 reversed, $Re_c = 5 \times 10^5$

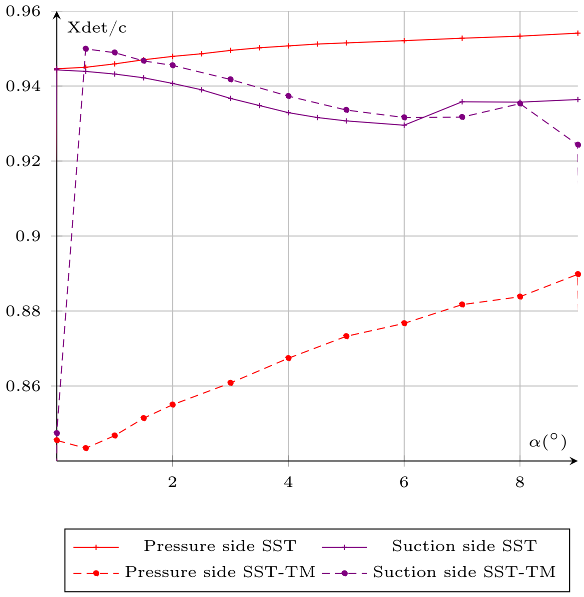

Figure 4.17: Position of the boundary layer detachment point along the foil chord, numerical results NACA 0015 reversed, $Re_c = 5 \times 10^5$

foil surface by the leading edge bubble. It is energetic enough to stick to the foil surface in the high curvature zone and transition occurs later (0.95c). Therefore pressure drag is drastically reduced, which compensates the viscous effects.

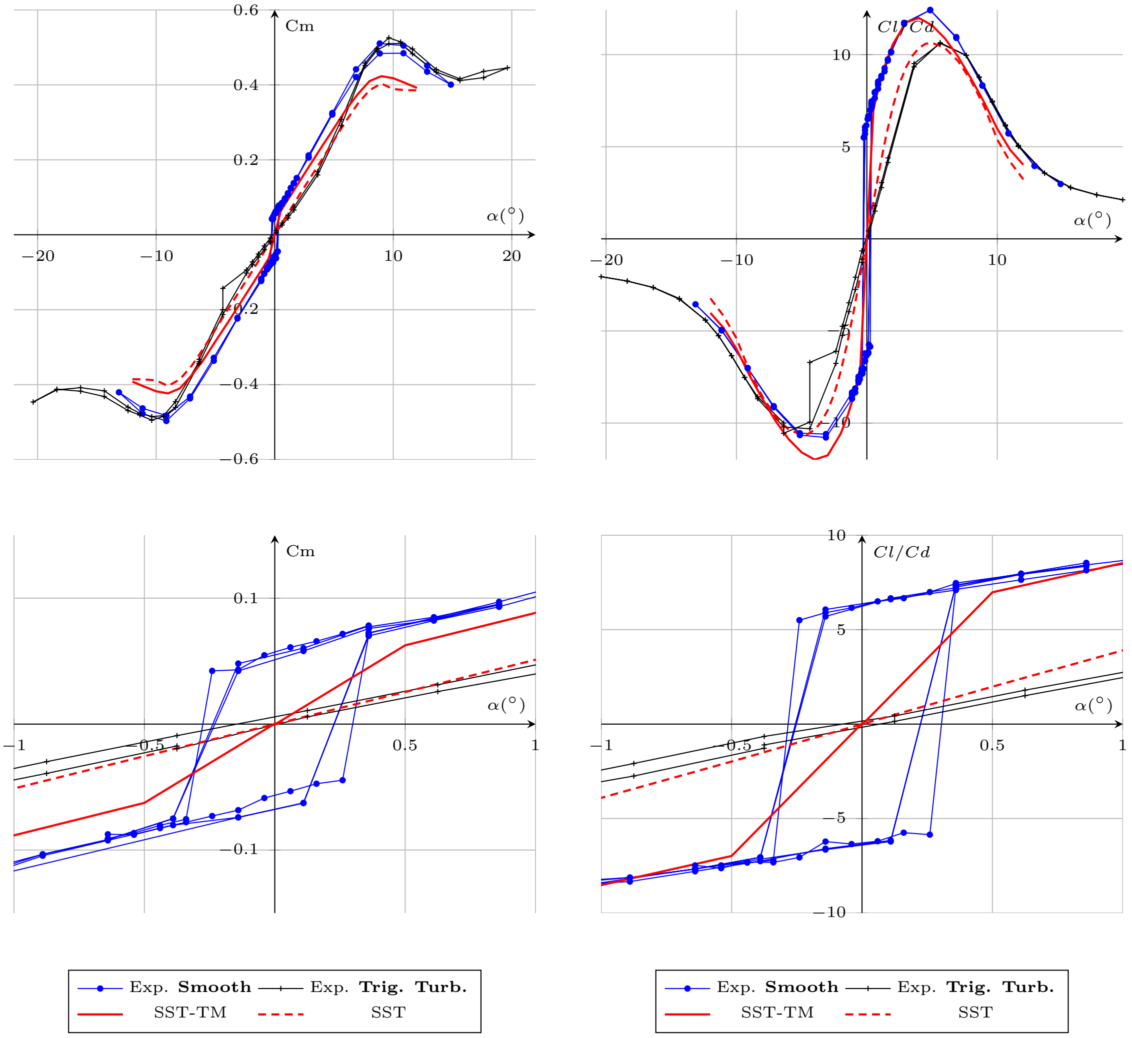

(a) Pitching moment (b) Lift to drag ratio

Figure 4.18: Experimental and numerical data for pitching moment coefficient and lift to drag ratio. NACA 0015 hydrofoil at $Re_c = 5 \times 10^5$ in reversed flow.

The pitching moment, presented in Figure 4.18, is measured at the rotational axis of the foil, meaning at 3/4 of the chord from the leading edge in reversed flow (1/4 c from the conventional leading edge). Due to this particular situation the moment curve is very similar to the lift. The position of the rotational axis is making the pitching moment positive over the whole range of angles of attack. A discontinuity is also observed between -0.25° and 0.25° AoA. Similarly to lift, calculations are able to capture most of the behavior around 0° AoA, but are less accurate at higher angles of attack.

The lift to drag ratio is also presented in Figure 4.18. Surprisingly, values of the lift to drag ratio are very similar between experiments and numerical results. It has been shown that the experimental lift is generally higher than that given by computations, whilst the experimental drag is higher than computational results. However, the ratio is astonishingly similar between experiments and numerical results.

Measurements carried out at lower Reynolds number values have shown another specificity of this reversed configuration. With an inflow velocity of $3.8m/s$ ($Re_c = 3.8 \times 10^5$), a hydro-elastic interaction behavior is observed, introducing important vibrations. Experimental results for average lift and drag coefficient and the associated standard deviation are presented in Figure 4.19.

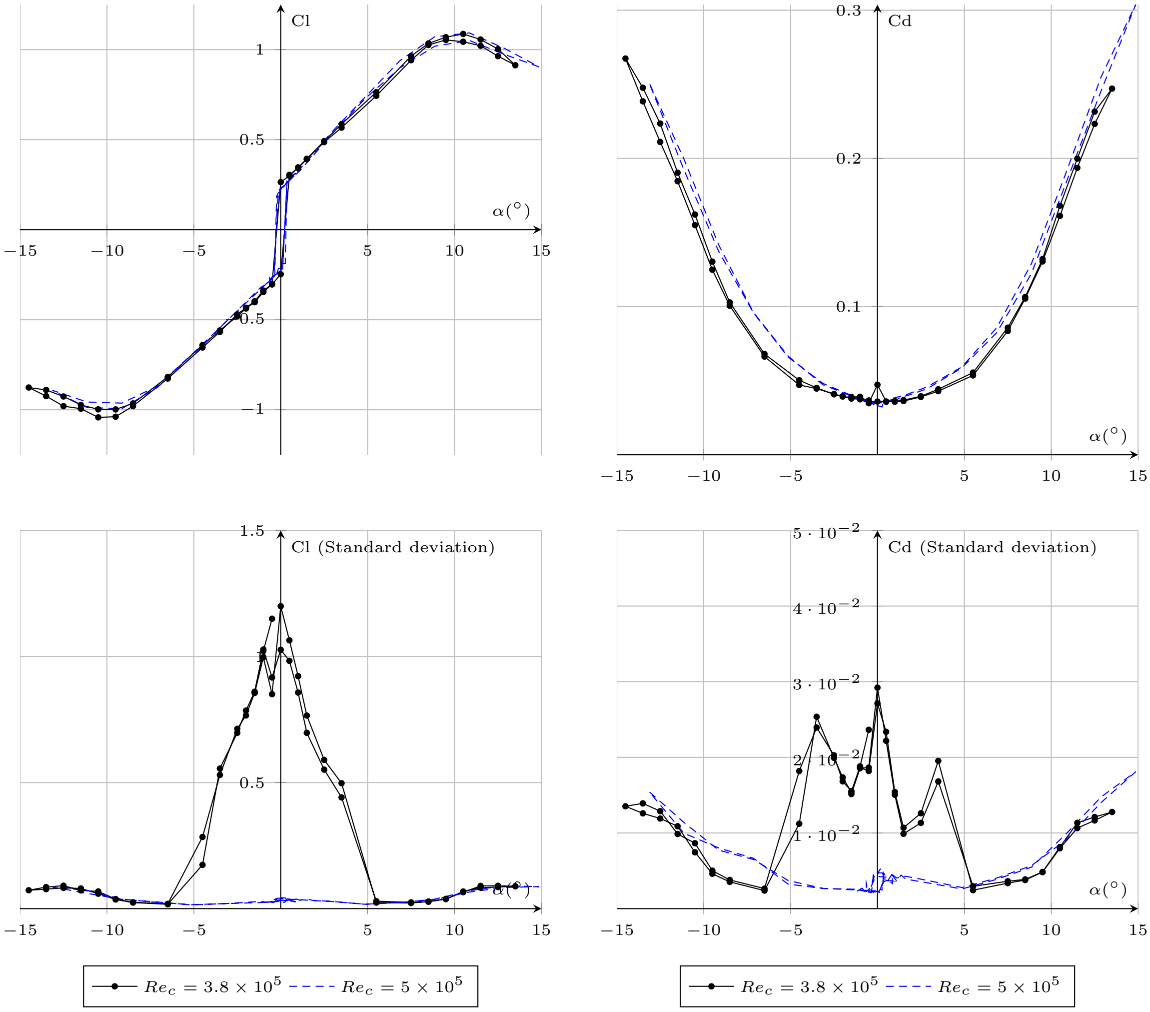

(a) Lift (b) Drag

Figure 4.19: Lift, drag coefficients and standard deviations, experimental data obtained with the smooth NACA 0015 hydrofoil at $Re_c = 3.8 \times 10^5$ and $Re_c = 5 \times 10^5$ in reversed flow

Average lift and drag values are very similar between both sets of data. However, standard deviations are very different between the two cases. At $3.8m/s$, the standard deviation level is high at angles around 0° AoA. Force fluctuations are particularly affecting lift, for which it reaches for example 1.2 in Cl close to 0° (more than 100 % of maximum lift). Drag is less fluctuating but the standard deviation still reaches 50 % of the drag level around 0° AoA.

Figure 4.20 gives an overview of the frequency spectrum observed on the reversed NACA 0015 at 3.8m/s compared to the 5m/s case.

At 5m/s, a frequency is clearly visible at 105 Hz on the tension. At 3.8 m/s the main

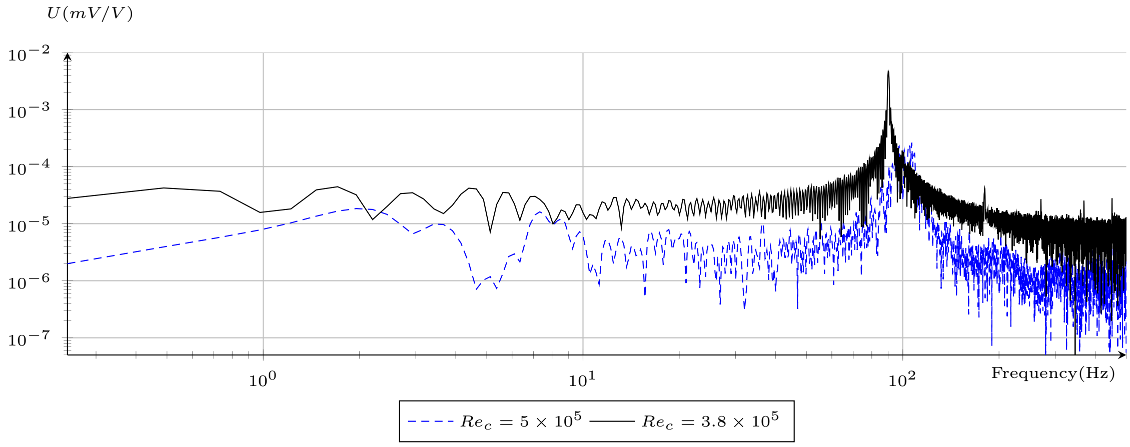

Figure 4.20: Power spectral density at 0° AoA extracted from the raw electric signal from strain gauge bridges. NACA 0015 hydrofoil at $Re_c = 3.8 \times 10^5$ and $Re_c = 5. \times 10^5$ in reversed flow. Logarithmic scales.

fluctuations are occurring at a lower frequency (90 Hz), with more amplitude. It shows that around the zero angle of attack the reversed flowing situation is particularly unsteady, the impact of such a hydro-elastic interaction on the blade design could be significant with regard to the structural integrity of a tidal turbine.

4.4 Bidirectional hydrofoil

A bidirectional foil must be rotationally symmetric, which results in leading edge geometries midway between the conventional rounded leading edge and the sharp trailing edge. The geometry used as an example in the present study is characterized by relatively thin and rounded extremities. These are unusual and could result in specific behaviors.

Firstly an investigation carried out from the literature on reversible profiles design and properties is presented. Then, measurements and numerical results on the elliptical foil section are exposed.

4.4.1 Bidirectional foil sections in the literature

A bidirectional section is designed to work identically in both forward and reversed flows. This requires for the geometry to be rotationally symmetric.

In the past, elliptic sections were studied experimentally by Zahm et al. [1929] or Schubauer [1939] experimentally. Their foreseen was more for profiling spares than to be used as a blade section. More recently, bidirectional types of hydrofoils have been studied for several types of applications.

For example, it has been thought to use bidirectional foil sections as reversible propellers. The patents from Monroe [1965] and Monroe [1952] are showing two types of geometries having been studied. Hydrodynamic properties are not available for these two sections. Pashias and Turnock [2003] also worked on a bidirectional propulsion system. Their studies resulted in a similar reversible airfoil to which that was proposed by Monroe [1952]. Foil geometries are

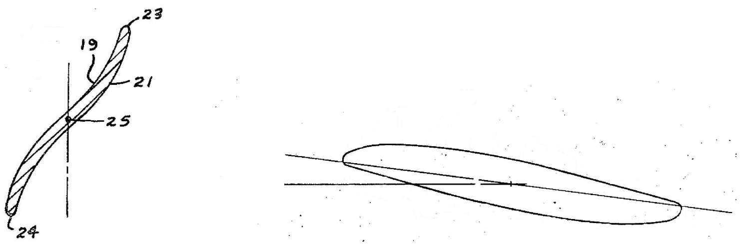

(a) Monroe [1965] (b) Monroe [1952]

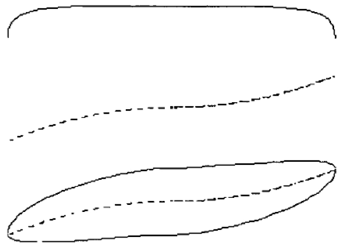

(c) Pashias and Turnock [2003]

Figure 4.21: Example of bidirectional sections for application to reversible propulsion systems.

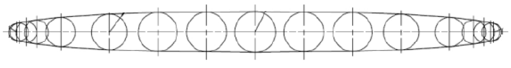

Figure 4.22: Example of bidirectional sections for application to air-cooling systems, Spasic et al. [2012]

illustrated in Figure 4.21.

Bidirectional foil section applications for an air-cooling system has also been studied, for example by Spasic et al. [2012]. Once again, the two-dimensional properties of the foil section are not available. The section is presented in Figure 4.22.

Chitta et al. [2012] numerically studied the properties of a two-dimensional elliptical foil section for application to unmanned vehicles. They compared the results to experimental data from Kwon and Park [2005] and Kwon et al. [2006]. They noticed that the lift of the elliptic foil was a non linear function of the angle of attack, at a Reynolds number value of $Re_c = 3 \times 10^5$.

For tidal turbine applications, bidirectional hydrofoil geometries are available in the literature. Nicholls-Lee et al. [2011b] or Nicholls-Lee [2011] gave an overview of a thin leading edge and trailing edge bidirectional hydrofoil. It had already been noticed that bidirectional sections are generally less performant compared to classic unidirectional foil sections such as a NACA 00xx in forward flow. However, the performance of reversible foils was observed to be generally higher compared to reversed flow on a classic NACA foil. Both foils were very thin at the leading edge, which would result in a significant pressure drop immediately at the leading edge when the stagnation point migrates to the pressure side. This may also favor cavitation. Moreover, the author noticed that the first half of the section generates positive lift while the second generates negative lift. This could result in high pitching moment level and additional structural constraints. An overview of one of the foils studied by Nicholls-Lee [2011]

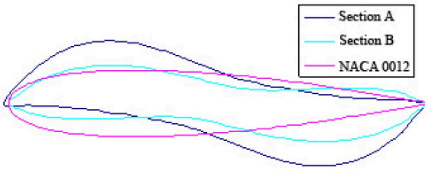

Figure 4.23: Example of bidirectional sections for application to tidal turbines designed by Nicholls-Lee [2011]

is presented in Figure 4.23.

The option to use a reversible hydrofoil has been chosen by some companies such as Voith Hydro to equip the industrial scale tidal turbine prototype. However, blade section design and hydrodynamic properties are not available, for reasons of confidentiality.

Globally, it can be stated that for tidal turbine applications, data on reversible hydrofoils is relatively rare in the literature. Most of the data is for other applications, for which data is only partially available and generally applies to inadequate flowing conditions. Rounded leading and trailing edges seem to be the most used type of design. Where experimental data is concerned, both force and flow measurements are rare.

The bidirectional section chosen for the present study is representative of the bidirectional sections available in the literature.

4.4.2 Results

Before presenting the results on the bidirectional foil, it must be noticed that experimental results in the turbulent case have been obtained using the first version of the turbulence triggering stripes. In fact measurements on this section were carried out before the effect of the stripe thickness was noticed. The corresponding turbulence triggering roughness is RT2 (see section 2.2). Turbulent experiments are however presented for information.

Lift, drag and pitching moment coefficients from both experimental and numerical studies are given in Figure 4.24 at $Re_c = 5\times10^5$. Experimental data is showing very different behaviors between the smooth and the roughness triggered turbulent configurations.

On lift in particular, the smooth configuration results in a much higher level compared to the turbulent configuration, with a maximum lift coefficient of 1.1 located between 10° and 11° AoA. In the case of the turbulent configuration, the maximum lift is 0.7, at the same angle. Lift for the smooth experiment displays a curved evolution with the angle of attack between -3° and 10° AoA. It is reminiscent of the behavior observed by Chitta et al. [2012]. In the turbulent case, lift is linear over that same range of angles of attack.

PIV observations for both the smooth and the turbulent cases are presented in Figure 4.25.

It clearly shows that the turbulent case, with the use of the RT2 type of turbulence triggering roughness, induces an early detachment of the upper boundary layer. At low angles of attack, an increase of the boundary layer thickness is also visible on the upper face. Both effects result in lower foil performance, with regard to both the maximum lift and the maximum lift to drag

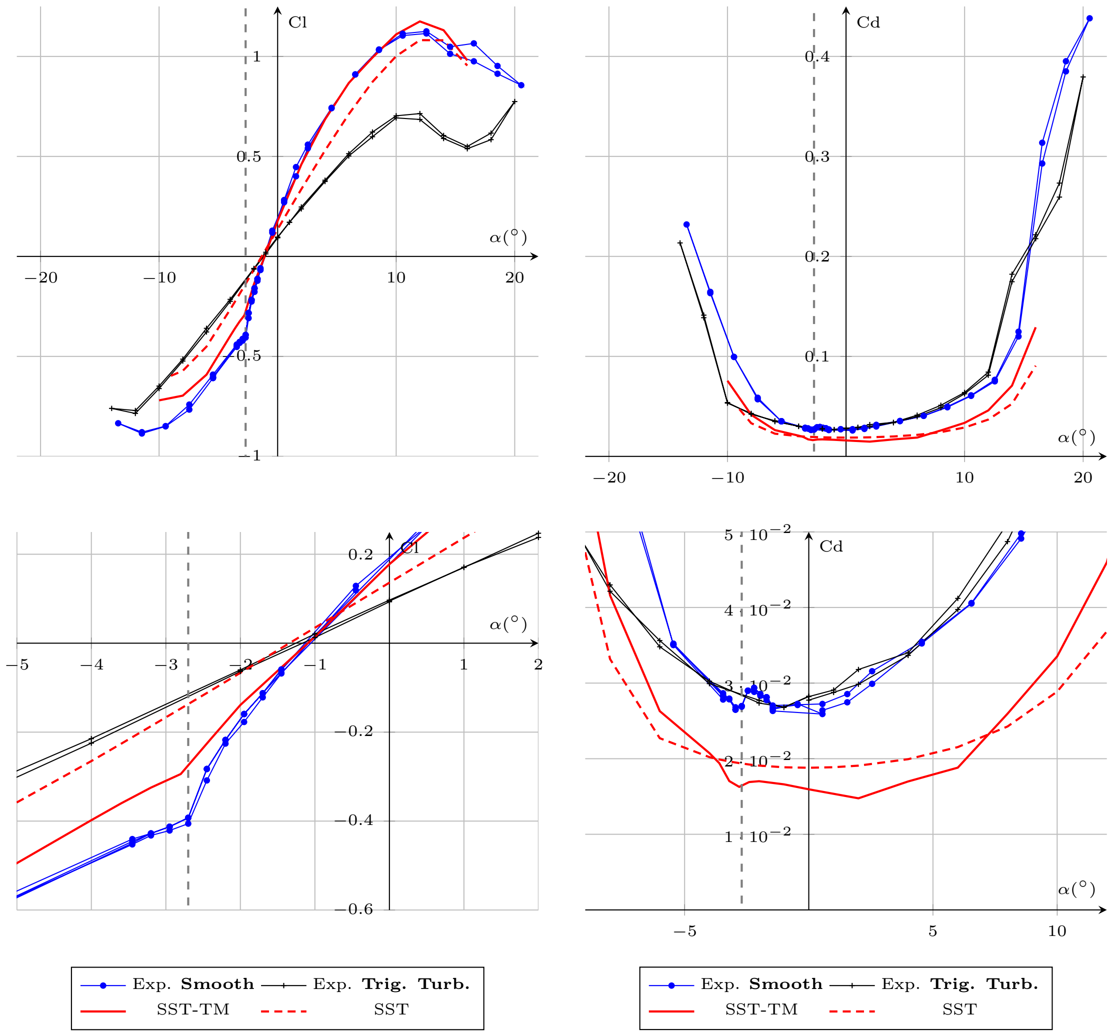

(a) Lift (b) Drag

Figure 4.24: Experimental and numerical data for lift and drag coefficients. Elliptical foil section at $Re_c = 5 \times 10^5$.

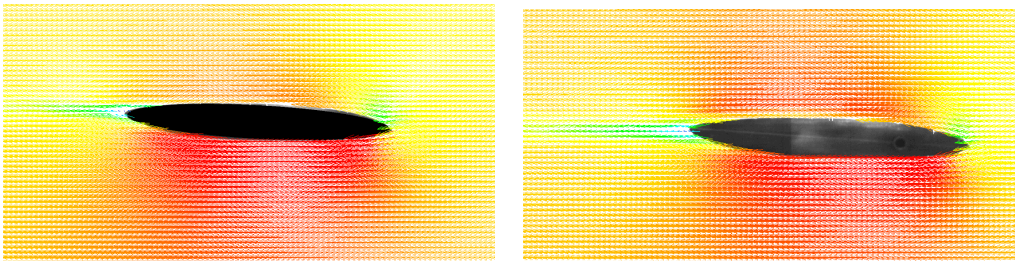

(a) $\alpha = -4°$ Smooth (b) $\alpha = -4°$ Turbulent

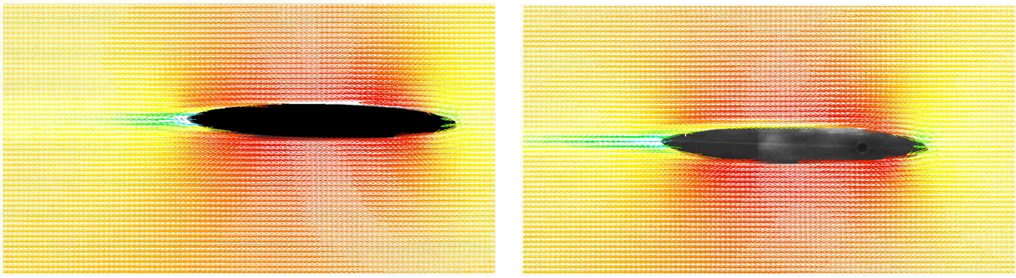

(c) $\alpha = -2°$ Smooth (d) $\alpha = -2°$ Turbulent

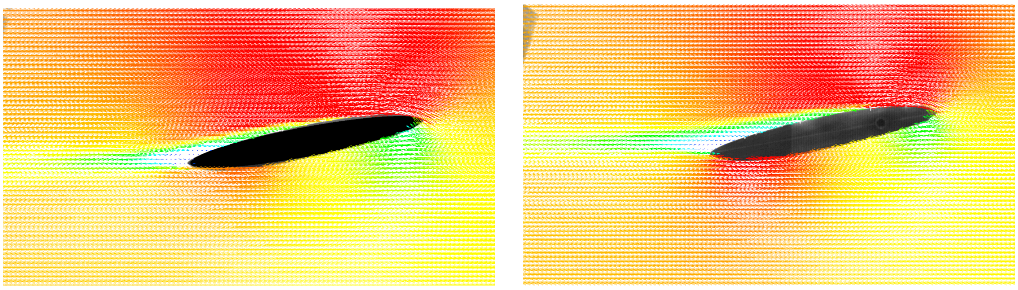

(e) $\alpha = 10°$ Smooth (f) $\alpha = 10°$ Turbulent

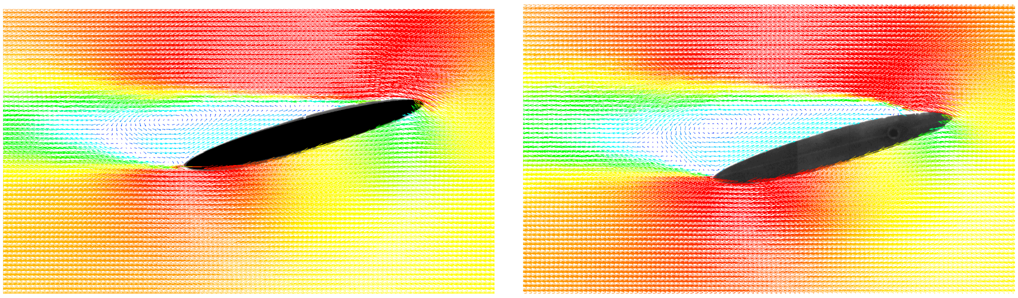

(g) $\alpha = 14°$ Smooth (h) $\alpha = 14°$ Turbulent

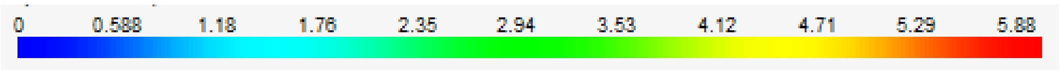

Figure 4.25: Velocity field around the elliptical foil at $Re_c = 5 \times 10^5$ (5m/s) for the smooth and the roughness triggered turbulent cases.

ratio.

Around -3° AoA, a discontinuity can be observed in smooth experiments. It looks to be located halfway between the discontinuities observed on the NACA 0015 reversed and the regular case. As seen on the NACA 0015, the leading edge sharpness helps in the creation of this discontinuity. In the present case, the elliptic hydrofoil is characterized by a relatively thin leading edge – particularly at negative angles, completed by a rounded trailing edge. A parallel with the reversed NACA 0015 can easily be drawn.

Increasing the velocity to 7.5 m/s makes the discontinuity disappear, as shown in Figure 4.26.

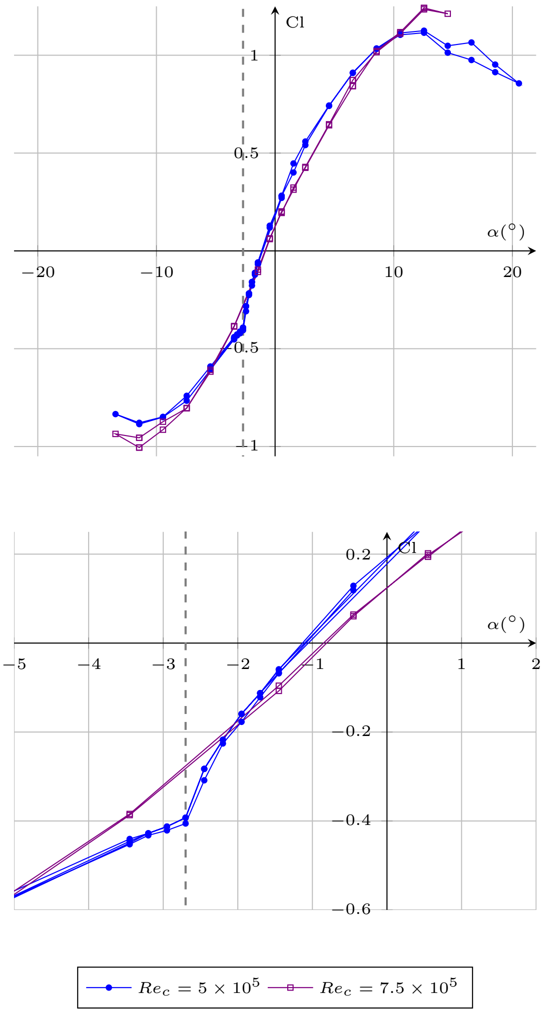

Figure 4.26: Experimental and numerical data for lift coefficient. Smooth elliptical foil section. Full data for $Re_c = 7.5 \times 10^5$ is available in Appendix B.

SST-TM numerical results are very close to experiments on lift in the smooth experiments. The maximum lift level is slightly overestimated, but predicted at the same angular position. The lift slope is also perfectly predicted between -3° and 10°. At -3° the lift discontinuity is predicted by calculations but with a lower lift level, similarly to the difference observed between smooth measurements and SST-TM calculations on the reversed NACA 0015. For lower angles of attack, the lift obtained with the SST-TM model remains below that of smooth experiments but with a similar slope.

The calculated position of the transition using SST-TM and given in Figure B.2, shows that the lift discontinuity at -3° AoA is linked with the position of the transition. Indeed, when the discontinuity is occurring, transition on the upper surface is occurring at the trailing edge while it occurs close to the leading edge on the lower surface. This is similar to statements made on the NACA 0015, particularly when reversed. It is due to the relative sharpness of the leading edge, as the position of the stagnation point on one side may result in an early transition on the other side.

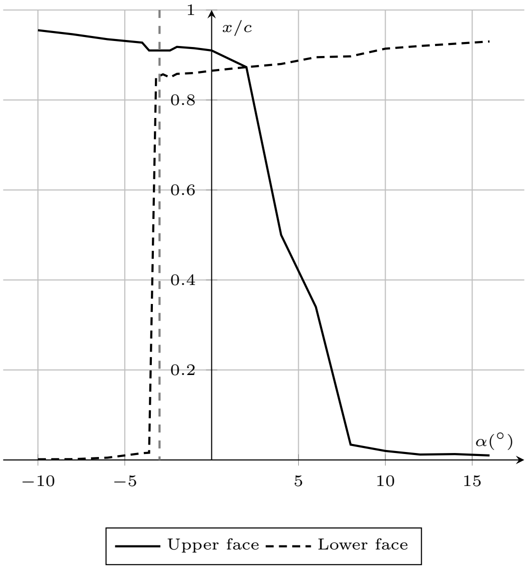

Figure 4.27: Predicted position of the transition using SST-TM calculation. Elliptical foil section, $Re_c = 5 \times 10^5$.

The SST calculated lift is very different from turbulent measurements (Figure 4.24). The calculated lift level is indeed higher, closer to the SST-TM than the turbulent experimental data is from the smooth ones. Use of turbulence triggering roughness may be the major reason for this observation. The RT2 roughness stripes are indeed too high and they are weakening the boundary layer, as well as resulting in a premature stall. SST calculation may be more representative of the real turbulent lift that should have been observed with the correct trigger, than that of the current turbulent measurements.

Between $-6°$ and $12°$, measured drag is very similar between the smooth and the turbulent configurations. For higher angles – in absolute values – the smooth foil drag is generally higher than the turbulent drag. Around the angle of attack for which the lift discontinuity is observed on the smooth configuration, a drag singularity is also visible. A decrease in drag is observed for angles just lower than -3°. Similarly to the case of the reversed NACA 0015, the turbulent boundary layer on the lower surface delays the detachment and reduces the pressure drag.

Numerical investigations using both the SST and the SST-TM configurations are resulting in lower drag than experiments. Once again, three-dimensional effects may account for an important part of the difference. The relative position of the two drag curves is not similar to experiments. The turbulent case presented here may include some roughness effects apart from the pure effect of transition removal. The SST-TM, however, shows a similar drag behavior, particularly close to -3°, where the lift discontinuity is occurring.

Figure B.2 presents both experimental and numerical data for the pitching moment.

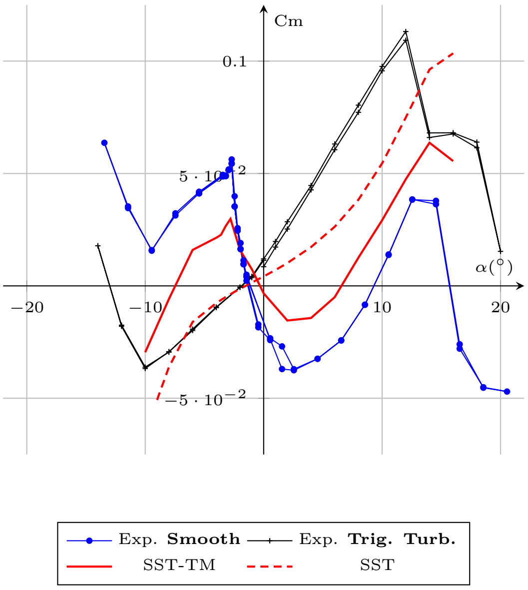

Figure 4.28: Numerical and experimental data for the pitching moment coefficient. Elliptical foil section, $Re_c = 5 \times 10^5$.

As for the drag, there is an important difference between experiments and calculation regarding the pitching moment. On most of the angles of attack, numerical models fail to predict the amount of moment measured. The curve shape of the measured turbulent pitching moment discords from SST numerical data. This is certainly due to the roughness stripes. On the other hand, SST-TM results are providing a similar evolution of the pitching moment with angle of attack. Angular positions of maxima are correctly predicted, and the global trend is good, but the amount of pitching moment is underestimated by calculations.

Figure 4.29 presents the lift to drag ratio for the elliptical hydrofoil.

It provides a good summary of the comparison between experiments and calculation on this span wise symmetric hydrofoil. Calculations are providing a higher lift to drag ratio, approximatively double that of the experiments. It mainly results from the higher drag measured due to span wise three-dimensional effects. There is a good agreement between measurements and SST-TM calculations regarding angle of lift to drag ratio maxima. Curve shapes, however, are different, and particularly so around the maximum, which is sharper in numerical results than in experiments.

The SST model predicts a maximum lift to drag ratio at higher angles than experiments, and a minimum at a lower absolute angle.

4.5 Summary and discussion

The main objective of this section was to propose a comparative study of two foil strategies that could be used to avoid reversing the turbine. An academic NACA 0015 foil in forward and reversed flow is compared to an elliptical bidirectional section with regard to lift, drag and pitching moment coefficients, obtained using both measurements and computations. For both foil strategies it is resulting in specific flowing conditions.

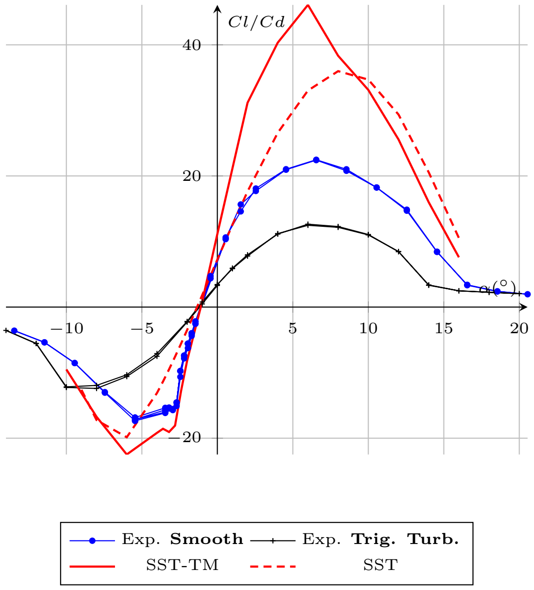

Figure 4.29: Numerical and experimental data for the lift to drag ratio. Elliptical foil section, $Re_c = 5 \times 10^5$.

The reversed NACA 0015 is characterized by a very sharp leading edge coupled with a round and relatively thick trailing edge. The results are showing an uncommon behavior. Around 0° AoA, lift changes sign and reaches 20 % of its maximum value over a range of angles of attack of less than a degree. It is caused by a laminar separation bubble generated by the leading edge sharpness and which leads to an asymmetry of the boundary layer behaviors as the angle of attack reaches 0.25°. The suction side is triggered turbulent while the pressure side remains laminar, as confirmed by calculations with a transition model. Turbulent measurements and computations are showing that the phenomenon is inherent to the laminar/turbulent transition as well.

This specific boundary layer configuration is also observed on the NACA 0015 in forward flow and on the bidirectional section at negative angles of attack. In both cases, a lift discontinuity is generated by the movement of the transition point towards the leading edge. The quicker this movement, the more important the discontinuity.

In the case of the bidirectional profile at negative angles of attack, the flow also encounters a relatively sharp leading edge and a laminar separation bubble can be observed. Development of such a configuration also depends on the position of the stagnation point on the leading edge.

Two main parameters are used for the preliminary specification of a hydrofoil for the design of a blade for tidal turbines – from a hydrodynamic point of view. The first parameter is the maximum lift to drag ratio and the second is maximum lift.

For both blade design strategies, the lift to drag ratio and lift data coming from numerical investigations are summarised in Table 4.1

For the reversed NACA 0015, the maximum lift level is relatively high. But the combined effects of the sharp leading edge and the round trailing edge drastically increase the drag. The lift to drag ratio is therefore very low compared to the NACA 0015 in forward configuration and to the bidirectional section. In case a NACA 0015 foil is used in forward and reversed flow, an average lift to drag ratio would be approximatively 35, between 20 % and 25 % lower than

SST-TM				
	Lift to drag ratio		Lift	
Foil Configuration	Max Cl/Cd	Ang. Position	Max Cl	Ang. Position
NACA0015 forward	58.75	7°	1.365	14°
NACA0015 reversed	11.98	4°	0.7622	9°
Bidirectional	46.08	6°	1.1752	12°
SST				
	Lift to drag ratio		Lift	
Foil Configuration	Max Cl/Cd	Ang. Position	Max Cl	Ang. Position
NACA0015 forward	45.76	10°	1.394	16°
NACA0015 reversed	10.64	5°	0.6512	9°
Bidirectional	35.98	8°	1.081	12°

Table 4.1: Global foil properties as estimated by calculations at $Re_c = 5 \times 10^5$.

the bidirectional case, whose properties are constant independently of the flowing direction. Moreover, angular position of the maximum lift to drag ratio is not the same in forward and reversed flow. Even if the flow is supposed to be perfectly bidirectional between ebb and flood, the angular positioning of the blade cannot be optimal in both regular and reversed flowing situations and a pitching system would be required.

The bidirectional section may provide a more important amount of power, which would be more stable as well. Compared to the NACA 0015 in forward flow its performance with regard to the lift to drag ratio is lower (-25 %). Therefore even with the use of a duct to canalize the flow, or with an important tip speed ratio to lower influence of upstream velocity fluctuations, the bidirectional solution – at its best – remains less performant than a simple unidirectional foil section equipped with a reversing system. Moreover, as in the difference in lift, the difference in lift to drag ratio that is observed in regular flow between the NACA 0015 and the bidirectional foil is an indicator of the difference between these two solution with regard to non-productive structural loads. For the same power outcome, the bidirectional blade produces more drag, thus resulting in increased structural constraints.

The angular position of the maximum lift compared to the angle of the maximum lift to drag ratio provides an information on the foil's tolerance to inflow velocity fluctuations. It is representative of the amount of angular fluctuation of inflow velocity required to reach stall when the blade is angled at the design angle. From that point of view, the NACA 0015 remains more performant, then come the bidirectional section and the reversed NACA 0015. Once again, the result is a machine with more structural constraints and less productivity when using the NACA0015 in forward and reversed flow compared to the bidirectional case.

All the statements presented here for the smooth configuration remain valid in the fully turbulent case, even though the behavior of the reversed NACA 0015 is drastically different. Indeed, the lift level is globally not very affected and drag is obviously higher. It leads to globally lower lift to drag ratios, and the NACA 0015 in forward flow remains the most performant, followed by the bidirectional foil and finally the reversed NACA 0015. For the whole triggered turbulent cases, the angular position of maximum lift to drag ratio increases compared to the smooth case, while stall occurs globally at the same angle. Tolerance to fluctuations of the flow direction is therefore lowered, as the difference between the angle of maximum lift to drag ratio and the stall angle decreases.

To summarise, it can be stated that the use of a unidirectional foil section reversed to suit the flow remains more performant than that of a bidirectional foil or a unidirectional foil in forward and reversed flow. Both experimental and numerical results are showing that it is the case for the NACA 0015 which is a simple foil section. For a higher performance – cambered – foil sections the difference may be even higher. The reversed foil configuration shows a very specific behavior around 0° AoA, which could result in a hydro-elastic instability as well as in additional dynamic structural loads.

Chapter 5

Surface roughness and upstream turbulence effects on a cambered foil section

Summary: On turbines equipped with pitch and yaw regulating systems, constraints such as surface roughness and upstream turbulence are predominant. Structural requirements are also inducing thicker blade sections. This chapter presents a comparative study of surface roughness and turbulence effects on the hydrodynamic properties of a DU 91-W2-250 foil.

Contents

5.1 Introduction

As seen in the previous part, designing a tidal turbine while relying solely on the blade section to adapt to the bidirectionality of the flow may cause various issues, such as lowered performances and additional structural stresses.

Turbines inspired from wind energy are equipped with pitch and yaw adjustment systems. The rotor can therefore be angled to face the current and power regulation is achieved through angular orientation of the blades. This strategy drastically modifies the blade design.

Moreover, the major constraints are changed compared the case of a turbine equipped with a system that regulates pitch and yaw. Among them, surface roughness and upstream turbulence must be considered with attention as they may modify the properties of foil sections, the blade loads and the turbine's power extraction rate. For the design team, there is a need for comparative studies of these effects to smooth and turbulent cases that can be obtained numerically with a good level of accuracy.

The industrial partner, after investigating the performances of ducted turbines using bidirectional blades, is now considering more common designs inspired by wind turbine. The set of profiles from the Delft university were chosen to be used for the blade design. Therefore, the DU91-W2-250 is chosen for the present study as being representative of high performance, relatively thick airfoils developed to efficiently harvest the kinetic energy of a flow. The normalized geometry of the foil is presented in Figure 5.1.

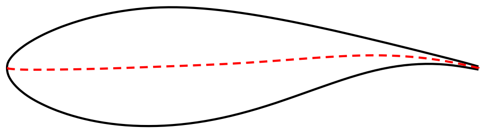

Figure 5.1: DU91-W2-250 foil geometry, $\alpha = 0°$

Experimental and numerical studies of this foil section are divided in three parts. Firstly, the basic properties of the foil are presented for both the smooth and the turbulent cases, and obtained using both experiments and computations. Then the effect of surface roughness is investigated through a comparative study of experimental results. Finally the effect of a high turbulence intensity is presented.

5.2 DU 91-W2-250, laminar-turbulent transition

This part of the chapter focuses on properties of the DU91-W2-250 foil. Characteristics presented here form the basis for the comparative study of roughness and turbulence presented further down.

Characteristics of the DU91-W2-250 as given in the literature are presented first. Then experimental and numerical results are introduced, including effect of the transition.

5.2.1 DU91-W2-250 in the literature

As described by Timmer and van Rooij [2003], this foil is part of a set designed using XFoil and RFoil by Delft University of Technology, for wind turbine applications. Timmer and van Rooij [2003] explain that in the early stages of wind energy development at an industrial scale, most of the manufacturers where using NACA based foils. Calculations and wind tunnel tests showed, however, that thick NACA foils suffered significant performance reduction due to early transition. The DU91-W2-250 has been specifically designed to lower that loss. The foil geometry is constituted of a restrained upper surface thickness in order to avoid the premature turbulent separation, and the resulting loss of lift on the suction side is compensated by a cambered aft on the pressure side. The foil has also been designed in order to lower its sensitivity to leading edge deterioration. It is widely used for horizontal axis wind turbines and has been intensively tested in a wind tunnel. This foil section is even considered to be installed on vertical axis turbines (Castelli et al. [2012a]). This type of foil could suit requirements for horizontal axis tidal turbine blades.

Reference experimental results for that foil have been published by Timmer and Van Rooij [1993]. Foil properties where measured in a wind tunnel at a Reynolds number value of $Re_c = 10^6$. During the following years measurements were verified through a comparison with experiments carried out in a second wind tunnel (D'Angelo and Timmer [1995]).

Franck Bertagnolio intensively studied airfoils for wind turbine application by means of, for example, three-dimensional computations on several wind turbine dedicated profiles including the DU 93-W-210 foil section (Bertagnolio et al. [2006]). Among the numerous foils investigated, Bertagnolio et al. [2001] compares experimental results on the DU 91-W2-250 from Timmer and Van Rooij [1993] to two-dimensional results obtained with the incompressible Navier-Stokes solver EllipSys2D and XFoil results, at a Reynolds number value of $Re_c = 10^6$.

A study from Castelli et al. [2012b] investigates this airfoil numerically using CFD calculations with the $\gamma - Re_\theta$ transition model described by Menter et al. [2006]. At the Reynolds number value of $Re_c = 3 \times 10^6$, he stated that the transition model results in significant improvement of performance prediction of the foil, particularly with regard to the drag level.

Van Rooij and Timmer [2003] also studied that foil section. Experiments and computations showed its performance compared to other profiles specifically designed for wind turbines such as the Risø-A1-24 (Dahl and Fuglsang [1998] or Fuglsang et al. [1999]) and the S814 (Tangler and Somers [1995]). Similarly to those, the DU foil is characterized by a high maxim high lift to drag ratio, high maximum lift and a limited reduction of the maximum lift due to leading edge pollution. These are also properties required for tidal turbine blade sections.

5.2.2 Results

Figure 5.2 presents experimental and numerical results for lift and drag coefficients at 5 m/s.

In smooth experiments, the lift curve is linear between -13° and 9°, and maximum lift coefficient reaches 1.75 at 12° AoA. Stall induces a lift coefficient loss of 0.3. The turbulent experiment is showing a more curved lift behavior. The maximum lift peak observed in the smooth configuration is removed in the turbulent case, replaced by a smoother behavior prior to stall. In that case, maximum lift is 1.45 and spreads between 12° and 20°. At negative angles of attack, experiments in the turbulent case also show a very different behavior compared the smooth case. A lift inflection is visible between -2° and -5°, followed by a linear lift behavior for lower angles with a slope lower than is observed in smooth experiments.

Globally, the SST-TM model satisfactorily predicts the properties of the smooth hydrofoil. The numerical lift slope is however slightly higher and the predicted maximum lift is higher but at the same angle as in the experiments. STT model very satisfactorily predicts the behavior of the turbulent experimental data. This statement is verified for both lift levels and the curve slopes. Even lift inflection at negative angles is correctly predicted. Only the post-stall behavior

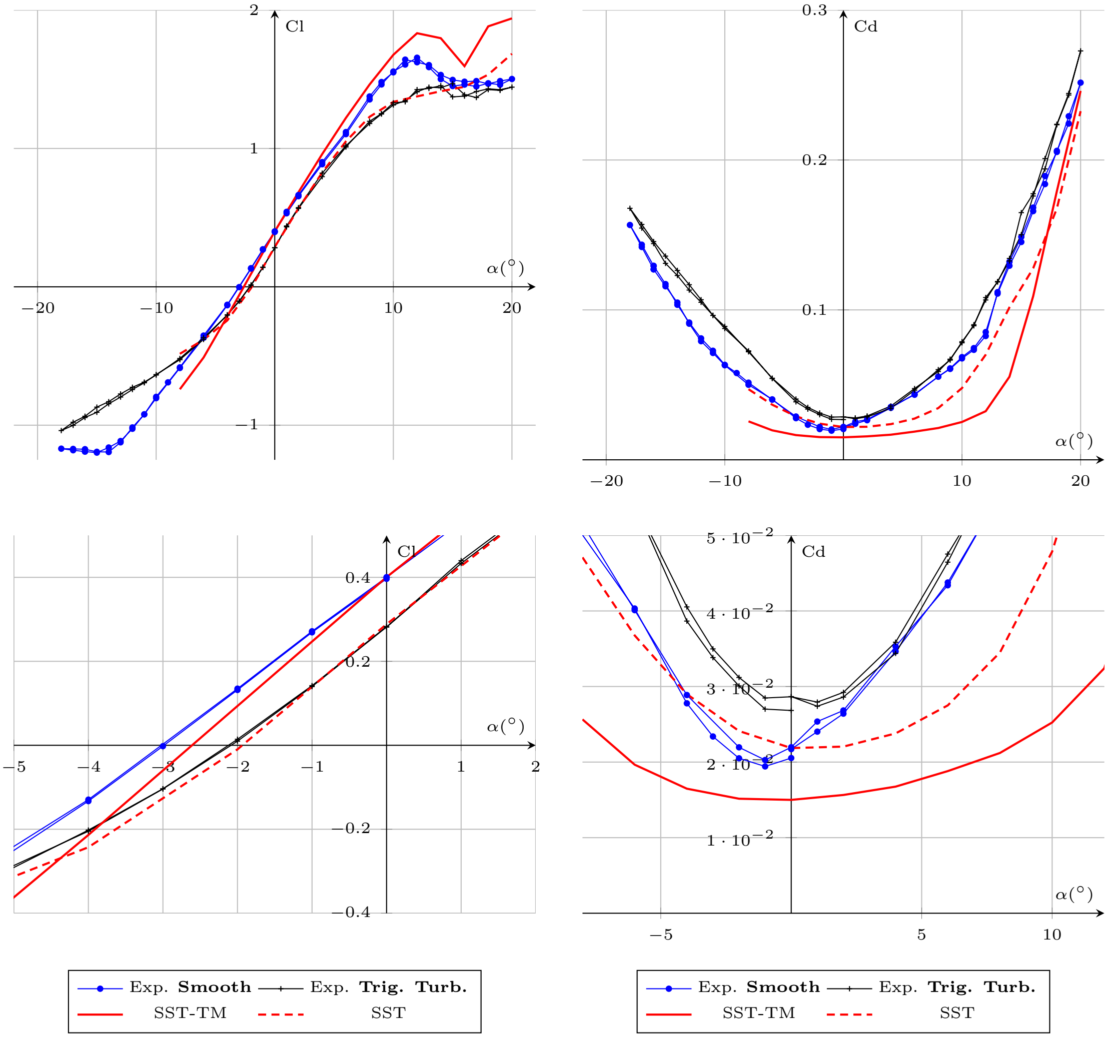

(a) Lift (b) Drag

Figure 5.2: Experimental and numerical data for lift and drag coefficients. DU foil section at $Re_c = 5 \times 10^5$.

is overestimated by SST calculations over 15° of angle of attack.

As is the case for most of the foil sections studied here, the measured drag level is generally higher than that which is predicted by calculations. Most of the differences observed are linked to three-dimensional effects. It can however be observed that drag levels are comparable between smooth and turbulent experiments at high angles of attack. This is well predicted by SST and SST-TM calculations.

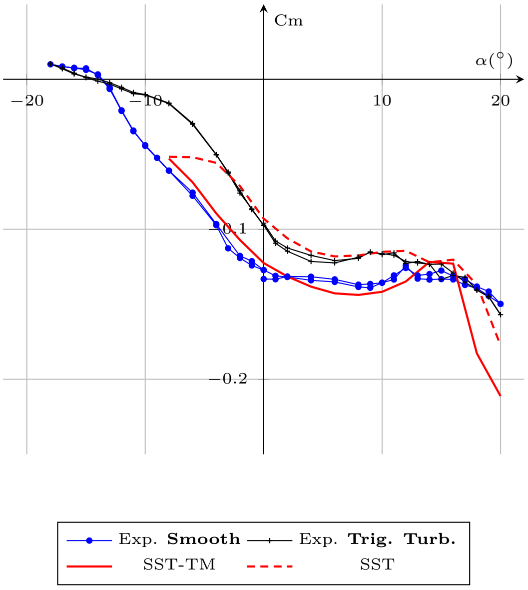

Figure 5.3: Experimental and numerical data for the pitching moment coefficient. DU foil section at $Re_c = 5 \times 10^5$.

As is the case for lift coefficient, the pitching moment presented in Figure 5.3 is well predicted by calculations, particularly on a range from -3° to 11° and for both SST and SST-TM models. At higher angles of attack, calculations are over predicting the pitching moment level, while at low negative angles of attack it is under predicted.

The lift to drag ratio sums up most of the statements made separately on coefficients (Figure 5.4). Indeed, the lift to drag ratio predicted by calculation is generally higher than that which is measured in experiments. The main reason for this is the three-dimensional aspect of drag. The maximum lift to drag ratio angle is also influenced by the presence of induced drag in experimental data. The smooth case is a good example. Experiments are showing a maximum lift to drag ratio between 4° and 6°, not clearly defined but materialised by a plateau, to the contrary of results obtained with the SST-TM model, with which maximum lift to drag ratio is obtained punctually at 8° AoA. The same statement can be made between turbulent experiments and SST calculation with the exception of the turbulent experiments which are resulting in a more determined position of the maximum lift to drag ratio. In that case, the angular position of the maximum lift to drag ratio is also lower in experiments than is predicted by calculations.

The maximum lift to drag ratio obtained here by calculations is lower than that which is given by Timmer and van Rooij [2003]. The Reynolds number value in the present case is also lower, which reduces the lift to drag ratio.

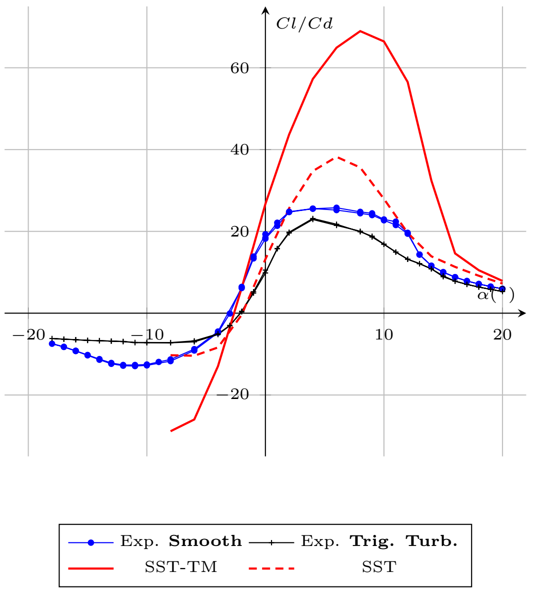

Figure 5.4: Experimental and numerical data for lift to drag ratio. DU foil section at $Re_c = 5 \times 10^5$.

5.3 Surface roughness

Any surface immersed in seawater is subjected to fouling and marine growth. Where the blades are concerned, a change in surface roughness can alter its properties and thus the amount of energy extracted.

This section presents an experimental study of several surface roughnesses, through a comparison between the smooth and the turbulent cases. Firstly, elements on the influence of surface roughness on the performance of a foil, as found in the literature, are presented. Secondly, a comparative study based on tunnel measurements is introduced.

5.3.1 Roughness effect in the literature

Roughness effect on foil properties has been largely studied and many studies are available in the literature.

In the past, Schrenck [1925] tested the effect of significant roughness on the properties of an airfoil. The airfoil was roughened using iron-wire gauze. He showed that roughness can drastically reduce the lift to drag ratio. The lift was shown to be lowered and the drag increased. Experiments carried out separately with roughened upper and lower surfaces showed that lift is mainly influenced by the upper surface finish.

Later, Hooker [1933] investigated the effect of over-all roughness and roughness stripes on the characteristics of a NACA 0012 airfoil. He tested several roughness heights at a Reynolds number value of $Re_c = 3.1 \times 10^6$ approximatively. He noticed that high roughness lowered the maximum lift value. By polishing the leading edge he also noticed that the major part of the roughness effect is coming from the leading edge on both lift and drag.

More recently, Lewis [1984] studied roughness effect on a NACA 0015 hydrofoil at relatively low Reynolds number values ($Re_c = 100000$ to $Re_c = 220000$ and roughness height from

0.00111c, 0.00282c and 0.00564c). He found that the pre-stall lift curve slope decreases when the roughness height is increased. Moreover, roughened foils were noticed to stall at lower maximum lift, but for higher roughness the stall is so progressive that it is not even visible. He stated that high roughnesses thickened the boundary layer to the extent that it became essentially separated, even at low AoA.

Cebeci [1987] also studied roughness effect on the properties of airfoils for aircraft applications. He presented a general scenario for roughness effect on lift and drag properties. It is summarized in Figure 5.5.

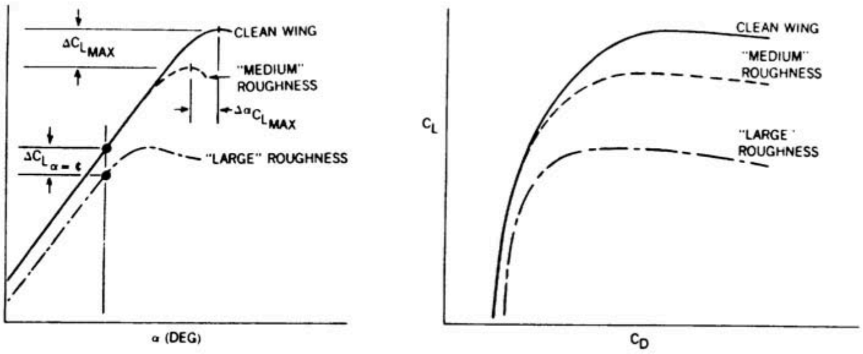

Figure 5.5: Typical roughness effect on lift and drag, extracted from Cebeci [1987]

Note that airfoils for airplane applications are generally lower than 15 % of relative thickness. The generalization of the roughness effect presented in Figure 5.5 may not suit the behavior of foil sections as thick as 20 % or 25 %.

Bekhti and Guerri [2012] have studied roughness effect on thicker airfoils by means of two-dimensional calculations. Using the Saturne code and a $k-\omega$SST model on a S809 airfoil, he compared the fully turbulent case to a case with addition of $1.9 \times 10^{-3} \times c$ roughness height. At a Reynolds number of $Re_c = 10^6$ no major difference was observed. The S809 is however 21 % thick and in fact not as thick as the DU 91-W2-250 (25 %), which could change roughness effect.

Similar airfoils were studied by Somers [2005] with regard to the effect of surface roughness. Properties of NREL (S901, S902 and S903) wind turbine dedicated Airfoils were determined experimentally. He stated that in some cases the Reynolds number is too low at the roughness position to support turbulent flow. Roughness is therefore so large that it increases the momentum thickness resulting in an abnormal decrease in the lift coefficient. Roughness effect is also stated as being to be proportional to the ratio of roughness height to boundary layer thickness.

Closer to the DU 91-W2-250, Freudenreich et al. [2004] studied a 30 % thick DU airfoil both experimentally and numerically. At high Reynolds number values, from 10^6 to 10^7, he showed that the rough configuration is generally less performant with regard to the lift to drag ratio, which is not due to lift drop but to the increased drag. Moreover, he noticed that the rough configurations lift to drag ratio increases along with the increase of the Reynolds number values.

Van Rooij and Timmer [2003] have studied roughness effect on the DU 91-W2-250 foil section. Both experimental and numerical studies were carried out. Studies included experimental measurements using vortex generators and roughness stripes put at 5 % chord from the leading edge. At a Reynolds number of $Re_c = 3 \times 10^6$, the DU 91-W2-250 in the rough configuration still showed a distinct lift peak, which is characteristics of those specially designed airfoils. As a result, the maximum lift to drag ratio remains acceptable compared to more standard airfoils such as the NACA 63-425. He also studied roughness effect on 30 % and 40 % thick DU type of airfoils. Results were slightly different. When roughened, such foils are characterized by a significant lift drop at low angle of attack which leads to zero lift or negative at angles close to the maximum lift to drag ratio in the smooth configuration.

Ren and Ou [2009] numerically studied effect of dust accretion on the blades of tidal turbines. Two-dimensional calculations where carried out on the NACA 63-430 airfoil at a Reynolds number of $Re_c = 1.6 \times 10^6$. Several surface roughness were calculated based on the turbine operational time. The results obtained showed an important decrease of the lift and an increase of the drag due to increased roughness height. The maximum lift becomes lower and less punctual until disappearing while roughness increases. Stall behavior remains identical between all the configurations.

Work carried out on profiles for wind turbine applications are showing two types of behaviors. The first is close to the one observed on airplane foils sections. It is characterized by lower lift and higher drag, resulting in lower performance. The second belongs to the behavior of thick profiles and shows that roughness can dramatically reduce lift, even resulting in counter performant foil configuration, at angles close to the design point (max. lift to drag ratio).

For marine applications, blade sections are subjected to fouling and marine growth. The question is: which of the two roughness-induced behaviors identified previously is likely to occur on a tidal turbine blade?

5.3.2 Results

A comparison of three roughness configurations with regard to the smooth and the turbulent cases is presented in this section. Roughness effect was investigated for two Reynolds number values: $Re_c = 5 \times 10^5$ and $Re_c = 7.5 \times 10^5$.

A reminder of the three roughnesses is provided in Table 5.1. The detailed description is available in section 2.2.

Name	Roughness type	$Ra(\mu m)$
DU-RS1	Mirror polished	0.088375
DU-RS2	Sanded	0.374375
DU-RS3	Sandblasted	1.375
DU-RS4	Sandpaper sticker	16.6

Table 5.1: Surface roughnesses used for the roughness sensitivity study of the DU foil

5.3.3 $Re_c = 5 \times 10^5$

The lift an drag coefficients are presented in Figure 5.6.

Surface roughness results in two different lift behaviors. RS2 and RS3 roughnesses are very similar to the smooth case. A slight difference is however visible in the maximum lift level,

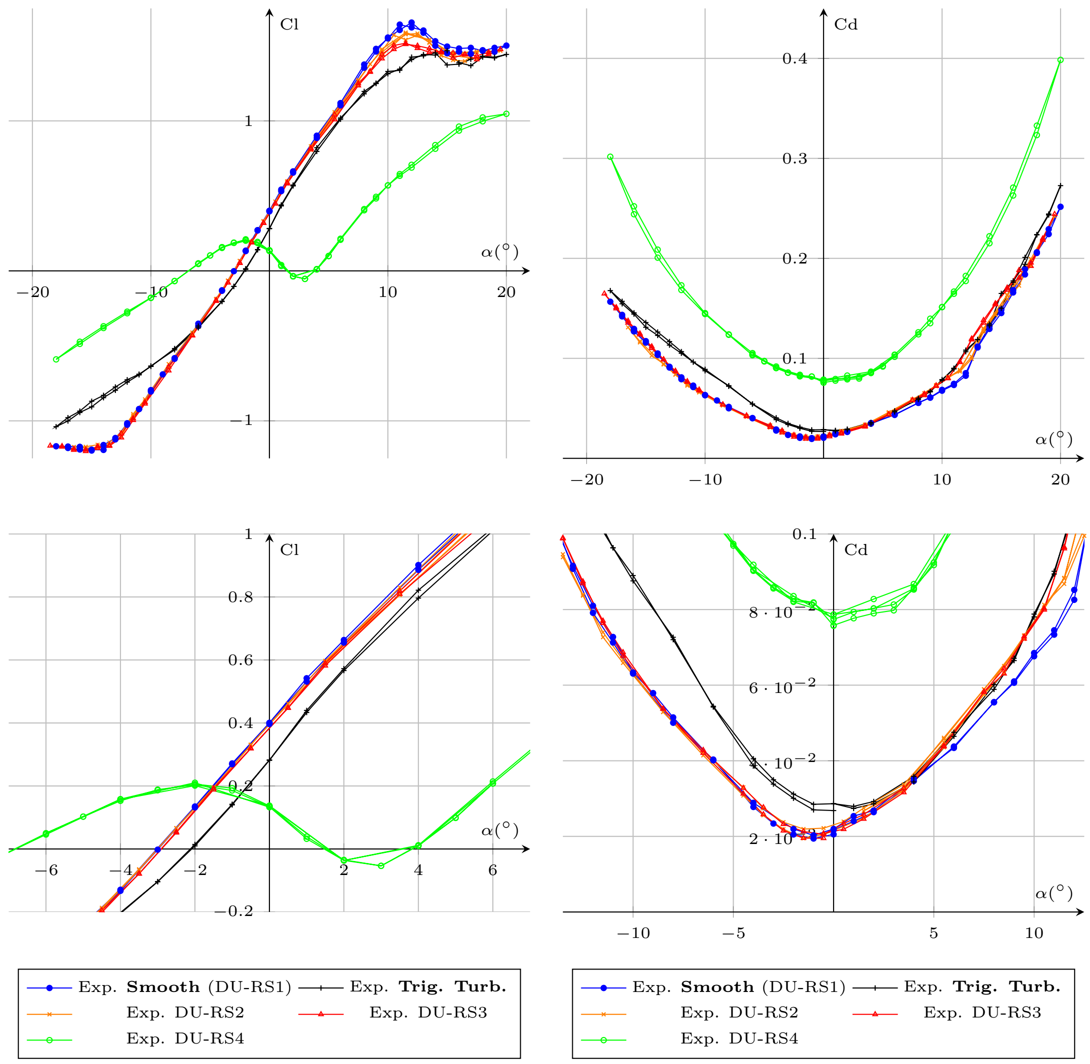

(a) Lift (b) Drag

Figure 5.6: Experimental data for lift and drag coefficients. DU foil section at $Re_c = 5 \times 10^5$.

which is lower, while the maximum lift angular position is identical to the smooth case. As roughness height increases (Ra), maximum lift decreases. Stalled behaviors are identical.

The RS4 roughness is very different. Maximum lift is not as well defined as in the RS1, RS2 and RS3 cases, the lift slope at high angles is regular and no clear maximum is observable. The lift curve slope is similar to that which is obtained with the turbulent case. Moreover, Cl only reaches a value of 1, which is low for such a foil section. But the most noticeable effect of this RS4 roughness on the DU lift is the change in the curve slope sign around 0° AoA. As angle is decreasing, the lift drops, resulting in a negative lift at 3° AoA. Then lift increases until a local maximum of 0.2 is reached at -2°, and drops again as the angle is becoming more negative. The situation at 3° AoA is particularly significant. For RS1, RS2 and RS3 roughnesses, the Cl value at this angle is 0.75, while for RS4 it is -0.05.

Similar lift behaviors have been observed in the literature on the same DU family of foils. For example, Van Rooij and Timmer [2003] have studied roughness effect on airfoils for wind turbine blades applications. Although they only used turbulence triggering roughness stripes (not full surface), they have shown similar lift drops for 40 % relative thickness hydrofoils, drops which were not observed in the smooth case. They explained that massive flow separation on both the suction and pressure sides was responsible for this particular behavior. It results in a change in the foil camber which explains the change in lift slope. At a lower angle than the lift kink, the flow is separated on the pressure side, which can be assimilated as a flat surface, while the upper surface remains effectively cambered. This results in positive lift. For higher angles than the kink, the opposite is occurring and the flow on the upper face is detached which considerably reduces the lift.

Although in the present case the foil is thinner (25 % relative thickness), a similar lift behavior was observed. A massively detached flow may also occur in the present case. However, as the thickness is lower, another factor than the foil surface curve is associated to the early boundary layer detachment: roughness. The following Figure 5.7 shows the PIV measured velocity field on the DU 91-W2-250 in the smooth configuration and with high surface roughness (RS4). Explainations put forward by Van Rooij and Timmer [2003] to explain the lift drop are verified in the present case. Surface roughness provokes the early detachment on the conventional suction side and thus completely alters the behavior of the foil. For a lower roughness height, the flow around the hydrofoil is identical to the smooth case, with fully attached boundary layers on both sides.

Calculations carried out at low Reynolds number values on the same section are also presenting the same kind of lift behavior (Figure 5.8).

They are showing that similarly to the increase of roughness height, a decrease in the Reynolds number can result in a similar flowing configuration at the foil surface. Both are characterized by an early detachment of the boundary layer, resulting in a drop of the lift.

Castillo et al. [2004] introduces a boundary layer separation criterion based on the definition of a pressure coefficient Λ_θ as expressed in Equation 5.3. It clearly shows that the separation of the turbulent boundary layer is the result of a balance between the momentum of the boundary layer, the inertia of the flow and the longitudinal pressure gradient.

$$\Lambda_\theta = \frac{\theta}{\rho U_\infty^2 \frac{\mathrm{d}\theta}{\mathrm{d}x}} \frac{\mathrm{d}P}{\mathrm{d}x} \tag{5.1}$$

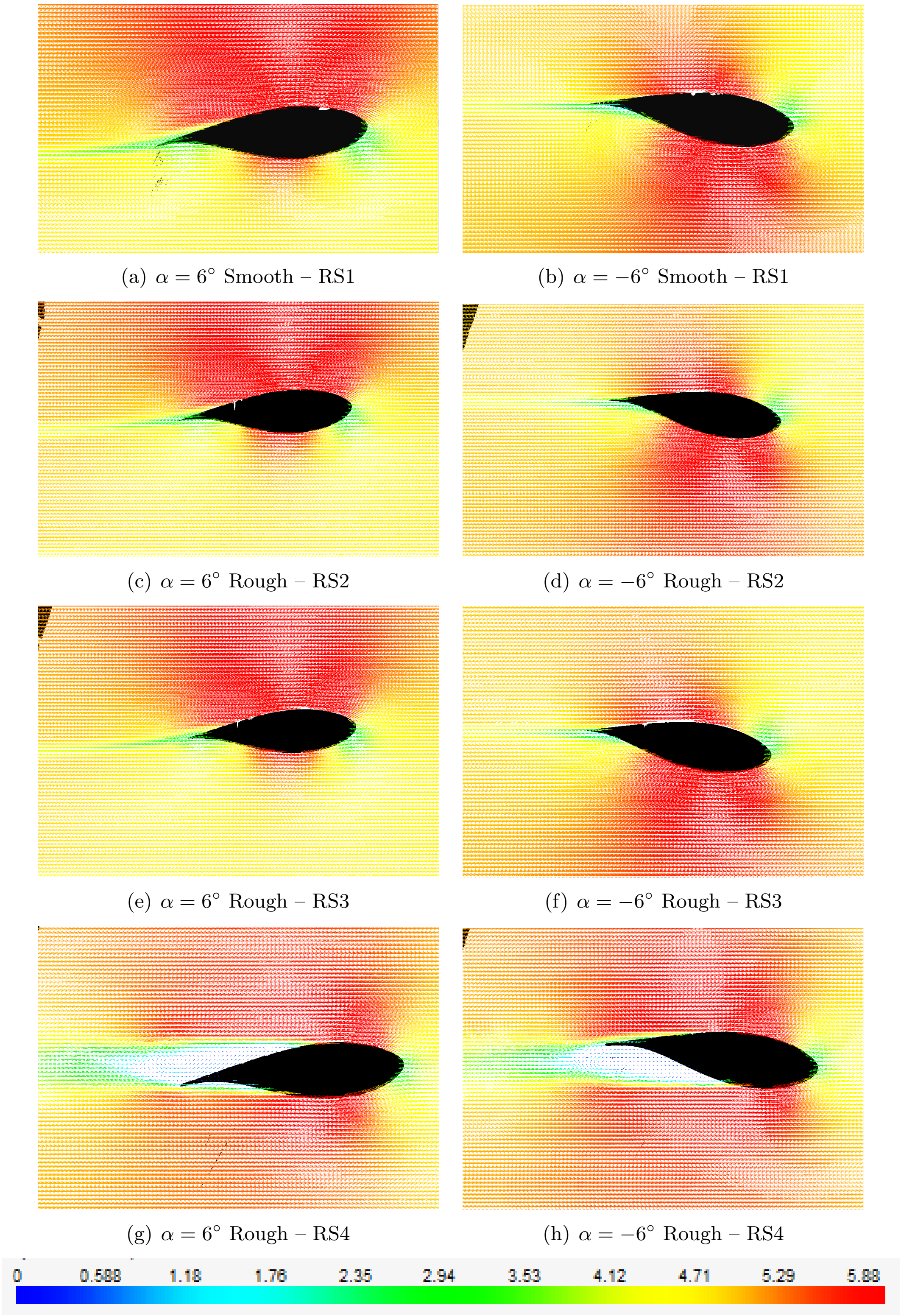

(a) $\alpha = 6°$ Smooth – RS1

(b) $\alpha = -6°$ Smooth – RS1

(c) $\alpha = 6°$ Rough – RS2

(d) $\alpha = -6°$ Rough – RS2

(e) $\alpha = 6°$ Rough – RS3

(f) $\alpha = -6°$ Rough – RS3

(g) $\alpha = 6°$ Rough – RS4

(h) $\alpha = -6°$ Rough – RS4

Figure 5.7: Velocity field around the DU 91-W2-250 at $Re_c = 5 \times 10^5$ (5m/s) for the different surface roughnesses.

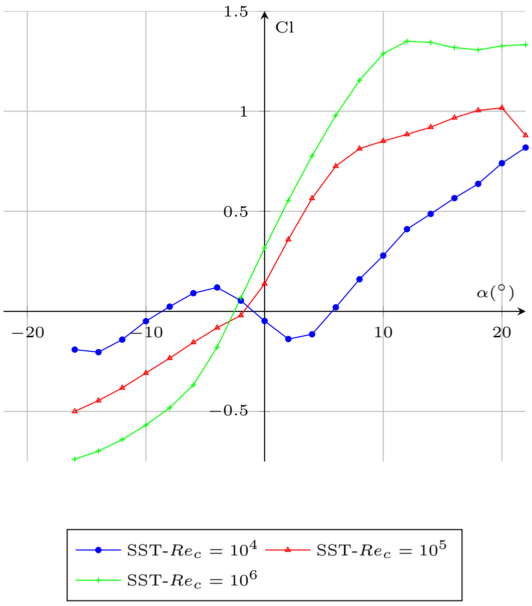

Figure 5.8: Numerical data for lift coefficient. DU foil section in an unconfined domain configuration using the SST model.

With:

$$\tau_p = \frac{1}{2}\rho U_\infty^2 \frac{\mathrm{d}\theta}{\mathrm{d}x} \tag{5.2}$$

Leading to:

$$\Lambda_\theta = \frac{\theta}{2\tau_p}\frac{\mathrm{d}P}{\mathrm{d}x} \tag{5.3}$$

In the case of high roughness surface, it can be assumed that the momentum of the boundary layer is strongly decreased relatively to the inertia of the flow as well as to the pressure gradient, which is dependent on the foil geometry. This results in a relative weakness of the boundary layer compared to the smooth or moderately roughened hydrofoil configurations, leading to a low resistance to detachment.

The drag coefficient is obviously affected by the addition of roughness. As for the lift, RS2 and RS3 cases are very similar. For angles between -18° and 4°, RS2 and RS3 drag coefficients are identical to the smooth case, while for angles higher than 4° they suit the turbulent case. The RS4 case is different and high roughness drastically increases drag level (about 4 times).

Pitching moment at a quarter of the chord is presented in Figure 5.10.

Once again RS2 and RS3 configurations are very close to the smooth case. For higher angles than 12° AoA, the smooth, the RS2, the RS3, and the turbulent pitching moment are similar. The turbulent case generates less moment than the RS1, RS2 and RS3 cases for angles between -12° and 12°. For these four cases the pitching moment is negative and its evolution is characterized by a plateau between 0° and 16° AoA, at a value of Cm between -0.12 and -0.14. The RS4 case is once again very different to the others. The pitching moment curve is characterized by a change in sign centered around 3° AoA. This precisely matches with the lift inflection previously described.

The lift to drag ratio presented in Figure 5.11 confirms the statements made regarding lift,

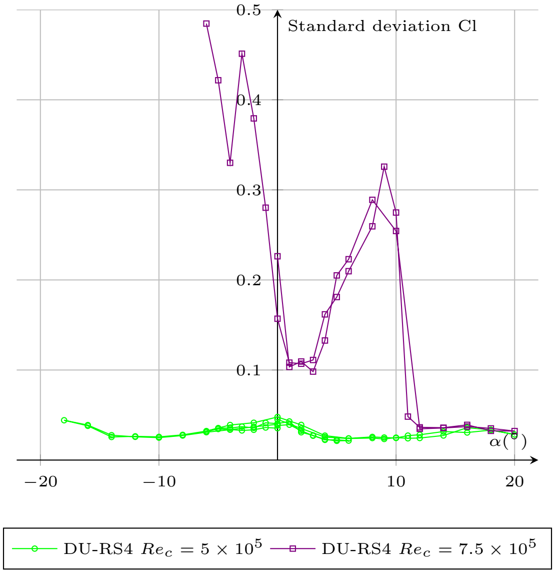

Figure 5.9: Experimental data, standard deviation of lift, DU foil in the high roughness configuration (RS4).

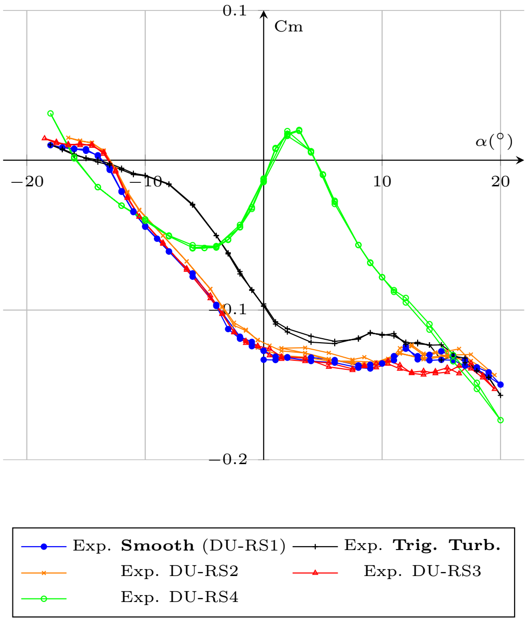

Figure 5.10: Experimental data for lift and drag coefficients. DU foil section at $Re_c = 5 \times 10^5$.

drag, and pitching moment.

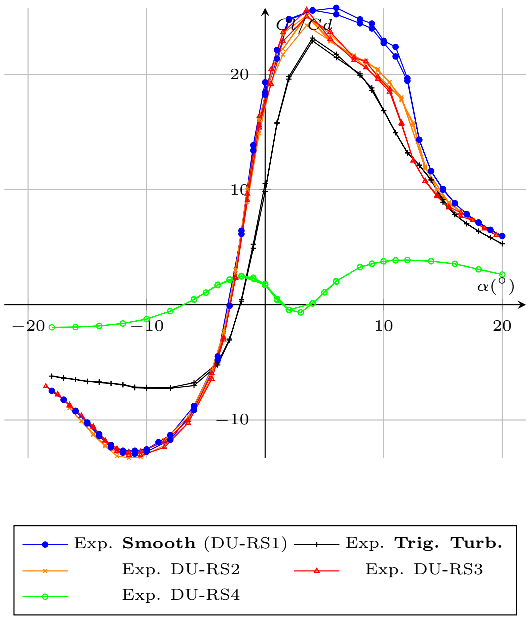

Figure 5.11: Experimental data for lift and drag coefficients. DU foil section at $Re_c = 5 \times 10^5$.

The RS2 and RS3 configurations are identical to the smooth one up to 6° AoA, then the slight increase of drag penalizes their lift to drag ratio which becomes closer from the turbulent case. The maximum lift to drag ratio remains as high as in the smooth case for these two configurations, but the maximum is more peaked and at a slightly lower angle (4° AoA). This means that at the design angle of attack, the RS2 and RS3 configurations will be as performant as in the smooth case. But as it is lower and sharper, any variation of more than 1° in the angle of attack will systematically lead to a quick decrease in performance. The RS4 case is completely different. As the lift is lower than the other cases and the drag drastically higher, it results in a very low lift to drag ratio. As the lift and drag curves are relatively smooth, the lift to drag ratio is also smooth, particularly at high angles of attack. The maximum is located at 12° AoA and remains constant for angles ranging from 10° to 12° AoA. Moreover as the lift becomes negative at 3°, the lift to drag ratio around this angle is negative, meaning the foil is counter productive.

During measurements on the RS4 configuration, strong vibrations were observed. Figure 5.12 presents the standard deviation measured on the lift coefficient for all the roughness configurations.

The RS2 and RS3 configurations are close to the smooth behavior in term of standard deviation. Measurements made with the triggered turbulent foil configuration are slightly different but remain within the same order of magnitude. The RS4 case is similar to the four others at high angles of attack, however around the 0° AoA, it presents a much more important standard deviation. The range of angles of attack for which the standard deviation is important are precisely those where is the singular lift evolution is observed. In this zone, the upper or the lower surface of the foil is subjected to a massive flow detachment responsible for most of the strong fluctuations observed.

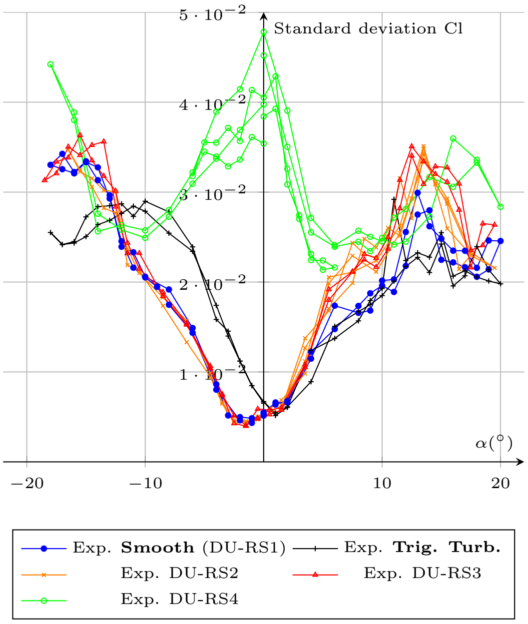

Figure 5.12: Experimental data, standard deviation of lift, DU foil section at $Re_c = 5 \times 10^5$.

5.3.4 $Re_c = 7.5 \times 10^5$

Measurements have also been carried out at a slightly higher Reynolds number value ($Re_c = 7.5 \times 10^5$). Lift and drag coefficients are presented in Figure 5.18.

As shown in Figure 5.18, roughness has a clear influence on the value of maximum lift. The increase of the roughness height progressively removes the maximum lift peak while the linear part and the stall remain identical. As for the previous Reynolds number value, the exception is the RS4 roughness. Indeed, this very high roughness induces a significant loss of lift on the whole range of angles of attack. This is coupled with a drastic increase in lift, resulting in a very poor performance level, which is even counter performant between 3° and 4° AoA.

Standard deviation of the lift presented in Figure 5.14, shows that important fluctuations are occurring during measurements at 7.5m/s.

The amplitude of the fluctuations is significantly higher than at 5 m/s and more particularly so for angles of attack lower than 10°, for which the lift kinks. The standard deviation peak around 9° AoA matches with the the discontinuity visible on the lift and the drag at the same angle. Moreover, the frequency of fluctuations is close to 90 Hz as observed with the reversed NACA 0015, which suggests that the natural frequency of the balance is achieved. Due to that phenomenon, lift and drag may be slightly overestimated at angles for which the standard deviation is high.

5.4 Upstream turbulence

One of the major constraints at the scale of the blade section is upstream turbulence. Underestimation of turbulence leads to an underestimation of loads on the blade, and thus increases the risk of failure.

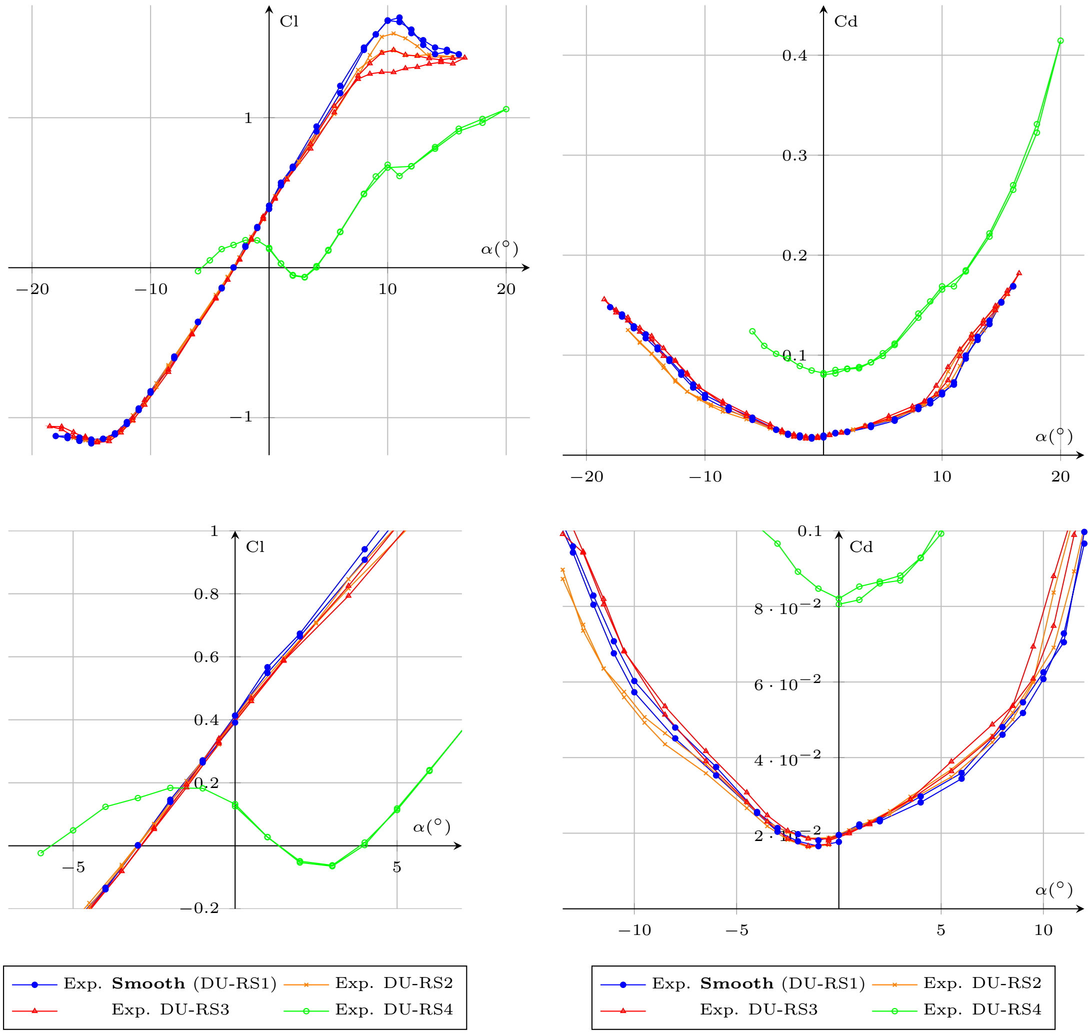

(a) Lift (b) Drag

Figure 5.13: Experimental data for lift and drag coefficients. DU foil section at $Re_c = 7.5 \times 10^5$. The complete force measurements are available in Appendix B.

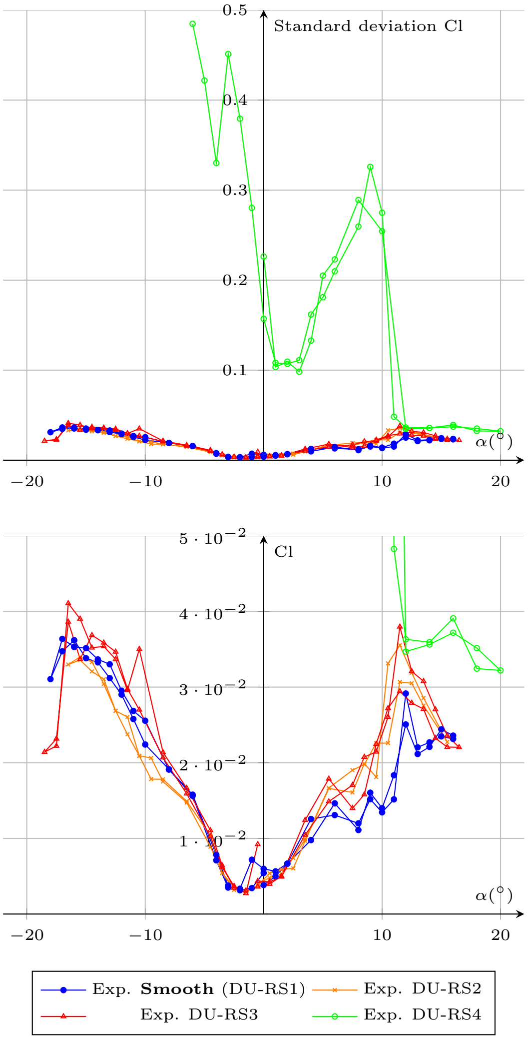

Figure 5.14: Experimental data, standard deviation of lift, DU foil section at $Re_c = 7.5 \times 10^5$.

Several scales of turbulence can be found in a tidal stream and some can be considered as variations of the direction and the velocity of the incoming flow. Others, of smaller scale, may be considered for their inherent effect on blade section characteristics.

This section investigates the effect of upstream turbulence on the DU 91-W2-250, in the limits of the hydrodynamic tunnel. Two turbulence intensities were tested: TL1 which is 1.81 % and TL3 which is 8.31 % (see section 2.1 for more details).

First, a review of the turbulence effect foil properties is presented, then experimental results are presented and discussed.

5.4.1 Effect of inflow turbulence on a foil properties

Stack [1931] studied the effect of turbulence on academic NACA foil geometries. He stated that increased turbulence removes the discontinuity in the lift curve for thick airfoils. He also showed that turbulence increases the maximum lift at high Reynolds number.

Hoffmann [1991b] experimentally studied the effect of free stream turbulence on the performances of a NACA 0015 airfoil. At a Reynolds number value of $Re_c = 2.5 \times 10^5$ he studied airfoil properties for free stream turbulence intensities of 0.25 % and 9 %. High turbulence (9 %) resulted in an increase of the lift peak (30 %) without inducing a change in lift slope, due to a serious delay in the separation. The angular position of maximum lift is also increased. No variation of the Cd was observed. The hysteresis loop observed in regular data is removed as the laminar separation disappears when turbulence is in the free stream.

Studies on flat plates by Jonas et al. [2000] showed that the larger the turbulence scale is, the earlier the transition process occurs.

Mish [2001] studied the effect of grid-generated free stream turbulence on a NACA 0015 at a Reynolds number of $Re_c = 1.17 \times 10^6$

Swalwell et al. [2001] studied the effect of turbulence on the NACA 0021 at a Reynolds number value of $Re_c = 3.5 \times 10^5$. Three set-ups were used. The low turbulence setup is characterized by an intensity of 0.6 %. Both turbulent configurations have a scale of $0.56c$ and intensities of 4 % and 7 %. Turbulence is once again found to delay stall. Maximum lift is therefore increased and stall angle is higher. Maximum lift increases as the turbulence intensity increases. Drag at high angles of attack (AoA$>$12.5°) is also reduced as turbulence increases.

Delnero et al. [2005] carried out experimental measurements on two low Reynolds number airfoils with a constant average velocity but two different turbulence structures: large and small eddies. At a Reynolds number of 2.02×10^5, both turbulence types upstream where found to increase maximum lift and its angular location. Drag is drastically increased as well.

Bertagnolio [2008] studied the effect of turbulence on a NACA 0015 and showed that at $Re_c = 1.6 \times 10^6$ stall angle is increased, and that maximum lift is increased by the inflow turbulence.

Watkins et al. [2010] studied the effect of turbulence for micro air vehicle applications. At a low Reynolds number (75 000), turbulence intensity was varied from 1.2 to 12.6 % and the longitudinal integral length scale from 0.17 m to 1.21 m. He found that an increase of the turbulence intensity decreased the lift slope but increased the maximum lift value. An increase of the integral length scale, on the other hand, was noticed to increase the lift slope and decrease maximum lift.

Globally, for high Reynolds snubber values, upstream turbulence delays stall and thus increases the maximum lift.

5.4.2 Results

Figure 5.15 presents experimental results for lift and drag coefficients on the DU section at 5 m/s with 8.31 % grid-generated upstream turbulence intensity.

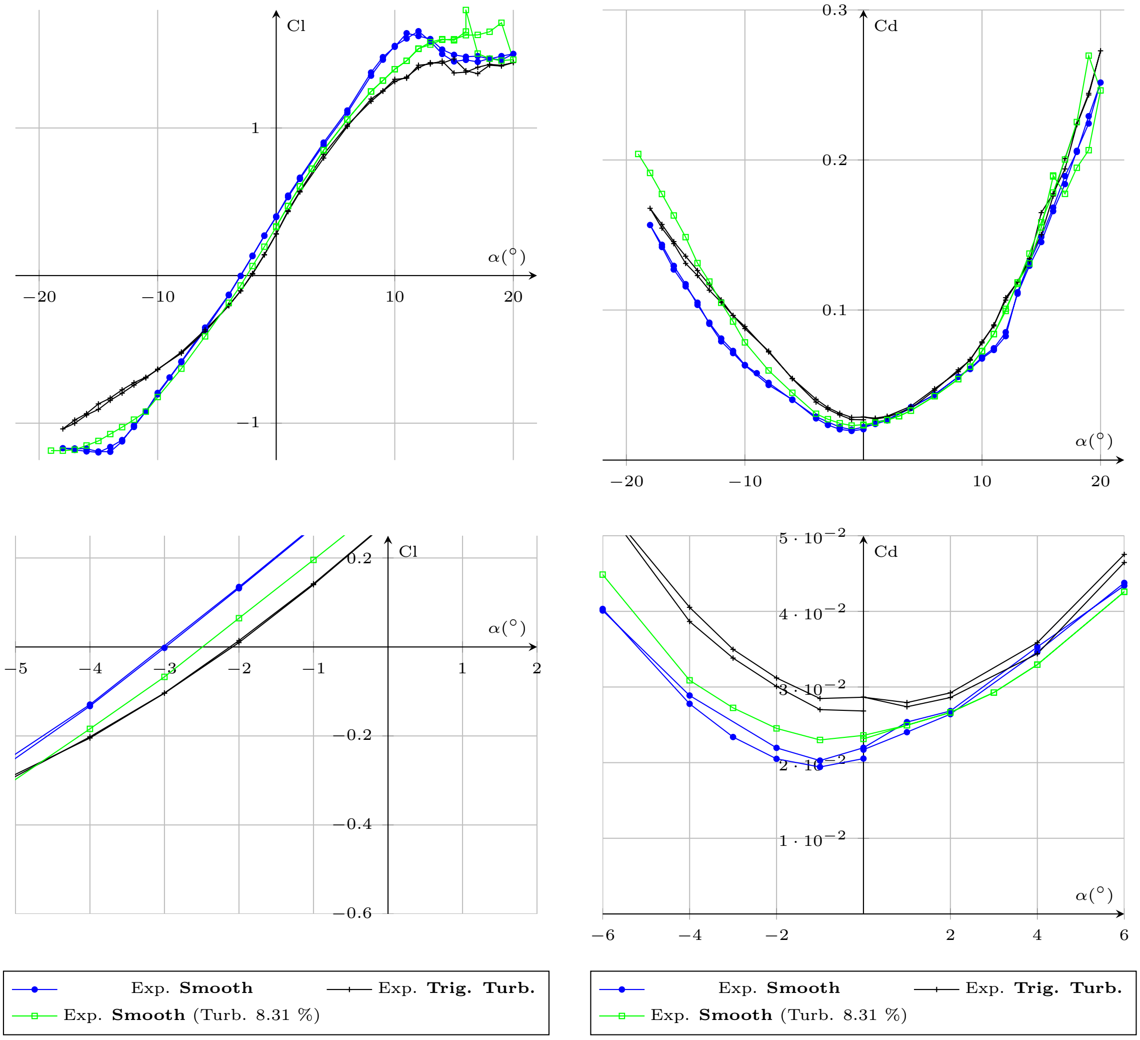

(a) Lift (b) Drag

Figure 5.15: Effect of upstream turbulence on experimental data for lift and drag coefficients. DU foil section at $Re_c = 5 \times 10^5$.

Lift behavior with 8.31 % of turbulence intensity stands between the smooth and the RT3 (roughness stripes, see section 2.2) behaviors. The maximum lift level is indeed higher than the RT3 behavior, and closer to the maximum lift measured in the smooth case. However, for positive angles, the shape of the lift curve is rather close to the turbulent configuration and stall occurs progressively. For negative angles, the minimum lift level is also close to the smooth configuration but also displays a smooth transition to stall, typical of the turbulent behavior observed on that foil.

A lift hysteresis is visible at high angles of attack due to blockage. Indeed together with the turbulence generating grids, blockage requires pushing the motor of the tunnel close to its upper limit. This results in differences in the upstream velocity between increasing and decreasing angles, which are generating the hysteresis loop.

Drag with high upstream turbulence is situated between the smooth and the turbulent configurations as well (Figure 5.15(b)). At low angles of attack, between -6° and 9°, it is close to the smooth drag behavior. For higher angles it better suits turbulent behavior. At important negative angles of attack, the behavior is more singular. Drag progressively increases from the smooth value to become higher than the turbulent value from -13° AoA as well as for lower angles.

The pitching moment is given in Figure 5.16.

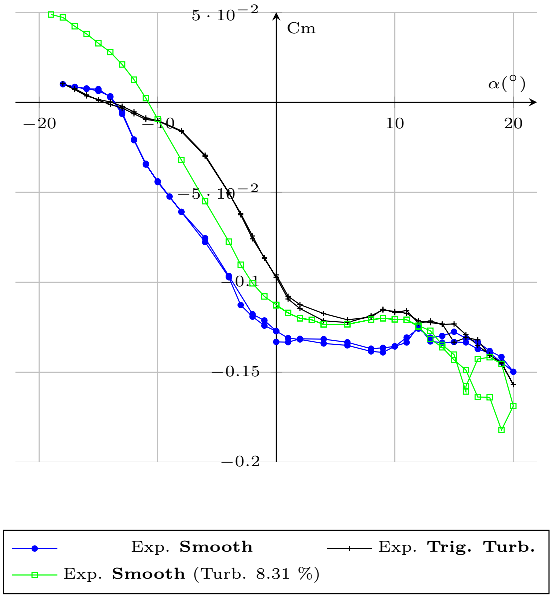

Figure 5.16: Effect of upstream turbulence on experimental data for the pitching moment coefficient. DU foil section at $Re_c = 5 \times 10^5$.

As previously stated, upstream turbulence on this DU hydrofoil produces a pitching moment which is between the turbulent and the smooth configurations. For angles between 2° and 12° the pitching moment with upstream turbulence is close to the turbulent configuration. For angles higher than 12°, it becomes more negative than both smooth and turbulent configurations. Between 2° and -10°, it is located midway from both other configurations. Finally, as angles are decreasing, passed -10°, the pitching moment measured with upstream turbulence becomes positive and stronger than both the smooth and turbulent measurements.

The lift to drag ratio measured with 8.31 % of intensity of turbulence is presented in Figure 5.17, compared to the smooth and the turbulent data.

Once again, upstream turbulence results in foil properties between the smooth and turbulent cases. The maximum lift to drag ratio is closer to the smooth case and higher than the turbulent one. The curve however is closer to the shape of the turbulent case, with a lower angle of

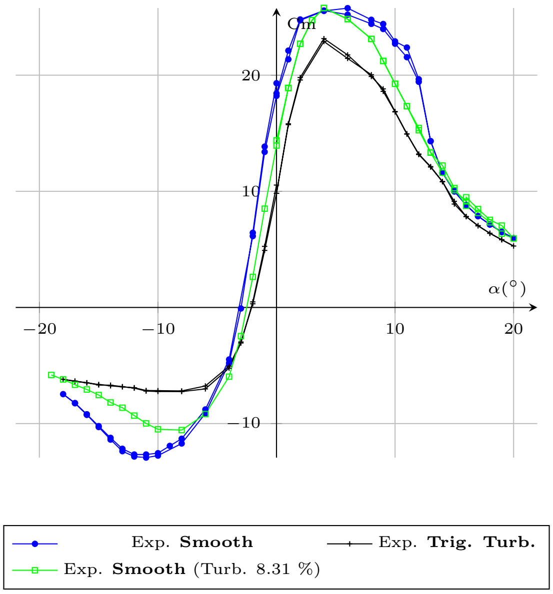

Figure 5.17: Effect of upstream turbulence on experimental data for the lift to drag ratio. DU foil section at $Re_c = 5 \times 10^5$.

maximum lift to drag ratio and an increased slope on both sides of the maximum, compared to the smooth case. At important angles of attack (negative and positive), all three configurations are converging.

5.5 Summary and discussion

The DU 91-W2-250 airfoil is a blade section developed by Delft university and used on horizontal axis wind turbines. This relatively thick blade section (25 $\%c$) has been designed after poor performances were measured on NACA 63-xxx foil sections of similar thickness, when turbulent. The high relative thickness also satisfactorily suits the structural requirements for a composite blade.

According to Timmer and van Rooij [2003] and Van Rooij and Timmer [2003], this foil has been designed to keep the sensitivity of the airfoil as low as possible with regard to nose contamination and contour imperfections. It has been designed considering that a clean blade is rare and its full high-lift potential is generally not frequently met. For tidal turbine applications, sensitivity to surface finish may be critical for manufacturing reasons, as well as for fouling and marine growth considerations.

Two main aspects were studied. They are the effect of full surface roughness and upstream turbulence on the properties of this foil. A comparative analysis is done on measurements carried out in the hydrodynamic tunnel, with reference to the smooth and turbulent configurations.

For the surface roughness study, three additional surface states were studied at a Reynolds number value of $Re_c = 5 \times 10^5$. A study of the effect of upstream turbulence is done for 8.31 % of turbulence intensity. It is the limited tunnel capacity to generate high turbulence intensity while using a passive turbulence generator.

Performance assessment is done primarily through the study of maximum lift to drag ratio and maximum lift. Their relative angular position is studied, and so are the shapes of the lift and lift to drag curves as well. The main results are summarized in Table 5.2.

Foil Configuration	Lift to drag ratio		Lift		Surface roughness (Ra/c)
	Max Cl/Cd	Ang. Position	Max Cl	Ang. Position	
Reference properties					
DU-Smooth (RS1)	25.77	6°	1.656	12°	0.08837×10^{-5}
DU-Trig. Turb.	23.15	4°	1.468	15°	0.08837×10^{-5}
Surface roughness effect					
DU-RS2	25.17	4°	1.589	12°	0.03744×10^{-5}
DU-RS3	25.59	4°	1.518	12°	1.375×10^{-5}
DU-RS4	3.883	12°	1.047	20°	16.6×10^{-5}
Upstream turbulence effect					
DU-UpstreamTurb	25.7850627773	4°	1.712737	19°	0.08837×10^{-5}

Table 5.2: DU 91-W2-250 properties as measured at $Re_c = 5 \times 10^5$, effect of surface roughness and upstream turbulence.

Prior to discussing about roughness and upstream turbulence effects on the DU 91-W2-250, smooth and triggered turbulent foil experimental properties were studied and compared to numerical simulations. Therefore, the effect of the laminar/turbulent transition on foil characteristics was investigated.

When the transition is triggered at the leading edge, drag is increased coupled with a slight decrease in lift. The increase of drag is due to the increase in skin friction. This therefore tends to decrease the lift to drag ratio. The triggered turbulent case is characterized by a smoother transition to stall compared to the smooth case, which could be an advantage in very disrupted tidal stream areas. This is corroborated by the angle of maximum lift to drag ratio which is lower in the triggered turbulent case. As a result, the design angle of attack is relatively far from the critical angle (stall) compared to the smooth case. The triggered turbulent foil may therefore be less sensitive to upstream velocity changes. Moreover, load fluctuations on the turbine may also be smoother as the foil properties are shifting smoothly. This last statement is also valid regarding power extraction. These advantages could compensate for the 10 % loss in lift to drag ratio compared to the smooth case.

Two-dimensional calculations have been able to accurately predict the lift force and the pitching moment over most of the angular range. However, drag is affected by three-dimensional effects which are not taken into account in the numerical model. This results in an optimistic prediction of the foil performances using the computations compared to experiments.

5.5.1 Roughness

In addition to the smooth and the triggered turbulent foils, three more configurations were used for studies of the effect of surface roughness on foil properties. Experimental data for these three roughened configurations were therefore compared to smooth and triggered turbulent cases.

The two finest roughnesses (RS2 and RS3) display a behavior between the smooth and fully turbulent cases. In that case, foil properties are slightly affected and its performance with regard to lift to drag ratio remains interesting. Between -18° and 4°, performances of the RS2 and RS3 foils are identical to the smooth case. Beyond these angles, the lift to drag ratio is closer to the fully turbulent case. The main drawback of these two light roughnesses is a tighter range of angles where the lift to drag ratio is at maximum. This results in a quick decrease of the performances with small angular variations of the incoming flow. The angle of maximum lift to drag ratio is identical to the fully turbulent case.

The largest roughness (RS4) produces a specific behavior. It is characterized by a lower lift level compared to the other cases studied. At small positive angles of attack, a negative lift is even observed (for example at 3° AoA). Lift at negative angles of attack is uncommonly high as well. Such a lift behavior can also be observed numerically on the same foil but at lower Reynolds number values. Moreover, a similar type of behavior as been observed on thicker DU foil models and for the same range of Reynolds numbers, when turbulent. Experiments and computations showed that this particular lift curve is the result of an early detachment of the boundary layer. For example, the lift is negative at 3° AoA, because the suction side is separated while the pressure side remains more attached, and the opposite is observed for small negative angles of attack.

More than the lift behavior, drag and the pitching moment are displaying very different behaviors compared to the other roughened cases. The drag level is larger but the drag function of the angle of attack is smoother. On the other hand, the pitching moment covers the same range of magnitude but presents a change of sign precisely at the angle of attack where the lift drop is observed.

This very rough configuration is characterized by a very low maximum lift to drag ratio, but its position is not as sharply defined as is the case in the other roughened cases. This results in very low performances but a tolerant configuration. The flow is separated at least on one face of the foil, which can result in vibrations and therefore additional structural constraints.

The effect of surface roughness on the maximum lift to drag ratio and maximum lift is summarized in Figure 5.18.

It is clear that several intermediate roughness heights would be required between RS3 and RS4 to accurately describe the evolution of the foil performance with roughness height. Nevertheless, the effect of roughness height on the DU 91-W2-250 can be observed. An increase in roughness height seems to regularly decrease maximum lift. The lift to drag ratio remains relatively constant between the three smaller roughnesses while the highest roughness implies a drastic decrease of lift to drag ratio, at $Re_c = 5 \times 10^5$. At a higher Reynolds number value, the lift to drag ratio is increased for the smallest roughnesses. Values for the largest roughness height remain identical independently of the Reynolds number.

The present study showed that degradation of the surface state can result in a drastic decrease of lift. Negative lifts can even be encountered at angles of attack that are generally close to the maximum lift to drag ratio in the smooth and triggered turbulent cases, which is also the angle of design.

5.5.2 Upstream turbulence

Due to the choice of a passive turbulence generator as well as to the properties of the hydrodynamic tunnel, the study of the upstream turbulence effect on the performances of the DU 91-W2-250 is done on one case only: 8.31 % of turbulence intensity with a flowing velocity of 5m/s ($Re_c = 5 \times 10^5$). As tidal currents are highly turbulent, the idea was to reach the highest turbulence intensity possible in the hydrodynamic tunnel.

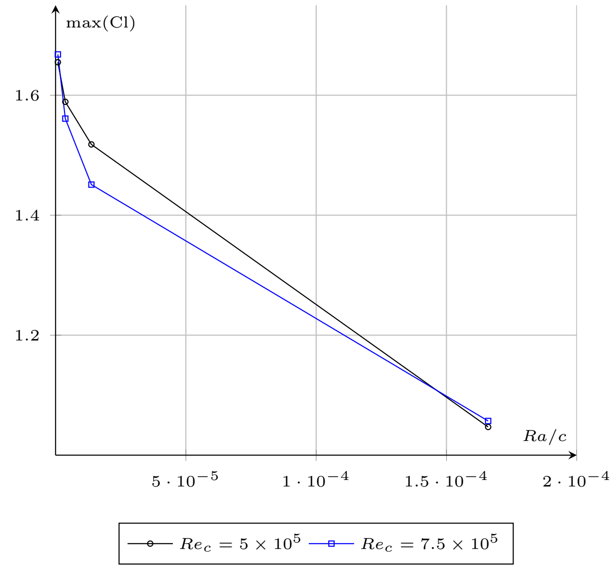

(a) Maximum lift

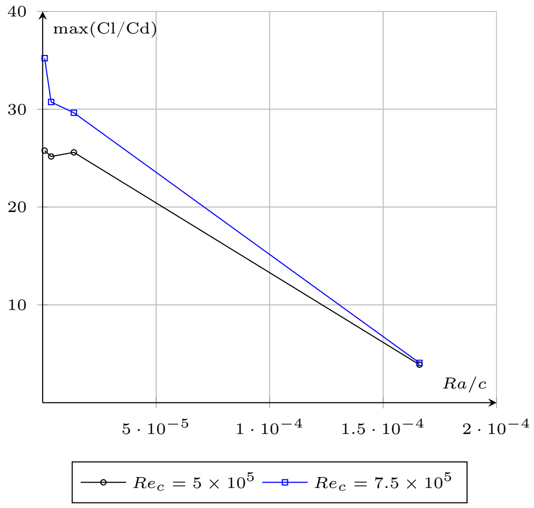

(b) Maximum lift to drag ratio

Figure 5.18: Effect of surface roughness on the global foil properties. DU 91-W2-250 foil section.

Compared to the smooth and the triggered turbulent configurations, measurements done with a high upstream turbulence intensity are at midway. The lift slope is indeed very similar to the triggered turbulent case, characterized by a smooth transition to stall. However, the maximum lift level is closer to the smooth case and the angle of the maximum lift is higher compared to the smooth configuration and closer to the triggered turbulent case. As drag remains comparable to the smooth case, at least for positive angles of attack, the lift to drag ratio is finally similar to the smooth case and located at a similar angle of attack.

Upstream turbulence does change the foil performance much, at least with regard to the maximum lift to drag ratio and maximum lift. Nevertheless, lift as a function of angle of attack is more progressive, which results in a more constant configuration compared to the triggered turbulent and the smooth cases.

Conclusion and perspectives

The work presented in this manuscript was both numerical and experimental and was carried out on academical two-dimensional configurations. The study consisted in the study of several blade sections in forward and reversed flowing configurations, which are representative of solutions that can be used for a tidal turbine. It was adapted to evolutions of the industrial partner's tidal turbine design.

The first part of the work focused on the way in which to achieve the bidirectionality of a tidal turbine without using a reversing system. For that purpose, a NACA 0015 was studied in forward and reversed flowing configurations. Results were compared to a 15 % thick bidirectional section, representative of the foils that could be used for tidal turbine rotors.

The second objective of the study dealt with the impact of surface roughness and upstream turbulence on the properties of a thick foil section inspired of wind energy turbines. The chosen foil in that case was 25 % thick and cambered, in order to meet performance as well as structural requirements. A DU 91-W2-250 foil section was studied.

Before any measurements were carried out, a significant amount of work was done on the experimental setup. An great effort was made to make it reliable, repeatable and accurate.

The force measurement device was one of the main centers of interest. At the beginning of the PhD, the hydrodynamic measurement device correctly measured the lift coefficient and pitching moment. The drag measurement, on the other hand, remained inconsistent. The symmetry was for example not respected on symmetric foils, while the flow into the test section was shown to be symmetric to PIV measurements. Several actions were undertaken to make this tool reliable and accurate. For example, the mechanical setup was modified, the balance acquiring process was also improved and the data processing was externalized and carried out using a reliable Matlab routine.

A calibration procedure was also proposed, based on the resultant hydrodynamic force (vector). As the hydrodynamic force is mainly lift driven on most of the hydrofoils, drag is particularly sensitive to angular position. The calibration was based on this statement. The idea was to measure the angular position of the balance for a range of angles and norms representative of the hydrodynamic force on a foil. An angular correction is then applied dependent on the measured force and added to the vector projection, to obtain the usual lift and drag forces.

This correction procedure properly works as long as the angle of the resultant force in the balance coordinate frame does not exceed a few tens of degrees. In that case however, the approximation made regarding lift will not be valid anymore. For this reason further work should be carried out on the calibration of hydrodynamic balance. The application of a similar calibration procedure to the lift could result in significant improvements of the measurements, particularly in uncommon situations (very high angles of attack, forces equally reported between lift and drag, etc.). This calibration could be done partially outside the tunnel test section, but a reliable point of reference has to be found in order to accurately position the balance. The work should be carried out directly on the tensions originating from the strain gauge bridges in order to avoid using the calibration matrix, which has been obtained using a calibration protocol from the balance builder that was not well known.

Regarding measurements, a second aspect was shown to be problematic: three-dimensional effects. As the test section is relatively small compared to the foil model size, blockage and other confinements are occurring. Lift is mostly affected by the vertical blockage, which can be corrected using two-dimensional calculations with the adequate domain geometry. However, drag is affected by tip and horseshoe vortices that are occurring close to the front and the back walls of the test section. These effects must be quantified. A method could be the use of induced drag principle.

Comparative studies using these experimental means are currently properly working.

Measurements carried out on the NACA 0015 in forward flow have displayed a good agreement with both numerical investigations and data from the literature, with regard to the lift force and the pitching moment coefficients. However, drag is still affected by three-dimensional effects. A slight discontinuity in the lift is also observed. It is linked to the laminar/turbulent transition.

The reversed configuration is more specific. An important lift increase at around 0° AoA is generated by the sharp leading edge geometry. It results from the development of a bubble close to the leading that triggers turbulent behavior on the upper face of the foil. The lower face however remains laminar. Computations were able to model this specific behavior, but the use of a transition model was required.

The elliptical foil section showed a specific behavior, with a non linear lift function of the angle of attack for low angles. A discontinuity in lift was also observed a negative angles of attack. The reason for this lift inflection is once again the transition, and more precisely the positioning of the transition at the leading edge on the suction side, and at the trailing edge on the pressure side. Experimental data showed an important difference between the smooth and the turbulent behaviors, due to the use of an exceedingly thick roughness stripe to trigger turbulence. In that case, numerical results using the SST calculations may be more accurate than the current experiments to qualify the turbulent behavior of the foil.

Comparison of experimental and numerical results regarding the maximum lift to drag ratio and the maximum lift are showing that the use of a bidirectional hydrofoil will result in a more performant turbine compared to the use of a unidirectional foil in forward and reversed flow. But performances reached by such a simple foil as the NACA 0015 equipped with a returning system are not sustainable for the bidirectional section. Using a high performance section the difference may be even larger.

The DU profile illustrates the second strategy, which is to equip the turbine with a returning system, often coupled with a pitch regulation system.

In that case the main constraint is no longer the bidirectionality of the flow but more the velocity variations, the surface roughness and the upstream turbulence. The last two constraints were studied experimentally.

Roughness effect was studied at two Reynolds number values, for four different roughness states, including the smooth case. Moderate roughness has been shown to have a limited effect on both the maximum lift to drag ratio and maximum lift. At the lowest Reynolds number value, performances of the foil remain constant, while a slight decrease was observed for the higher Reynolds number value. Globally, an increase of the roughness height has been observed to progressively remove the maximum lift peak. A case with a high roughness was tested for both Reynolds number values. It showed a very specific behavior which is generally characteristic of thick foil sections. Independently of the Reynolds number value, it indeed showed a significant lift inflection at low absolute angles of attack. This is due to the weakening effect of the high roughness on the boundary layer, which cannot counterbalance the adverse pressure gradient due to foil curvature. It has also been observed by calculations that a similar behavior can be obtained at lower Reynolds number values with the same foil in a turbulent case. An early detachment is observed and, when the lift inflection occurs, the suction side that should be attached is fully detached while the pressure side remains partially attached. This results in a change in the lift sign.

At the scale of the turbine, this situation could induce significant drawbacks. Fouling can indeed produce very high roughnesses and consequences on turbine efficiency may be significant as lift inflection occurs at angles of attack close to the maximum lift to drag ratio in the smooth and the triggered turbulent cases.

For future work, the effect of surface roughness on the properties of the DU foil could be supplemented by several intermediate roughnesses to be more accurately qualified. Therefore, a maximum acceptable roughness height could be determined.

In practice, roughness and upstream turbulence effects at the scale of the blade section can be estimated using the $k-\omega$ SST CFD model. A critical roughness height at the blade surface can therefore be specified for manufacturing in order to ensure that the foil properties remain correctly estimated by calculations. Fouling should also be studied and a period of time spent in seawater should be determined, past which critical roughness would be reached and foil properties estimation would be incorrect.

Upstream turbulence effect has been studied on a unique case. To generate the high turbulence intensity that is characteristic of tidal streams, limits of the hydrodynamic tunnel were reached. The use of an active turbulence generator could make it possible to reach higher turbulence levels.

Lift and drag where only slightly affected by the upstream turbulence, at least regarding the maximum lift to drag ratio and maximum lift. The lift curve with upstream turbulence, however, is more comparable to the triggered turbulent case and the transition to stall is particularly smooth. This results in a more tolerant foil configuration.

To complete this study at the scale of the blade section, aspects such as velocity variations and cavitation are the two other main issues for tidal turbines. Velocity variation could be divided in quasi static variations and dynamic variations should be studied with regard to the foil section as well as properties of the blade angle regulation system. The effect of cavitation could be studied both experimentally and numerically through a comparison of the minimum pressure coefficient. The influence of the surface roughness on the development of cavitation could also be studied.

Appendix A

Experimental determination of the divergence angle of the test section using the set square method

The theoretical geometry of the tunnel test section is given in Figure A.1. The top face is positioned horizontally, while the bottom face is diverging so as to compensate the increase of the boundary layer thickness.

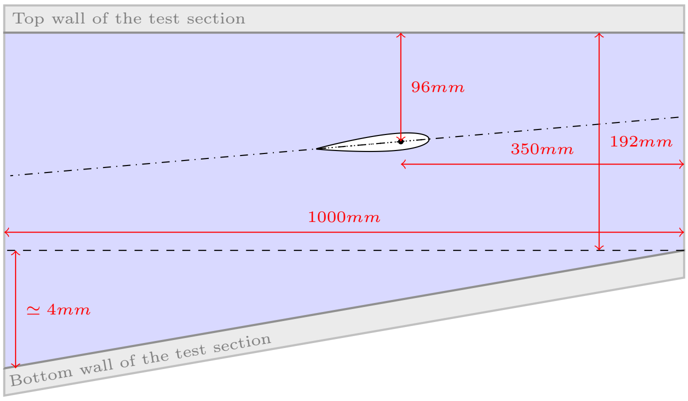

Figure A.1: Geometrical characteristics of the tunnel test section, (the slope of the bottom face is exaggerated)

The angular inclination of the bottom face can be calculated using trigonometry. Its value is 0.23°. However, the real test section is composed of numerous parts, meaning that numerous small positioning error can be found with regard to the relative positioning of the top and bottom faces.

A procedure has been designed to determine the angular position of the median line in the gravity coordinate frame simply. This method is based on the foil positioning stepper used as an angle measurement tool. Its definition is $1/60000°$, however in practice its precision is closer to $1/100$th of a degree. As shown in Figure A.2, a calibrated set square makes it possible to position the foil parallel to each of the top and bottom walls.

Firstly, the sharp foil trailing edge is positioned at a given distance from the top wall using

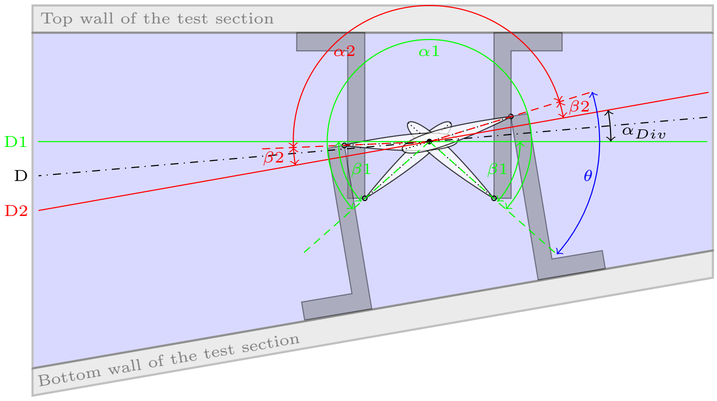

Figure A.2: Relative positioning of the geometrical and the hydrodynamic 0° AoA using the set square method. The slope of the bottom wall is exaggerated.

the set square. The angle of attack is set to zero in this position. The foil's trailing edge is then positioned again using the same set square and compared to the same wall, but with the trailing edge in the opposite direction. The angle between these two positions is measured and gives the value of α_1. Equation A.1 is used to determine the "angle of attack" corresponding to the foil chord positioned parallel to the top wall β_1. The angle of attack is once more set to 0.

$$\alpha_1 - 2\beta_1 = 180^\circ \tag{A.1}$$

Then, the set square is positioned on the bottom wall and the foil's trailing edge positioned at the top of the set square, with the trailing edge remaining in the same direction. The measured angle is kept under the value θ.

The value of α_2 is finally measured using on the bottom wall the same method as applied on the top wall. The angle β_2 for the foil chord to be positioned parallel to the bottom wall is then determined using Equation A.2.

$$\alpha_2 + 2\beta_2 = 180^\circ \tag{A.2}$$

Finally the angle between the top and bottom walls (α_{Div}) is determined using θ and Equation A.3.

$$\alpha_2 + \alpha_1 + \alpha_{Div} = \theta \tag{A.3}$$

Appendix B

Force measurements at $Re_c = 7.5 \times 10^5$

Most of the force measurement presented at 5 m/s have also been carried out at 7.5 m/s. However some of the major configurations have not been measured at this velocity for planning reasons. As Results are not consistent they have not been fully presented in the main part of the manuscript, but are shown thereafter for information.

B.1 NACA 0015, forward flow

Measurements have been carried out on the smooth configuration of the NACA 0015 in forward flow at a Reynolds number value of $Re_c = 7.5 \times 10^5$. Results are presented in Figure B.1.

B.2 Bidirectional section

For the bidirectional section, both smooth and turbulent configurations have been measured at 7.5 m/s. Results are presented in Figure B.2.

B.3 DU 91-W2-250

Forces have been measured for most of the roughness levels on the DU 91-W2-250 at 7.5 m/s. They are presented in Figure B.4.

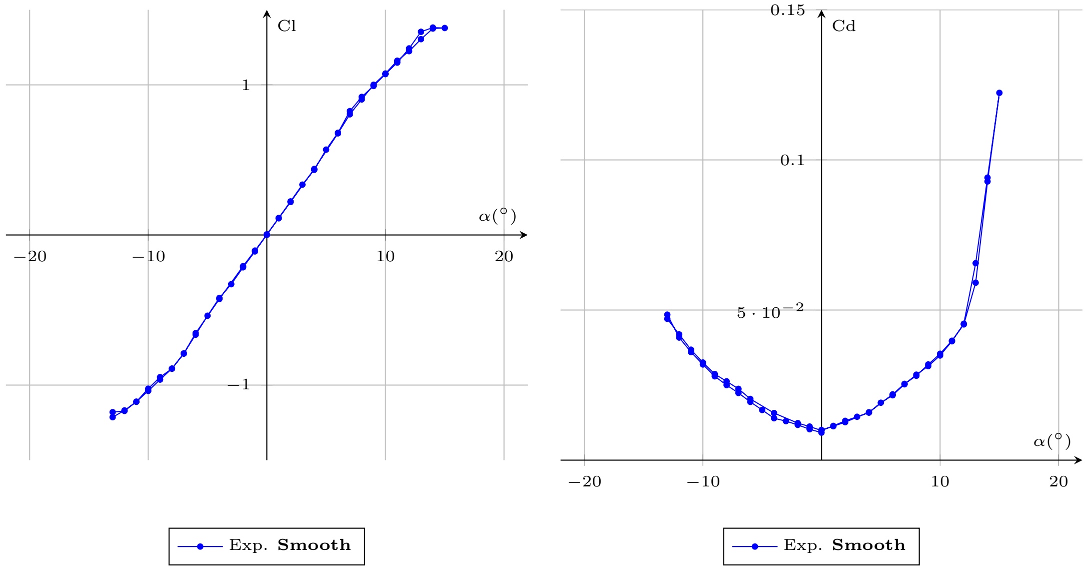

(a) Lift (b) Drag

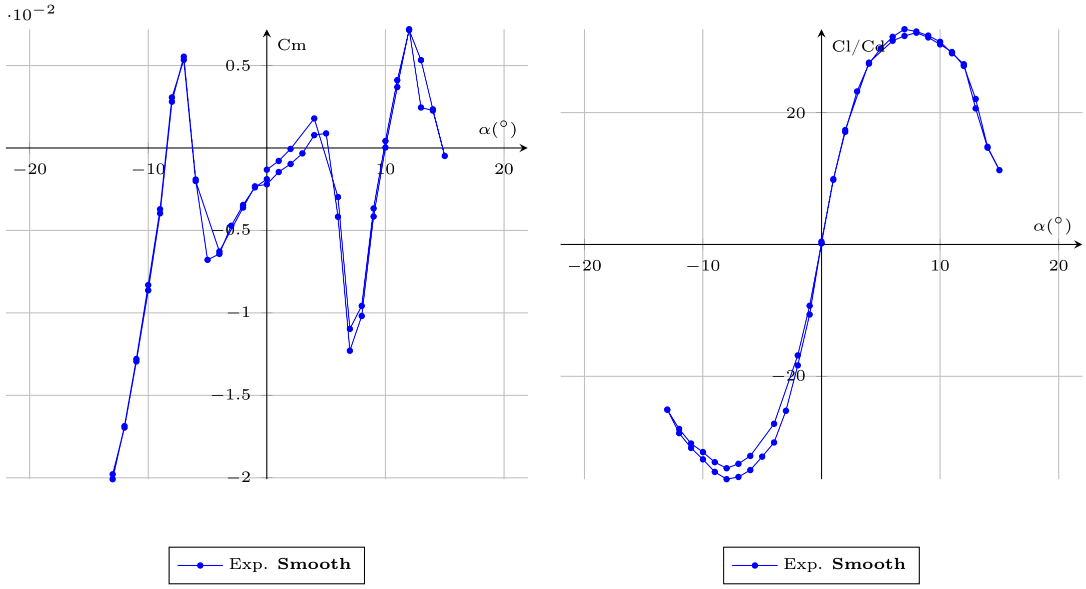

(c) Pitching moment (d) Lift to drag ratio

Figure B.1: Experimental data for lift, drag and pitching moment coefficients and lift to drag ratio. NACA 0015 hydrofoil at $Re_c = 7.5 \times 10^5$ in forward flow.

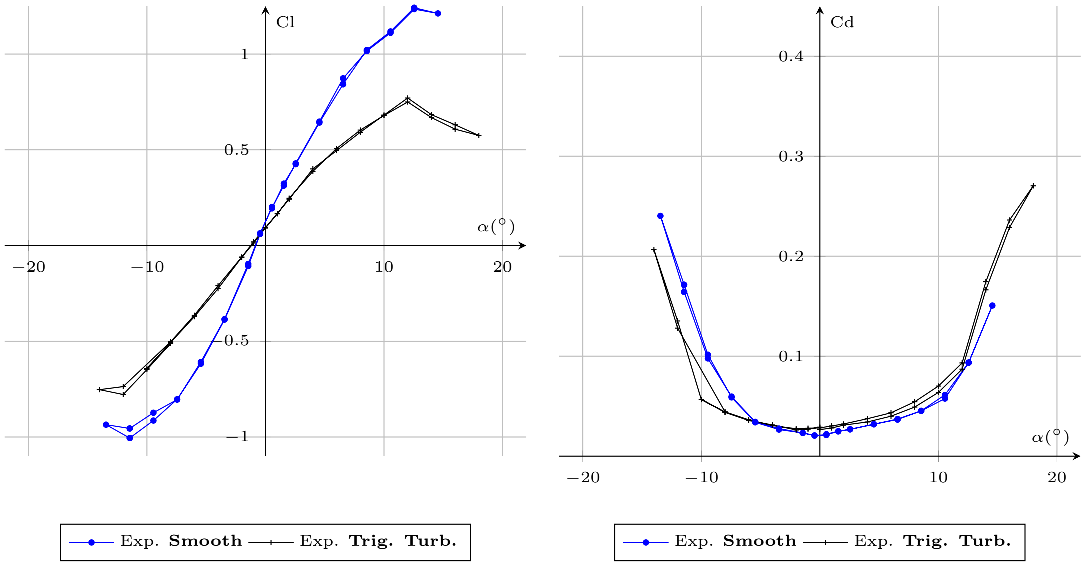

(a) Lift (b) Drag

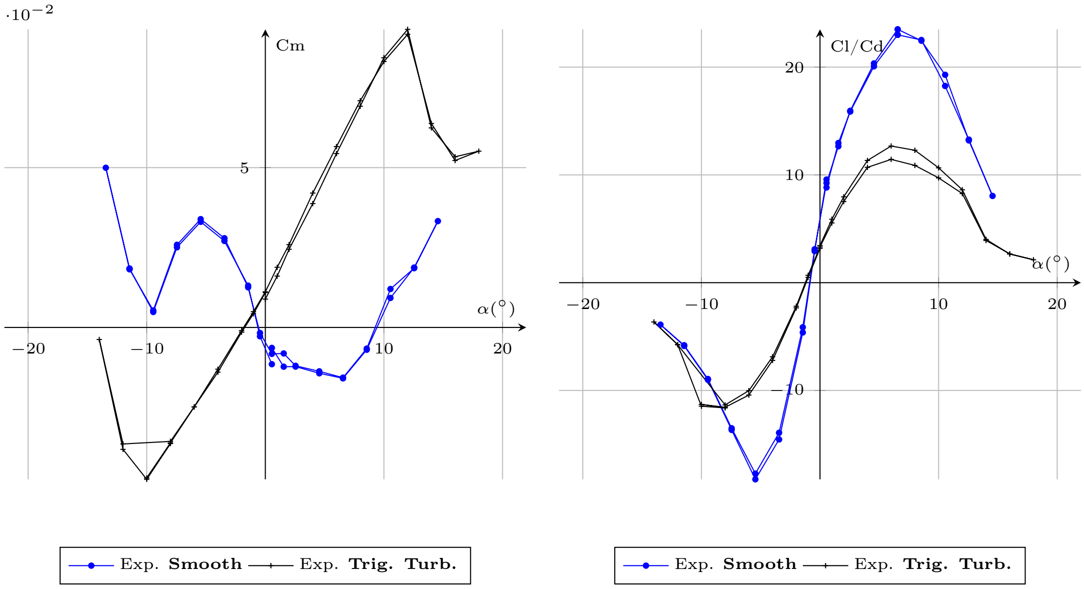

(c) Pitching moment (d) Lift to drag ratio

Figure B.2: Experimental and numerical data for lift, drag and pitching moment coefficients and lift to drag ratio. Elliptical foil section at $Re_c = 7.5 \times 10^5$.

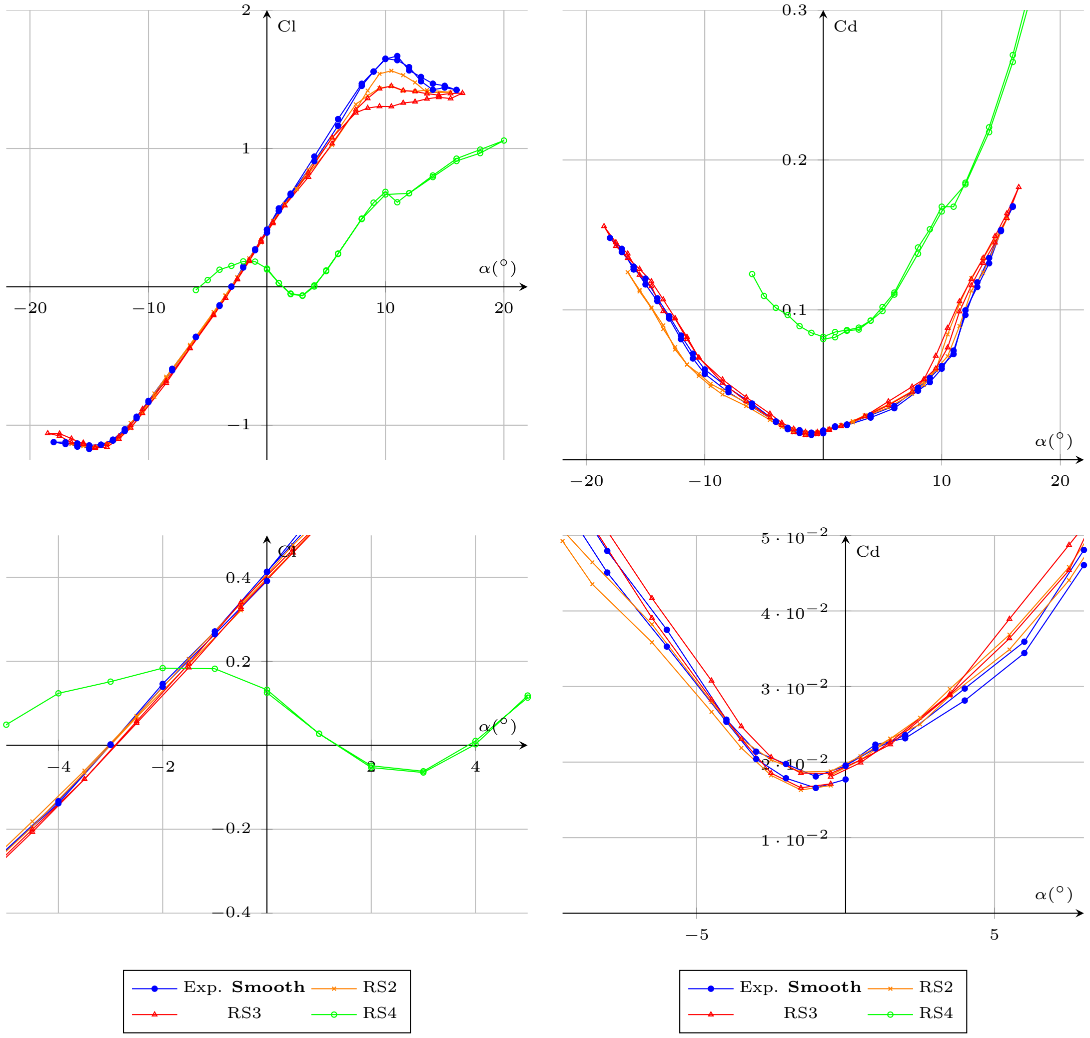

(a) Lift (b) Drag

Figure B.3: Experimental and numerical data for lift and drag coefficients. DU foil section at $Re_c = 7.5 \times 10^5$.

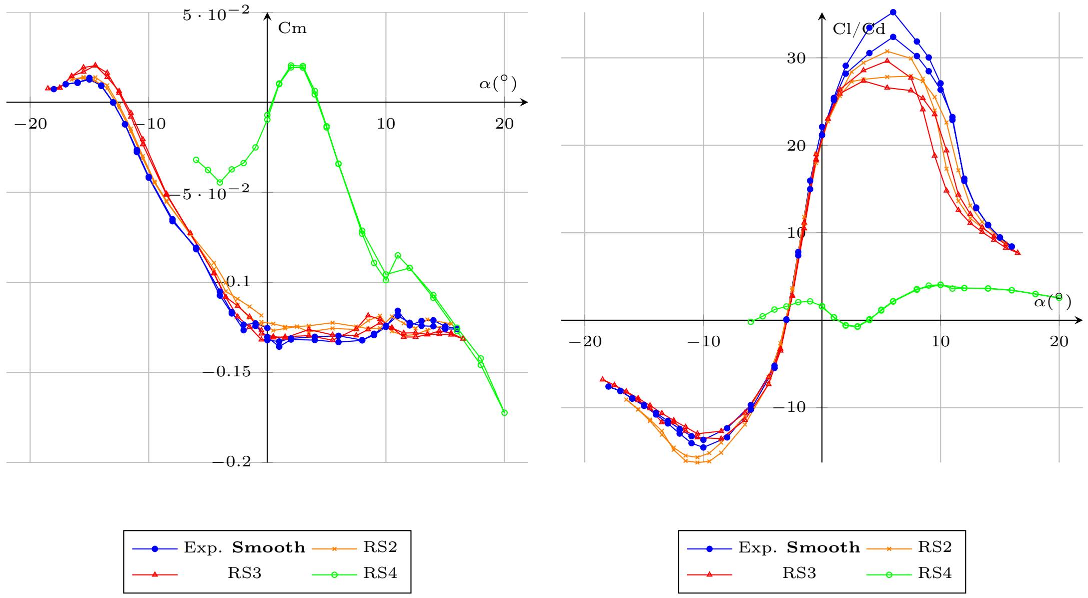

(a) Pitching moment (b) Lift to drag ratio

Figure B.4: Experimental and numerical data for the pitching moment coefficient, and the lift to drag ratio. DU foil section at $Re_c = 7.5 \times 10^5$.

Appendix C

Cavitation, minimum pressure coefficient

C.1 Cavitation

Cavitation occurs when the pressure at the foil surface reaches the vapor pressure of the liquid in which the foil is immersed. Cavitation generally results in performance losses associated to additional constraints on the material (fluctuating forces, corrosion).

Therefore, the following conditions can be used to determine the risk of cavitation based on two-dimensional data of the pressure coefficient at the foil surface:

$$\sigma = -Cp_{min} \tag{C.1}$$

Where σ is the cavitation number and Cp_{min} the minimum value of the pressure coefficient at the foil surface for a given flowing situation.

As the Cp_{min} goes under the value of σ, there is a risk for cavitation occurring, as conditions for the formation of vapor are reached. Cavitation can also appear before the theoretical value of the cavitation number is reached. For example, the surface roughness or the quality of the water can trigger cavitation inception.

Cp_{min} depends on the geometry of the foil and the flowing conditions, while σ depends mainly on the depth and the temperature of the water.

Pressure at the foil surface was not measured during experiments. Moreover, the timing did not allowed to study cavitation experimentally. However, numerical value are available.

Numerical results obtained using SST and SST-TM computations are presented below, for all three foils studied in the present work, i.e. the NACA 0015 hydrofoil in forward and reversed flow, the elliptical section, and the DU 91-W2-250. Calculations are made using the tunnel domain.

Experimental values of the σ, determined using the disappearance of cavitation are also plotted in the following figures.

C.2 NACA 0015, forward and reversed

Figure C.1 provides an overview of the cavitation risk through the Cp_{min} for the NACA 0015 foil.

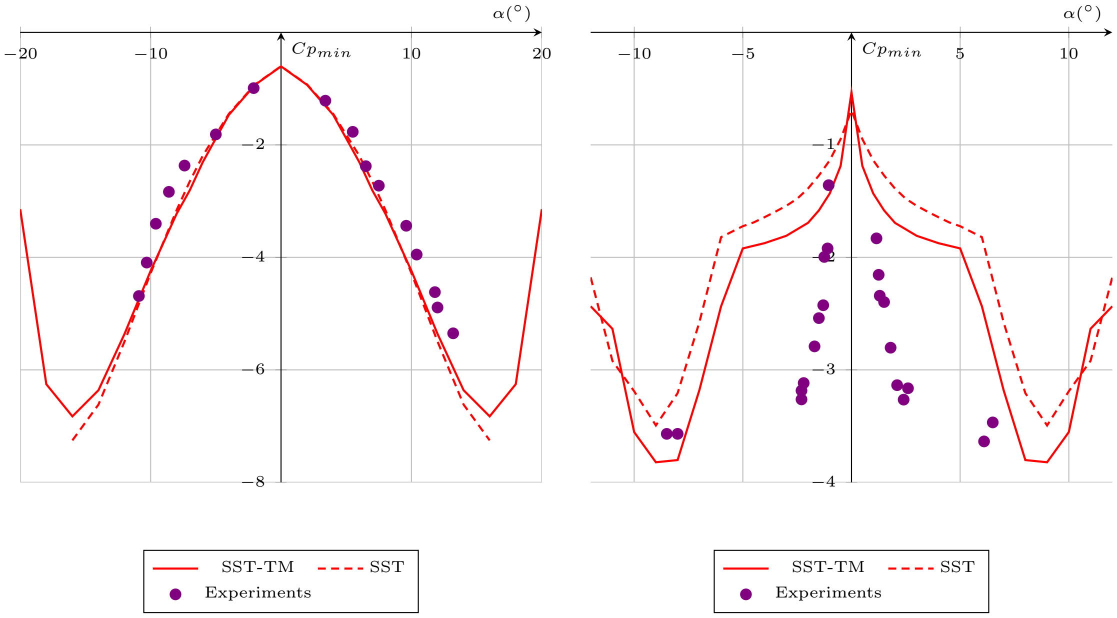

(a) Forward

(b) Reversed

Figure C.1: Numerical data for the minimum values of the pressure coefficients. NACA 0015 foil section at $Re_c = 5 \times 10^5$, tunnel domain.

In the case of the reversed NACA 0015, the sharp leading edge leads to the development of a laminar separation bubble. In that case, the value of the minimum pressure coefficient obtained at the foil surface is not necessarily representative of the cavitation risk. Indeed, the bubble also presents a low pressure peak at its surface, which results in an earlier cavitation development observed experimentally.

C.3 Elliptical foil section

Figure C.2 provides an overview of the cavitation risk through the Cp_{min} for the elliptical foil section.

C.4 Numerical results on the DU 91-W2-250

Figure C.3 presents the Cp_{min} as a function of the angle of attack obtained on the DU foil section using computations. Both the fully turbulent and the transitions model are used. The numerical domain remains at the tunnel test section's dimensions.

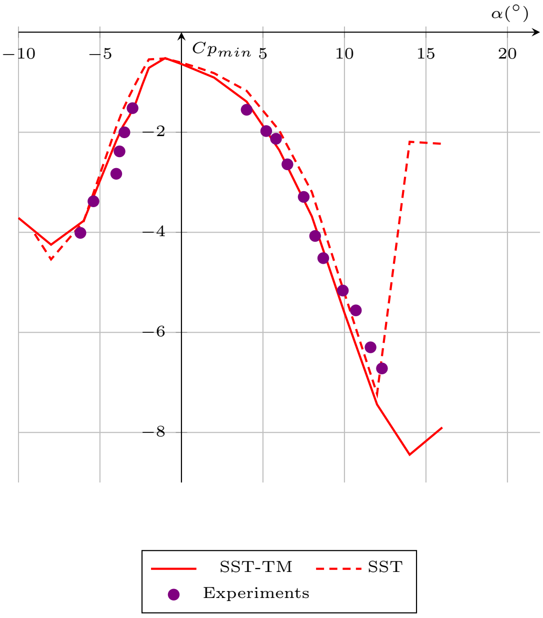

Figure C.2: Numerical data for the minimum values of the pressure coefficients. Elliptical foil section at $Re_c = 5 \times 10^5$, tunnel domain.

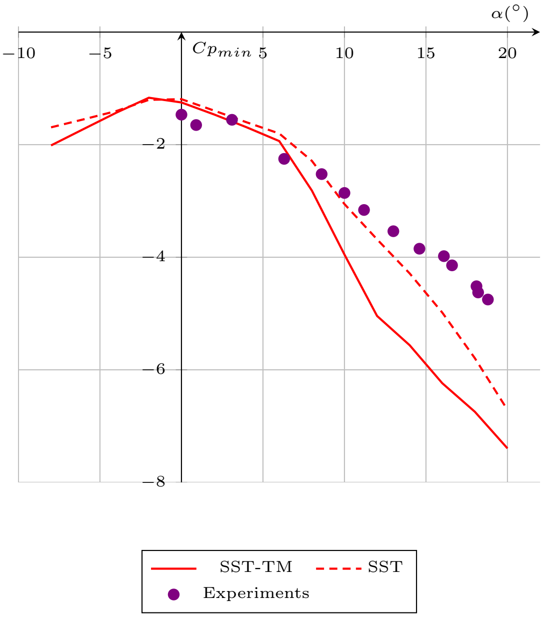

Figure C.3: Numerical data for the minimum values of the pressure coefficients. DU foil section at $Re_c = 5 \times 10^5$, tunnel domain.

Appendix D

XFoil calculations, setup

D.1 Introduction

The XFoil code developed by Drela [1989] was used for first stage determination of the foil's hydrodynamic properties.

The XFOIL code is based on an inviscid linear-vorticity panel method with addition of a Karman-Tsien compressibility correction. Source distributions superimposed on the airfoil and the wake account for the viscous layer's influence on the potential flow. The viscous layer is represented by a two-equation lagged dissipation integral method. Laminar and turbulent layers are treated with an e^9-type amplification formulation which determines the transition point. Boundary layer and transition equations are solved simultaneously with the inviscid flow field using a global Newton method.

The procedure is particularly suitable for rapid analysis of low Reynolds number airfoil flows with transition separation bubbles.

This appendix describes the parameters for XFoil (using XFLR5) calculations as used in the present work. Firstly, values of the code setup parameters are introduced. Then is described a sensitivity study carried out on a NACA 63-415 and regarding the definition of the geometry, the angle-step, as well as the N_{crit}.

D.2 Setup

The values of all the parameters are summarized in Tables D.1 and D.2.

D.3 Sensitivity study

D.3.1 Foil definition

The foil geometry is imported. A standard quality foil coordinate file is required. Poor foil description can lead to convergence difficulties and calculation errors.

Parameter	Default value	Used value
VAccel	0.01	Default
Iteration limit to reach convergence	100	150
N_{crit}	9	9 or 0.02
Top trip position	1	Default
Bottom trip position	1	Default
BL init. between unconverged iter.	not toggled	Toggled
BL init. between polars	not toggled	Toggled
Start from 0° AoA	not toggled	Toggled
Angle-step (°)	1°	0.5°

Table D.1: Global calculation parameters

Parameter	Default value	Used value
Number of panel nodes	100	160 -220
Pannel bunching parameter	1	Default
TE/LE pannel density ratio	0.15	Default
Refined area/LE panel density ratio	0.2	Default
Top side refined area x/c limits	1 - 1	Default
Bottom side refined area x/c limits	1 - 1	Default

Table D.2: Geometry definition parameters

First, as explained in the code documentation (Drela [1989]), it is recommended to set a trailing edge gap even for sharp trailing edges. This improves the convergence. In XFoil, the trailing edge gap is set using two parameters: the gap value – i.e. trailing edge thickness or distance between upper and lower coordinate endpoints – and the blending distance which controls how the new trailing edge gap blends into the original foil – length scale for the exponential blending function (Drela [1995]). In most cases a gap of 0.20 % of the chord and with a blending distance of 80 % of the chord is used for foils characterized by a relative thickness of 25 % to 15 %. However, for very sharp or thin foils, it can be set thinner.

Using this setup, the foil is re-meshed independently of the original points and using default XFOIL mesh parameters. The NACA 63-415 properties are obtained and compared for six geometry refinements and for three values of the Reynolds number. Figure D.1 provides an overview of the foil mesh, for both coarsened and refined versions.

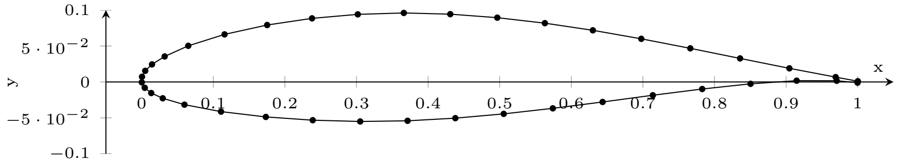

(a) 40 points

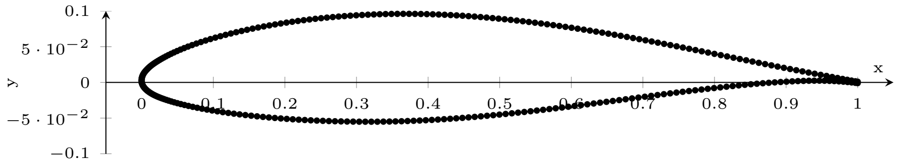

(b) 300 points

Figure D.1: Normalized Naca 63-415 geometry refinement, $\alpha = 0°$

$Re_c = 10^5$

The following figure (D.2) presents the influence of the number of points for the foil geometry description at a Reynolds number value of $Re_c = 10^5$.

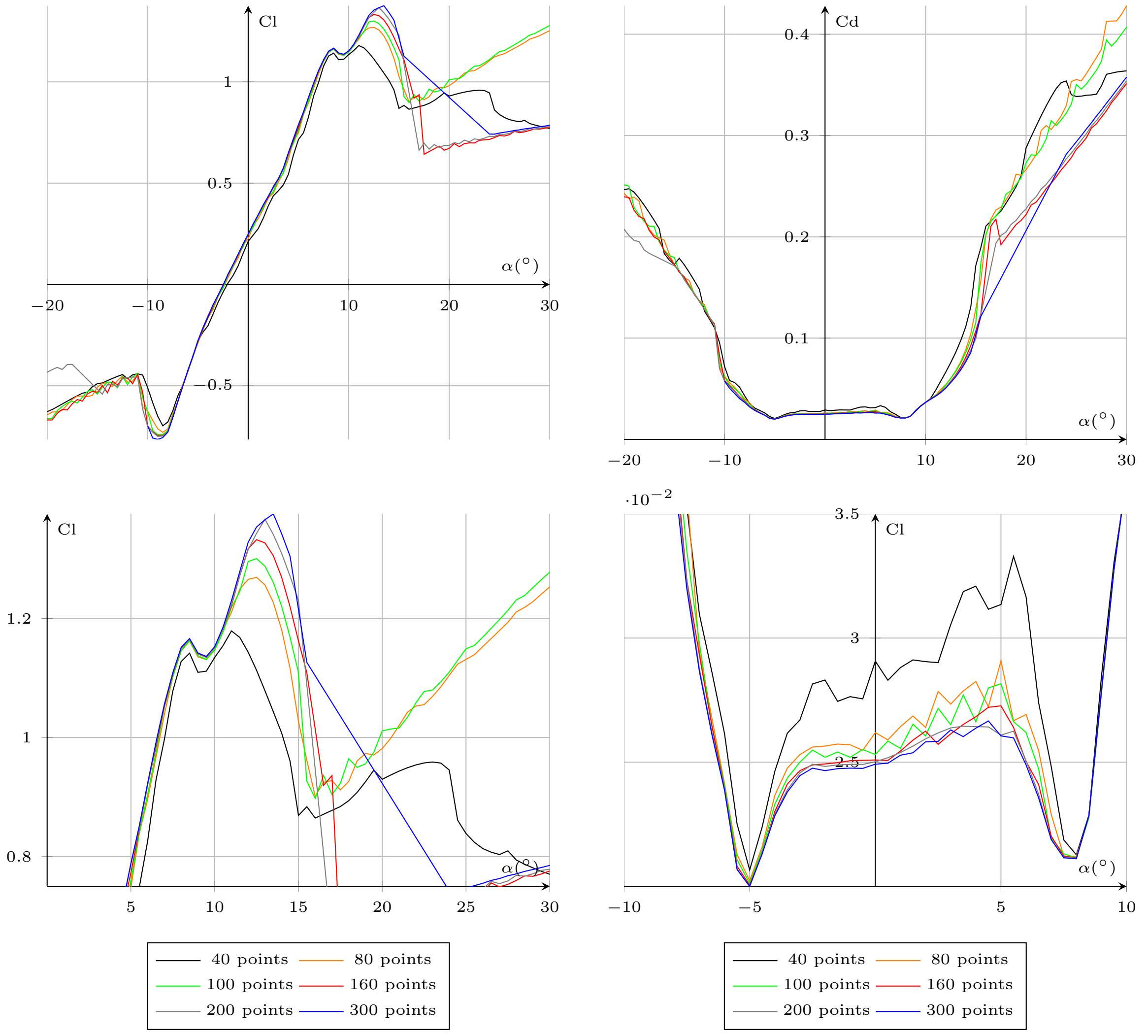

(a) Lift (b) Drag

Figure D.2: Sensitivity of lift and drag forces to geometry definition, NACA 63-415 section, $Re_c = 10^5$

The lift curves are showing that 40 points is not sufficient. Fluctuations can indeed be observed, as well as a global underestimation of lift. Maximum lift is therefore particularly underestimated. Between 80 and 300 points, the curves are very similar. However a slight increase of maximum lift is observed as the number of points increases. Passed stall, behaviors are very different between all the geometries, but this last statement must be linked to the inaccuracy of the model in predicting detached flows. For example convergence difficulties can be observed with the 300 points foil description. Indeed, a straight part is visible in the lift and drag curves, which comes from unconverted angles – between 15° and 24° AoA.

The drag trend leads to similar conclusions: 40 points is too low to correctly describe the flow. It can therefore be noticed that drag fluctuations are visible between -4° and 6° AoA, for foil refinement under 160 points.

$Re_c = 10^6$

Figures D.3 is illustrating the influence of the geometry definition at a medium Reynolds number value ($Re_c = 10^5$).

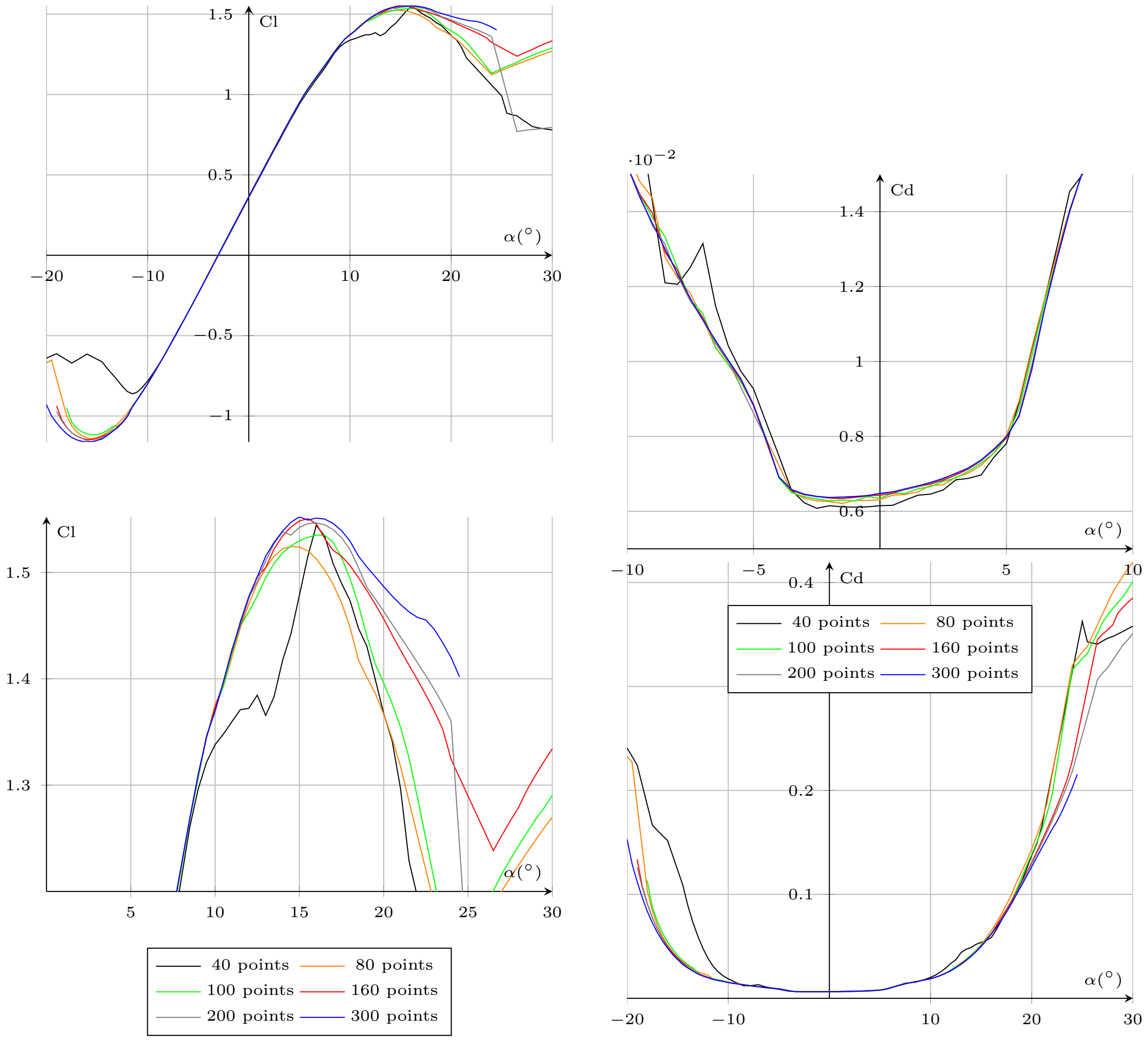

(a) Lift

(b) Drag

Figure D.3: Sensitivity of lift and drag forces to geometry definition, NACA 63-415 section, $Re_c = 10^6$

Figure D.3 shows that the influence of the number of points for geometry description is limited, particularly in the linear zone on both lift and drag. However, it slightly affects the value of maximum lift and its position. Indeed, it can be seen that under 40 points, there is a clear divergence of the maximum lift position and value. Between 80 and 300 points, most of the behavior is captured and curves are very similar, with however an increase of maximum lift with the number of points.

As for the lower Reynolds number value, prediction is messed-up by an inadequacy of the model to detached flows after stall.

$Re_c = 10^7$

Figure D.4 illustrates the influence of the number of points for the foil geometry description at a bigh Reynolds number value.

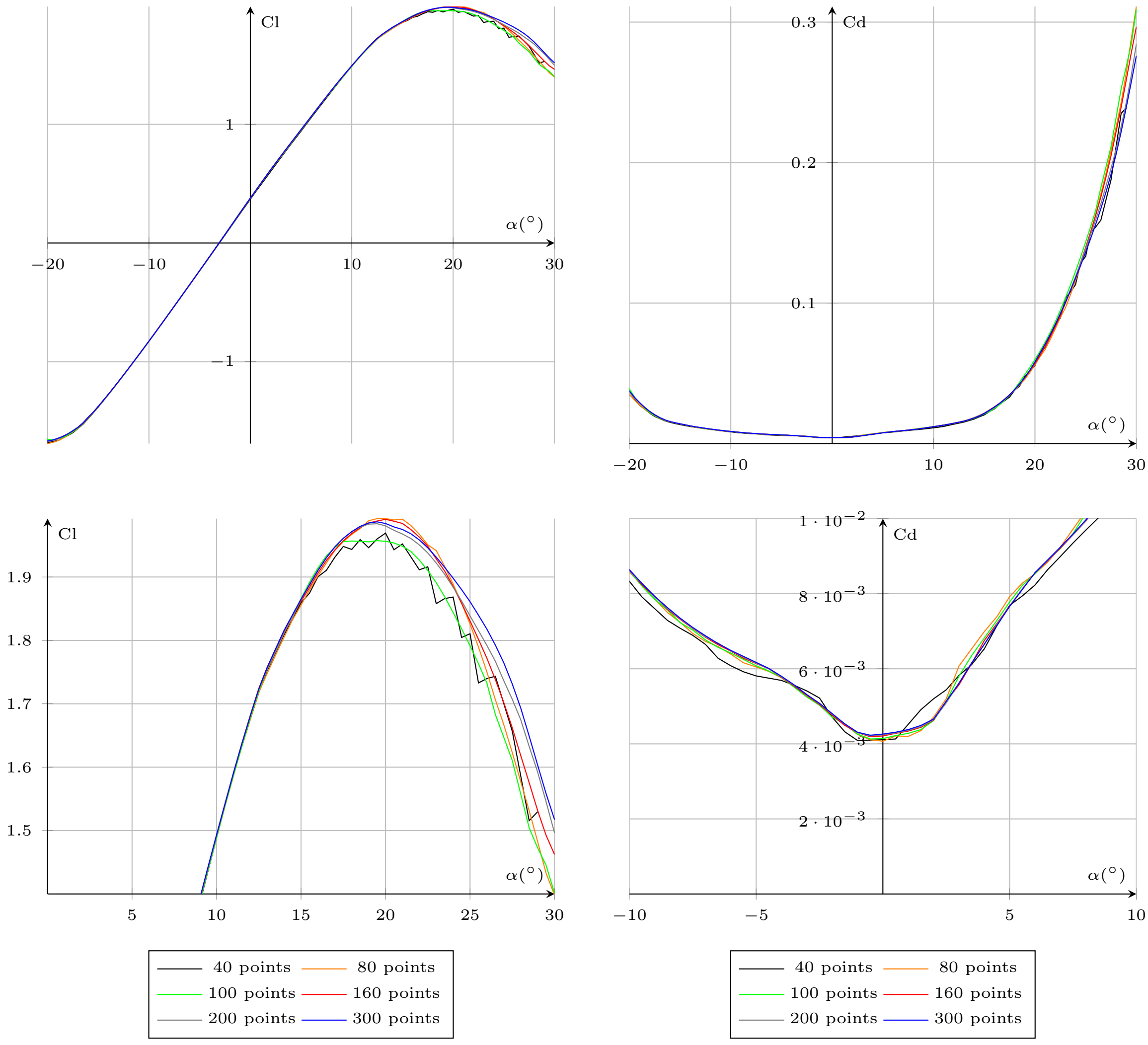

(a) Lift (b) Drag

Figure D.4: Sensitivity of lift and drag forces to geometry definition, NACA 63-415 section, $Re_c = 10^7$

The umber of points seems to have a limited impact as the Reynolds value increases. In that last case, very slight differences can be observed as the geometry refinement changes. The most coarsened geometry however shows discontinuities induced by convergence difficulties.

Summary

The minimum geometry requirement for foil properties calculation for an "all purpose" has been shown to be between 160 and 220 points. This seems to be a good compromise between CPU time and accuracy of results. This number of points is a guideline and must be adjusted to the foil's geometry.

D.3.2 Laminar/turbulent transition

As explained in the manual by Deperrois [2010], there are two methods for transition management in XFOIL.

The first can be called a free transition mode, where transition is triggered when a specified e^n criterion is reached. The second is forced transition for which a trip position or the trailing edge is encountered. They are simultaneously active, meaning that transition can occur before a specified trip, due to the e^n criterion.

The user can specify the e^n criterion through its exponent, called the N_{crit} in the code and thereafter. The value of this parameter must be adapted to the ambient turbulence in which the foil operates. It models the effect of such a turbulence on boundary layer transition.

As specified in the documentation, the default value for calculations with transition taken into account is set to $N_{crit} = 9$. A lower value can therefore be used for very early transition trigger, to model a fully turbulent kind of boundary layer.

The following study discusses the value to be chosen to properly approximate a fully turbulent boundary layer. The objective is to trigger turbulence as close as possible from the leading edge.

Several values have been tested between $N_{crit} = 1$ and $N_{crit} = 0$, using the NACA 63-415 foil at $Re_c = 10^6$, which is a standard value for tidal turbine blade applications.

Forces

Figure D.5 presents the lift and drag forces depending on the choice of the N_{crit} value and at a Reynolds number value of $Re_c = 10^6$. $N_{crit} = 9$, which correspond to the natural transition, is added for comparison.

It can be seen that change in the N_{crit} value does not much affect the linear behavior of the foil. However, it changes the value of maximum lift. It also slightly increases drag for relatively low angles of attack, as also stated by Drela [1989].

Note that for values of the factor lower than 0.5, there is no more visible evolution on both the lift and drag coefficients.

Position of the transition point

The position of the transition point along the chord on both the upper and lower faces of the foil may provide some additional information. This is plotted in Figure D.6

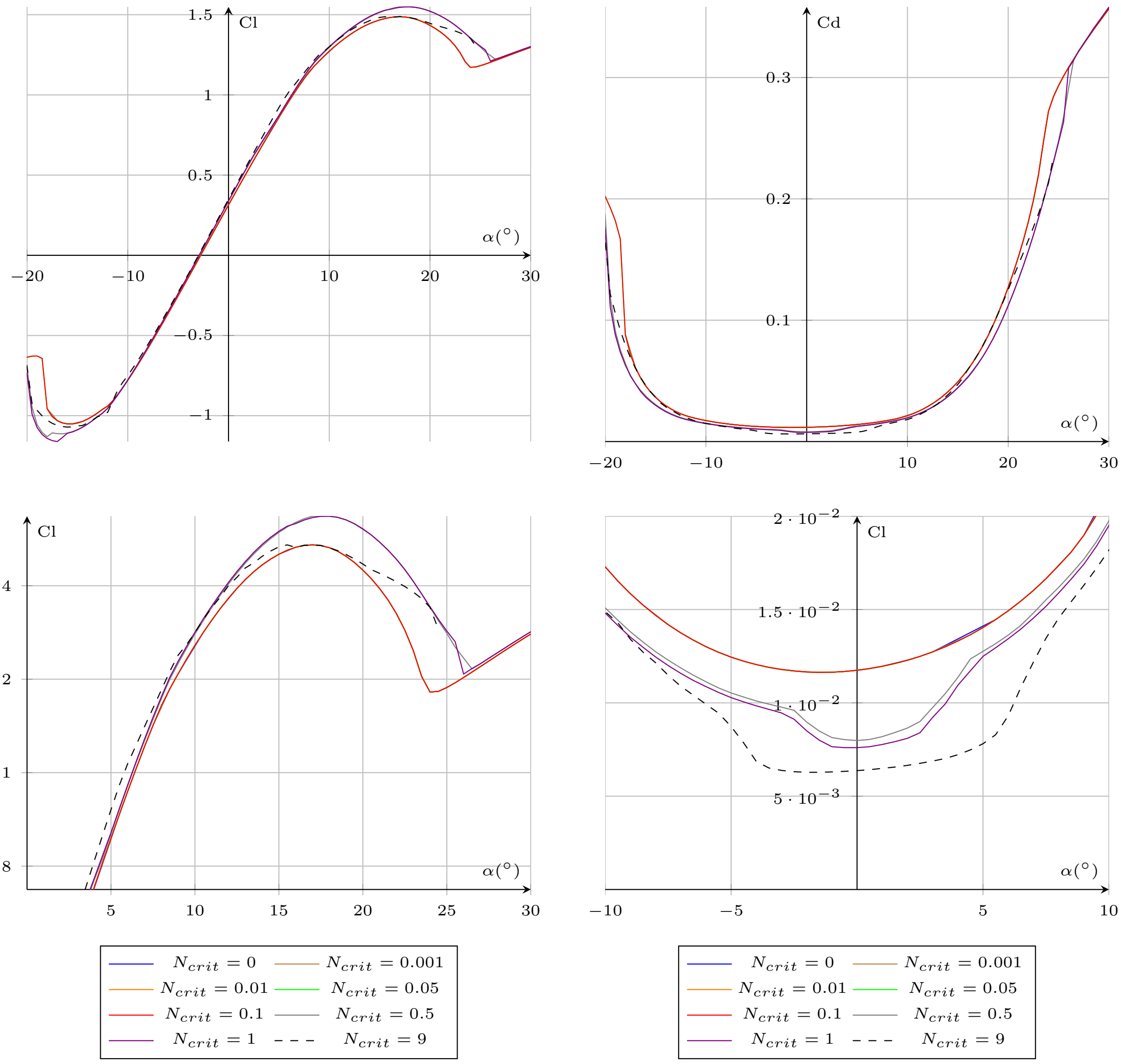

(a) Lift (b) Drag

Figure D.5: N_{crit} sensitivity, NACA 63-415 section, $Re_c = 10^6$

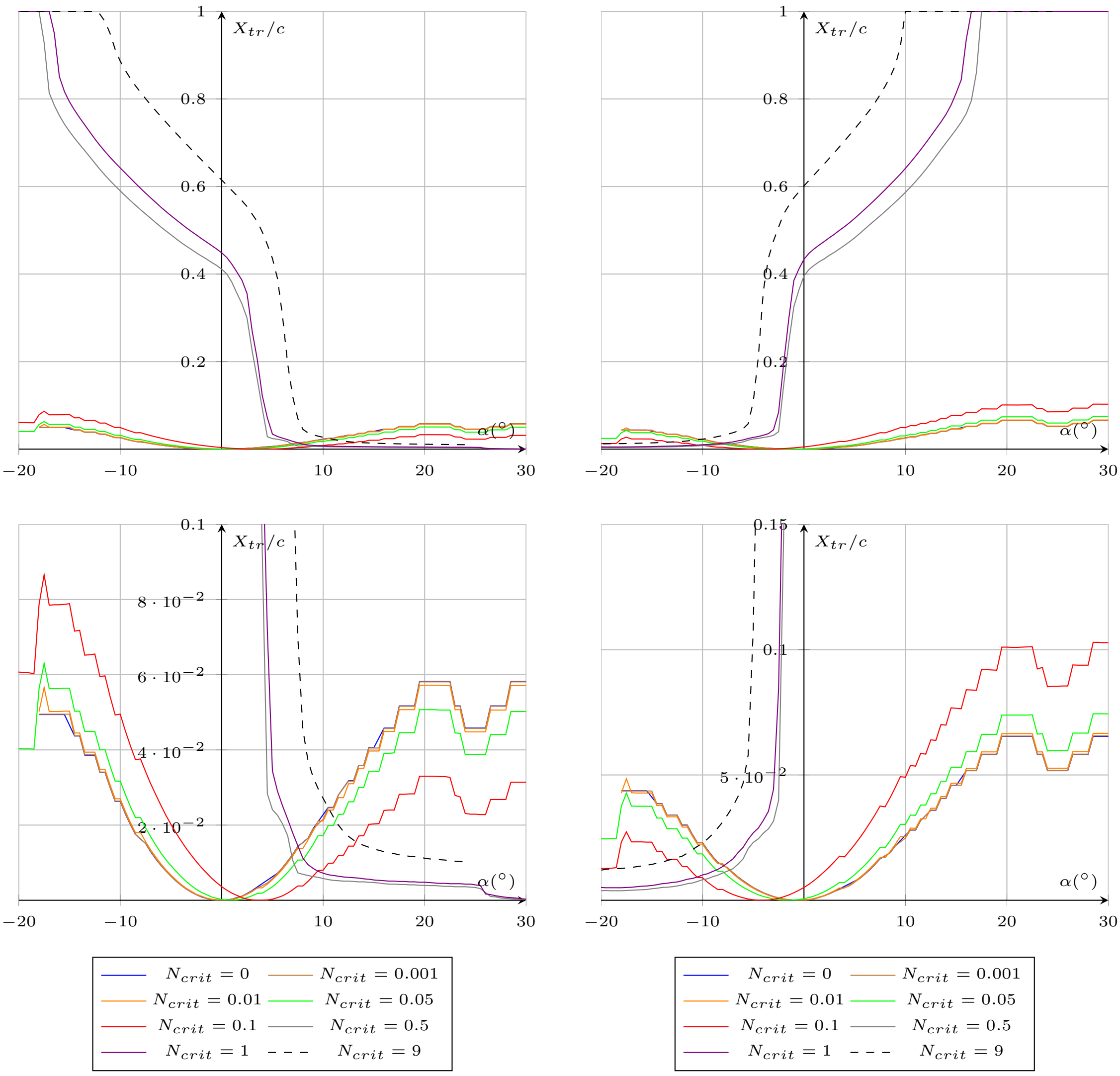

(a) Top face (b) Bottom face

Figure D.6: N_{crit} sensitivity, position of the transition point at the foil surface, NACA 63-415 section, $Re_c = 10^6$

To model a "fully turbulent" behavior, it is required to trigger transition closer to the leading edge.

For values between 9 and 0.5, transition reaches the trailing edge on both sides. There is however an evolution in this range of N_{crit} values, and as the N_{crit} decreases, the transition reaches the leading edge at lower angles of attack. For values lower than 0.5, there is a clear new kind of behavior. Transition therefore occurs "at most" before 10 % of the chord, meaning close to the leading edge. A value of 0.1 triggers transition before 10 % of the chord, and 0.05 before 7 %. N_{crit} values lower than 0.01 are triggering turbulence at very similar positions, even closer to the leading edge.

For N_{crit}<0.05, it can be considered as a fully turbulent calculation. However, transition is not occurring perfectly at 0 % of the chord (LE) because it follows the position of the stagnation point.

Summary

For calculations with transition taken into account, a N_{crit}=9 value is used. Adjustement can then be done for each case, according to the code documentation and real onsite conditions.

To model a fully turbulent behavior, requirements for earliest transition position are leading to N_{crit} values set between 0.01 and 0.05. This way transition occurs very close to the stagnation point and the boundary layer can be considered as fully turbulent.

Finally, for fully turbulent calculations, a quick comparison has been carried out between this method and by hand-triggered transition. Results are identical between both, but with substantial time saving in the case of the N_{crit} method.

D.3.3 Angle-step

Sensitivity of the results to the angle step is studied in this section. In practice, angle step has been observed to influence the convergence rate. Two Reynolds number are studied: $Re_c = 10^5$ and $Re_c = 10^6$.

$Re_c = 10^5$

The following figure (D.7) presents the influence of the angle step at a relatively low Reynolds number value ($Re_c = 10^5$).

At a Reynolds number value of $Re_c = 10^5$, the value assigned to the angle step has a limited effect on lift (Figure D.7). However, refinement obviously permits to more precisely locate the maximum lift position and, for the smallest angle step, oscillations can be observed in the lift curve. The post-stall behavior is predicted differently depending on the angle step, but mainly because it exceeds the domain of validation of the code.

The drag prediction is also slightly affected by the angle step choice. It can however be noticed that with an angle step of 0.05 small fluctuations are appearing.

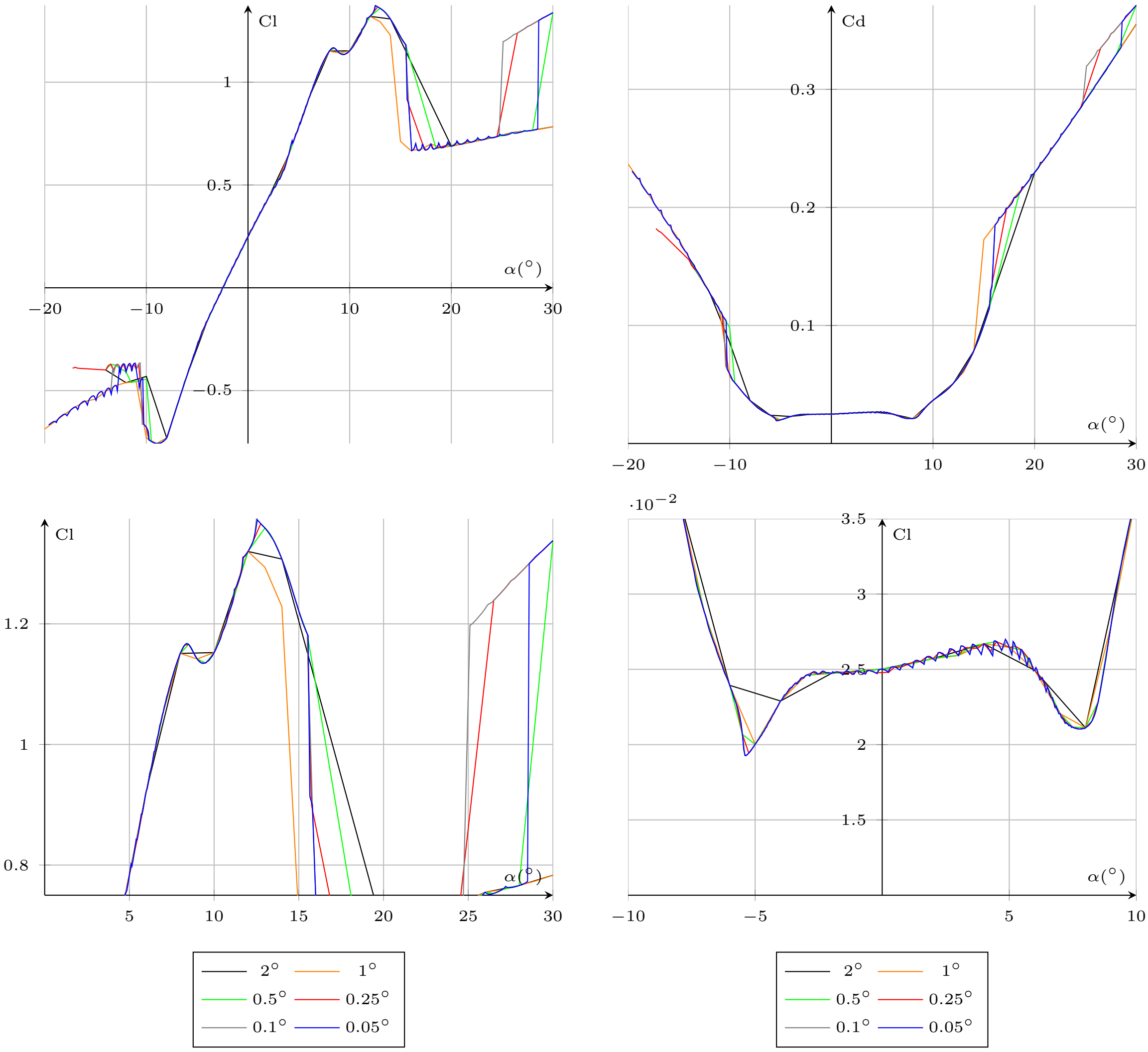

(a) Lift

(b) Drag

Figure D.7: Sensitivity of lift and drag forces to angle step, NACA 63-415 section, $Re_c = 10^5$

$Re_c = 10^6$

Figure D.8 is also illustrating angle step influence on results, but at a Reynolds number value of $Re_c = 10^6$.

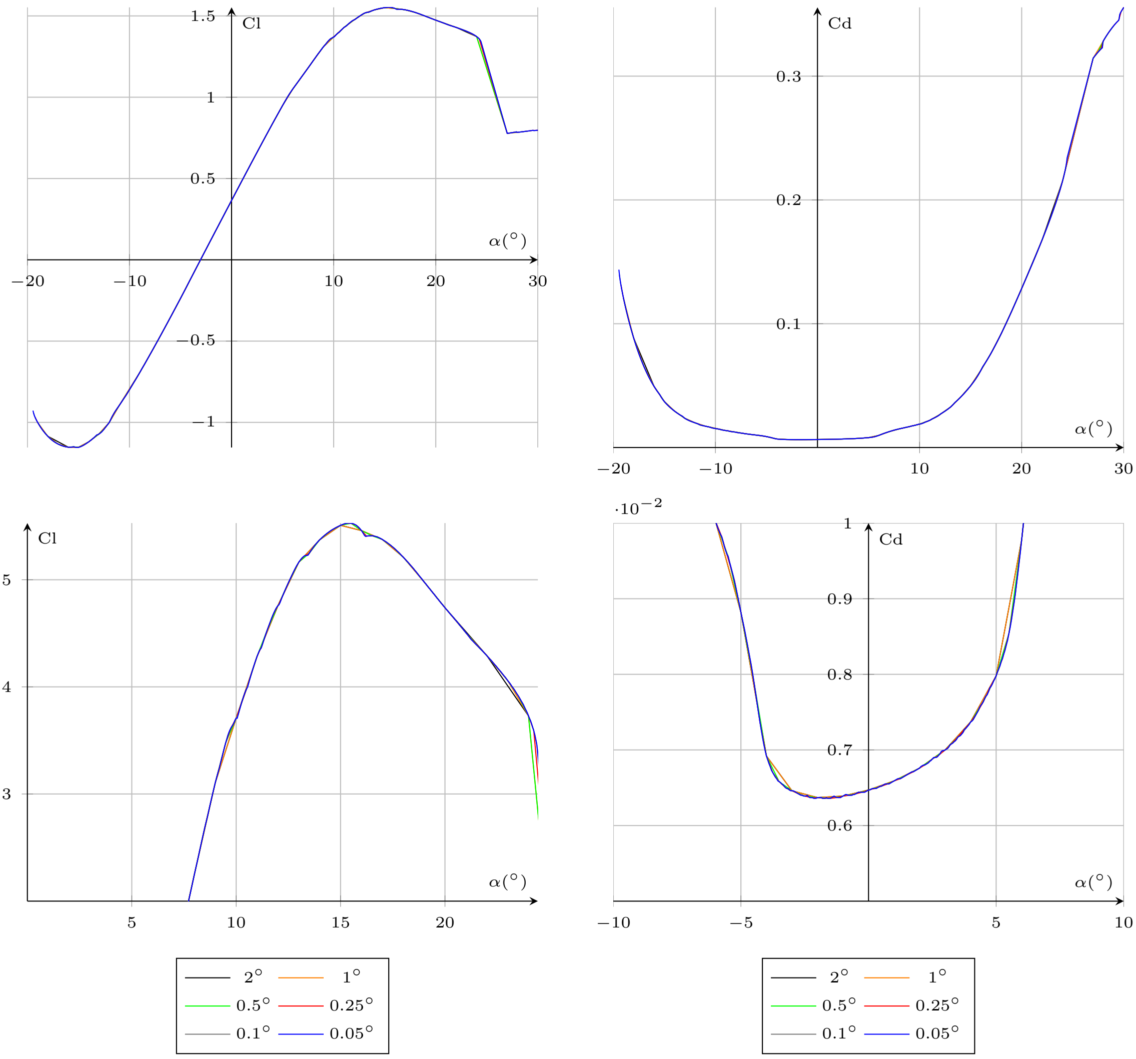

(a) Lift (b) Drag

Figure D.8: Sensitivity of the lift and drag forces to angle step, NACA 63-415 section, $Re_c = 10^6$

Figure D.8 shows that there is no effect of the refinement of the angle step on overall results. This is the case for both the lift and drag. As previously noticed for $Re_c = 10^5$, with the smallest angle step both curves tend to oscillate slightly.

Summary

Angle step has no influence on calculated results obtained with XFOIL. An angle step that is too small seems to induce small instabilities, at least. Yet, properly defined calculation geometry and parameters are preliminary requirements. The angle steps must be chosen according to the angular accuracy required by these results' foreseen application.

Moreover, refining the angle step also induces more iteration and more CPU time. More iterations also means more risk for the occurrence of an iteration that is not converged, which can make the polar calculation fail. This way, as angle step is refined, it is required to reinitialize the boundary layer to its default value after an unconverted iteration, to insure the overall polar convergence.

In practice it has also been experimented that a reduction of the angle step allows the facilitation of the overall result convergence, for certain specific geometries.

Finally, an angle step between 0.5° and 1° seems to be a compromise between the accuracy of the solution and the robustness of computations.

Appendix E

Raw data, experimental force measurements

This appendix provides the measured average force values for all the foil configurations studied under the framework of the present thesis. Measurements are not corrected for blockage effect.

E.1 NACA 0015, forward flow

E.1.1 Smooth

$Re_c = 5 \times 10^5$				$Re_c = 7.5 \times 10^5$			
$\alpha(^\circ)$	**Cl**	**Cd**	**Cm(1/4c)**	$\alpha(^\circ)$	**Cl**	**Cd**	**Cm(1/4c)**
0.0	0.0023	0.0103	0.0019	0.0	0.0043	0.0101	0.0013
1.0	0.1076	0.0120	0.0025	1.0	0.1109	0.0113	0.0008
2.0	0.2119	0.0135	0.0064	2.0	0.2195	0.0127	0.0001
4.0	0.4289	0.0178	0.0045	4.0	0.4398	0.0159	-0.0018
6.0	0.6944	0.0246	0.0158	6.0	0.6770	0.0219	0.0030
7.0	0.8121	0.0282	0.0171	7.0	0.8037	0.0254	0.0110
8.0	0.9034	0.0320	0.0106	8.0	0.9028	0.0281	0.0096
9.0	0.9938	0.0364	0.0040	9.0	1.0008	0.0319	0.0037
10.0	1.0580	0.0402	-0.0014	10.0	1.0755	0.0354	-0.0004
11.0	1.1217	0.0447	-0.0058	11.0	1.1609	0.0398	-0.0041
12.0	1.1945	0.0516	-0.0092	12.0	1.2246	0.0452	-0.0071
13.0	1.2324	0.0606	-0.0099	13.0	1.3046	0.0591	-0.0053
14.0	1.2451	0.0782	0.0008	14.0	1.3753	0.0928	-0.0023
15.0	1.2402	0.1011	0.0141	15.0	1.3788	0.1223	0.0005
16.0	1.2459	0.1240	0.0243	14.0	1.3816	0.0941	-0.0023
17.0	1.2241	0.1446	0.0316	13.0	1.3536	0.0656	-0.0025
18.0	1.2412	0.1721	0.0418	12.0	1.2429	0.0454	-0.0072
19.0	0.8331	0.3747	0.1119	11.0	1.1484	0.0396	-0.0037
20.0	0.8743	0.4094	0.1197	10.0	1.0715	0.0349	0.0000
19.0	0.8555	0.3847	0.1160	9.0	0.9927	0.0313	0.0042
18.0	0.8460	0.3609	0.1117	8.0	0.9197	0.0285	0.0102
17.0	0.8323	0.3305	0.1067	7.0	0.8251	0.0253	0.0123
16.0	0.8810	0.3108	0.1037	6.0	0.6808	0.0216	0.0042
15.0	0.9015	0.2738	0.0952	5.0	0.5686	0.0191	-0.0009
14.0	1.2930	0.0819	0.0023	4.0	0.4339	0.0158	-0.0008
13.0	1.2439	0.0602	-0.0098	3.0	0.3354	0.0144	0.0003
12.0	1.2067	0.0518	-0.0094	2.0	0.2236	0.0131	0.0010
11.0	1.1273	0.0451	-0.0059	1.0	0.1130	0.0114	0.0015
10.0	1.0551	0.0393	-0.0018	0.0	0.0016	0.0099	0.0022
9.0	0.9790	0.0355	0.0025	-1.0	-0.1041	0.0112	0.0023
8.0	0.9001	0.0322	0.0081	-2.0	-0.2076	0.0123	0.0036
7.0	0.8274	0.0281	0.0139	-4.0	-0.4266	0.0157	0.0063
6.0	0.7122	0.0250	0.0105	-6.0	-0.6540	0.0204	0.0020
5.0	0.5694	0.0219	0.0012	-7.0	-0.7904	0.0238	-0.0053
4.0	0.4338	0.0178	-0.0028	-8.0	-0.8909	0.0262	-0.0031
3.0	0.3291	0.0162	-0.0023	-9.0	-0.9471	0.0287	0.0037
2.0	0.2241	0.0145	-0.0008	-10.0	-1.0240	0.0325	0.0083
1.0	0.1136	0.0125	0.0000	-11.0	-1.1108	0.0368	0.0128
0.0	0.0072	0.0113	0.0013	-12.0	-1.1720	0.0419	0.0169
-1.0	-0.0974	0.0126	0.0028	-13.0	-1.1804	0.0471	0.0201
-2.0	-0.1986	0.0137	0.0050	-13.0	-1.2139	0.0485	0.0198
-4.0	-0.4020	0.0165	0.0084	-12.0	-1.1688	0.0408	0.0170
-6.0	-0.6754	0.0231	-0.0040	-11.0	-1.1107	0.0360	0.0129
-7.0	-0.7845	0.0261	-0.0067	-10.0	-1.0387	0.0319	0.0086
-8.0	-0.8610	0.0291	-0.0005	-9.0	-0.9634	0.0279	0.0040

$Re_c = 5 \times 10^5$				$Re_c = 7.5 \times 10^5$			
$\alpha(°)$	**Cl**	**Cd**	**Cm(1/4c)**	$\alpha(°)$	**Cl**	**Cd**	**Cm(1/4c)**
-9.0	-0.9401	0.0328	0.0055	-8.0	-0.8899	0.0250	-0.0028
-10.0	-1.0226	0.0375	0.0102	-7.0	-0.7889	0.0224	-0.0055
-11.0	-1.0637	0.0410	0.0144	-6.0	-0.6641	0.0194	0.0019
-12.0	-1.1333	0.0474	0.0185	-5.0	-0.5378	0.0167	0.0068
-13.0	-1.1665	0.0540	0.0221	-4.0	-0.4193	0.0140	0.0064
-14.0	-1.1861	0.0672	0.0180	-3.0	-0.3279	0.0130	0.0047
-15.0	-1.2148	0.0896	0.0046	-2.0	-0.2155	0.0118	0.0035
-16.0	-1.1859	0.1114	-0.0078	-1.0	-0.1095	0.0103	0.0024
-17.0	-1.1744	0.1348	-0.0183	0.0	0.0015	0.0092	0.0019
-18.0	-1.1741	0.1600	-0.0273				
-19.0	-1.1757	0.1899	-0.0391				
-20.0	-0.8120	0.3849	-0.1092				
-19.0	-0.8197	0.3719	-0.1087				
-18.0	-0.7976	0.3448	-0.1043				
-17.0	-0.7997	0.3200	-0.0991				
-16.0	-0.8154	0.2916	-0.0926				
-15.0	-0.9225	0.2638	-0.0852				
-14.0	-1.2376	0.0689	0.0181				
-13.0	-1.1907	0.0539	0.0229				
-12.0	-1.1352	0.0464	0.0188				
-11.0	-1.0708	0.0407	0.0147				
-10.0	-1.0185	0.0363	0.0105				
-9.0	-0.9382	0.0313	0.0058				
-8.0	-0.8516	0.0276	-0.0002				
-7.0	-0.7960	0.0253	-0.0066				
-6.0	-0.6888	0.0221	-0.0045				
-5.0	-0.5425	0.0186	0.0046				
-4.0	-0.4212	0.0153	0.0091				
-3.0	-0.3043	0.0133	0.0074				
-2.0	-0.2027	0.0124	0.0054				
-1.0	-0.1036	0.0109	0.0033				
0.0	0.0053	0.0098	0.0024				
0.0	0.0040	0.0217	0.0026				

E.1.2 Turbulent, roughness triggered

$Re_c = 5 \times 10^5$			
$\alpha(°)$	**Cl**	**Cd**	**Cm(1/4c)**
-0.1	-0.0135	0.0164	-0.0008
0.9	0.0885	0.0182	-0.0038
1.9	0.1929	0.0190	0.0001
3.9	0.4023	0.0216	-0.0024
5.9	0.6220	0.0269	-0.0017
7.9	0.8271	0.0332	-0.0008
8.9	0.9386	0.0376	-0.0037
9.9	1.0173	0.0436	-0.0086
10.9	1.0694	0.0519	-0.0150
11.9	1.0548	0.0626	-0.0155
12.9	1.0404	0.0937	0.0101
13.9	1.0493	0.1270	0.0291
14.9	1.0451	0.1504	0.0382
15.9	1.0469	0.1717	0.0453
16.9	0.7901	0.3110	0.0985
17.9	0.8392	0.3576	0.1096
18.9	0.8633	0.3879	0.1153
19.9	0.8786	0.4130	0.1185
18.9	0.8705	0.3908	0.1166
17.9	0.8521	0.3632	0.1111
16.9	0.8460	0.3342	0.1052
15.9	0.8802	0.3081	0.1035
14.9	1.0972	0.1583	0.0421
13.9	1.0587	0.1305	0.0299
12.9	1.0742	0.0963	0.0106
11.9	1.0594	0.0630	-0.0154
10.9	1.0626	0.0521	-0.0157
9.9	0.9958	0.0419	-0.0097
8.9	0.9213	0.0371	-0.0055
7.9	0.8213	0.0335	-0.0039
5.9	0.6410	0.0282	-0.0059
3.9	0.4135	0.0226	-0.0079
1.9	0.1984	0.0196	-0.0061
0.9	0.0874	0.0176	-0.0053
-0.1	-0.0148	0.0176	-0.0052
-1.1	-0.1189	0.0185	-0.0026
-2.1	-0.2185	0.0196	-0.0009
-4.1	-0.4244	0.0221	0.0011
-6.1	-0.6175	0.0261	0.0030
-8.1	-0.8187	0.0325	0.0048
-9.1	-0.9185	0.0357	0.0055
-10.1	-1.0050	0.0394	0.0076
-11.1	-1.0558	0.0448	0.0125
-12.1	-1.0861	0.0531	0.0187
-13.1	-1.1009	0.0665	0.0165
-14.1	-1.1161	0.0901	0.0019
-15.1	-1.1070	0.1137	-0.0122
-16.1	-1.0919	0.1355	-0.0219
-17.1	-1.0795	0.1602	-0.0333
-18.1	-0.7297	0.3154	-0.0984
-19.1	-0.8190	0.3718	-0.1126
-20.1	-0.8434	0.3989	-0.1167

$Re_c = 5 \times 10^5$			
$\alpha(^\circ)$	**Cl**	**Cd**	**Cm(1/4c)**
-19.1	-0.8455	0.3827	-0.1156
-18.1	-0.8041	0.3466	-0.1084
-17.1	-0.8046	0.3222	-0.1036
-16.1	-0.8569	0.2945	-0.0979
-15.1	-1.1731	0.1210	-0.0147
-14.1	-1.1248	0.0913	-0.0002
-13.1	-1.1189	0.0675	0.0156
-12.1	-1.0881	0.0524	0.0187
-11.1	-1.0509	0.0446	0.0123
-10.1	-1.0011	0.0383	0.0076
-9.1	-0.9208	0.0346	0.0056
-8.1	-0.8336	0.0319	0.0046
-6.1	-0.6315	0.0257	0.0027
-4.1	-0.4347	0.0210	0.0010
-2.1	-0.2224	0.0189	-0.0012
-1.1	-0.1213	0.0171	-0.0025
-0.1	-0.0152	0.0164	-0.0051

E.2 NACA 0015, reversed flow

E.2.1 Smooth

$Re_c = 5 \times 10^5$			
$\alpha(^\circ)$	**Cl**	**Cd**	**Cm(1/4c)**
0.86	0.3066	0.0364	0.0932
1.11	0.3280	0.0371	0.1073
1.36	0.3559	0.0391	0.1236
1.61	0.3833	0.0396	0.1373
1.86	0.4108	0.0405	0.1511
2.86	0.5224	0.0446	0.2062
2.86	0.5224	0.0446	0.2062
4.86	0.7284	0.0587	0.3207
6.86	0.8983	0.0824	0.4207
8.86	1.0189	0.1223	0.4838
10.86	1.0505	0.1837	0.4845
12.86	0.9737	0.2454	0.4352
14.86	0.9044	0.3038	0.4006
12.86	1.0075	0.2548	0.4512
10.86	1.0924	0.1906	0.5047
8.86	1.0717	0.1290	0.5105
6.86	0.9388	0.0857	0.4415
4.86	0.7368	0.0593	0.3250
2.86	0.5344	0.0458	0.2118
1.86	0.4196	0.0415	0.1515
1.61	0.3914	0.0402	0.1380
1.36	0.3660	0.0395	0.1253
1.11	0.3384	0.0388	0.1109
0.86	0.3103	0.0381	0.0971
0.61	0.2817	0.0369	0.0843
0.36	0.2596	0.0364	0.0721
0.36	0.2552	0.0360	0.0779
0.11	0.2385	0.0361	0.0603
-0.14	0.2155	0.0355	0.0481
-1.14	-0.3193	0.0383	-0.1170
-3.14	-0.5108	0.0482	-0.2215
-5.14	-0.6952	0.0659	-0.3283
-7.14	-0.8711	0.0959	-0.4318
-9.14	-0.9631	0.1374	-0.4824
-11.14	-0.9570	0.1925	-0.4632
-13.14	-0.8920	0.2511	-0.4204
-11.14	-0.9877	0.1997	-0.4776
-9.14	-0.9938	0.1418	-0.4968
-7.14	-0.8789	0.0961	-0.4367
-5.14	-0.7090	0.0666	-0.3362
-3.14	-0.5099	0.0473	-0.2235
-1.14	-0.3292	0.0379	-0.1235
-0.14	-0.2354	0.0354	-0.0740
0.11	-0.2151	0.0346	-0.0627
0.36	0.2693	0.0365	0.0715
0.36	0.2650	0.0360	0.0772
0.61	0.2954	0.0371	0.0849
0.86	0.3170	0.0371	0.0953
0.86	0.3102	0.0371	0.0931
0.61	0.2864	0.0362	0.0822
0.36	0.2607	0.0360	0.0700
0.36	0.2564	0.0355	0.0758
0.11	0.2382	0.0358	0.0580
-0.14	0.1987	0.0349	0.0422
-0.39	-0.2472	0.0351	-0.0750
-0.64	-0.2857	0.0372	-0.0917
-0.89	-0.3074	0.0378	-0.1034
-1.14	-0.3233	0.0384	-0.1199
-1.14	-0.3249	0.0380	-0.1218
-0.89	-0.3082	0.0370	-0.1045
-0.64	-0.2844	0.0365	-0.0923
-0.39	-0.2608	0.0359	-0.0802
-0.14	-0.2369	0.0359	-0.0741

$Re_c = 5 \times 10^5$			
$\alpha(^\circ)$	**Cl**	**Cd**	**Cm(1/4c)**
0.11	-0.2166	0.0352	-0.0625
0.36	0.2647	0.0360	0.0702
0.36	0.2603	0.0355	0.0759
0.61	0.2887	0.0364	0.0828
0.86	0.3145	0.0374	0.0947
0.36	0.2716	0.0364	0.0725
0.36	0.2672	0.0359	0.0783
0.26	0.2497	0.0357	0.0716
0.16	0.2369	0.0355	0.0658
0.06	0.2272	0.0350	0.0610
-0.04	0.2126	0.0345	0.0547
-0.14	0.2041	0.0346	0.0432
-0.24	0.1864	0.0339	0.0423
-0.34	-0.2554	0.0354	-0.0755
-0.44	-0.2631	0.0359	-0.0804
-0.54	-0.2764	0.0370	-0.0865
-0.64	-0.2845	0.0372	-0.0909
-0.64	-0.2678	0.0358	-0.0875
-0.54	-0.2790	0.0366	-0.0879
-0.44	-0.2673	0.0366	-0.0826
-0.34	-0.2601	0.0355	-0.0779
-0.24	-0.2501	0.0354	-0.0730
-0.14	-0.2171	0.0349	-0.0683
-0.04	-0.2142	0.0337	-0.0587
0.06	-0.2042	0.0329	-0.0533
0.16	-0.1882	0.0327	-0.0473
0.26	-0.1887	0.0322	-0.0445
0.36	0.2615	0.0360	0.0702
0.36	0.2571	0.0355	0.0760

E.2.2 Turbulent, roughness triggered

$Re_c = 5 \times 10^5$			
$\alpha(^\circ)$	**Cl**	**Cd**	**Cm(1/4c)**
-0.375	-0.0275	0.0250	-0.0196
0.125	0.0036	0.0250	0.0057
0.625	0.0372	0.0247	0.0258
1.125	0.0696	0.0250	0.0445
1.625	0.1063	0.0257	0.0659
3.625	0.2723	0.0292	0.1597
5.625	0.5572	0.0524	0.2914
7.625	0.9330	0.0937	0.4521
8.625	1.0228	0.1164	0.4925
9.625	1.0706	0.1432	0.5096
10.625	1.0919	0.1765	0.5105
11.625	1.0535	0.2076	0.4828
13.625	0.9682	0.2707	0.4341
15.625	0.9121	0.3264	0.4113
17.625	0.9090	0.3801	0.4192
19.625	0.9402	0.4436	0.4453
17.625	0.9465	0.3972	0.4359
15.625	0.9221	0.3329	0.4158
13.625	0.9839	0.2761	0.4411
11.625	1.0810	0.2156	0.4956
10.625	1.0992	0.1793	0.5146
9.625	1.1025	0.1486	0.5256
8.625	1.0306	0.1175	0.4970
7.625	0.9374	0.0942	0.4581
5.625	0.5684	0.0536	0.3076
3.625	0.2821	0.0296	0.1688
1.625	0.1147	0.0261	0.0739
1.125	0.0800	0.0262	0.0523
0.625	0.0459	0.0255	0.0312
0.125	0.0110	0.0254	0.0107
-0.375	-0.0169	0.0260	-0.0091
-0.875	-0.0540	0.0259	-0.0298
-1.375	-0.0893	0.0257	-0.0514
-1.875	-0.1245	0.0262	-0.0725
-2.375	-0.1622	0.0266	-0.0938
-4.375	-0.2482	0.0370	-0.1430
-4.375	-0.3739	0.0376	-0.2000
-6.375	-0.5947	0.0563	-0.3323
-6.375	-0.6679	0.0668	-0.3385
-8.375	-0.9000	0.1049	-0.4455
-9.375	-0.9849	0.1308	-0.4828
-10.375	-1.0145	0.1601	-0.4851
-11.375	-1.0198	0.1937	-0.4763
-12.375	-1.0041	0.2279	-0.4600
-14.375	-0.9288	0.2833	-0.4166
-16.375	-0.9063	0.3424	-0.4081
-18.375	-0.9019	0.3940	-0.4138
-20.375	-0.9558	0.4656	-0.4464
-18.375	-0.9004	0.3926	-0.4122
-16.375	-0.9258	0.3513	-0.4174
-14.375	-0.9589	0.2960	-0.4317
-12.375	-1.0250	0.2320	-0.4692
-11.375	-1.0336	0.1969	-0.4811
-10.375	-1.0397	0.1637	-0.4949
-9.375	-0.9929	0.1321	-0.4846
-8.375	-0.9328	0.1075	-0.4608

$Re_c = 5 \times 10^5$			
$\alpha(^\circ)$	**Cl**	**Cd**	**Cm(1/4c)**
-6.375	-0.6768	0.0663	-0.3433
-4.375	-0.3962	0.0384	-0.2128
-2.375	-0.1744	0.0258	-0.1024
-1.875	-0.1327	0.0253	-0.0804
-1.375	-0.0991	0.0251	-0.0598
-0.875	-0.0674	0.0245	-0.0392
-0.375	-0.0315	0.0247	-0.0173

E.3 Elliptical foil

E.3.1 Smooth

$Re_c = 5 \times 10^5$				$Re_c = 7.5 \times 10^5$			
$\alpha(^\circ)$	**Cl**	**Cd**	**Cm(1/4c)**	$\alpha(^\circ)$	**Cl**	**Cd**	**Cm(1/4c)**
0.55	0.2802	0.0264	-0.0233	0.55	0.1940	0.0220	-0.0064
1.55	0.4007	0.0275	-0.0269	1.55	0.3235	0.0250	-0.0123
2.55	0.5408	0.0299	-0.0371	2.55	0.4248	0.0268	-0.0123
4.55	0.7410	0.0352	-0.0324	4.55	0.6421	0.0320	-0.0143
6.55	0.9106	0.0405	-0.0243	6.55	0.8424	0.0366	-0.0159
8.55	1.0323	0.0491	-0.0084	6.55	0.8424	0.0366	-0.0159
10.55	1.1043	0.0605	0.0138	8.55	1.0216	0.0454	-0.0070
12.55	1.1149	0.0751	0.0385	10.55	1.1180	0.0613	0.0092
14.55	1.0132	0.1199	0.0363	12.55	1.2417	0.0936	0.0187
16.55	0.9757	0.2929	-0.0279	12.55	1.2417	0.0936	0.0187
18.55	0.9135	0.3851	-0.0451	14.55	1.2122	0.1506	0.0333
20.55	0.8562	0.4381	-0.0470	12.55	1.2346	0.0935	0.0185
18.55	0.9524	0.3952	-0.0453	10.55	1.1109	0.0576	0.0120
16.55	1.0653	0.3137	-0.0260	8.55	1.0158	0.0453	-0.0066
14.55	1.0483	0.1247	0.0379	6.55	0.8729	0.0371	-0.0157
12.55	1.1256	0.0766	0.0384	6.55	0.8729	0.0371	-0.0157
10.55	1.1137	0.0611	0.0140	4.55	0.6472	0.0318	-0.0137
8.55	1.0349	0.0498	-0.0084	2.55	0.4290	0.0269	-0.0120
6.55	0.9096	0.0406	-0.0242	1.55	0.3130	0.0247	-0.0081
4.55	0.7431	0.0355	-0.0324	0.55	0.1980	0.0214	-0.0083
2.55	0.5590	0.0316	-0.0375	-0.45	0.0641	0.0207	-0.0017
1.55	0.4468	0.0285	-0.0370	-1.45	-0.0958	0.0232	0.0126
0.55	0.2821	0.0272	-0.0237	-3.45	-0.3842	0.0276	0.0279
-1.45	-0.0589	0.0270	0.0042	-5.45	-0.6081	0.0343	0.0339
-1.70	-0.1126	0.0281	0.0096	-7.45	-0.8047	0.0596	0.0259
-1.95	-0.1593	0.0285	0.0164	-9.45	-0.8732	0.0977	0.0053
-2.20	-0.2175	0.0294	0.0246	-11.45	-0.9554	0.1643	0.0182
-2.45	-0.2829	0.0290	0.0353	-11.45	-0.9554	0.1643	0.0182
-2.70	-0.3926	0.0270	0.0544	-13.45	-0.9356	0.2403	0.0500
-2.95	-0.4126	0.0265	0.0516	-11.45	-1.0053	0.1714	0.0184
-3.20	-0.4277	0.0279	0.0489	-11.45	-1.0053	0.1714	0.0184
-3.45	-0.4405	0.0287	0.0492	-9.45	-0.9140	0.1015	0.0048
-5.45	-0.5912	0.0351	0.0412	-7.45	-0.8030	0.0588	0.0251
-5.45	-0.5912	0.0351	0.0412	-5.45	-0.6172	0.0338	0.0330
-7.45	-0.7408	0.0571	0.0313	-3.45	-0.3868	0.0266	0.0271
-9.45	-0.8484	0.0995	0.0159	-1.45	-0.1075	0.0233	0.0131
-11.45	-0.8787	0.1633	0.0346	-0.45	0.0604	0.0206	-0.0028
-13.45	-0.8342	0.2319	0.0637	0.55	0.2018	0.0211	-0.0115
-11.45	-0.8854	0.1646	0.0353				
-9.45	-0.8498	0.0995	0.0156				
-7.45	-0.7659	0.0586	0.0323				
-5.45	-0.6080	0.0350	0.0418				
-5.45	-0.6080	0.0350	0.0418				
-3.45	-0.4494	0.0278	0.0494				
-3.20	-0.4277	0.0279	0.0489				
-2.95	-0.4126	0.0265	0.0516				
-2.70	-0.3926	0.0270	0.0544				
-2.45	-0.2829	0.0290	0.0353				
-2.20	-0.2175	0.0294	0.0246				
-1.95	-0.1593	0.0285	0.0164				
-1.70	-0.1126	0.0281	0.0096				
-1.45	-0.0667	0.0263	0.0050				
0.55	0.2708	0.0259	-0.0241				
-0.45	0.1288	0.0273	-0.0184				
-1.45	-0.0599	0.0265	0.0023				
-1.70	-0.1126	0.0281	0.0096				
-1.95	-0.1593	0.0285	0.0164				
-2.20	-0.2175	0.0294	0.0246				
-2.45	-0.2829	0.0290	0.0353				
-2.70	-0.3926	0.0270	0.0544				
-2.95	-0.4126	0.0265	0.0516				
-3.20	-0.4277	0.0279	0.0489				
-3.45	-0.4455	0.0284	0.0487				
-5.45	-0.6036	0.0352	0.0412				
-5.45	-0.6036	0.0352	0.0412				
-3.45	-0.4524	0.0282	0.0488				
-3.20	-0.4323	0.0279	0.0491				
-2.95	-0.4212	0.0268	0.0518				
-2.70	-0.4057	0.0269	0.0563				
-2.45	-0.3086	0.0290	0.0399				
-2.20	-0.2257	0.0288	0.0257				
-1.95	-0.1771	0.0283	0.0190				
-1.70	-0.1218	0.0277	0.0113				

$Re_c = 5 \times 10^5$				$Re_c = 7.5 \times 10^5$			
$\alpha(^\circ)$	**Cl**	**Cd**	**Cm(1/4c)**	**$\alpha(^\circ)$**	**Cl**	**Cd**	**Cm(1/4c)**
-1.45	-0.0680	0.0267	0.0041				
-0.45	0.1188	0.0271	-0.0172				

E.3.2 Turbulent, roughness triggered

Note that in that case, the RT2 turbulence triggering roughness was used instead of the RT3 that was used on the other "fully turbulent" configurations.

$Re_c = 5 \times 10^5$				$Re_c = 7.5 \times 10^5$			
$\alpha(^\circ)$	**Cl**	**Cd**	**Cm(1/4c)**	**$\alpha(^\circ)$**	**Cl**	**Cd**	**Cm(1/4c)**
0.00	0.0946	0.0277	0.0085	0.00	0.0916	0.0265	0.0089
1.00	0.1709	0.0288	0.0173	1.00	0.1657	0.0282	0.0161
2.00	0.2378	0.0298	0.0253	2.00	0.2471	0.0310	0.0244
4.00	0.3747	0.0337	0.0427	4.00	0.3874	0.0342	0.0388
6.00	0.5023	0.0397	0.0606	6.00	0.5067	0.0400	0.0544
8.00	0.5985	0.0487	0.0772	8.00	0.6030	0.0491	0.0692
10.00	0.6926	0.0626	0.0957	10.00	0.6793	0.0637	0.0844
12.00	0.6849	0.0812	0.1092	12.00	0.7498	0.0870	0.0933
14.00	0.5897	0.1747	0.0660	14.00	0.6683	0.1663	0.0624
16.00	0.5385	0.2177	0.0676	16.00	0.6077	0.2287	0.0534
18.00	0.5840	0.2593	0.0614	18.00	0.5749	0.2703	0.0551
20.00	0.7744	0.3795	0.0153	16.00	0.6304	0.2362	0.0522
18.00	0.6166	0.2733	0.0639	14.00	0.6835	0.1744	0.0638
16.00	0.5500	0.2216	0.0681	12.00	0.7705	0.0932	0.0917
14.00	0.6047	0.1822	0.0681	10.00	0.6814	0.0701	0.0832
12.00	0.7143	0.0843	0.1132	8.00	0.5917	0.0544	0.0709
10.00	0.7031	0.0639	0.0976	6.00	0.4957	0.0433	0.0566
8.00	0.6218	0.0511	0.0804	4.00	0.4002	0.0374	0.0420
6.00	0.5138	0.0412	0.0631	2.00	0.2421	0.0322	0.0259
4.00	0.3811	0.0340	0.0446	1.00	0.1674	0.0302	0.0188
2.00	0.2472	0.0318	0.0285	0.00	0.0937	0.0283	0.0111
1.00	0.1702	0.0291	0.0198	-1.00	0.0190	0.0279	0.0049
0.00	0.0969	0.0282	0.0120	-2.00	-0.0600	0.0274	-0.0010
-1.00	0.0207	0.0268	0.0042	-4.00	-0.2100	0.0306	-0.0131
-2.00	-0.0600	0.0274	-0.0006	-6.00	-0.3641	0.0363	-0.0248
-4.00	-0.2147	0.0302	-0.0094	-8.00	-0.5028	0.0443	-0.0356
-6.00	-0.3595	0.0348	-0.0192	-12.00	-0.7367	0.1280	-0.0364
-8.00	-0.5138	0.0430	-0.0295	-14.00	-0.7527	0.2065	-0.0038
-10.00	-0.6483	0.0533	-0.0361	-12.00	-0.7781	0.1352	-0.0381
-12.00	-0.7707	0.1387	-0.0175	-10.00	-0.6479	0.0565	-0.0475
-14.00	-0.7600	0.2135	0.0178	-8.00	-0.5117	0.0440	-0.0363
-12.00	-0.7851	0.1412	-0.0180	-10.00	-0.6414	0.0568	-0.0471
-10.00	-0.6608	0.0539	-0.0368	-8.00	-0.5063	0.0438	-0.0361
-8.00	-0.5231	0.0421	-0.0293	-6.00	-0.3716	0.0356	-0.0249
-6.00	-0.3777	0.0356	-0.0198	-4.00	-0.2253	0.0312	-0.0140
-4.00	-0.2247	0.0299	-0.0097	-2.00	-0.0612	0.0262	-0.0015
-2.00	-0.0635	0.0277	-0.0006	-1.00	0.0132	0.0270	0.0043
-1.00	0.0127	0.0268	0.0037	0.00	0.0923	0.0290	0.0109
0.00	0.0931	0.0283	0.0114				

E.4 DU 91-W2-250

E.4.1 Smooth (RS1)

$Re_c = 5 \times 10^5$				$Re_c = 7.5 \times 10^5$			
$\alpha(^\circ)$	**Cl**	**Cd**	**Cm(1/4c)**	**$\alpha(^\circ)$**	**Cl**	**Cd**	**Cm(1/4c)**
0.00	0.4002	0.0217	-0.1331	0.00	0.4136	0.0195	-0.1321
1.00	0.5314	0.0240	-0.1333	1.00	0.5485	0.0218	-0.1328
2.00	0.6550	0.0264	-0.1314	2.00	0.6646	0.0236	-0.1311
4.00	0.8859	0.0346	-0.1316	4.00	0.9081	0.0297	-0.1302
6.00	1.1033	0.0438	-0.1334	6.00	1.1637	0.0359	-0.1297
8.00	1.3542	0.0555	-0.1369	8.00	1.4520	0.0481	-0.1320
9.00	1.4625	0.0610	-0.1365	9.00	1.5549	0.0546	-0.1293
10.00	1.5559	0.0685	-0.1357	10.00	1.6488	0.0626	-0.1247
11.00	1.6060	0.0745	-0.1307	11.00	1.6378	0.0705	-0.1158
12.00	1.6557	0.0852	-0.1258	12.00	1.5877	0.0997	-0.1239
13.00	1.5877	0.1109	-0.1308	13.00	1.4854	0.1153	-0.1214
14.00	1.5011	0.1295	-0.1298	14.00	1.4241	0.1311	-0.1210
15.00	1.4509	0.1453	-0.1275	15.00	1.4398	0.1526	-0.1244
16.00	1.4614	0.1659	-0.1312	16.00	1.4234	0.1691	-0.1257
17.00	1.4479	0.1839	-0.1332	16.00	1.4219	0.1688	-0.1259
18.00	1.4712	0.2061	-0.1382	15.00	1.4527	0.1532	-0.1259
19.00	1.4605	0.2243	-0.1415	14.00	1.4680	0.1346	-0.1244
20.00	1.5020	0.2516	-0.1497	13.00	1.5168	0.1184	-0.1241

$Re_c = 5 \times 10^5$				$Re_c = 7.5 \times 10^5$			
$\alpha(^\circ)$	**Cl**	**Cd**	**Cm(1/4c)**	$\alpha(^\circ)$	**Cl**	**Cd**	**Cm(1/4c)**
19.00	1.4871	0.2292	-0.1445	12.00	1.5638	0.0966	-0.1224
18.00	1.4674	0.2054	-0.1393	11.00	1.6680	0.0728	-0.1185
17.00	1.4870	0.1893	-0.1371	10.00	1.6463	0.0608	-0.1241
16.00	1.4825	0.1682	-0.1334	9.00	1.5563	0.0518	-0.1285
15.00	1.4955	0.1487	-0.1332	8.00	1.4677	0.0461	-0.1322
14.00	1.5312	0.1321	-0.1335	6.00	1.2124	0.0344	-0.1332
13.00	1.6026	0.1119	-0.1329	4.00	0.9413	0.0281	-0.1320
12.00	1.6229	0.0826	-0.1242	2.00	0.6735	0.0231	-0.1317
11.00	1.6420	0.0734	-0.1335	1.00	0.5669	0.0223	-0.1357
10.00	1.5500	0.0676	-0.1356	0.00	0.4129	0.0195	-0.1303
9.00	1.4802	0.0606	-0.1390	-1.00	0.2712	0.0181	-0.1242
8.00	1.3758	0.0555	-0.1384	-2.00	0.1463	0.0197	-0.1266
6.00	1.1185	0.0434	-0.1351	-3.00	0.0021	0.0214	-0.1165
4.00	0.9013	0.0353	-0.1340	-4.00	-0.1332	0.0256	-0.1051
2.00	0.6633	0.0268	-0.1318	-6.00	-0.3635	0.0375	-0.0816
1.00	0.5419	0.0254	-0.1311	-8.00	-0.5922	0.0479	-0.0649
0.00	0.4003	0.0220	-0.1271	-10.00	-0.8240	0.0603	-0.0414
-1.00	0.2715	0.0203	-0.1212	-11.00	-0.9384	0.0708	-0.0265
-2.00	0.1349	0.0220	-0.1178	-12.00	-1.0291	0.0829	-0.0122
-4.00	-0.1294	0.0289	-0.0965	-13.00	-1.1041	0.0959	0.0000
-6.00	-0.3523	0.0401	-0.0755	-14.00	-1.1414	0.1077	0.0091
-8.00	-0.5818	0.0515	-0.0609	-15.00	-1.1716	0.1209	0.0135
-9.00	-0.6902	0.0579	-0.0524	-16.00	-1.1326	0.1270	0.0108
-10.00	-0.7951	0.0634	-0.0439	-16.00	-1.1326	0.1270	0.0108
-11.00	-0.9212	0.0727	-0.0346	-17.00	-1.1362	0.1407	0.0101
-12.00	-1.0257	0.0810	-0.0211	-18.00	-1.1223	0.1480	0.0073
-13.00	-1.1143	0.0916	-0.0065	-17.00	-1.1225	0.1386	0.0100
-14.00	-1.1611	0.1034	0.0028	-16.00	-1.1544	0.1288	0.0110
-15.00	-1.1980	0.1172	0.0073	-16.00	-1.1544	0.1288	0.0110
-16.00	-1.1905	0.1294	0.0075	-15.00	-1.1455	0.1170	0.0126
-16.00	-1.1905	0.1294	0.0075	-14.00	-1.1405	0.1059	0.0093
-17.00	-1.1809	0.1435	0.0085	-13.00	-1.1117	0.0942	-0.0002
-18.00	-1.1694	0.1567	0.0100	-12.00	-1.0427	0.0804	-0.0123
-17.00	-1.1712	0.1420	0.0085	-11.00	-0.9498	0.0676	-0.0277
-16.00	-1.1739	0.1270	0.0076	-10.00	-0.8334	0.0573	-0.0419
-16.00	-1.1739	0.1270	0.0076	-8.00	-0.6039	0.0451	-0.0660
-15.00	-1.1921	0.1158	0.0063	-6.00	-0.3607	0.0353	-0.0807
-14.00	-1.1938	0.1049	0.0033	-4.00	-0.1382	0.0253	-0.1073
-13.00	-1.1237	0.0908	-0.0055	-3.00	0.0007	0.0204	-0.1172
-12.00	-1.0159	0.0791	-0.0207	-2.00	0.1393	0.0179	-0.1235
-11.00	-0.9216	0.0713	-0.0342	-1.00	0.2645	0.0166	-0.1227
-10.00	-0.8045	0.0631	-0.0444	0.00	0.3913	0.0177	-0.1253
-8.00	-0.5864	0.0501	-0.0609				
-6.00	-0.3680	0.0403	-0.0777				
-4.00	-0.1329	0.0278	-0.0973				
-3.00	-0.0021	0.0234	-0.1127				
-2.00	0.1318	0.0205	-0.1191				
-1.00	0.2691	0.0194	-0.1241				
0.00	0.3965	0.0205	-0.1272				

E.4.2 Turbulent, roughness triggered

$Re_c = 5 \times 10^5$			
$\alpha(^\circ)$	**Cl**	**Cd**	**Cm(1/4c)**
0.00	0.2817	0.0287	-0.0959
1.00	0.4332	0.0274	-0.1078
2.00	0.5664	0.0286	-0.1124
4.00	0.7962	0.0344	-0.1174
6.00	1.0103	0.0465	-0.1209
8.00	1.1964	0.0602	-0.1194
9.00	1.2518	0.0665	-0.1150
10.00	1.3296	0.0788	-0.1168
11.00	1.3370	0.0894	-0.1157
12.00	1.4252	0.1082	-0.1228
13.00	1.4338	0.1186	-0.1215
14.00	1.4535	0.1343	-0.1234
15.00	1.3727	0.1502	-0.1232
16.00	1.3782	0.1760	-0.1291
17.00	1.4113	0.2010	-0.1352
18.00	1.4311	0.2238	-0.1404
19.00	1.4247	0.2444	-0.1451
20.00	1.4430	0.2728	-0.1569
19.00	1.4195	0.2433	-0.1447
18.00	1.4253	0.2235	-0.1406
17.00	1.3681	0.1940	-0.1320
16.00	1.3882	0.1775	-0.1308
15.00	1.4683	0.1649	-0.1333
14.00	1.4388	0.1326	-0.1232
13.00	1.4427	0.1189	-0.1225
12.00	1.4089	0.1066	-0.1214
11.00	1.3452	0.0901	-0.1173
10.00	1.3141	0.0781	-0.1162
9.00	1.2488	0.0671	-0.1154
8.00	1.1802	0.0589	-0.1186
6.00	1.0193	0.0475	-0.1224
4.00	0.8214	0.0359	-0.1214
2.00	0.5725	0.0292	-0.1146
1.00	0.4398	0.0279	-0.1093
0.00	0.2817	0.0286	-0.0972
-1.00	0.1399	0.0285	-0.0868

$Re_c = 5 \times 10^5$			
$\alpha(^\circ)$	**Cl**	**Cd**	**Cm(1/4c)**
-2.00	0.0098	0.0312	-0.0743
-3.00	-0.1040	0.0350	-0.0618
-4.00	-0.2047	0.0405	-0.0504
-6.00	-0.3680	0.0544	-0.0300
-8.00	-0.5178	0.0720	-0.0162
-10.00	-0.6374	0.0890	-0.0104
-11.00	-0.6889	0.0963	-0.0096
-12.00	-0.7260	0.1051	-0.0064
-13.00	-0.7742	0.1132	-0.0032
-14.00	-0.8299	0.1229	-0.0012
-15.00	-0.8695	0.1311	0.0011
-16.00	-0.9352	0.1442	0.0041
-17.00	-0.9787	0.1546	0.0075
-18.00	-1.0387	0.1678	0.0103
-17.00	-1.0007	0.1570	0.0070
-16.00	-0.9445	0.1456	0.0035
-15.00	-0.9067	0.1359	0.0015
-14.00	-0.8456	0.1263	0.0002
-13.00	-0.7965	0.1168	-0.0022
-12.00	-0.7420	0.1068	-0.0054
-11.00	-0.6936	0.0963	-0.0088
-10.00	-0.6340	0.0876	-0.0101
-8.00	-0.5266	0.0727	-0.0158
-6.00	-0.3802	0.0542	-0.0294
-4.00	-0.2020	0.0387	-0.0502
-3.00	-0.1035	0.0338	-0.0625
-2.00	0.0143	0.0301	-0.0759
-1.00	0.1421	0.0270	-0.0864
0.00	0.2828	0.0268	-0.0975

E.4.3 Rough – RS2

$Re_c = 5 \times 10^5$				$Re_c = 7.5 \times 10^5$			
$\alpha(^\circ)$	**Cl**	**Cd**	**Cm(1/4c)**	$\alpha(^\circ)$	**Cl**	**Cd**	**Cm(1/4c)**
-0.50	0.3314	0.0204	-0.1251	-0.50	0.3342	0.0183	-0.1219
1.50	0.5857	0.0249	-0.1304	0.50	0.4605	0.0203	-0.1230
3.50	0.8059	0.0321	-0.1314	1.50	0.5919	0.0231	-0.1246
5.50	1.0268	0.0449	-0.1340	2.50	0.7059	0.0259	-0.1245
7.50	1.2377	0.0575	-0.1341	3.50	0.8170	0.0297	-0.1241
9.50	1.4353	0.0730	-0.1348	5.50	1.0252	0.0369	-0.1224
11.50	1.5814	0.0883	-0.1291	7.50	1.2781	0.0458	-0.1245
13.50	1.5389	0.1290	-0.1321	8.50	1.4179	0.0519	-0.1257
15.50	1.4354	0.1633	-0.1300	9.50	1.5394	0.0603	-0.1255
17.50	1.4140	0.1927	-0.1296	10.50	1.5614	0.0691	-0.1189
19.50	1.4674	0.2422	-0.1434	11.50	1.5296	0.0893	-0.1227
17.50	1.4623	0.1993	-0.1339	12.50	1.4769	0.1127	-0.1255
15.50	1.4534	0.1636	-0.1312	13.50	1.4040	0.1249	-0.1206
14.50	1.4416	0.1442	-0.1284	15.50	1.4058	0.1609	-0.1230
13.50	1.5240	0.1270	-0.1290	13.50	1.4217	0.1343	-0.1264
12.50	1.5704	0.0995	-0.1232	12.50	1.4125	0.1212	-0.1290
11.50	1.5409	0.0868	-0.1254	11.50	1.4162	0.1040	-0.1295
10.50	1.5715	0.0813	-0.1355	10.50	1.4486	0.0837	-0.1272
9.50	1.4686	0.0723	-0.1356	9.50	1.4368	0.0599	-0.1185
8.50	1.3791	0.0651	-0.1360	8.50	1.3814	0.0500	-0.1212
7.50	1.2651	0.0589	-0.1349	7.50	1.3190	0.0441	-0.1262
5.50	1.0592	0.0461	-0.1335	5.50	1.0728	0.0349	-0.1256
3.50	0.8308	0.0330	-0.1287	3.50	0.8462	0.0287	-0.1274
1.50	0.5935	0.0267	-0.1254	2.50	0.7099	0.0250	-0.1246
3.50	0.8087	0.0323	-0.1251	1.50	0.5977	0.0231	-0.1256
5.50	1.0220	0.0435	-0.1286	0.50	0.4770	0.0208	-0.1267
7.50	1.2418	0.0576	-0.1331	-0.50	0.3376	0.0188	-0.1233
8.50	1.3281	0.0632	-0.1314	-1.50	0.2060	0.0187	-0.1196
9.50	1.4578	0.0732	-0.1351	-2.50	0.0699	0.0203	-0.1127
10.50	1.5224	0.0805	-0.1325	-3.50	-0.0603	0.0230	-0.1001
11.50	1.5770	0.0884	-0.1281	-4.50	-0.1813	0.0280	-0.0891
12.50	1.5826	0.1016	-0.1242	-6.50	-0.4187	0.0382	-0.0729
13.50	1.5208	0.1269	-0.1301	-8.50	-0.6496	0.0464	-0.0553
14.50	1.4353	0.1436	-0.1282	-9.50	-0.7704	0.0507	-0.0448
15.50	1.4052	0.1596	-0.1275	-10.50	-0.9001	0.0574	-0.0313
16.50	1.3979	0.1727	-0.1259	-11.50	-0.9836	0.0636	-0.0163
17.50	1.4609	0.1993	-0.1341	-12.50	-1.0948	0.0752	-0.0030
15.50	1.4457	0.1629	-0.1308	-13.50	-1.1421	0.0873	0.0077
13.50	1.5401	0.1300	-0.1329	-14.50	-1.1647	0.1011	0.0119
11.50	1.5889	0.0882	-0.1287	-15.50	-1.1471	0.1123	0.0135
9.50	1.4780	0.0722	-0.1368	-16.50	-1.1357	0.1251	0.0126
7.50	1.2738	0.0589	-0.1357	-15.50	-1.1518	0.1133	0.0140
5.50	1.0473	0.0457	-0.1326	-14.50	-1.1553	0.1016	0.0138
3.50	0.8186	0.0338	-0.1286	-13.50	-1.1351	0.0897	0.0094
1.50	0.5972	0.0275	-0.1273	-12.50	-1.0901	0.0736	-0.0016
0.50	0.4623	0.0239	-0.1237	-11.50	-1.0219	0.0636	-0.0147
-0.50	0.3301	0.0222	-0.1198	-10.50	-0.9102	0.0559	-0.0299
-1.50	0.1951	0.0219	-0.1137	-9.50	-0.7949	0.0492	-0.0441
-2.50	0.0662	0.0238	-0.1103	-8.50	-0.6595	0.0435	-0.0547
-3.50	-0.0643	0.0274	-0.0982	-6.50	-0.4277	0.0359	-0.0734
-4.50	-0.1868	0.0330	-0.0859	-4.50	-0.1939	0.0266	-0.0927
-6.50	-0.4114	0.0423	-0.0674	-3.50	-0.0656	0.0219	-0.1050
-8.50	-0.6214	0.0529	-0.0504	-2.50	0.0668	0.0182	-0.1091
-10.50	-0.8568	0.0667	-0.0336	-1.50	0.1926	0.0163	-0.1134
-11.50	-0.9542	0.0740	-0.0219	-0.50	0.3213	0.0169	-0.1183
-12.50	-1.0756	0.0837	-0.0068				

$Re_c = 5 \times 10^5$				$Re_c = 7.5 \times 10^5$			
$\alpha(^\circ)$	**Cl**	**Cd**	**Cm(1/4c)**	$\alpha(^\circ)$	**Cl**	**Cd**	**Cm(1/4c)**
-13.50	-1.1443	0.0939	0.0058				
-14.50	-1.1804	0.1054	0.0118				
-15.50	-1.1804	0.1171	0.0127				
-16.50	-1.1741	0.1310	0.0150				
-15.50	-1.1728	0.1159	0.0131				
-14.50	-1.1594	0.1027	0.0114				
-13.50	-1.1619	0.0946	0.0065				
-12.50	-1.1021	0.0840	-0.0059				
-11.50	-0.9652	0.0727	-0.0211				
-10.50	-0.8703	0.0659	-0.0331				
-8.50	-0.6455	0.0529	-0.0502				
-6.50	-0.4244	0.0414	-0.0676				
-4.50	-0.1911	0.0308	-0.0860				
-3.50	-0.0666	0.0256	-0.0974				
-2.50	0.0663	0.0219	-0.1084				
-1.50	0.1942	0.0195	-0.1131				
-0.50	0.3292	0.0206	-0.1202				

E.4.4 Rough – RS3

$Re_c = 5 \times 10^5$				$Re_c = 7.5 \times 10^5$			
$\alpha(^\circ)$	**Cl**	**Cd**	**Cm(1/4c)**	$\alpha(^\circ)$	**Cl**	**Cd**	**Cm(1/4c)**
-0.50	0.3195	0.0208	-0.1240	-0.50	0.3295	0.0180	-0.1285
0.50	0.4472	0.0219	-0.1303	0.50	0.4588	0.0199	-0.1301
1.50	0.5817	0.0246	-0.1327	1.50	0.5869	0.0227	-0.1308
3.50	0.8094	0.0316	-0.1341	3.50	0.7934	0.0290	-0.1262
5.50	1.0092	0.0437	-0.1352	5.50	1.0349	0.0389	-0.1292
7.50	1.2357	0.0582	-0.1392	7.50	1.2798	0.0487	-0.1295
8.50	1.3260	0.0644	-0.1370	8.50	1.3618	0.0537	-0.1262
9.50	1.4156	0.0723	-0.1357	9.50	1.4318	0.0608	-0.1224
10.50	1.4776	0.0799	-0.1338	10.50	1.4514	0.0748	-0.1250
11.50	1.5110	0.0965	-0.1367	11.50	1.4186	0.0989	-0.1303
12.50	1.5007	0.1197	-0.1422	12.50	1.4120	0.1163	-0.1303
13.50	1.4830	0.1382	-0.1431	13.50	1.3955	0.1313	-0.1290
14.50	1.4573	0.1549	-0.1409	14.50	1.3862	0.1449	-0.1270
15.50	1.4209	0.1685	-0.1385	15.50	1.3973	0.1613	-0.1281
16.50	1.4438	0.1881	-0.1423	16.50	1.3999	0.1819	-0.1313
17.50	1.4098	0.1923	-0.1354	15.50	1.3605	0.1644	-0.1291
18.50	1.4441	0.2184	-0.1435	14.50	1.3698	0.1492	-0.1288
19.50	1.4771	0.2443	-0.1528	13.50	1.3587	0.1347	-0.1288
18.50	1.4578	0.2198	-0.1451	12.50	1.3376	0.1205	-0.1280
17.50	1.4341	0.1957	-0.1391	11.50	1.3292	0.1056	-0.1281
16.50	1.4421	0.1805	-0.1373	10.50	1.3029	0.0880	-0.1254
15.50	1.4526	0.1706	-0.1414	9.50	1.3040	0.0693	-0.1205
14.50	1.4628	0.1539	-0.1423	8.50	1.2921	0.0536	-0.1184
13.50	1.4572	0.1355	-0.1407	7.50	1.2577	0.0454	-0.1258
12.50	1.4847	0.1188	-0.1415	5.50	1.0780	0.0364	-0.1321
11.50	1.5180	0.0961	-0.1392	3.50	0.8249	0.0289	-0.1295
10.50	1.5027	0.0803	-0.1359	1.50	0.5892	0.0223	-0.1302
9.50	1.4433	0.0728	-0.1383	0.50	0.4673	0.0203	-0.1306
8.50	1.3308	0.0630	-0.1376	-0.50	0.3403	0.0185	-0.1318
7.50	1.2501	0.0583	-0.1401	-1.50	0.1944	0.0185	-0.1248
5.50	1.0414	0.0440	-0.1379	-2.50	0.0570	0.0206	-0.1191
3.50	0.8187	0.0327	-0.1321	-3.50	-0.0808	0.0247	-0.1083
1.50	0.5897	0.0258	-0.1311	-4.50	-0.2005	0.0308	-0.0951
0.50	0.4485	0.0234	-0.1259	-6.50	-0.4414	0.0417	-0.0727
-0.50	0.3194	0.0205	-0.1239	-8.50	-0.6792	0.0536	-0.0514
-1.50	0.1928	0.0213	-0.1220	-10.50	-0.8831	0.0681	-0.0234
-2.50	0.0542	0.0232	-0.1145	-11.50	-1.0004	0.0819	-0.0080
-3.50	-0.0791	0.0277	-0.1027	-12.50	-1.0817	0.0945	0.0052
-4.50	-0.1951	0.0328	-0.0922	-13.50	-1.1378	0.1069	0.0163
-6.50	-0.4293	0.0428	-0.0732	-14.50	-1.1596	0.1190	0.0203
-8.50	-0.6394	0.0538	-0.0550	-15.50	-1.1354	0.1273	0.0193
-10.50	-0.8757	0.0687	-0.0378	-16.50	-1.0969	0.1346	0.0144
-11.50	-0.9834	0.0770	-0.0253	-17.50	-1.0603	0.1426	0.0081
-12.50	-1.0849	0.0869	-0.0077	-18.50	-1.0582	0.1558	0.0076
-13.50	-1.1630	0.0988	0.0042	-17.50	-1.0775	0.1451	0.0079
-14.50	-1.1824	0.1119	0.0106	-16.50	-1.1254	0.1375	0.0145
-15.50	-1.1934	0.1238	0.0100	-15.50	-1.1265	0.1233	0.0169
-16.50	-1.1943	0.1375	0.0107	-14.50	-1.1654	0.1157	0.0205
-17.50	-1.1689	0.1498	0.0112	-13.50	-1.1577	0.0991	0.0139
-18.50	-1.1663	0.1647	0.0145	-12.50	-1.0995	0.0942	0.0062
-17.50	-1.1730	0.1511	0.0122	-11.50	-1.0184	0.0805	-0.0060
-16.50	-1.1871	0.1355	0.0099	-10.50	-0.9147	0.0683	-0.0206
-15.50	-1.2026	0.1247	0.0111	-8.50	-0.6955	0.0513	-0.0509
-14.50	-1.1707	0.1101	0.0095	-6.50	-0.4456	0.0391	-0.0728
-13.50	-1.1677	0.0989	0.0054	-4.50	-0.2068	0.0283	-0.0949
-12.50	-1.1116	0.0874	-0.0068	-3.50	-0.0805	0.0231	-0.1081
-11.50	-0.9956	0.0764	-0.0245	-2.50	0.0526	0.0185	-0.1131
-10.50	-0.8859	0.0677	-0.0375	-1.50	0.1851	0.0166	-0.1191
-8.50	-0.6648	0.0537	-0.0558	-0.50	0.3245	0.0171	-0.1266
-6.50	-0.4316	0.0421	-0.0722				
-4.50	-0.2015	0.0313	-0.0903				
-3.50	-0.0782	0.0258	-0.1023				
-2.50	0.0516	0.0215	-0.1150				
-1.50	0.1882	0.0195	-0.1206				
-0.50	0.3188	0.0195	-0.1240				

E.4.5 Rough – RS4

$Re_c = 5 \times 10^5$				$Re_c = 7.5 \times 10^5$			
$\alpha(^\circ)$	**Cl**	**Cd**	**Cm(1/4c)**	$\alpha(^\circ)$	**Cl**	**Cd**	**Cm(1/4c)**
0.00	0.1359	0.0787	-0.0146	0.00	0.1253	0.0806	-0.0071
2.00	-0.0363	0.0803	0.0162	1.00	0.0278	0.0817	0.0104
4.00	0.0093	0.0856	0.0060	2.00	-0.0531	0.0861	0.0204
6.00	0.2078	0.1015	-0.0292	3.00	-0.0648	0.0869	0.0201
8.00	0.4040	0.1240	-0.0566	4.00	0.0023	0.0928	0.0063
9.00	0.4830	0.1351	-0.0683	5.00	0.1185	0.0993	-0.0133
10.00	0.5705	0.1513	-0.0782	6.00	0.2404	0.1102	-0.0341
11.00	0.6338	0.1646	-0.0867	8.00	0.4899	0.1375	-0.0713
12.00	0.6886	0.1773	-0.0919	10.00	0.6671	0.1657	-0.0956
14.00	0.8143	0.2151	-0.1094	12.00	0.6756	0.1837	-0.0920
16.00	0.9353	0.2629	-0.1301	14.00	0.7933	0.2186	-0.1071
18.00	0.9973	0.3233	-0.1485	16.00	0.9095	0.2654	-0.1252
20.00	1.0472	0.3985	-0.1734	18.00	0.9663	0.3225	-0.1422
18.00	1.0231	0.3327	-0.1526	20.00	1.0572	0.4146	-0.1724
16.00	0.9619	0.2708	-0.1342	18.00	0.9917	0.3311	-0.1459
14.00	0.8386	0.2221	-0.1131	16.00	0.9264	0.2700	-0.1271
12.00	0.7071	0.1825	-0.0949	14.00	0.8045	0.2218	-0.1086
11.00	0.6454	0.1668	-0.0879	12.00	0.6768	0.1848	-0.0920
10.00	0.5696	0.1512	-0.0780	11.00	0.6110	0.1688	-0.0850
9.00	0.4937	0.1396	-0.0686	10.00	0.6866	0.1689	-0.0988
8.00	0.4121	0.1261	-0.0565	9.00	0.6085	0.1538	-0.0892
6.00	0.2143	0.1037	-0.0271	8.00	0.4932	0.1416	-0.0730
4.00	0.0116	0.0867	0.0060	6.00	0.2376	0.1115	-0.0343
2.00	-0.0367	0.0828	0.0194	5.00	0.1135	0.1019	-0.0140
0.00	0.1377	0.0787	-0.0124	4.00	0.0104	0.0929	0.0044
-2.00	0.2011	0.0820	-0.0432	3.00	-0.0619	0.0881	0.0192
-4.00	0.1575	0.0918	-0.0575	2.00	-0.0487	0.0865	0.0193
-6.00	0.0493	0.1031	-0.0567	1.00	0.0274	0.0852	0.0101
-8.00	-0.0682	0.1235	-0.0503	0.00	0.1322	0.0821	-0.0097
-10.00	-0.1790	0.1443	-0.0394	-1.00	0.1823	0.0847	-0.0251
-12.00	-0.2721	0.1684	-0.0303	-2.00	0.1838	0.0892	-0.0338
-14.00	-0.3691	0.2007	-0.0180	-3.00	0.1516	0.0966	-0.0372
-16.00	-0.4726	0.2441	0.0012	-4.00	0.1238	0.1014	-0.0445
-18.00	-0.5901	0.3017	0.0312	-5.00	0.0491	0.1093	-0.0377
-16.00	-0.4869	0.2521	0.0021	-6.00	-0.0234	0.1239	-0.0320
-14.00	-0.3810	0.2087	-0.0180				
-12.00	-0.2824	0.1731	-0.0304				
-10.00	-0.1807	0.1453	-0.0405				
-8.00	-0.0676	0.1240	-0.0508				
-6.00	0.0458	0.1052	-0.0583				
-4.00	0.1572	0.0905	-0.0573				
-2.00	0.2104	0.0836	-0.0448				
0.00	0.1325	0.0776	-0.0122				
0.00	0.1353	0.0758	-0.0141				
1.00	0.0391	0.0777	0.0075				
2.00	-0.0346	0.0790	0.0168				
3.00	-0.0536	0.0798	0.0195				
4.00	0.0115	0.0858	0.0051				
5.00	0.0986	0.0918	-0.0095				
6.00	0.2077	0.1034	-0.0279				
5.00	0.0995	0.0924	-0.0098				
4.00	0.0102	0.0853	0.0057				
3.00	-0.0535	0.0813	0.0202				
2.00	-0.0363	0.0803	0.0176				
1.00	0.0323	0.0794	0.0081				
0.00	0.1338	0.0774	-0.0132				
-1.00	0.1858	0.0817	-0.0314				
-2.00	0.2036	0.0822	-0.0445				
-3.00	0.1884	0.0856	-0.0528				
-4.00	0.1528	0.0902	-0.0576				
-5.00	0.1027	0.0969	-0.0585				
-6.00	0.0501	0.1039	-0.0588				
-5.00	0.1027	0.0974	-0.0586				
-4.00	0.1582	0.0905	-0.0583				
-3.00	0.1863	0.0859	-0.0532				
-2.00	0.2057	0.0828	-0.0446				
-1.00	0.1932	0.0819	-0.0325				
0.00	0.1367	0.0757	-0.0142				

E.4.6 Smooth, 8.31 % upstream turbulence intensity

$Re_c = 5 \times 10^5$			
$\alpha(^\circ)$	**Cl**	**Cd**	**Cm(1/4c)**
0.00	0.3329	0.0231	-0.1129
1.00	0.4715	0.0249	-0.1170
2.00	0.6048	0.0266	-0.1201
3.00	0.7241	0.0293	-0.1209
4.00	0.8498	0.0330	-0.1234
6.00	1.0576	0.0426	-0.1234
8.00	1.2473	0.0539	-0.1208
9.00	1.3214	0.0623	-0.1201
10.00	1.3982	0.0726	-0.1206
11.00	1.4552	0.0840	-0.1209
12.00	1.5383	0.1008	-0.1247
13.00	1.5651	0.1174	-0.1316
14.00	1.5976	0.1376	-0.1361

$Re_c = 5 \times 10^5$			
$\alpha(^\circ)$	**Cl**	**Cd**	**Cm(1/4c)**
15.00	1.6014	0.1585	-0.1432
16.00	1.6285	0.1783	-0.1488
17.00	1.6308	0.2003	-0.1638
18.00	1.6520	0.2253	-0.1639
19.00	1.7127	0.2695	-0.1821
20.00	1.4635	0.2463	-0.1687
19.00	1.4562	0.2065	-0.1454
18.00	1.4695	0.1948	-0.1417
17.00	1.5042	0.1774	-0.1427
16.00	1.7994	0.1897	-0.1579
16.00	1.6537	0.1890	-0.1607
15.00	1.5939	0.1551	-0.1402
14.00	1.6017	0.1311	-0.1348
13.00	1.5816	0.1184	-0.1270
12.00	1.5358	0.0994	-0.1241
11.00	1.4552	0.0840	-0.1209
10.00	1.3982	0.0726	-0.1206
9.00	1.3214	0.0623	-0.1201
8.00	1.2473	0.0539	-0.1208
6.00	1.0576	0.0426	-0.1234
4.00	0.8498	0.0330	-0.1234
3.00	0.7241	0.0293	-0.1209
2.00	0.6048	0.0266	-0.1201
1.00	0.4715	0.0249	-0.1170
0.00	0.3291	0.0236	-0.1126
-1.00	0.1957	0.0230	-0.1079
-2.00	0.0646	0.0245	-0.1006
-3.00	-0.0672	0.0272	-0.0903
-4.00	-0.1841	0.0309	-0.0774
-6.00	-0.4118	0.0449	-0.0550
-8.00	-0.6306	0.0597	-0.0321
-10.00	-0.8229	0.0784	-0.0093
-11.00	-0.9217	0.0923	0.0023
-12.00	-0.9760	0.1048	0.0126
-13.00	-1.0271	0.1190	0.0210
-14.00	-1.0738	0.1313	0.0279
-15.00	-1.1202	0.1486	0.0328
-16.00	-1.1513	0.1630	0.0380
-17.00	-1.1801	0.1773	0.0422
-18.00	-1.1860	0.1914	0.0471
-19.00	-1.1858	0.2040	0.0487

Bibliography

Guide to Wave Analysis and Forecasting. World Meteorological Organization, 1998.

I.H. Al-Bahadly and A.F.T. Petersen. A ducted horizontal wind turbine for efficient generation. Technical report, Massey University, New Zealand, 2007.

M. Atlar, E. J. Glover, M. Candries, R. J. Mutton, and C. D. Anderson. The effect of a foul release coating on propeller performance. In *International Conference on Marine Science and Technology for Environmental Sustainability (ENSUS 2002)*, 2002.

M. Baragona. *Unsteady Characteristics of Laminar Separation Bubbles, An Experimental and Numerical Investigation.* PhD thesis, Technische Universiteit Delft, 2004.

A. Bekhti and O. Guerri. Influence de la rugosité sur les caractéristiques aérodynamiques d'un profil de pale d'eolienne. *Revue des Energies Renouvelables*, 15:235–247, 2012.

F. Bertagnolio. Naca 0015 measurements in lm wind tunnel and turbulence generated noise. Technical report, Riso DTU National Laboratory for Sustainable Energy, 2008.

F. Bertagnolio, N. Sorensen, J. Johansen, and P. Fuglsang. Wind turbine airfoil catalogue. Technical report, Riso National Laboratory, Roskilde, Denmark, 2001.

F. Bertagnolio, N. N. Sørensen, and J. Johansen. Profile catalogue for airfoil sections based on 3d computations. Technical report, Risø National Laboratory, Roskilde, Denmark, 2006.

K. Biber and G. W. Zumwalt. Hysteresis effect on wind tunnel measurements of a two-element airfoil. *AIAA Journal*, 31:326–330, 1993.

A. Brient. *Etude de l'Influence du Processus de Fabrication sur les Performances des Propulseurs Marins: Approche Multimétiers de l'Usinage d'Hélices.* PhD thesis, Ecole Centrale de Nantes, Université de Nantes, Juillet 2004.

T. Burton, D. Sharpe, N. Jenkins, and E. Bossanyi. *Wind Energy Handbook.* 2011.

M. R. Castelli, G. Grandi, and E. Benini. Numerical analysis of the performance of the du91-w2-250 airfoil for straight-bladed vertical-axis wind turbine application. *World Academy of Science, Engineering and Technology*, 63:855–860, 2012a.

M. R. Castelli, G. Grandi, and E. Benini. Numerical analysis of laminar to turbulent transition on the du91-w2-250 airfoil. *International Journal of Mechanical and Aerospace Engineering*, 6:335–340, 2012b.

Luciano Castillo, Xia Wang, and William K. George. Sepraration criterion for turbulent boundary layers via similarity analysis. *Journal of Fluids Engineering*, 126:297–304, 2004.

T. Cebeci. Effect of environementally imposed roughness on airfoil performance. Contractor Report 179639, National Aeronautics and Space Administration (N. A. S. A.), 1987.

P. Chassaing. *Turbulence en mécanique des fluides.* collection POLYTECH, 2000.

V. Chitta, T.P. Dhakal, and D.K. Walters. Prediction of aerodynamic characteristics for elliptic airfoils in unmanned aerial vehicle applications. In Dr Mustafa Serdar Genc, editor, *Low Reynolds Number*, chapter 3, pages 59–78. InTech, 2012.

L. J. Clancy. Aerodynamics. book, 1986.

Chris C. Critzos, Heyson Harry H., and Robert W. Jr. Boswinkle. Aerodynamic characteristics of naca 0012 airfoil section at angles of attack from 0° to 180°. Technical report, National Advisory Committee for Aeronautics, 1955.

K. S. Dahl and P. Fuglsang. Design of the wind turbine airfoil family riso-a-xx. Technical report, Riso National Laboratory, 1998.

S. D'Angelo and W. A. Timmer. Two wind turbines dedicated airfoils tested in two different wind tunnels: Comparison and results. In *Windpower'95 Conference*, pages 555–563, 1995.

A. Defant. *Physical Oceanography.* Pergamon, New York, 1961.

P.-L. Delafin, F. Deniset, and J.-A. Astolfi. Effect of the laminar separation bubble induced transition on the hydrodynamic performance of a hydrofoil. *European Journal of Mechanics*, 46:190–200, July-August 2014.

J.S. Delnero, J. Maranon Di Leo, F.A. Bacchi, J. Colman, and U. Boldes. Experimental determination of the influence of turbulent scale on the lift and drag coefficients of low reynolds number airfoils. *Latin American Applied Research*, 35:183–188, 2005. Qualification expérimentale du comportement d'un foil selon l'échelle de la turbulence, en terme de portance et de trainée.

Navale Postgraduate School Department of Oceanography. website. URL `http://www.oc.nps.edu/nom/day1/partc.html`.

A. Deperrois. *Xflr5: Analysis of Foils and Wings Operating at Low Reynolds Numbers*, 2010.

M. Drela. Xfoil: An analisys and design system for low reynolds number airfoils. *Low Reynolds Number Aerodynamics*, 54, 1989.

M. Drela. *XFOIL 6.5 User Primer.* MIT Aero and Astro, 1995.

A. Ducoin. *Etude expérimentale et numérique du chargement hydrodynamique des corps portants en régime transitoire avec prise en compte du couplage fluide structure.* Dynamique des fluides et des transferts, Ecole Centrale de Nantes, 2008.

Jean Délery, Jean-François Bret, and Jean-Philippe Vieira. *Méthode de Mesure en Aerodynamique - Partie 1: Mesure des efforts.* ONERA.

European-Commission. The exploitation of tidal marine currents. Technical Report EUR16683EN, European Commission, 1996.

P.L. Fraenkel. *Water Lifting Devices.* Food and Agriculture Organization of the United Nations, 1986.

P.L. Fraenkel. Power from marine currents. *Institution of Mechanical Engineers (IMechE)*, Part A: J. Power and Energy:216, 2002.

K. Freudenreich, K. Kaiser, A. P. Schaffarczyk, H. Winkler, and B. Stahl. Reynolds number and roughness effects on thick airfoils for wind turbines. *Wind Engineering*, 28:529–546, 2004.

P. Fuglsang, K. S. Dahl, and I. Antoniou. Wind tunnel tests of the riso-a1-18, riso-a1-21 and riso-a1-24 airfoils. Technical report, Risø National Laboratory, 1999.

David L.F. Gaden and Eric L. Bibeau. A numerical investigation into the effect of diffusers on the performance of hydro kinetic turbines using a validated momentum source turbine model. *Renewable Energy*, 35:1152–1158, 2010.

Simon Gant and Tim Stallard. Modelling a tidal turbine in unsteady flow. *ISOPE*, 2008.

J. Gash and J. Twele. *wind Power Plants*. Solarpraxis:Berlin,Germany, 2002.

G. Germain, F. Maganga, B. Gaurier, J.V. Facq, T. Bacchetti, G. Pinon, E. Rivoalen, and J.M. Etancelin. Vers une caractérisation réaliste des conditions de fonctionnement des hydroliennes. 12èmes Journées de l'Hydrodynamique, Novembre 2010.

L. Gilling. *Airfoils in Turbulent Inflow*. PhD thesis, Aalborg University Department of Civil Engineering Division of Structural Mechanics, 2009.

S. Gooch, J. Thomson, B. Polagye, and D. Meggit. Site caracterization for tidal power. Technical report, Sound and Sea Technology, Washington Research Foundation, 2009.

F. Grasso. Design and optimization of a tidal turbine airfoil. In *29th AIAA Applied Aerodynamics conference*, 2011.

T. Gruber, M. M. Murray, and D. W. Fredriksson. Effect of humpback whale inspired tubercles on marine tidal turbine blades. In *ASME 2011 International Mechanical Engineering Congress and Exposition*, 2011.

Florent Guinot and Marc Le Boulluec. Realistic marine flow conditions for current turbines studies. In *ICOE, Brest*, 2008.

Florent. Guinot, Marc Le Boulluec, and Vincent Rey. Interaction houle-courant en bathymétrie variable via une approche de type boussinesq. *European Journal of Environmental and Civil Engineering*, 12(5):615–627, 2008.

T. S. Hedges. Combinations of waves and currents: an introduction. In *Institution of Civil Engineers*, volume 82, pages 567–585, 1987.

L. A. Hoerner. *Fluid-Dynamic Lift Information on Lift and its Derivatives, in Air and in Water*. Mrs. Liselotte A. Hoerner, 1985.

J. A. Hoffmann. Effects of freestream turbulence on the performance characteristics of an airfoil. *AIAA Journal*, 29:1353–1354, 1991a.

J. A. Hoffmann. Effects of freestream turbulence on the performance characteristics of an airfoil. *AIAA Journal*, 29:1353–1354, 1991b.

L. H. Holthuijsen, A. Herman, and N. Booil. Phase-decoupled refraction-diffraction for spectral wave models. *Coastal Engineering*, 49(4):291–305, 2003.

Ray W. Hooker. The aerodynamics characteristics of airfoils as affected by surface roughness. Technical notes 457, National Advisory Commitee for Aeronautics (N.A.C.A), 1933.

E. N. Jacobs and A. Sherman. Airfoil section characteristics as affected by variations of the reynolds number. Technical Report 586, National Advisory Committee for Aeronautics (N.A.C.A), 1937.

E. N. Jacobs, K. A. Ward, and R. M. Pinkerton. The characteristics of 78 related airfoil sections from tests in the variable-density wind tunnel. Technical report, National Advisory Committee for Aeronautics, 1935.

P. Jonas, O. Mazur, and V. Uruba. On the receptivity of the by-pass transition to the length scale of the outer stream turbulence. *European Journal of Mechanics*, 19:707–722, 2000.

Richard Karsten, J. M. McMillan, M. J. Lickley, and R. D. Haynes. Assessment of tidal current energy in the minas passage, bay of fundy. *Journal of Power and Energy*, 222:493–507, 2008.

Richard Karsten, Amanda Swan, and Joel Culina. Assesment of arrays of in-stream tidal turbines in the bay of fundy. *Philosophical Transaction of the Royal Society A: Mathematical, Physical and Engineering Sciences*, 371, 2013.

B. Kirke. Developments in ducted water current turbines. 2003.

E.P. Kvale. The origin of neap-spring tidal cycles. *Marine Geology - Internationnal Journal of Marine Geology, Geochemistry and Geophysics*, 235:5–18, 2006.

K. Kwon, B. Chang, J. Lee, and S. O. Park. Boundary layer transition measurement using piv with high magnification. 2006.

Kijung Kwon and Seung O. Park. Aerodynamic characteristics of an elliptic airfoil at low reynolds number. *Journal of Aircraft*, 42(6):1642–1644, 2005.

E. V. Laitone. Wind tunnel tests of wings at reynolds number below 70 000. *Experiments in Fluids*, 23(5):405–409, November 1997.

C. J. Lawn. Optimization of the power output for ducted turbines. In *Institution of Mechanical Engineers (IMechE)*, 2002.

M.J. Lawson, Y. Li, and D.C. Sale. Development and verification of a computational fluid dynamics model of a horizontal-axis tidal current turbine. In *30th International Conference on Ocean, Offshore ans Arctic Engineering*, 2011.

J. Leishman. Aerodynamic characteristics of a helicopter rotor airfoil as affected by simulated balistic damage. Technical report, Army Research Laboratory, 1993.

J.B. Leroux. *Etude expérimentale en tunnel hydrodynamique des instabilités de la cavitation par poche sur hydrofoil par la mesure spatio-temporelle du champ de pression pariétal.* PhD thesis, Ecole Centrale de Nantes, 2003.

K. W. Lewis. The cumulative effects of roughness and reynolds number on naca 0015 airfoil section characteristics. Master's thesis, Faculty of Texas Technical University, 1984.

M. G. U. Lundin and M. Leijon. Ocean energy. Technical report, Department of Electricity and Lightning Research Uppsala University, 2001.

R. Luquet, D. Bellevre, D. Frechou, and P. Guinard. Développement d'un concept novateur d'hydrolienne. Technical report, Association Technique Maritime et Aéronautique (ATMA), 2010.

D.H. MacMillan. *Tides.* American Elsevier Publishing Company, New York, 1966.

F. Maganga, G. Germain, J. King, G. Pinon, and E. Rivoalen. Experimental study to determine flow caracteristic effects on marine current turbine behaviour. In *The 8th European Wave and Tidal Energy Conference*, 2009.

F. Maganga, G. Germain, J. King, G. Pinon, and E. Rivoalen. Experimental characterisation of flow effects on marine current turbine behaviourand on its wake properties. *Renewable Power Generation*, 4(6):498–509, 2010.

I. Master, J. A. C Orme, and J. Chapman. Towards realistic marine flow conditions for tidal stream turbine. In *7th. EWETEC, Porto*, 2007.

G.N. McCann. Tidal current turbine fatigue loading sensitivity to waves and turbulence - a parametric study. In *7th European Wave and Tidal Energy Conference*, 2007.

F. R. Menter, R. Langtry, and S. Völker. Transition modelling for general purpose cfd codes. *Flow Turbulence Combust*, 77:277–303, 2006.

F.R. Menter. Improved two equation k-turbulence models for aerodynamic flows. Technical memorandum 103975:34, NASA, 1993.

F.R. Menter, M. Kuntz, and R. Langtry. Ten years of industrial experience with the sst turbulence model. *Turbulence, Mass ans Heat Transfer*, 4, 2003.

Djalal Merkoune, Julien Touboul, Nizar Abcha, Dominique Mouaze, and Alexander Ezersky. Interaction houle focalisée-courant dans une profondeur finie. In *XII eme Journées Nationales Génies Côtier - Génie civile*, 2012.

I. A. Milne, R. N. Sharma, R. G. J. Flay, and S. Bickerton. The role of onset turbulence on tidal turbine blade loads. In *17th Australasian Fluid Mechanics Conference*, 2010.

P. F. Mish. Mean loading and turbulence scale effects on the surface pressure fluctuations occurring on a naca 0015 in grid generated turbulence. Master's thesis, Faculty of Virginia Polytechnic Institute and State University, 2001.

S. Mittal and P. Saxena. Prediction of hysteresis associated with static stall of an airfoils. *AIAA Journal*, 38:933–935, 2002.

H. K. Monroe. Reversible propeller blade. Patent-US2609055, Septembre 1952.

H. K. Monroe. Reversible propeller blade. Patent-US3174681, March 1965.

T. J. Mueller. The influence of laminar separation and transition on low reynolds number airfoil hysteresis. *Journal of Aircraft*, 22:763–770, 1985.

L. Myers and A.S. Bahaj. Simulated electrical power potential harnessed by marine current turbine in the alderney race. *Renewable Energy*, 30:1713–1731, 2005.

C. Münch, M. Vonlanthen, J. Gomes, R. Luquet, P. Guinard, and F. Avellan. Design and performance assesment of a tidal ducted turbines. Technical report, Workgroup on Cavitation and Dynamic Problems in hydraulic Machinery and systems, 2009.

R. F. Nicholls-Lee. *Adaptative Composite Blades for Horizontal Axis Tidal Turbines.* PhD thesis, University of Southampton, Faculty of Engineering and the Environment, School of Engineering and Sciences, 2011.

R.F. Nicholls-Lee, S.R. Turnock, and W. Boyd. Tidal turbine blade selection for optimal performance in an array. In ASME, editor, *30th International Conference on Ocean, Offshore ans Arctic Engineering*, number OMAE2011-49943, Rotterdam, The Netherlands, 2011a.

R.F. Nicholls-Lee, S.R. Turnock, and W. Boyd. Tidal turbine blade selection for optimal performance in an array. In ASME, editor, *30th International Conference on Ocean, Offshore ans Arctic Engineering*, number OMAE2011-49943, Rotterdam, The Netherlands, 2011b.

J. V. Norris and E. Droniou. Update on emec activities, resource description, and characterisation of wave-induced velocities in a tidal flow. In *7th European Wave and Tidal Energy Conference*, 2007.

D. M. O'Doherty, A. Mason-Jones, T. O'Doherty, and C. B. Byrne. Considerations of improved tidal stream turbine performance using double rows of contra-rotating blades. In *8th European Wave and Tidal Energy Conference*, 2009.

ltd OG+1, ltd ALSTOM Power, and WUMTIA. Economic viability of a simple tidal stream energy device, final report, ,. Technical report, University of Southampton, WOLFSON Unit, 2007.

Benoit Paillard. *Simulation numérique et Optimisation d'une hydrolienne à axe transverse avec contrôle actif de l'angle de calage.* PhD thesis, Université de Bretagne Occidentale, 2011.

C. Pashias and S. R. Turnock. Hydrodynamic design of a bi-directional rim-driven ducted thruster suitable for underwater vehicle. Ship Science Report 128, University of Southampton, 2003.

B. Polagye and J. Thomson. Screening for biofouling and corrosion of tidal energy device materials: In-situ results for admiralty inlet, puget sound, washington. Technical report, Northwest National Marine Renewable Energy Center Technical Memorandum, University of Washington, 2010.

A. Pope. The forces and pressures over an naca 0015 airfoil through 180 degrees angle of attack. Technical report, Georgia Institute of Technology, Atlanta, 1947.

D.T. Pugh. *Tides, Surges and Mean Sea Level.* John Wiley and Sons Ltd, 1987.

N. Ren and J. Ou. Dust effect on the performance of wind turbine airfoils. *Journal of Electromagnetic Analysis & Applications*, (1):102–107, June 2009.

Vincent Rey, Florent Guinot, and Marc Le Boulluec. Interaction houle-courant par profondeur finie: Impact sur la cinematique. Technical report, Ecole Centrale de Nantes, 2008.

T. P. Rippeth, E. Williams, and J. H. Simpson. Reynolds stress and turbulent energy production in a tidal channel. *Journal of Physical Oceanography*, 32:1242–1251, 2002.

K. W. Robinson. Aerodynamics characteristics of rotor airfoils as affected by simulated ballistic damage. Master's thesis, University of Maryland, 1995.

A. Rokke and R. Nilssen. Marine current turbines and generator preference, a technology review. *Renewable Energy and Power Quality Journal*, 11, 2013.

Evaluation of the Durability of Composite tidal Turbine Blades, volume 371, 2012. Royal Society of London.

H. Schlichting. *Boundary layer theory.* McGraw-Hill series in mechanical engineering. McGraw-Hill, 1960.

O. Schrenck. Effect of roughness on properties of airfoils. Technical memorandum 375, National Advisory Commitee for Aeronautics (N.A.C.A), 1925.

G. B. Schubauer. Air flow in boundary layer of an elliptic cylinder. Technical Report 652, National Advisory Commitee for Aeronautics (N.A.C.A), 1939.

P. J. Schubel and R. J. Crossley. Wind turbine blade design. *Energies*, 5:3425–3449, 2012.

R.E. Sheldahl and P.C. Klimas. Aerodynamics characteristics of seven symmetrical airfoil sections through 180-degree angle of attack for use in aerodynamic analysis of vertical axis wind turbine. Technical report, Sandia National Laboratories, 1981.

M. R. Shives. Hydrodynamic modeling, optimization and performance assesment for ducted and non-ducted tidal turbines. Master's thesis, University of Victoria, Department of Mechanical Engineering, 2011.

M. J. Smith, N. D. Liggett, and B. C. G. Koukol. Aerodynamics of airfoils at high and reverse angles of attack. *Journal of Aircraft*, 48(6):2012–2023, 2011.

D. M. Somers. Design and experimental results for the s827 airfoil. Technical report, National Renewable Energy Laboratory, 2005.

Zivan T. Spasic, Sasa M. Milanovic, Vanja M. Sustersic, and Boban D. Nikolic. Low-pressure reversible axial fan with straight profile blades and relatively high efficiency. *Thermal Science*, 16(2):S593–S603, 2012.

J. Stack. Tests in variable density wind tunnel to investigate the effects of scale and turbulence on airfoil characteristics. Technical report, National Advisory Committee for Aeronautics, 1931.

K. E. Swalwell, j. Sheridan, and W. H. Melbourne. The effect of turbulence on stall of the naca 0021 aerofoil. In *14th Australasian Fluid Mechanics Conference*, 2001.

J. L. Tangler and D. M. Somers. Nrel airfoil families for hawts. Technical report, National Renewable Energy Laboratory, 1995.

S. C. Tedds, R. J. Poole, and I. Owen. Wake characteristics of horizontal axis tidal stream turbines in uniform and non-uniform steady flows. In *4th International Conference on Ocean Energy*, 2012.

K. A. Thole, D. G. Bogard, and J. L. Whan-Tong. Generating high freestream turbulence levels. *Experiments in Fluids*, 17(375-380), 1994.

J. Thomson, B. Polagye, M. Richmond, and V. Durgesh. Quantifying turbulence for tidal power applications. 2010.

W. Timmer. Aerodynamic characteristics of wind turbine blade airfoils at high angles-of-attack. In *TORQUE 2010: The Science of Making Torque from Wind*, 2010.

W. A. Timmer. Two-dimensional low-reynolds number wind tunnel results for airfoil naca 0018. *Wind Engineering*, 32(6):525–537, 2008.

W. A. Timmer and R. P. J. O. M. Van Rooij. Wind tunnel results for a 25*European Community Wind Energy Conference*, 1993.

W.A. Timmer and R.P.J.O.M. van Rooij. Summary of the delft university wind turbine dedicated airfoils. *AIAA Aerospace Sciences Meeting*, 0352, 2003.

M. Trevethan, H. Chanson, and R. Brown. Turbulent measurements in a small subtropical estuary with semidiurnal tides. *Journal of Hydraulic Engineering*, pages 1665–1670, 2010.

S. R. Turnock, R. F. Nicholls-Lee, R. J. K. Wood, and J. A. Wharton. *Tidal Turbines That Survive ?* University of Southampton, 2009.

D.T. Valentine. The effect of nose radius on the cavitation inception caracteristics of two dimensional hydrofoils. Technical Report 3813, Naval Ship Research and Development Center, Bethesda, Maryland 20034, July 1974.

R. Van Rooij and W. Timmer. Design of airfoils for wind turbine blades. Technical report, Delft University of Technology, 2004.

R.P.J.O.M. Van Rooij and W.A. Timmer. Roughness sensitivity considerations for thick rotor blade airfoils. *ASME Journal of Solar Energy Engineering*, 125:468–478, 2003.

D. Wang, M. Atlar, and R. Sampson. An experimental investigation on cavitation, noise, and slipstream characteristics of ocean stream turbines. *Journal of Fluids Engineering (IMEchE)*, 221:219–231, 2007.

J.-F. Wang, J. Piechna, and N. Müller. Numerical investigation of the power generation of a ducted composite material marine current turbine. *Journal of Zheijiang University-Applied Physics and Engineering*, 2013.

S. Watkins, S. Ravi, and B. Loxton. The effect of turbulence on the aerodynamics of low reynolds number wings. *Engineering Letters*, 18(3), 2010.

D.C. Wilcox. A half century historical review of the k-omega model. *AIAA Aerospace Sciences Meeting*, 0615, 1991.

Z. Yang, H. Igarashi, M. Martin, and H. Hu. An experimental investigation on aerodynamic hysteresis of a low-reynolds number airfoil. *American Institute of Aeronautics and Astronautics*, AIAA-2008-0315, 2008.

J. E. Yates. Viscous thin airfoil theory. Technical report, Aeronautical Research Associates of Princeton, Inc., 1980.

A. F. Zahm, R. H. Smith, and F. A. Louden. Forces on elliptic cylinders in uniform air stream. Technical Report 289, National Advisory Commitee for Aeronautics (N.A.C.A), 1929.

EXPERIMENTAL ANALYSIS AND NUMERICAL SIMULATION OF FOIL SECTIONS FOR TIDAL TURBINE APPLICATIONS

ABSTRACT : In a context of development of renewable energies, there is a growing interest in marine energies. Among them, tidal currents are promising due to the density of seawater and the predictability of tidal oscillations at a given location. For horizontal axis tidal turbines and according to the industrial partner, constraints at the scale of the blade section include the bi-directionality of the flow, surface roughness and upstream turbulence. The first part of the present work studied two solutions to achieve bi-directionality of the flow at the scale of the blade section. A specific bi-directional hydrofoil was compared to a NACA 0015 in forward and reversed flow. The second part focused on the effect of surface roughness and upstream turbulence on a unidirectional blade section designed for current turbines. Both studies were carried out on academic two-dimensional hydrofoils, using both numerical investigation and a specifically developed experimental approach. Computations using fully turbulent and transition models were compared to balance force measurements coupled with PIV flow observations. The bidirectional foil, as well as the NACA foil in forward and reversed flow, showed specific behaviors that could considerably reduce their performances if they were to be used as a tidal turbine rotor. It was also observed that roughness height deeply alters the foil's properties, beyond a critical height. Finally, upstream turbulence resulted in moderate performance changes, less significant at the scale of the machine.

Keywords : experimental analysis, numerical simulation, tidal turbine, surface roughness, upstream turbulence, bi-directionality, reversed flow.

ANALYSE EXPERIMENTALE ET SIMULATION NUMERIQUE DE SECTIONS DE PALES POUR APPLICATION AUX HYDROLIENNES

RESUME : Dans un contexte de développement des énergies renouvelables, les énergies marines suscitent un grand intérêt. Parmi elles, les courants de marée paraissent constituer une ressource intéressante du fait de la densité de l'eau de mer et de la possibilité de prévoir les oscillations de marée à un endroit donné. Pour une turbine à axe vertical et en accord avec le partenaire industriel, les contraintes à l'échelle de la section de pale incluent la bidirectionnalité de l'écoulement, l'état de surface ainsi que la turbulence amont. La première partie du travail présentée ici s'est donc attachée à étudier deux solutions permettant de répondre à la bidirectionnalité de l'écoulement à l'échelle d'une section de pale. Un profil bidirectionnel spécifique a ainsi été comparé à un NACA 0015 en écoulement directe et inversé. La seconde partie s'est attachée à caractériser l'effet de la rugosité de surface et de la turbulence amont sur les propriétés d'un profil unidirectionnel spécifiquement développé pour les turbines à axe horizontal. Les deux sujets ont été abordés sur des profils académiques 2D, au travers d'une approche expérimentale originale et d'étude numériques. Des calculs tout turbulents et avec prise en compte de la transition ont été comparés à des mesures d'effort par balance, couplés à des observations de l'écoulement par PIV. Le foil bidirectionnel ainsi que le foil NACA en écoulement direct et inversé ont montrés des comportements singuliers qui pénalisent leurs performances dans l'optique d'une utilisation en tant que section de pale. A partir d'une valeur seuil, la hauteur de la rugosité de surface a montré engendrer un changement profond de la nature de l'écoulement autour du foil unidirectionnel. Finalement, il a été observé que la turbulence amont modifiait modérément les propriétés de ce type de foils, mais de façon moins significative à l'échelle de la pale.

Mots-clefs : analyse expérimentale, simulation numérique, hydrolienne, rugosité de surface, turbulence amont, bidirectionnalité, écoulement inversé.